Investigation of Moisture Influence and Solution Processable Encapsulation Strategies for Flexible Printed Electronics

Zur Erlangung des akademischen Grades einer

DOKTORIN DER INGENIEURWISSENSCHAFTEN (Dr.-Ing.)

von der KIT-Fakultät für
Maschinenbau des
Karlsruher Instituts für Technologie (KIT)

angenommene

DISSERTATION

von

M.Sc. Zehua Chen
geb. in Zhangping, Fujian, China

Tag der mündlichen Prüfung:	11.07.2025
Hauptreferent:	Prof. Dr.-Ing. Ulrich Gengenbach
Korreferent:	Prof. Dr. Veit Hagenmeyer
	Prof. Dr. Jasmin Aghassi-Hagmann

Kurzfassung

Flexible gedruckte Elektronik (FPE) ist ein schnell wachsendes Forschungsfeld mit vielversprechenden Anwendungen, z.B. Wearables, Sensoren und flexible Displays. Eine der größten Herausforderungen stellt dabei jedoch die feuchtigkeitsbedingte Degradation dar, da diese die Leistung, Lebensdauer und Zuverlässigkeit dieser Geräte beeinträchtigt.

Die vorliegende Dissertation konzentriert sich auf die Auswirkungen von Feuchtigkeit auf gedruckte Silberleiterbahnen und Kondensatoren, die mit zwei verschiedenen Nanopartikel-Tinten hergestellt werden. Zur Bewertung der Auswirkungen von Feuchtigkeit auf die elektrischen Eigenschaften der gedruckten Komponenten werden Umwelttests gemäß internationalen Standards entwickelt.

Die Ergebnisse der Umwelttests zeigen, dass Feuchtigkeit positive Effekte auf das Sintern von Tinten mit Polyvinylpyrrolidon- (PVP-) beschichteten Silbernanopartikeln (Ag NPs) hat. Zur Analyse des Einflusses von Feuchtigkeit beim Sintern dieser PVP-beschichteten Ag NPs werden Untersuchungen durchgeführt. Der Sintermechanismus der PVP-beschichteten Ag NPs im niedrigen Temperaturbereich wird dargestellt in Abhängigkeit der Zustände der PVP-Schicht unter verschiedenen Bedingungen. Basierend auf diesen Erkenntnissen werden zwei neuartige Sintermethoden bei niedrigen Temperaturen entwickelt: Feuchte-Wärme-Sintern und Wassersintern.

Zudem zeigen die Ergebnisse der Umwelttests, dass die Feuchtigkeitsaufnahme und -abnahme im dielektrischen Material (BST/P(VDF-TrFE)) der gedruckten Kondensatoren zu Schwankungen ihrer Kapazität führen. Eine Kapselung für diese gedruckten Kondensatoren ist erforderlich, um die feuchtigkeitsbedingten Kapazitätsänderungen zu minimieren.

Verschiedene Kapselungsmaterialien und -methoden für flexible gedruckte Elektronikkomponenten werden untersucht, wobei die lösemittelbasierte Kapselung mithilfe von Polymeren besonders hervorgehoben wird. Die Verlängerung der effektiven Weglänge der Permeation in einem Polymer gilt als vielversprechender Ansatz zur Verbesserung der Barriereeigenschaften. Diese kann erzielt werden durch das Einbringen von Füllstoffen in die Polymermatrix. Vier verschiedene Füllstoffe in Polyvinylalkohol (PVA) werden untersucht. Der Vergleich ihrer Wasserdampfdurchlässigkeitsraten (WVTR) zeigt, dass Glasflocken (GF) der effektivste Füllstoff sind, und ihre optimale Konzentration in PVA wird bestimmt. Die Barriereeigenschaft der PVA/GF-Filme wird durch die Kapselung von gedruckten Silberleiterbahnen und feuchtigkeitsempfindlichen Kondensatoren validiert.

Darüber hinaus wird ein kommerziell erhältliches Hybridpolymer, OrmoClear30, eingesetzt, um eine weitere lösemittelbasierte Kapselung zu realisieren. Eine neuartige "Dam and Fill" Dispensmethode für OrmoClear30 wird entwickelt, die die lokale Kapselung für die feuchtigkeitsempfindlichen Kondensatoren ermöglicht. Die signifikante Reduktion der feuchtigkeitsbedingten Kapazitätsänderung bestätigt die Wirksamkeit der Feuchtigkeitsbarriere dieser OrmoClear30-Kapselung. Im Anschluss werden die PVA/GF Kapselung und die OrmoClear30 Kapselung verglichen.

Abschließend werden zukünftige Forschungsfelder vorgeschlagen: die Untersuchung des Einflusses von Feuchtigkeit beim Sintern anderer metallischer Nanopartikel-Tinten, die Erforschung weiterer lösemittelbasierte Hybridpolymere als Kapselungsmaterialien sowie die Entwicklung eines automatisierten Biegesystems zur Bewertung der mechanischen Biegfestigkeit und der langfristigen Zuverlässigkeit von gekapselten FPE-Komponenten.

Zusammenfassend bietet diese Dissertation wertvolle Einblicke in die Auswirkungen von Feuchtigkeit auf spezifische FPE-Komponenten, die mit ausgewählten Nanopartikel-Tinten gedruckt sind. Sie präsentiert Ansätze zur Verbesserung ihrer Leistung und Haltbarkeit und leistet damit einen Beitrag zur Weiterentwicklung alternativer Sinterprozesse für PVP-beschichtete Ag NPs sowie zur Erweiterung der Einsatzmöglichkeiten von FPE-Komponenten in feuchtigkeitsempfindlichen Anwendungen.

Abstract

The development of flexible printed electronics (FPE) is a rapidly growing field with promising applications, including wearables, sensors, and flexible displays. However, moisture-induced degradation remains one of the key challenges, affecting the performance, longevity, and reliability of these devices.

This dissertation focuses on the moisture impact on printed silver tracks and capacitors fabricated using two nanoparticle inks. Environmental tests are designed in accordance with international standards to evaluate the impact of moisture on their electrical properties.

The environmental results show that moisture has positive effects on sintering of the polyvinyl pyrrolidone (PVP) capped silver nanoparticles (Ag NPs) ink. Systematic investigations are conducted to explore the role of moisture in the sintering of PVP capped Ag NPs. Taking the states of the capping layer under different conditions into account, a comprehensive explanation of the sintering mechanism of Ag NPs at low temperature ranges is provided. Based on these findings, two novel sintering methods at low temperatures, damp heat sintering and water sintering are developed.

The environmental test results also indicate that moisture absorption and desorption in the dielectric material (BST/P(VDF-TrFE)) of the printed capacitors lead to a variation in their capacitance. An encapsulation is needed for those printed capacitors to minimize this moisture-induced capacitance change.

Various encapsulation materials and methods for FPE devices are discussed and the solution processable encapsulation realized by using polymers is emphasized. One promising approach to improve a polymer's moisture barrier property is to create tortuous paths e.g. by adding fillers into the polymer matrix. Therefore, four fillers added in poly(vinyl alcohol) (PVA) are investigated. By comparing their water vapor transmission rate (WVTR) values, glass flakes (GFs) turn out to be the most effective filler type and its optimal concentration in PVA is determined. The moisture barrier property of PVA/GF films is validated by encapsulating the printed Ag tracks and the printed moisture-sensitive capacitors.

Moreover, a commercially available hybrid polymer, OrmoClear30, is utilized to form another solution processable encapsulation. A novel "dam and fill" dispensing method for OrmoClear30 is developed and a local OrmoClear30 encapsulation for the printed moisture-sensitive capacitors is realized. The significant reduction of moisture-induced capacitance change confirms the

moisture barrier effectiveness of this OrmoClear30 encapsulation. A comparison between the PVA/GF encapsulation and the OrmoClear30 encapsulation is provided.

Suggestions for future work include investigating the role of moisture in sintering of other metallic NP inks, exploring other solution processable hybrid polymers as encapsulation materials, and establishing an automated bending setup to evaluate the mechanical bendability and long-term reliability of encapsulated FPE devices.

In summary, this dissertation provides insights into the moisture impact on specific FPE components printed with selected NP inks. It presents solutions to enhance their performance and durability, thereby contributing to the development of alternative sintering processes for PVP capped Ag NPs and broadening the application of FPE devices in moisture-sensitive applications.

Acknowledgments

Completing this dissertation has been a long, challenging, yet rewarding journey, and I am deeply grateful to all the individuals and institutions that have supported me along the way.

Foremost, I would like to express my sincere gratitude to my supervisor, Prof. Dr.-Ing. Ulrich Gengenbach, for his invaluable guidance, encouragement, and unwavering support. His insights and expertise have been instrumental in shaping my academic growth, and I am truly fortunate to have had this opportunity to learn from him.

I would also like to extend my appreciation to Dr.-Ing. Liane Koker for her cosupervision and thought-provoking discussions, which have significantly enriched my work.

I would also like to thank Prof. Dr. Veit Hagenmeyer and Prof. Dr. Jasmin Aghassi-Hagmann for being reviewers of my dissertation and their constructive feedback, which has improved the quality of this work. I am grateful to Prof. Dr. Hans Jürgen Seifert for serving as the chair of my PhD examination committee.

In addition, I would like to thank the financial and institutional support provided by KIT, invaluable organisational support provided by Andreas Hofmann, the scientific administrative manager of the institute, and Annette Mika, Manuela Lang and Bernadette Lehmann.

Special thanks go to my colleagues at IAI (Nowab Reza MD Ashif, Moritz Böhland, Karin Chen, Liyu Huang, Moritz Lindmüller, Jianlei Liu, Maher Mansour, Daniel Moser, Andre Orth, Lisa Petani, Maxim Polomoshnov, Klaus-Martin Reichert, Martin Ungerer, Stefan Vollmannshauser, Yingcong Zhong, Shant Gananian, Kaixing Lei, Xinnan Liu, Yuxin Liu, and Junfeng Chen), IAM-ESS (Tim P. Mach), INT (Alexander Scholz), IMT (Richard Thelen), whose collaboration, stimulating conversations, and moral support have made this journey enjoyable.

I am also indebted to my family for their unconditional love and support.
谢谢爸爸妈妈!

A special thank you to my adorable cat Michio for bringing irreplaceable joy to my life.

This dissertation is a culmination of the collective support and encouragement of so many, and I am truly grateful for each and every one of you.

My deepest thanks to the Lord for making all this possible.

Contents

Acronyms

AAF	accelerated aging factor
AAT	accelerated aging time
AC	alternating current
AFM	atomic force microscopy
Ag	silver
AgNP	silver nanoparticle
ALD	atomic layer deposition
Ar	argon
AR	aspect ratio
ASTM	American Society for Testing and Materials
Au	gold
BA	boric acid
BST	$Ba_{0.6}Sr_{0.4}TiO_3$
Ca	calcium
CA	citric acid
CH	cyclic humidity
CIJ	continuous inkjet
CNF	cellulose nanofiber
Cr	chromium
CS	chitosan
CSPE	composite solid polymer electrolyte
Cu	copper
CV	coefficients of variation

CVD	chemical vapor deposition
DC	direct current
DIW	deionized water
DMSO	dimethyl sulfoxide
DOD	drop-on-demand
EAB	elongation at break
EDX	energy-dispersive X-ray spectroscopy
EGFET	eletrolyte-gated field-effect transistor
FET	field-effect transistor
FHE	flexible hybrid electronics
FOLED	flexible organic light emitting diode
FPE	flexible printed electronics
GA	glutaraldehyde
GF	glass flake
GO	graphene oxide
HDPE	high density polyethylene
IAI	Institute for Automation and applied Informatics
IAM – ESS	Institute for Applied Materials - Energy Storage Systems
IAPWS	International Association for the Properties of Water and Steam
INT	Institute of Nanotechnology
IPL	intense pulsed light
ITO	indium tin oxide
KCl	potassium chloride
KIT	Karlsruhe Institute of Technology
LLDPE	linear low density polyethylene
MA	malonic acid
MMT	montmorillonite
NaCl	sodium chloride

NaOH	sodium hydroxide
OLED	organic light emitting diode
OPSZ	organic polysilazane
ORMOCER	organically modified ceramics
OTR	oxygen transmission rate
P3HT	poly(3-hexylthiophene)
P_4O_{10}	phosphorus pentoxide
PAA	polyacrylic acid
PC	polycarbonate
PDAC	poly(diallyldimethylammonium chloride)
PDMS	polydimethylsiloxane
PE	printed electronics
PEDOT : PSS	poly (3,4-ethylenedioxy-thiophene): poly (styrenesulfonate)
PEEK	polyether-ether-ketone
PEN	polyethzlene naphthalate
PET	polyethylene terephthalate
PHPS	perhydropolysilazane
PI	polyimide
PMMA	polymethyl methacrylate
PVA	polyvinyl alcohol
PVB	polyvinyl butyral
PVC	polyvinyl chloride
PVD	physical vapor deposition
PVDF	polyvinylidene fluoride
P(VDF – TrFE)	polyvinylidene fluoride-co-trifluoroethylene
PVP	polyvinyl pyrrolidone
PIB	pure butyl rubber
PLA	polylactide

PLGA	polylactic-co-glycolic acid
PSZ	polysilazane
PTFE	polytetrafluorethylen
RH	relative humidity
RT	room temperature
SAG	static accelerated aging
SDH	static damp heat
SEM	scanning electron microscopy
TFT	thin film transistor
TGME	triethylene glycol monomethyl ether
TIPS	triisopropylsilyl
UM	ultramicrotome
UV	ultra violet
WVTR	water vapor transmission rate

1 Introduction

Conventional silicon-based electronics has been applied to fabricate numerous devices, e.g. computers, smartphones, and tablets, to perform various functions such as processing and storing information for more than 60 years [1]. Conventional silicon-based electronics are manufactured using deposition processes paired with high-resolution lithography. This approach allows for achieving exceptionally fine feature sizes, approaching just a few nanometers. The primary benefit is the ability to pack numerous circuits into a small area, resulting in a high integration density and enabling the creation of powerful components. However, the fabrication of conventional silicon-based electronics requires complicated repeated thin-film depositions, baking, lithography, developing, etching and packaging steps [2].

Printed electronics (PE) is an emerging technology that utilizes printing, coating, and dispensing techniques to deposit newly developed functional inks to fabricate electronic devices on diverse substrates. In addition, as shown in **Figure 1.1**, its fabrication requires less complicated process steps and less loss of raw materials compared to conventional silicon-based electronics [2, 3, 4, 5]. Flexible printed electronics (FPE) are devices printed on flexible substrates. The use of flexible substrates expands the application scope of PE devices, making them suitable for wearables, smart packaging, and healthcare monitoring systems due to their mechanical flexibility.

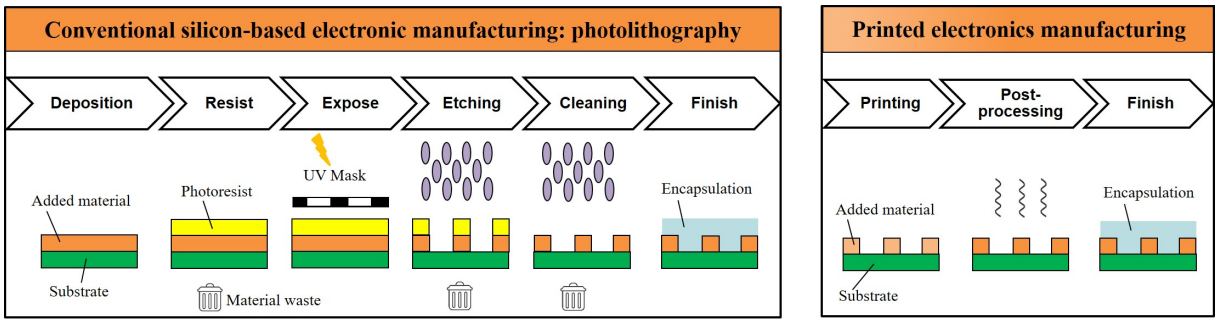

Figure 1.1: Comparison of process steps of conventional silicon-based electronics manufacturing using photolithography and printed electronics using printing techniques. In both process chains for a final product all but the last step have to be repeated multiple times (adapted from [2]).

However, the downside of PE technology is that the current printing techniques cannot reach the level of the conventional silicon-based electronic technology with respect to the integration degree, information capacity, resolution, etc [1, 4]. PE devices alone frequently do not suffice to achieve full functionality. To address this issue, one common approach is called flexible hybrid

electronics (FHE) [6, 7]. Silicon-based devices are mounted onto the substrate with printed structures. With this hybrid setup, the most beneficial properties of functional printing and silicon-based electronics are combined.

However, performance and reliability of printed components still remain as a challenge, since they can be significantly influenced by environmental factors, particularly moisture and oxygen. These can interact with the materials used in printed components, altering their electrical and mechanical properties. These interactions may happen along the entire product lift cycle, including during its fabrication processes and operational use, leading to failure in the device's performance [8].

To broaden the use of the FPE devices, depending on the application, they should be well encapsulated and protected from adverse environmental influences such as moisture and oxygen. There is a wide range for encapsulation requirements, varying from applications to applications [9]. Barrier property against moisture or oxygen is the most crucial factor of an encapsulation [10]. An overview of the order of magnitude of water vapor transmission rate (WVTR) and oxygen transmission rate (OTR) requirements of different kinds of FPE devices are shown in **Figure 1.2**. Organic light emitting diodes (OLEDs) have the most strict barrier requirements, the WVTR and OTR of their encapsulation should not exceed $10^{-6}\,\mathrm{g\,m^{-2}\,d^{-1}}$ and $10^{-5}\,\mathrm{mL\,m^{-2}\,d^{-1}}$ respectively. Wearables require less demanding barrier properties.

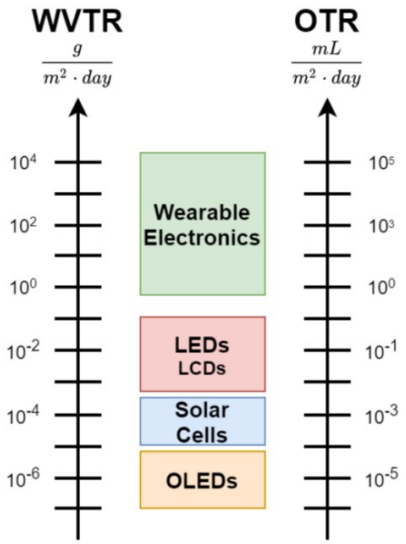

Figure 1.2: WVTR and OTR required for common flexible electronic devices. Adapted from [10].

Moreover, for FPE devices, a flexible or conformal encapsulation that globally or locally protects the devices is required [11, 12], but it should add little volume and weight to the devices. A global encapsulation covers the entire device while a local encapsulation protects the sensitive parts of the device (see **Figure 1.3 (b) and (c)**). For some specific devices, e.g for monitoring devices, a selective encapsulation which only allows the analyte to permeate the encapsulation layer is required. Furthermore, it is quite common for FPE devices to work under bending, stretching or

twisting forces. Therefore, another requirement of the encapsulation is its flexibility to make sure that even under those forces, the device still works stably [13] (see **Figure 1.3 (d)**).

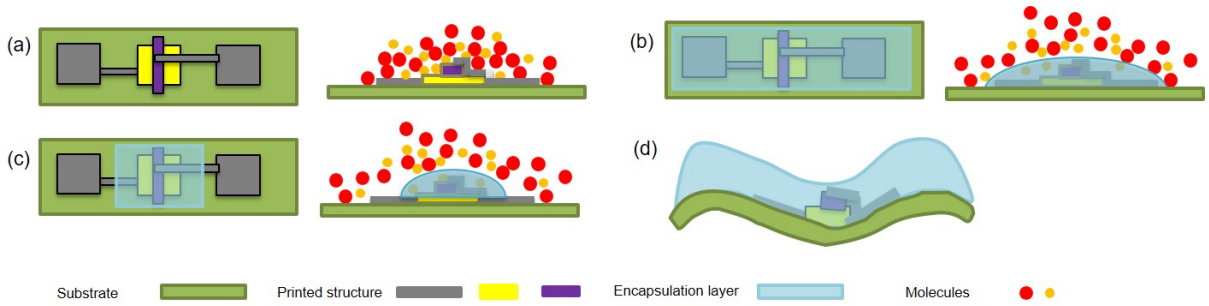

Figure 1.3: Encapsulation requirements. (a) FPE device without encapsulation. (b) FPE device with a global encapsulation layer. (c) FPE device with a local encapsulation layer. (d) illustration for the flexibility of an encapsulation layer.

The complexity, environmental friendliness and the cost of the encapsulation process also are considerable factors in industry. Thus, the encapsulation requirements for FPE devices can be concluded as follows.

- Low moisture or oxygen permeability: the encapsulation should provide a sufficient protection of the devices from moisture or oxygen.
- Flexibility: the encapsulation should be flexible enough, along with the devices substrates without the formation of cracks.
- Stability: the encapsulation should withstand the mechanical forces, such as bending, stretching or twisting forces.
- Processing simplicity: a simple, environmental friendly and low-lost encapsulation processing can help realizing the marketization of FPE devices.

Nowadays, encapsulation methods for FPE devices can be categorized into three main approaches: barrier film lamination, vacuum-deposited thin film encapsulation, and solution processable encapsulation [14].

In the barrier film lamination method, a barrier film is attached to the substrate or printed structures by adhesion, thermal bonding, or laser welding. However, this technique has a significant limitation — it does not allow for conformal encapsulation on non-planar surfaces, making it less suitable for complex device geometries.

Vacuum-deposited thin film encapsulation, on the other hand, involves depositing organic (such as Parylene C [15]) or inorganic materials (such as Al_2O_3 [16], TiO_2 [17], SiOx [18] or SiNx [19]) by chemical and physical deposition techniques, such as physical vapor deposition (PVD), chemical vapor deposition (CVD), and atomic layer deposition (ALD). Furthermore, multilayer

strategies combining both organic and inorganic layers are often applied to improve the barrier property. These methods achieve very low WVTR, reaching values as low as 10^{-5} g m^{-2} d^{-1} [16], thereby providing excellent moisture protection. Vacuum-deposited thin film encapsulation is widely utilized for protecting flexible organic light emitting devices (FOLEDs) used in displays, wearable devices and biomedical devices [20, 21]. However, a drawback of this approach is the requirement for sophisticated and costly vacuum equipment, such as an ALD reactor, which increases both production complexity and cost [14].

Solution processable encapsulation is an promising approach for FPE devices for its low cost and ease of processing. Solution processable polymers can be used as encapsulation materials directly deposited on the device surface to form barrier films using various printing, coating or dispensing techniques. Both global and local encapsulation can be realized by selecting suitable polymer materials and techniques. Moreover, the encapsulation process can also be integrated into the printing process chain.

As moisture-induced degradation to date is still a challenge for the longevity and reliability of FPE devices, the objective of this dissertation is to develop solution processable moisture barrier films for the encapsulation of FPE devices. Above all, this dissertation investigates the moisture impacts on the electrical properties of specific FPE components fabricated by nanoparticle inks. Solutions are sought to harness its positive effects while mitigating the negative ones. By selecting suitable materials and techniques, solution processable encapsulation methods are successfully developed to protect specific FPE components from moisture.

The content of this dissertation is organized as follows (see also **Figure 1.4**):

- Chapter 2 offers an overview of the materials and fabrication processes used in FPE. This chapter reviews the reported moisture impacts on FPE devices during both fabrication and usage. Fundamental principles of permeation are introduced, followed by a review of state-of-the-art solution processable encapsulation methods for flexible printed electronics. Lastly, current measurement techniques for assessing WVTR of barrier films are introduced.
- Chapter 3 investigates the moisture impacts on the performance of FPE components fabricated using specific nanoparticle inks. Environmental tests are designed and conducted in accordance with relevant international standards. The moisture influence is analyzed, and potential solutions are proposed to harness its positive influences while mitigating the negative ones.
- Chapter 4 explores the role of moisture in sintering of printed silver tracks using a specific silver nanoparticle ink at low temperature ranges. Experiments are systematically designed and conducted. The underlying sintering mechanisms are explained based on the experiment results. Two novel sintering methods for this silver nanoparticle ink are proposed and compared. Environmental tests are conducted to examine the durability of the electrical performance of printed silver tracks sintered by these two novel sintering approaches.

- Chapter 5 utilizes polymers to develop two solution processable barrier films for the encapsulation of the printed test structures. One approach involves incorporating fillers into the polymer matrix to enhance its moisture barrier properties. Four polymer/filler barrier films are investigated and compared. WVTRs are measured to choose the most effective filler. The moisture barrier effect of the selected polymer/filler films is further validated by encapsulating printed silver tracks and moisture sensitive capacitors. Another approach utilizes a commercially available hybrid polymer as the encapsulation material. Two dispensing methods for this hybrid polymer are developed. The moisture barrier effect of the resulting hybrid polymer films are validated by encapsulating moisture sensitive capacitors. Finally, a comparison between the polymer/filler encapsulation and the hybrid polymer encapsulation is provided.
- Chapter 6 summarizes the findings and achievements of this dissertation and outlines potential directions for future research.

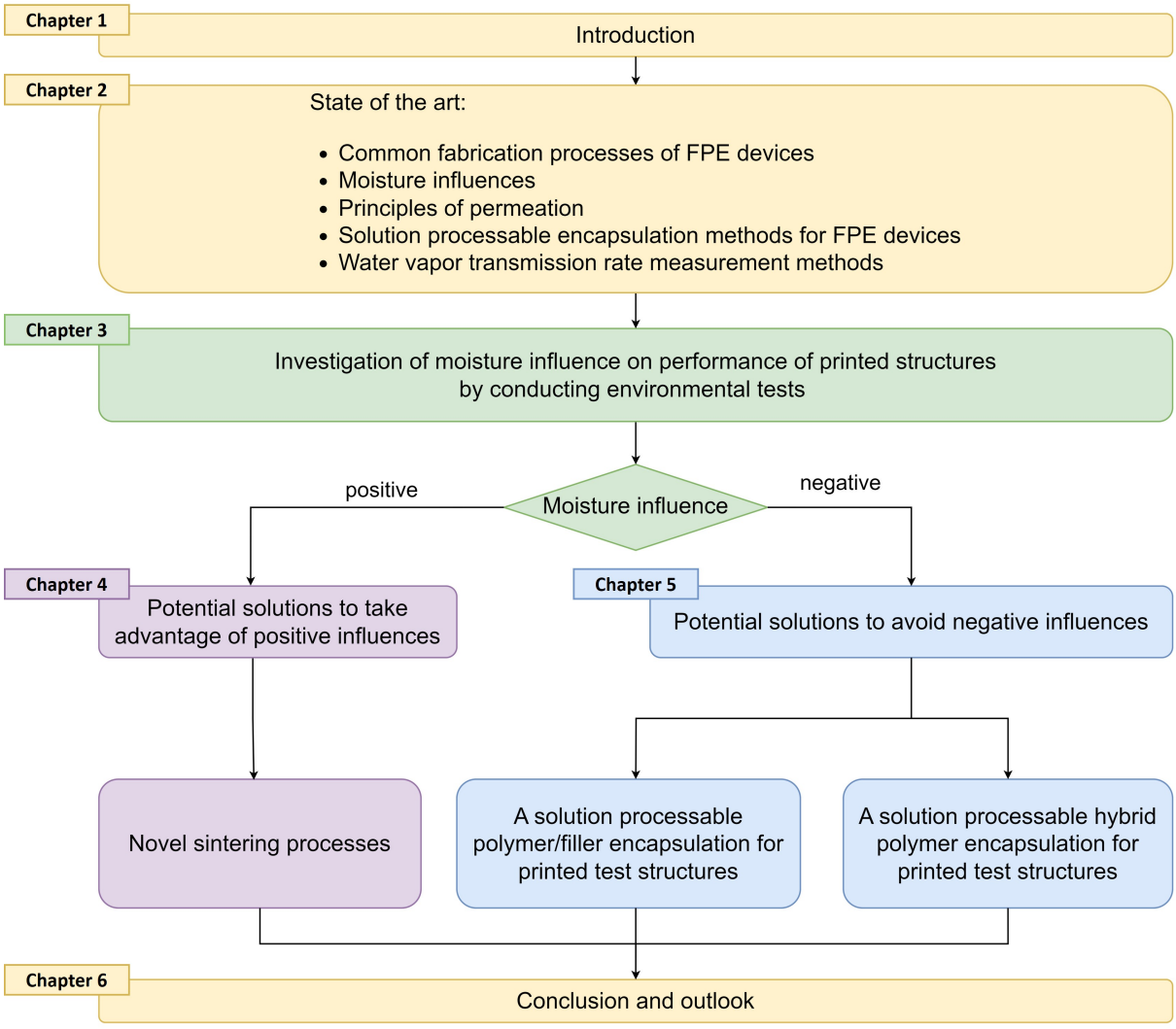

Figure 1.4: Overview of the dissertation.

2 State of the art

This dissertation focuses on the moisture influence on the performance of flexible printed electronics (FPE) both during its fabrication processes and operational use. Therefore, this chapter begins with an overview of the materials and fabrication processes commonly applied in FPE device development, followed by a review of reported moisture-related effects. The fundamental principles of permeation are introduced to provide a theoretical understanding of how moisture penetrates. Furthermore, current solution processable encapsulation approaches for FPE devices are reviewed. Measurement methods for water vapor transmission rate for the assessment of moisture barrier effectiveness of encapsulation are introduced. These foundational insights form the basis for the investigations presented in this dissertation. [1]

2.1 Fabrication of flexible printed electronic devices

Various novel materials, printing, coating and dispensing technologies, and post-treatments are applied to fabricate a variety of FPE devices [22, 23, 6]. The following sections provide an overview of the materials and fabrication processes commonly used in the development of FPE devices.

2.1.1 Materials

A FPE device can consist of multiple printed electronic components, such as conductive tracks, resistors, capacitors, and transistors, similar to those applied in conventional electronics. Flexible substrates provide the mechanical flexibility, while functional inks enable the desired electronic functionalities. This section introduces the commonly used flexible substrates and functional inks for the fabrication of FPE devices.

Flexible substrates Flexible substrates provide the mechanical flexibility of FPE devices. Nowadays, polymers, textiles, paper and biodegradable substrates such as silk and cellulose nanofiber (CNF) are commonly used as substrates in FPE [24]. Various polymers are utilized such as

[1] Parts of this chapter are published in: [14] Zehua Chen, Ulrich Gengenbach, Maher Mansour, and Liane Koker. Approaches for solution-processed encapsulation of printed medical wearable devices. Current Directions in Biomedical Engineering, 6(3):131–134, sep 2020. doi: 10.1515/cdbme-2020-3034.

polyethylene terephthalate (PET), polyethylene naphthalate (PEN), polycarbonate (PC), polyimide (PI), polyether-ether-ketone (PEEK), polyvinylidene fluoride (PVDF) and polydimethylsiloxane (PDMS) [25, 6, 26]. Among them, PET, PEN and PI are the most common substrates for FPE. **Table 2.1** summarizes the key properties of these three polymer materials. In the literature, PET is most frequently used due to its optical transparency and the great benefit of low cost. However, PET has a poor heat resistance, necessitating careful handling during processing, where low temperatures below 130 °C are required [27]. For applications requiring higher heat resistance, alternatives like PEN and PI offer better performance, but these may come with drawbacks such as reduced transparency and increased cost.

Table 2.1: Three commonly used polymer substrates for FPE and their key properties [25].

Substrate	Typical thickness (µm)	Transparency (%)	Density ($g\,cm^{-3}$)	Tg[1] (°C)	Youngs modulus (GPa)	A_H_2O[2] (%)	Ref.
PET	16-175	90	1.38	80	2.8	0.4-0.6	[6, 25]
PEN	12-250	87	1.4	120-155	3	0.3-0.4	[6, 25]
PI	12-125	30-60	1.4	410	2.5	1.3-3.0	[6, 25]

[1] Tg: glass transition temperature.
[2] A_H_2O: water absorption.

Functional inks Functional inks are printed on the flexible substrates to fabricate conductors and electronic devices such as resistors, capacitors, transistors. According to their electrical properties, functional inks can be classified into three types: conductive inks, semi-conductive inks, and insulating/dielectric inks [6].

In order to realize electrical conductivity, conductive materials such as metallic materials (silver (Ag), copper (Cu), and gold (Au) [25]), organic molecules (poly (3,4-ethylenedioxy-thiophene): poly (styrenesulfonate) (PEDOT:PSS) [28]), and ceramics (indium tin oxide (ITO) [29], carbon nanomaterials [30] and graphene [31, 32, 33]) are widely utilized in ink development. **Table 2.2** summarizes the most relevant conducting materials applied in conductive inks [27]. Among all the different types of conductive material, metallic materials, especially Ag, Au and Cu, possess the best conductivity values. Among them, Ag is more widely used due to its chemical stability (compared to Cu), relatively low cost (compared to Au), and the conductivity of its oxide form [34]. Recent advancements in nanomaterials and surface modification techniques have made it possible to effectively disperse metallic nanoparticles in solvents to develop metallic nanoparticle inks [1]. For instance, Ag nanoparticle (Ag NP) ink consists of a dispersion of Ag NPs, coated with capping agents to avoid agglomeration in the surrounding solvents. Many types of solvents are available, such as water, glycerol, ethylene glycol, ethanol, acetone, ethyl acetate, etc [35].

Capping agents commonly used in Ag NP inks are polyvinyl pyrolidone (PVP), polyacrylic acid (PAA), polyvinyl alcohol (PVA), alkanethiols, alkylamines, and carboxylic acids [35, 36].

Table 2.2: Materials used in conductive ink development for FPE [25].

Materials		Electrical conductivity ($S\,m^{-1}$)	Ref.
Metal	Ag	6.3×10^7	[34, 25]
	Cu	5.9×10^7	[37, 25]
	Au	4.4×10^7	[38, 25]
Organic	PEDOT:PSS	$100 - 10^5$	[28]
Ceramics	ITO	$10^5 - 10^6$	[29]
	CNT	10^6	[30]
	Graphene	2×10^6	[31, 32, 33]

Semi-conductive materials exhibit electrical conductivity between that of conductors and insulators, making them versatile for applications such as resistance control, signal amplification switching, and energy conversion. Their conductivity can be tuned through doping. Inorganic semi-conductive micro/nanoscale particles, wires, ribbons, and sheets (ZnO, TiO_2, CuO, SnO_2, In_2O_3, and MoS_2), are active components in semi-conductive inks [25, 28]. Organic materials such as poly (3-hexylthiophene) (P3HT) and triisopropylsilyl pentacene (TIPS-pentacene) have been successfully utilized in semi-conductive inks [25]. They offer flexibility, low-cost processing, and tunable optoelectronic properties but suffer from low carrier mobility and poor environmental stability [25]. **Table 2.3** summarizes the most relevant semi-conductive materials utilized in the ink development for FPE [25].

Table 2.3: Materials used in semi-conductive ink development for FPE [25].

Materials		Carrier mobility ($cm^2\,V^{-1}\,s^{-1}$)	Ref.
Inorganic	ZnO	≈ 150	[39]
	In_2O_3	≈ 3	[28]
	Cu_2O	≈ 90	[40]
	TiO_2	≈ 10	[41]
	SnO_2	≈ 500	[42]
Organic	P3HT	≈ 0.01	[43]
	TIPS-Pentacene	≈ 2	[44]

Insulator materials are crucial in FPE devices for forming non-conductive layers between conductive tracks, enabling multilayer structures such as capacitors and thin film transistors (TFTs) [45, 25]. In TFTs, insulators impact performance by affecting morphology, surface properties,

and the dielectric constant (ε), which influences threshold and operation voltages. Insulator materials can be inorganic ceramics, such as $Ba_{0.6}Sr_{0.4}TiO_3$ (BST) and $BaTiO_3$ (BTO) [46, 47], or organic, such as PVA, PVP, polymethyl methacrylate (PMMA) and PVDF [6, 25, 48, 49]. **Table 2.4** summarizes the most relevant insulator/dielectric materials utilized in the ink development for FPE. Organic dielectric materials are lightweight and flexible but have lower dielectric constant. Adding ceramic nanoparticles in polymers to improve their dielectric constants is a common approach to develop dielectric inks [50, 47].

Table 2.4: Insulator/dielectric materials used in ink development for FPE.

Materials		dielectric constant ε	Ref.
Inorganic	BST	283	[51]
	BTO	2000	[25, 52]
Organic	PVA	2.5	[50]
	PVP	5	[53, 54]
	PMMA	4	[46]
	PVDF	≈ 10	[55, 47]

2.1.2 Substrate treatment

In general, before printing functional inks on a flexible substrate, substrate treatment is performed to improve printing resolution and enhance adhesion between the printed structures and the substrate. Printing resolution is primarily determined by the wetting of the deposited ink on the substrate. The contact angle is the primary descriptor of surface wettability: a contact angle of 0° represents complete wetting. A surface is considered wettable if the contact angle is between 0° and 90°; if it exceeds 90°, the surface is classified as non-wettable. Various substrate treatment methods, such as wet chemical treatment and plasma treatment, are widely used to modify substrate wettability [23, 56, 57].

2.1.3 Printing and coating techniques

Functional inks can be deposited on flexible substrates using various printing and coating techniques. As defined by Nisato [58], printing is the reproduction of patterns, while coating techniques, such as spin coating and doctor blading, are more suitable for large-area coverage and coarse patterning. According to [59], printing techniques can be divided into two categories: conventional printing (with a master), such as screen printing, offset printing, and gravure printing, and non-impact printing (masterless), such as inkjet printing. The following sections describe

the printing and coating techniques used in this dissertation, namely inkjet printing and doctor blading.

Inkjet printing Inkjet printing is a digital printing process that does not require the patterning of plates, cylinders, or masks. Inkjet printing can be classified into two main categories: continuous inkjet (CIJ) printing and drop-on-demand (DOD) inkjet printing. In CIJ, a continuous stream of ink droplets flows from the nozzle. These droplets are electrically charged by a pair of electrodes and pass through a deflection system with two plates. The plates deflect the droplets more strongly based on the charge applied to them. This system directs the ink either onto the substrate or deflect it if no pixel is to be printed. A collection system recycles the ink back into the tank to minimize material losses (see **Figure 2.1 (a)**). However, ink that flows past the substrate and could theoretically be reused often becomes unusable due to external factors, such as solvent evaporation and contamination, leading to high material wastage and low cost-effectiveness. DOD printers emit an ink droplet only when it is needed to form the print pattern (see **Figure 2.1 (b)**), making more efficient use of available resources [60].

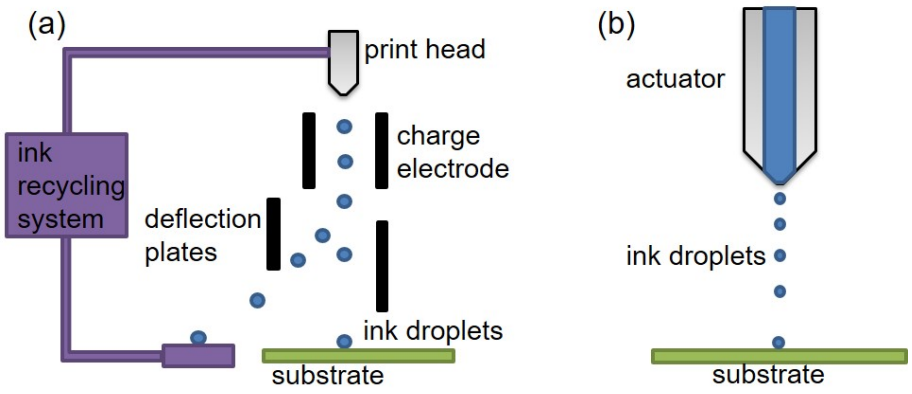

Figure 2.1: Illustration of two types of inkjet printing: (a) continuous inkjet (CIJ) printing and (b) drop-on-demand (DOD) inkjet printing. Adapted from [60].

DOD inkjet printing is commonly utilized in the development of FPE devices [60, 61]. Thermally actuated and piezoelectric print heads are the two primary types for generating ink droplets [60]. In a thermally actuated print head, when the heating element of the ink reservoir is activated, a part of the ink evaporates, forming a gas bubble and providing the pressure to expel the ink [60]. A piezoelectric print head utilizes piezoelectric crystals that deform under an electric signal to generate pressure. When a voltage pulse is applied, the piezoelectric reservoir walls contract, generating the pressure to eject ink droplets [60]. For every ink a proper waveform of the voltage pulse has to be determined to achieve proper droplet ejection (i.e. no satellite droplets) and to control droplet size [61, 62]. Single nozzle piezoelectric print heads are frequently used for vector printing, while multi-nozzle print heads are used for raster printing [59].

Doctor blading Doctor blading is a widely used coating technique for producing thin films on large-area surfaces [63]. It involves a blade, which is typically made of metal or plastic and is used to scrape or "doctor" the coating material onto the substrate to achieve a uniform and controlled thickness. Doctor blading begins by positioning the blade at a fixed distance from the substrate. A coating material is placed in front of the blade, and the blade is moved along the surface to create a wet film (see **Figure 2.2**). The film thickness can be controlled at the micrometer level by adjusting the gap between the blade and the substrate.

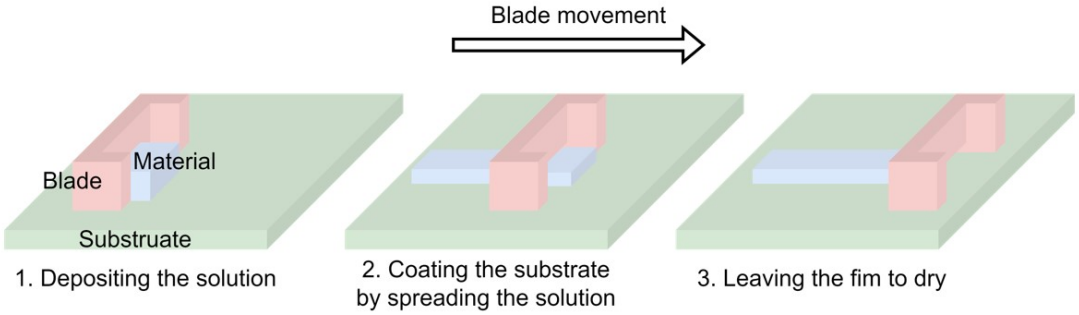

Figure 2.2: Schematic illustration of a doctor blading process.

2.1.4 Fluid dispensing techniques

Besides the printing and coating techniques mentioned above, the fluid dispensing technique is commonly used in the fabrication of FPE devices. This method is typically applied to relatively high-viscosity materials such as silver paste and adhesives, used to build conductive tracks or for electrical and mechanical interconnections between printed structures and rigid components in FHE devices [64].

Fluid dispensing techniques are commonly classified into two categories: contact and non-contact dispensing [65]. Contact dispensing involves both the needle tip and the substrate in contact with the fluid. Non-contact dispensing, also called jetting dispensing, involves ink being ejected directly from the nozzle without the dispenser contacting the substrate [66].

In contact dispensing, time-pressure dispensing is commonly used. A time-pressure dispensing system consists of a cartridge with a dispensing needle and a compressed air connection. The liquid is conveyed through the dispensing needle under switchable pressure. The amount of liquid dispensed depends on the duration the valve is open and the air pressure applied to the cartridge. Due to the compressibility of air and the increasing dead volume within the cartridge as it is emptied, as well as the continuous heating of the fluid due to the cyclical compression and expansion of the air, the system tends to have poor reproducibility. Variations in the dispensed volume can be observed over time, even though the pressure and dispensing time remain unchanged. The main advantages of this dispensing system are its low cost and the easy-to-use, disposable dispensing needle [65].

2.1.5 Post-treatments of printed structures

After printing, post-treatment may be required to achieve the final performance of FPE devices. This step helps to improve the electrical conductivity, mechanical strength, surface finish, or a combination of these properties in the printed structures [25]. Different types of functional inks require different post-treatment processes. Generally, the printed wet structures require a drying process. Printed structures made with metallic NP inks require a sintering process to enhance their functionality, while polymer inks may require a curing process to complete the final polymerization.

Drying of inks The printable inks are fluids. The printed wet structures need be dried to remove the solvents and adhere to the substrate. They can be dried under room temperature (RT), or thermally dried on a hotplate or in an oven, or vacuum dried in a vacuum chamber. Thermal and vacuum drying accelerate the drying process.

Sintering of metallic NP inks Metallic NP inks are widely used in FPE devices. After drying, most solvents are removed. However, due to the residues of solvents and the capping agents around the NPs, the contact area between NPs is limited, the dried printed structures are generally not conductive or have a high resistance [2]. A suitable sintering process is required. During sintering, diffusion processes ensure the formation and growth of necks between touching NPs, thus leading to their growth and ultimately to a densification of the porous network of the printed structures [2, 36, 67]. Depending on the type of metallic NPs, the sintering process can require a protective atmosphere such as vacuum, inert gas, or reducing atmospheres to avoid unwanted oxidation. In addition, except for more expensive high-temperature substrates such as PI films, most polymer films can not withstand high temperatures above 150 °C, the temperature of the sintering process must be carefully adjusted to avoid substrate damage [68].

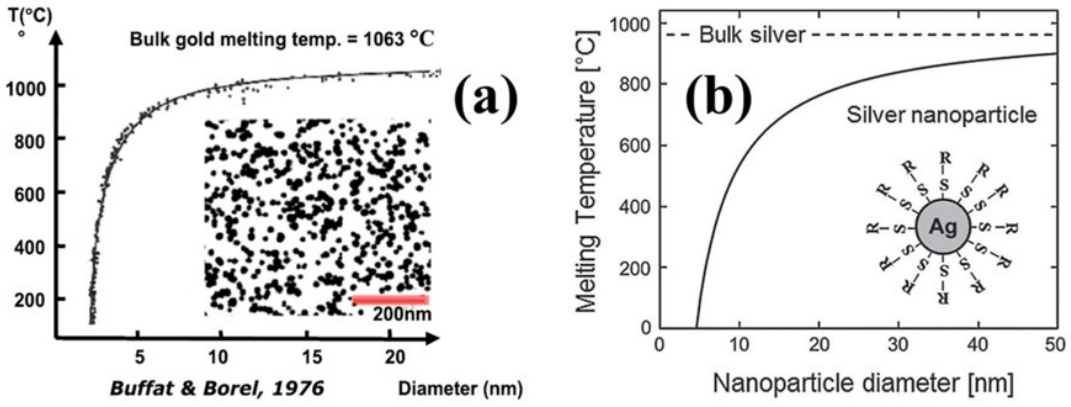

Figure 2.3: Experimental and theoretical values of the melting point temperature of (a) Au NPs and (b) Ag NPs [36]. Reproduced with permission. Copyright 2019, the authors. Licensee MDPI, Basel, Switzerland.

As metal particles are scaled down towards single nanometer level, their melting temperatures exhibit a decrease in line with their reduced dimensions [69]. This melting point depression behavior is depicted in **Figure 2.3**, the melting temperature of Au particles experiences a substantial reduction when their diameter falls below the range of five to seven nanometers [70]. This phenomenon of size-dependent melting temperature decrease has also been observed in Ag NPs [71]. Specifically, Ag NPs with diameters of approximately six nanometers exhibit a distinct melting behavior at significantly lower temperatures, around 150 °C, in sharp contrast to the melting temperature of bulk silver, which stands at 960 °C.

In this dissertation, an Ag NP ink is utilized. Therefore, the following sections focus on various sintering methods for Ag NP inks.

Thermal sintering: Ag NPs show a melting point depression compared to bulk Ag [72]. Thus, thermal sintering is the most commonly used sintering method for Ag NP inks [73, 74, 25]. The printed structures along with the substrate are together subjected to high temperatures, typically between 100 °C to 400 °C, in an oven or on a hot plate [75]. A thermal sintering process usually takes more than 30 min [76].

Electrical sintering: By applying direct current (DC) or alternating current (AC), across the printed region, the resulting ohmic heat can be locally and rapidly transfered to sinter Ag NPs [77, 78]. However, the printed structures need to be slightly conductive in order to generate ohmic heating, thus a drying process is required prior to an electrical sintering process. It is found that the initial resistance and input voltage greatly affect the resulting conductivity [79]. If the initial resistance is too high, the electrical sintering might not work even by rising the applied input current; if the initial resistance is too low, the printed region might be burn when high input currents are applied.

Photonic sintering: The heat for sintering can also be locally and rapidly transfered by the absorption of light (IPL [80, 81], laser [80, 82], or infrared light [83]). The selection of a particular wavelength, the control of irradiation parameters and the use of specific photo-responsive chemical agents are crucial factors for the performance of a photonic sintering process [84].

Plasma sintering: Plasma is an ionized gas generated by applying high energy (heat, electric current, or electromagnetic irradiation) on the desired gaseous species. These excited species like ions, electrons, and neutrals can decompose the capping agents on the surface of Ag NPs, leading to a sintering effect of the printed structures [85, 67]. This process can be conducted at low temperatures. A plasma sintering process usually requires a processing time of at least 30 min, as the process occurs from the top to the bottom of the printed layer [67].

Chemical sintering: Chemical sintering is a simple, effective, and low-temperature (down to room temperature) sintering process. The capping agents on the surface of Ag NPs can be removed by using destabilizing agents such as poly(diallyldimethylammonium chloride) (PDAC) [86], sodium chloride (NaCl) [87], potassium chloride (KCl) [88] and sodium hydroxide (NaOH) [89].

After this destabilization process, coalescence of the Ag NPs occurs, resulting in neck formation between the Ag NPs and thus, improved conductivity of the printed Ag structures. However, since chemical sintering is typically a solution-based process, the printed structures must be dried before being immersed in the destabilizing agent solution. Moreover, the destabilizing agent needs to be subsequently removed by washing [87, 90]. This additional step can weaken the adhesion between the printed layer and the substrate, which can require an additional post-treatment for the adhesion improvement [68, 87, 91, 92].

Curing of polymer inks In FPE, polymer inks are often used as insulator/dielectric inks to print non-conductive layers between conductive tracks, enabling multilayer structures such as capacitors and TFTs [25, 45]. After printing, a further curing process, such as thermal or UV curing, can be required to toughen or harden the polymer material by cross-linking of polymer chains [93, 94]. Similar to a sintering process, it is also beneficial when the curing process can be executed at low temperatures to avoid polymer substrate damage [95]. **Table 2.5** lists some typical curing processes for various polymer insulator/dielectric inks and their curing process parameters.

Table 2.5: Curing process for various polymer insulator/dielectric inks

Insulator/dielectric ink	Substrate	Printing/coating technique	Curing technique	Curing temperature	Curing time	Ref.
PVA	PI	Aerosol jet	Thermal	80 °C to 90 °C	15 min	[96]
PVP	PET	Inkjet	Thermal	130 °C	20 min	[97]
PMMA	Glass	Spin coating	Thermal	100 °C	10 min	[98]
PVDF-TrFE	PI, PET	Inkjet	Thermal	140 °C	2 h	[99]
SU-8	PI	Inkjet	UV	RT	seconds	[100, 101]

2.2 Moisture influences on flexible printed electronic devices

Nowadays, most of the FPE devices are still on lab scale. In order to broaden the use of FPE devices, long-time stable functionalities of these devices should be guaranteed. It is crucial to investigate the influences of moisture and oxygen on the performance of FPE devices, both during their fabrication process and in the use/storage phase [102, 103]. In this section, these influences of moisture are discussed in detail.

2.2.1 Moisture influences during FPE device fabrication

The presence of moisture can lead to various issues during different stages of fabrication, affecting the performance and reliability of the final FPE devices. This influence can be both positive and negative. Moisture is found to be beneficial for the sintering of Ag NPs. Allen et al. obtain a resistivity of printed Ag patterns of 5.88 µΩ cm by exposing substrates with ink-receptive coatings to 85 % relative humidity (RH) at room temperature before and after printing [104]. Olkkonen et al. find that a significant enhancement in conductivity can be obtained with pure boiling water treatment after drying of Ag NPs [87]. Bourassa et al. expose the printed Ag pattern to water vapor by placing a measured amount of water (10 g) in a bottom tray in the oven during the sintering process at 120 °C for 60 min, resulting in a resistivity of 3.24 µΩ cm [105]. They assume an influence of moisture on the capping agents on the surface of Ag NPs and an influence of capillary forces, which promote the neck formation between Ag NPs and result in a better conductivity [105]. Moisture improves the sintering effect of Ag NPs, however, for other metallic NP inks, moisture is a negative factor, for instance, owing to the atomic structure, copper can easily react with water and oxygen to produce oxides (CuO, Cu_2O) under ambient conditions [106]. Especially on the nanometer level, the higher specific surface area makes Cu NPs more susceptible to oxidation, which seriously hinders electron transfer and increases the resistance of the printed film [107]. Cu produces oxides in an air atmosphere. Thus, it is necessary to carry out the thermal sintering under vacuum or inert gas [107]. **Table 2.6** summarizes the positive/negative influence of moisture on Ag and Cu NPs in different FPE fabrication processes.

Table 2.6: Moisture influence during fabrication

Material	Fabrication process	Moisture influence on conductivity [1]	Ref.
Ag NP	Substrate treatment	++	[104]
Ag NP	Sintering	++	[87, 105]
Cu NP	Sintering	–	[107]

[1] Positive influence: "++"; negative influence: "–".

2.2.2 Moisture influences during FPE device use

Moisture can play a positive or a negative role in the fabrication of FPE devices. Similarly, it can also impact the performance and reliability of FPE devices during use, either positively or negatively. This section first introduces the negative influences of moisture.

Organic and inorganic materials are often used for the fabrication of FPE devices. Organic materials are much more vulnerable to moisture compared to inorganic materials. When organic layers are exposed to moisture, they undergo oxidation and crystallization, leading to degradation, morphological changes, and functional impairments in devices [108]. Moisture is a major concern

for the lifetime of FPE devices that utilize moisture-sensitive organic materials, such as printed flexible OLEDs (FOLEDs). The bending of the FOLEDs can create stress points which may lead to encapsulation layer breaches. Once moisture penetrates the OLED structure, it can trigger chemical reactions with the organic materials, breaking chemical bonds and leading to decomposition. Moisture can also corrode the electrodes, leading to electrical shorts and device failure. As moisture interacts with the OLED layers, it can cause delamination, where layers separate from each other. This moisture-induced degradation accelerates the aging of FOLEDs, significantly reducing their operational lifetime [109].

Moisture is a negative factor for FOLEDs, however, it can also be a necessary factor or have beneficial effects for other FPE devices, as they require a certain level of humidity for the device functionality. Printed electrolyte-gated field-effect transistors (EGFETs) are widely used in biosensing applications due to their high sensitivity, low operating voltage, and compatibility with flexible substrates. Their ability to detect ionic and biochemical interactions in real-time makes them ideal for applications in healthcare monitoring, environmental sensing, and lab-on-a-chip devices [110].

Composite solid polymer electrolytes (CSPEs) are commonly used as gate-insulators in a field-effect transistor (FET) due to their high gate capacitance, printability, and high ion conductivity [111]. Marques et al. fabricate EGFETs with a CSPE comprising PVA, propylene carbonate, dimethyl sulfoxide (DMSO), and lithium perchlorate and precursor derived indium oxide as the semiconductor channel. **Figure 2.4** illustrates the schematic structure of such a CSPE-gated FET [111].

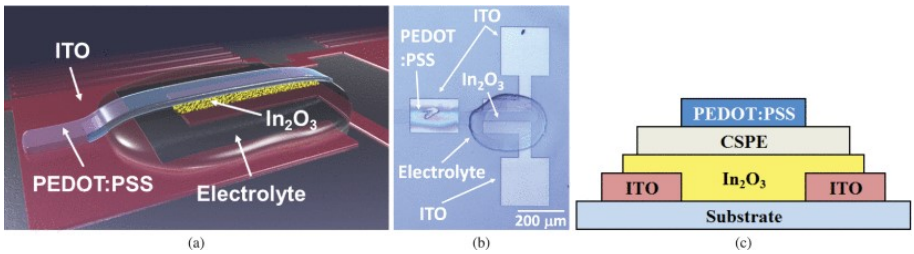

Figure 2.4: Schematic structure of a CSPE-gated FET [111]. Reproduced with permission. Copyright 2019, IEEE.

They conduct a comprehensive study to investigate the effect of humidity on CSPE-gated FETs. As shown in **Figure 2.5**, their results indicate that at RH levels below 20 %, the CSPE-gated FET does not switch off, regardless of the applied gate–source voltage. This scenario occurs since the printed CSPE has a high surface-to-volume ratio, causing trapped solvents to evaporate. This disconnects the solvent channels, resulting in situations similar to dry polymer electrolyte with much lower conductivity values [111]. The printed thin CSPE layers require a minimum humidity level to establish conducting pathways for ion mobility and to obtain high conductivity, which is essential for the device operation.

An encapsulation layer prevents moisture from both entering and escaping the device's functional layer. A proper encapsulation can maintain the humidity in a certain level under which the FPE device works stably.

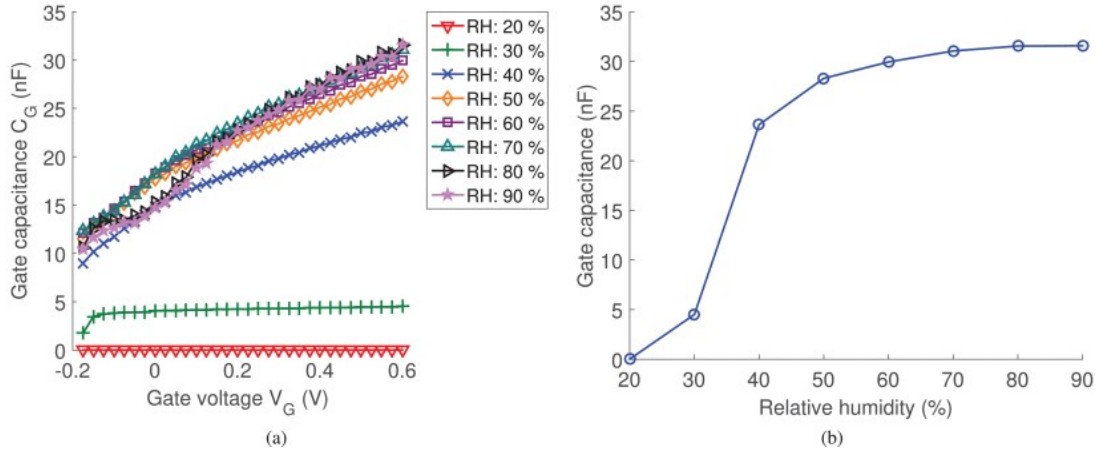

Figure 2.5: (a) Transistor capacitance (C_G) versus the gate voltage (V_G) at different RH levels. (b) Gate capacitance (C_G) plotted against the RH at a gate voltage (V_G) of 0.6 V [111]. Reproduced with permission. Copyright 2019, IEEE.

2.3 Fundamental principles of permeation

Moisture can negatively impact the performance of FPE devices during their operational use, making encapsulation essential for protection. Permeation of moisture through the encapsulation layers into FPE devices is a major concern for the lifetime of FPE devices [112, 113, 114].

This section presents the theoretical background of permeation principles to explain how moisture penetrates. Furthermore, since this dissertation focuses on using polymers to form flexible barrier films for encapsulation, factors affecting polymer permeability are introduced. Finally, methods to enhance the barrier properties of polymers are discussed.

2.3.1 Theoretical background of permeation principles

The permeation of a gas or vapor across an encapsulation layer depends both on the solubility of the permanent molecules into the encapsulation layer and their ability to diffuse through it [115, 114].

The permeation mechanism of a gas or vapor through an encapsulation layer with thickness l, area A, permeant pressure p_1 on the side with high permeant molecules concentration c_1 and pressure p_2 on the side with low permeant molecules concentration c_2 (where $p_1 > p_2$ and $c_1 > c_2$) involves three steps: adsorption, diffusion and desorption as shown in **Figure 2.6**.

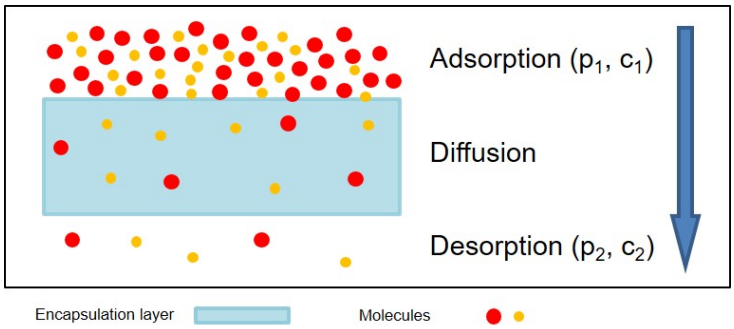

Figure 2.6: General mechanism of gas or vapor permeation through an encapsulation layer.

- **Adsorption**: permeant molecules attach to the surface of the encapsulation layer at the side with higher potential (p_1 and c_1). If the gas or vapor is soluble in the encapsulation material, the molecules dissolve in the upper layer [116].
- **Diffusion**: permeant molecules physically diffuse across the entire thickness of the encapsulation layer (l), moving from an area of high concentration to an area of low concentration, eventually reaching the opposite side.
- **Desorption**: permeant molecules are released from the encapsulation layer into the lower potential region (p_2 and c_2).

Fick's first law is the fundamental law of diffusion. Fick's first law states that the flux of a substance through a medium is directly proportional to the concentration gradient of that substance. Referring to Fick's first law, the quantity of substance Δm that passes through a unit area A in a unit time Δt, which is known as flux (J), can be obtained as follows:

$$J = \frac{1}{A} \times \frac{dm}{dt} = -D \times \frac{dC}{dx} \tag{2.1}$$

where: J is the flux of the substance, D is the diffusion coefficient of the substance in the medium, $\frac{dC}{dx}$ is the concentration gradient of the substance along the distance x.

In the steady state, where concentration is not varying with time and the diffusion flux (J) remains constant, the flux of diffusion across a membrane with a thickness (l) and concentrations (C_1 and C_2) of the permeant on opposite sides of the membrane can be obtained as follows:

$$J = \frac{1}{A} \times \frac{\Delta m}{\Delta t} = -D \times \frac{C_2 - C_1}{l} \tag{2.2}$$

The total amount of permeant Δm diffusing through the encapsulation layer is obtained as:

$$\Delta m = -A \times \Delta t \times D \times \frac{C_2 - C_1}{l} \tag{2.3}$$

Rather than measuring concentrations at the encapsulation surfaces, it's more practical to measure the permeant's partial pressure, denoted as p, on both sides of the encapsulation layer. The adsorption of gases in polymers is described by Henry's law [117]. Assuming Henry's law is valid on both surfaces, the concentration C of permeant that will dissolve in the polymer at a partial pressure p of the permeant can be mathematically expressed as:

$$C = S \times p \tag{2.4}$$

where S is the solubility coefficient of the permeant in the medium, the unit of S is mol m^{-3} Pa^{-1}.

Thus, the total amount of the permeant can also be obtained as:

$$\Delta m = -A \times \Delta t \times D \times S \times \frac{p_2 - p_1}{l} \tag{2.5}$$

The permeability P:

$$P = D \times S = -\frac{\Delta m}{A \times \Delta t} \times \frac{l}{p_2 - p_1} \tag{2.6}$$

For the diffusion of the permeant, permeability is the proportionality constant between the flow of the permeant through an encapsulation layer thickness per unit area per unit time and per pressure drop across the encapsulation layer. Permeability can vary with both pressure drop and film thickness [115, 118]. Thus, in the case of water vapor, data is usually expressed in terms of WVTR, which is defined as the rate of passage of water vapor through a given area of material in a specific time:

$$WVTR = \frac{\Delta m}{A \times \Delta t} \tag{2.7}$$

Permeability calculated using equation 2.6 represents the average vapor or gas permeability under specific test conditions. Hence, it's crucial to record the relative humidity and the temperature on both sides of the encapsulation layer during experimental determination of permeability or WVTR [119, 115, 118]. The WVTR is usually given in mass unit as g m^{-2} d^{-1} [114].

2.3.2 Factors affecting moisture permeability of polymers

Polymer films are usually applied as encapsulation materials for FPE devices. Various chemical and physical factors can influence the moisture permeability of these films [120, 121]. In this section, factors which can increase or decrease the moisture permeability of polymer films are described.

Positively correlated factors

- **Temperature of polymer/permeant**: Elevating the temperature of a polymer or permeant increases the permeation rate due to two primary factors. Firstly, higher temperatures enhance the solubility of the permeant within the polymer. Secondly, increased thermal energy enhances polymer chain mobility, allowing the permeant to diffuse more easily [121]. The temperature dependence of diffusion D, solubility S, and permeability P coefficients follows the Arrhenius relationship [120].

$$D = D_0(e^{-\frac{E_D}{RT}}) \tag{2.8}$$

$$S = S_0(e^{-\frac{\Delta H_s}{RT}}) \tag{2.9}$$

$$P = P_0(e^{-\frac{E_p}{RT}}) \tag{2.10}$$

  Where E_D and E_p are the activation energies of diffusion and permeation, respectively. ΔH_s is the heat of the permeant in the polymer and D_0, S_0 and P_0 are the pre-exponential factors. R is the universal gas constant and T is temperature. E_P and E_D are related as follows:

$$E_p = E_D + \Delta H_s \tag{2.11}$$

  Referring to the equations above, the permeation rate is increased as temperature rises. Hence, it's crucial to record the temperature during experimental determination of permeability.

- **Pressure/permeant concentration**: Since diffusion is driven by the pressure/concentration gradients, the permeation rate of gases increases at higher partial pressures. For liquids, permeation rates rise with an increase in the concentration of the permeant [122]. Unless the permeant species are highly soluble in the polymer, the permeation rate increases linearly with pressure and concentration [121, 122].

- **Polymer/permeant chemical similarity**: A similarity of chemical functional structures of the polymer and the permeant will promote solubility and permeation rate [121]. A polar chemical exhibits a lower permeation rate in a nonpolar polymer compared to a polar polymer, and vice versa. This phenomenon occurs because chemicals with similar structures to the polymer can cause swelling, thereby increasing the space between polymer chains and facilitating permeation [121]. Permeants dissolve in polymers with similar solubility parameters [123]. Using Hansen solubility parameters is an approach to predict the solubility of permeants in polymers [123].

- **Voids in polymers**: Voids are gaps or air bubbles within the polymer structure that can effect the movement of gases or liquids within the polymer. A higher number of voids

generally increases permeability, as they provide pathways for gases or liquids to travel through the polymer, making diffusion through the polymer easier.

Negatively correlated factors

- **Permeant size**: The molecular size of the permeant, its chemical structure, and its condensation characteristics affect permeation. Diffusion of the permeant increases as its molecular size decreases, thus contributing to an increase in permeation.
- **Polymer thickness**: For a typical hydrophobic polymer film, the rate of permeation experiences a significant decline as the film thickness increases. Initially, at lower thickness levels, the permeation rate is notably high, but it gradually decreases in an almost exponential manner as the thickness increases. Once a critical thickness is surpassed, the influence of thickness diminishes, and the permeation rate levels off, forming a plateau (see **Figure 2.7**) [121, 122].

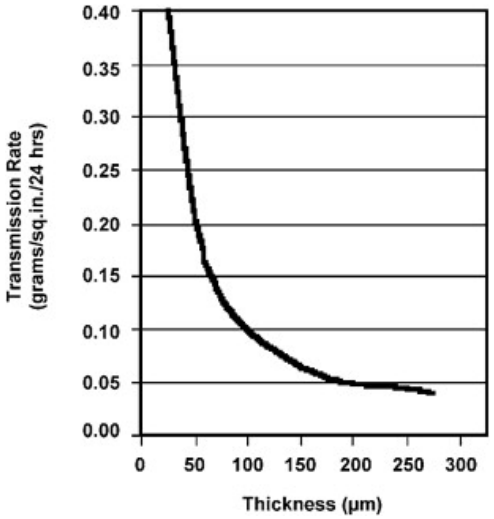

Figure 2.7: Water vapor transmission rate of Teflon® perfluorinated ethylene propylene resins at 40 °C [121]. Reproduced with permission. Copyright 2015, Elsevier.

- **Polymer crystallinity**: Polymer crystallinity refers to the degree of structural order in a polymer, where molecular chains are arranged in a regular, repeating pattern, forming crystalline regions within the material. Crystallinity is an important factor, which depends on the polymer chemistry and can to some extent be controlled during the processing of the polymer. For semicrystalline polymers:

$$S = S_0(1 - \phi_c) \tag{2.12}$$

where S_0 is the solubility coefficient of the amorphous phase, ϕ_c is the volume fraction of the crystalline phase [113]. For a purely crystalline phase, $S = 0$, thus, the crystalline phase

is generally considered impermeable due to its tightly packed, highly ordered structure, which reduces its specific volume. As a result, there is little to no free space between polymer chains for permeants to pass through. In contrast, the amorphous phase has a random, less compact structure with interchain spaces that allow for permeation. The specific volumes of the crystalline ($0.43\,cm^3\,g^{-1}$) and amorphous ($0.5\,cm^3\,g^{-1}$) phases of polytetrafluoroethylene (PTFE) support this argument. The amorphous phase has a 13 % higher specific volume, providing additional space for permeation [121, 124, 117].
The presence of crystallites has dual effects on the diffusion process. Firstly, they serve as barriers to permeant molecules, compelling them to traverse longer routes. Furthermore, the existence of crystals can immobilize side-chains within the amorphous phase, subsequently diminishing the available free space. This reduction leads to elevated activation energies for diffusion [117].

- **Polymer cross-linking grade**: Cross-linking refers to the formation of covalent bonds between polymer chains, creating a three-dimensional network. Cross-linking acts somewhat similar to crystallinity [121]. Highly cross-linked polymers tend to have lower permeability [120]. The interconnected network limits the movement of permeant molecules, preventing them from easily diffusing through the polymer. On the other hand, less cross-linked or non-cross-linked polymers have higher permeability. The absence of strong interconnections between polymer chains allows for more open pathways for permeant molecules to move through the polymer.

- **Polymer chain stiffness**: The permeability of a polymer is influenced by the stiffness of its chain structure. A polymer with rigid and closely packed chains tends to have lower permeability. This is because the restricted movement of stiff polymer chains creates fewer pathways for gas or vapor molecules to diffuse through the polymer. As a result, the permeant encounters more resistance, leading to a lower permeability value. On the other hand, a polymer with more flexible and loosely arranged chains allows for greater free volume between the chains. This increased free volume provides more room for gas or vapor molecules to move, promoting higher permeability [125].

- **Polymer interchain forces**: Polymer interchain forces influence how tightly polymer chains are packed together, which in turn affects the ability of gases or vapors to diffuse through the polymer. Strong interchain forces, such as hydrogen bonding or dipole-dipole interactions, can lead to a more closely packed polymer structure. This reduces the available free volume for permeant molecules to move within the polymer. As a result, the permeability of the polymer decreases because the movement of permeant molecules is hindered by the strong interchain forces. Conversely, weaker interchain forces result in a more loosely arranged polymer structure with increased free volume. This allows permeant molecules to diffuse more easily through the polymer, leading to higher permeability [121].

Table 2.7 summarizes the aforementioned factors affecting permeability of polymers. It can be seen clearly that thickness of the polymer film, polymer type, and ambient conditions of the use/storage environment influence the transfer of the permeant into and out of the polymer films.

Table 2.7: Summary of factors affecting permeability of polymers [126].

Factor	Change	Permeability
Temperature of polymer/permeant	↑ [1]	↑
Pressure/permeant concentration	↑	↑
Polymer/permeant chemical similarity	↑	↑
Voids in polymer	↑	↑
Permeant size	↑	↓ [2]
Polymer thickness	↑	↓
Polymer crystallinity	↑	↓
Polymer cross-linking grade	↑	↓
Polymer chain stiffness	↑	↓
Polymer interchain forces	↑	↓

[1] ↑: increase
[2] ↓: decrease

2.3.3 Methods enhancing moisture barrier properties of polymer films

Various methods can modify/control the barrier properties of polymer films [113]. The following sections introduce polymer post-treatments, polymer blends, creation of tortuous paths in polymers, and a combination of these methods.

Polymer post-treatments As summarized in **Table 2.7**, the structure of the polymer has strong impacts on its permeability. Thus, with suitable modification, the barrier properties of polymer can be improved. The crystallites are obstacles and the permeant molecules have to pass around them. They are generally considered to be impermeable. Therefore, treatments to increase the crystallinity of polymers are often applied to improve the barrier properties. For instance, crystallinity of PVA can be further raised by an appropriate heat treatment [124]. PVA films with an initial crystallinity of 25 % to 27 % can obtain a final crystallinity of 56 % after the heat treatment at 150 °C for 155 min [124]. **Table 2.8** shows the final crystallinity of PVA films obtained after various heat treatments [124].

Table 2.8: Average crystallinity of PVA films (initial crystallinity: 25 % to 27 %) after heat treatment at 70 °C, 130 °C, and 150 °C [124]. Reproduced with permission. Copyright 1993, Wiley.

	Temperature (°C)						
	70	130				150	
Heating time (min)	900	10	30	120	780	25	155
Final crystallinity (%)	29	35	37	39	44	33	56

Highly cross-linked polymers tend to have better barrier properties, hence, chemical cross-linking modification is a promising approach to enhance the barrier properties of polymers. For instance, the hydroxyl group on the PVA chain can react with organic acids or anhydrides in high-temperature esterification reactions, leading to the incorporation of carbonyl groups between the molecular chains of PVA [127]. For PVA, there are numerous kinds of cross-linking agents such as boric acid (BA), glutaraldehyde (GA), malonic acid (MA), and citric acid (CA) [128, 129, 130, 131, 132, 133].

Polymer blends A polymer blend refers to a system where one type of polymer is dispersed within a matrix mainly composed of another polymer, which exhibits different crystalline or amorphous and rubbery or glassy characteristics [113]. Generally, the barrier properties are mainly defined by the interaction between the polymers, degree of heterogeneity, the extents of crystallinity and rubbery/glassy characteristics [120, 117, 113].

Passador et al. investigate blends of high density polyethylene (HDPE) with linear low density polyethylene (LLDPE) and find that incorporating LLDPE into a HDPE matrix (without a compatibilizing agent) has a substantial impact on the barrier properties against moisture and oxygen. Due to the lower crystallinity of LLDPE compared to HDPE, the resulting blend exhibits enhanced oxygen permeation, while the blend's non-polar nature restricts the diffusion of water vapor [134].
Other blends that have been developed are chitosan (CS) in PVA [135] and polylactide (PLA) in PVA [136]. Compared to the pure PVA film, the PVA-CS films show greater elongation at break, lower oxygen permeability, higher moisture barrier properties, and greater antibacterial properties [135]. As shown in **Figure 2.8**, with PLA, the crystallinity of the blend film gradually increases, from 31.9 % of the pure PVA film to 47 % of the PVA film with 15 wt% PLA. Thus, the blend PVA/PLA films show increased mechanical properties and water resistance [136].
Hah et al. indicate that by adding 33 % of pure butyl rubber (PIB) into PDMS, a transparent, flexible encapsulant with high moisture stability can be formed [137].

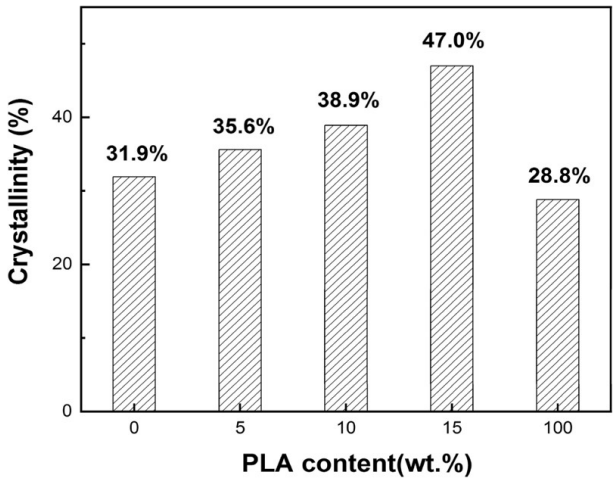

Figure 2.8: Crystallinity of PVA/PLA blend films with different PLA content. Reproduced with permission. Copyright 2021, Wiley.

Creation of tortuous paths in polymers The effective diffusion path of permeants from one side of a polymer layer to the other side is determined by both the physical thickness and the internal structure of the polymer [138]. An increase in thickness leads to reduced permeation rates. However, simply increasing thickness is not the optimal solution due to drawbacks such as added weight, increased cost, and reduced mechanical flexibility [139]. The concept of tortuosity involves increasing the effective diffusion path length while keeping the geometric polymer thickness constant. This aspect is described by the tortuosity factor, denoted as τ and can be given by [113]:

$$\tau = \frac{l}{l_0} \tag{2.13}$$

Where l is the actual diffusion path length and l_0 is the nominal polymer thickness.

The diffusion coefficient D:

$$D = \frac{D_0}{\tau} \tag{2.14}$$

Where D_0 is the diffusion coefficient of the pure polymer.

Creating tortuous paths in the polymer can be achieved by adding impermeable fillers into the polymer matrix [118], resulting in zigzag or tortuous pathways (as illustrated in **Figure 2.9**) for diffusing permeant molecules. As a result, permeability decreases [139, 118, 114].

Well-aligned filler platelets can provide a very good barrier property. The tortuosity factor τ is influenced by the concentration, size, shape, and orientation of the fillers [139]. τ reaches its highest value, when the fillers are oriented perpendicular with respect to the diffusion direction. In this case, the Nielsen model can be used to calculate τ [140]:

$$\tau = 1 + \frac{\alpha\phi_f}{2} \tag{2.15}$$

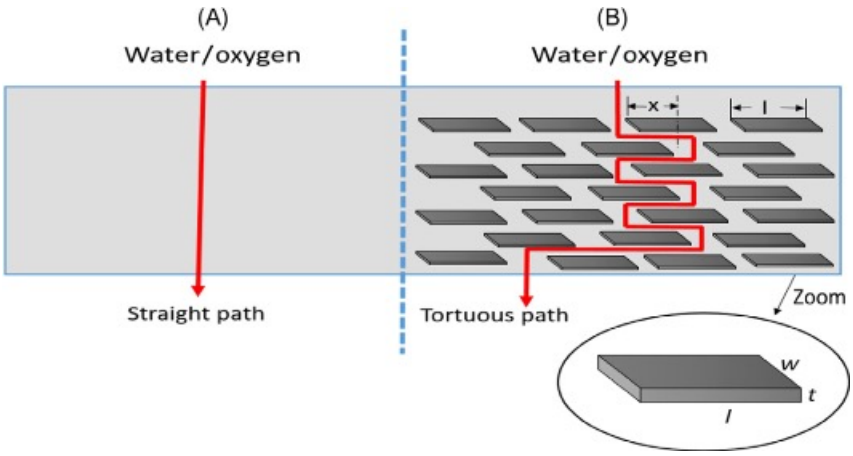

Figure 2.9: Schematic diagram of a film (A) without fillers, leading to a straight diffusion path, and (B) a film filled with platelets arranged perpendicular to the diffusion direction, creating a tortuous path [114]. Reproduced with permission. Copyright 2021, Elsevier.

Where α is aspect ratio of the fillers, and ϕ_f is the volume fraction of the filler.

For non-oriented fillers, Bharadwaj et al. introduce an order parameter (O) to quantify the degree of orientation of fillers with respect to the diffusion direction [141].

$$O = \frac{1}{2}(3cos^2\theta - 1) \tag{2.16}$$

Where θ represents the angle between the direction of preferred orientation (n) and the sheet normal unit vectors (p) as shown in **Figure 2.10**.

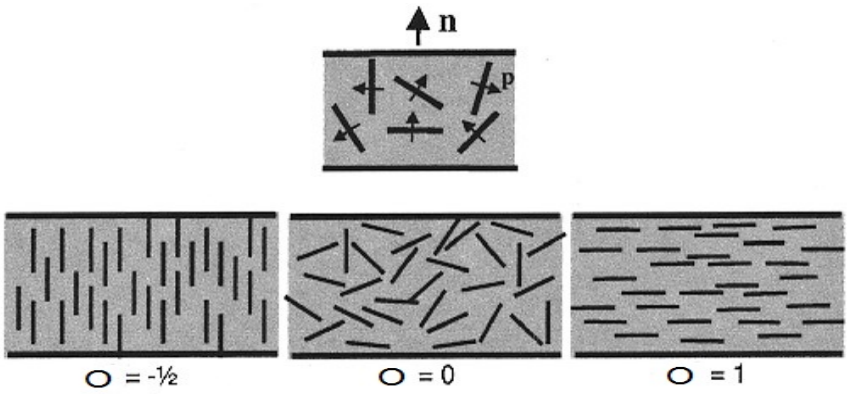

Figure 2.10: Values of the order parameter for three orientations of the fillers [141]. Reproduced with permission. Copyright 2001, American Chemical Society.

The modified tortuosity factor τ:

$$\tau = 1 + \frac{\alpha}{2}\phi_f(\frac{2}{3})(O + \frac{1}{2}) \tag{2.17}$$

The permeation behavior of polymer/filler systems is also influenced by the compatibility of the two components, which in turn is determined by their chemical nature. When the filler is compatible with the polymer, it occupies the voids within the polymer, leading to a tortuous diffusion path [142]. In contrast, if the filler and polymer are incompatible, the adhesion between them diminishes. With increasing concentration, the filler particles tend to aggregate, causing a random arrangement of platelets. This, in turn, raises the fractional free volume, resulting in reduced resistance to permeation [143, 144, 145].

Combination of methods Combining the aforementioned methods can greatly reduce the voids in a polymer, increase permeation paths of permeants as shown in **Figure 2.11**, and the barrier property of the polymer is improved.

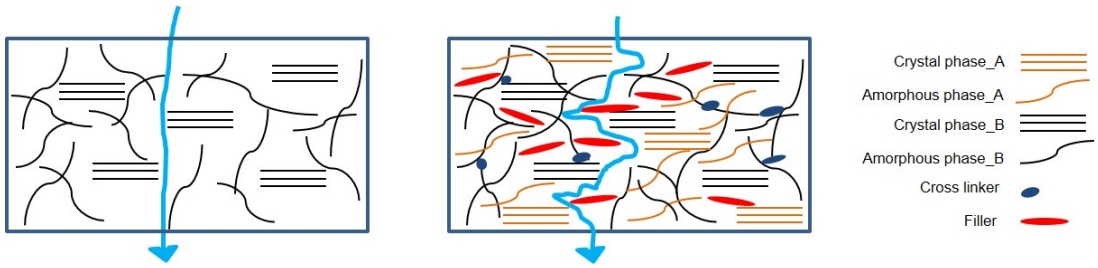

Figure 2.11: Combined methods to enhance the barrier properties of polymer.

2.4 Solution processable encapsulation for flexible printed electronic devices

Moisture can negatively impact the performance and the reliability of FPE devices. Thus, a encapsulation layer is required. This dissertation focuses on the solution processable encapsulation using polymers for its low cost and ease of processing. Solution processable polymers can be deposited directly on the devices' surface to form barrier films using various printing, coating or dispensing techniques. Thus, both global and local encapsulation can be realized. The encapsulation process can be integrated into the printing process chain. Furthermore, the flexibility of polymer layers are advantageous for FPE. While the resulting WVTRs are significantly higher than those achieved with vacuum-deposited thin film encapsulation, they are sufficient for various applications [146, 147]. In addition, as described in section 2.3.3, the barrier properties of polymers can be significantly improved by various methods.

In this section, solution processable barrier films are classified into polymer barrier films and polymer/filler barrier films. The relevant work of solution processable encapsulation and the materials associated with it are introduced.

2.4.1 Solution processable polymer barrier films

Organic polymers such as Ecoflex [148, 149], SU-8 [150, 151], PDMS [152, 153], polyvinyl chloride (PVC) [154], polylactic-co-glycolic acid (PLGA) [155], fluoropolymer (Cytop) [156], photopolymer NOA63 [157] and silicon rubber [158] are materials used for solution processable polymer barrier films.

Ecoflex is a printable biopolymer with special properties such as flexibility, toughness and water resistance [159]. Lee et al. screen print an Ecoflex encapsulation layer onto a strain sensor on a glove for the detection of finger motion. In this work, the waterproof performance of the Ecoflex encapsulation is validated by demonstrating that a LED-integrated sample remained fully functional after being immersed in water for one hour. Additionally, the strain sensors exhibit outstanding mechanical resilience, with a stretchability of up to 70 %, the ability to bend to a radius of 1.5 mm, and durability in dynamic stretching and bending tests for ten thousand cycles [148].

SU-8 is a photoresist. The viscosity of SU-8 can be adjusted from 1 cp to 15 cp [160], thus SU-8 inks with different viscosities are compatible with inkjet printing and spin-coating [161]. Moya et al. inkjet print a SU-8 ink as the encapsulation layer onto the oxygen sensor devices [150].

Inorganic-organic hybrid polymer is another type of polymer to produce solution processable barrier films. The inorganic network is formed as a result of controlled hydrolysis and condensation of alkoxysilanes, organoalkoxysilanes, acryloxysilanes or metal alcoholates. The organic network results from subsequent thermal or UV induced polymerization of organo-functional groups [162]. Due to the control of the inorganic and organic network densities and the insertion of specific functional groups to control the polarity of the resulting material, it is possible to develop high-barrier coatings with excellent adhesion properties on a wide variety of polymer films. In the following sections, promising hybrid polymers are introduced.

ORMOCER ORMOCER, an acronym for organically modified ceramics, describes a group of hybrid polymer materials. During sol–gel processing of ORMOCERs, an inorganic network is built up by the targeted hydrolysis and condensation of organically modified silicon alkoxides. In addition, co-condensation with other metal alkoxides (Ti, Zr, Al alkoxides) is possible [162, 163]. Organic cross-linking is the final curing step [162, 164]. The basic structural elements of ORMOCERs are shown in **Figure 2.12**. Through a complex synthesis process, the properties of ORMOCERs can be adapted to the respective application [165, 166, 167, 168, 169].

WVTR values of individual ORMOCER layer can be achieved in a range between approximately $1\,\mathrm{g\,m^{-2}\,d^{-1}}$ to $5\,\mathrm{g\,m^{-2}\,d^{-1}}$ (calculated for 100 µm layer thickness) [170]. Amberg-Schwab et al. measure the WVTR values of uncoated, SiOx-coated, and SiOx/ORMOCER-coated PET films under the test condition of 23 °C and 85 %. The results show that the application of an ORMOCER layer can improve the moisture barrier properties of the SiOx-coated PET films

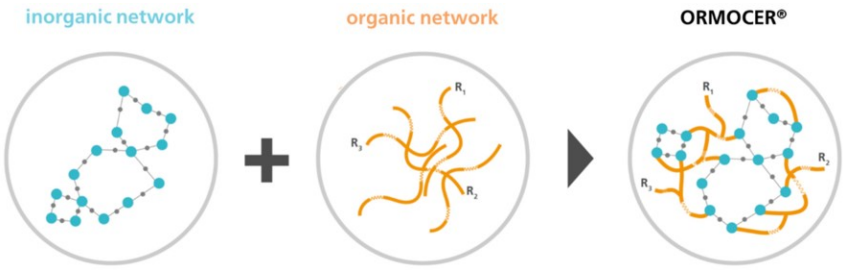

Figure 2.12: Hybrid polymers ORMOCER developed by Fraunhofer ISC [169]. Reproduced with permission. Copyright 2023, the authors, MDPI, Basel, Switzerland.

from 0.51 to 0.16 g m^{-2} d^{-1}. This improvement can be explained as a synergistic barrier effect through combination of the SiOx and the ORMOCER layer. As illustrated in **Figure 2.13 (a)**, the macroscopic defects formed in the SiOx layer are compensated by the ORMOCER layer. The ideal scheme of interfacial bonding is shown in **Figure 2.13 (b)**.

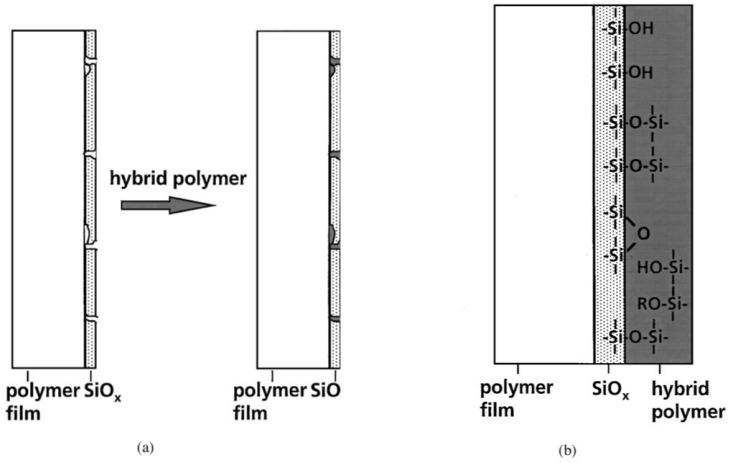

Figure 2.13: (a) Compensation of the macroscopic defects formed in the SiOx layer. (b) Idealized scheme of interfacial bonding [162]. Reproduced with permission. Copyright 1998, Kluwer Academic Publishers.

Polysilazane Polysilazane (PSZ) is another promissing hybrid polymer consisting of a basic Si–N backbone, to which various reactive and/or inert side groups are attached at either the Si or N atoms [171, 146, 172, 147]. Depending on the nature of side groups, polysilazanes can be categorized as either inorganic or organic polysilazanes (OPSZ) (see **Figure 2.14**). Perhydropolysilazane (PHPS) is a typical inorganic polysilazane material, due to the exclusive presence of hydrogen side groups [173]. PHPS is an attractive encapsulation material due to its ability to produce dense silica barrier films, providing excellent barrier properties, high transparency, hardness, and density [146, 172, 174, 147]. However, with increasing thickness, the volume change increases the inner stress of the coating, resulting in crack formation on the coating [171]. On the other hand, OPSZ offers the advantage of forming thick, elastic coatings due to the presence of organic groups in the molecular chains. This increases flexibility and reduces volume shrinkage [173].

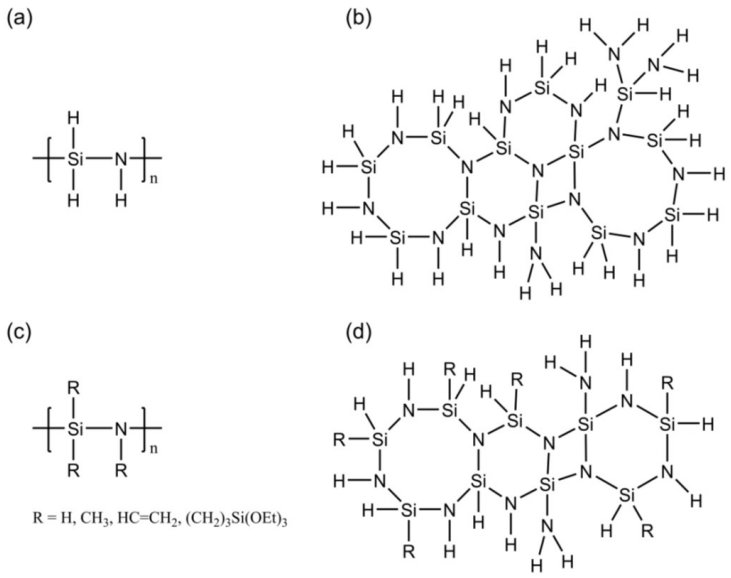

Figure 2.14: Simplified chemical formulas of (a) perhydropolysilazane (PHPS) and (c) organopolysilazane (OPSZ). (b) and (d) illustrate the possible molecular structures of PHPS and OPSZ, respectively [173]. Reproduced with permission. Copyright 2022, The Authors.

PSZ coatings provide excellent barrier properties because they can be converted into SiOx, SiCO, SiCN, or Si_3N_4 ceramic coatings after curing [175]. However, along with the favorable barrier properties come inherent issues of non-ideal coating thicknesses due to a great dependence on perfect ambient curing conditions [176]. It is reported that the permeability of PHPS against oxygen and moisture are heavily dependent on the curing methods and the curing environment [177]. Optimal curing processes should be further investigated to accelerate the conversion of PHPS into silica [177]. **Table 2.9** selects some studies on fabrication of such barrier films made from hybrid polymers.

Table 2.9: Solution processable hybrid polymer barrier films.

Substrate	Material	Solution deposition	Thickness	Test conditions		WVTR ($g\,m^{-2}\,d^{-1}$)	Ref.
				Temperature (°C)	RH (%)		
SiOx coated PET (30 µm)	ORMOCER	R2R[1]	5 µm	23	85	0.16	[162]
-	ORMOCER	R2R	100 µm	-	-	1-5	[170]
PET (50 µm)	PHPS	DB[2]	250 nm	-	-	0.2	[172]
PET (125 µm)	PHPS	DB	400 nm	40	85	0.15	[147]

[1] R2R: roll-to-roll coating.
[2] DB: doctor blading.

2.4.2 Solution processable polymer/filler barrier films

As outlined above in section 2.3.3, creating tortuous paths in a polymer improve its moisture barrier property. Therefore, another method to form solution processable barrier films is to add less permeable inorganic materials as fillers into a polymer matrix. In this way, tortuous paths can be built within the polymer matrix, enhancing its barrier property [178, 118, 179]. Several polymers, such as PVA, polyvinyl butyral (PVB), polyurethane, and fillers, such as clays, lignin, mica flakes, glass flakes, ZnO, and silica, are already utilized in the literature to develop such barrier films as encapsulation materials [144, 180, 181, 182, 183, 184, 185, 186]. In the following section, the polymer and filler materials utilized in this dissertation are introduced.

PVA PVA is often utilized as the polymer matrix due to its biocompatibility, biodegradability, film-forming properties, ease of modification, and non-toxic nature [187]. PVA is a water-soluble, semicrystalline polymer. The properties of PVA typically rely on two main factors: its molecular weight and degree of hydrolysis. The molecular weight generally ranges between 20,000 and 40,000, determined by the length of the vinyl acetate polymer chain used in its production.

Clay Clay is a widely used inorganic filler in polymers for barrier film production [188, 118] due to its abundance, simple processing, non-toxicity and the relatively high aspect ratio (AR, defined as the ratio of diameter to thickness) of its particles with their sheet like structures (platelets). Clays are filler particles of layered mineral silicates. The most commonly used clays as fillers in polymer/filler composites are montmorillonite (MMT), hectorite (Hec) and vermiculite. The difference among them is based on their chemical composition and nanoparticle morphology.

Chandio et al. add MMT Na^+ into a PVA solution. The resulting barrier films (100 µm thick) yield a WVTR of 2.8 g m^{-2} d^{-1} (test condition: 40 °C and 85 %RH) and exhibit excellent flexibility and maintain their moisture barrier property after undergoing 10000 bending cycles [189]. Roehrl et al. utilize Hec as fillers in the PVA matrix. The resulting films (3.7 µm thick) along with their PET carrier substrate (36 µm thick) yield a WVTR of 0.02 g m^{-2} d^{-1} under the test conditions of 23 °C and 50 %RH [190].

Silica Silica particles are also widely used as filler embedded in a polymer matrix to improve the mechanical and morphological properties [191, 191]. Silica particles are of hydrophilic nature, they exist as white amorphous powder or as colloid suspension. The most important characteristics are their extremely large surface area and smooth nonporous surface. When dispersed in polymer systems, nonporous silica particles reduce polymer permeability by decreasing the polymer's free volume and increasing the tortuosity of the diffusion path. Chen et al. develop PVA/silica barrier films, yielding a WVTR of 1.28 g m^{-2} d^{-1} under the test conditions of 37.8 °C and 90 %RH. Compared to pure PVA films, the addition of silica reduced the WVTR by 39.6 % [184].

Graphene Graphene is two-dimensional sheet of sp^2 bonded carbon atoms densely packed in a honeycomb crystal lattice. It is produced by the exfoliation (separation) of graphite nanoplatelets [192]. One application of graphene is its incorporation as filler in polymer nanocomposites. Due to its unique structure, polymer/graphene nanocomposites have shown excellent thermal, mechanical and electrical properties, much better than the polymer/clay nanocomposites.

Among graphene-family nanomaterials, graphene oxide (GO) stands out as the most promising nanofiller for nanocomposites due to its lower tendency to agglomerate compared to pristine graphene [193]. Studies on polymer/GO nanocomposites have shown that their aspect ratio values are significantly higher than those reported for polymer/clay composites [194, 195, 196, 197, 198]. In Kim's study, two fillers (MMT Na^+ and GO) and two polymers (PDAC and PVA) are used to form flexible barrier films with multilayers on the PEN carrier substrates, yielding a improved flexibility and a decreased WVTR of 3.1×10^{-3} g m^{-2} d^{-1} under test conditions of 23 °C and 50 %RH [183].

Glass flakes Glass flakes (GFs) possess a high AR, typically featuring thicknesses of less than a micrometer and average lengths ranging from 100 µm to 300 µm [114]. Due to their large lateral extension, which is on the same order as the film thickness, they can be easily aligned parallel to the film surface during the coating process [186].

Polymer/GF composites exhibit enhanced gas/moisture barrier properties, improved thermal stability, and superior mechanical strength due to the increased tortuosity of the diffusion path [199, 200]. Channa et al. develop an oxygen and moisture barrier film for encapsulating organic (opto-)electronic devices by incorporating GFs into PVB solutions. The resulting 78 µm thick barrier films achieve a WVTR of 2.1 g m^{-2} d^{-1}, a significant improvement compared to pristine 70 µm thick PVB films, which exhibit a WVTR of 65 g m^{-2} d^{-1} under the test conditions of 40 °C and 85 %RH [186]. In another study by the same authors, GFs are added into PVA solutions to develop sustainable and eco-friendly barrier films for food packaging. The resulting barrier films yield a WVTR of 1.2 g m^{-2} d^{-1} compared to pristine PVA films with a WVTR of 22.5 g m^{-2} d^{-1} under the test conditions of 25 °C and 75 %RH [201].

Table 2.10 provides an overview of relevant studies on polymer/filler systems and their measured WVTRs.

Table 2.10: Permeability results of studies on polymer/fillers.

Material			Processing	Structure	Thickness	Test conditions		WVTR ($g\,m^{-2}\,d^{-1}$)	Ref.
Substrate	Polymer	Filler				Temperature (°C)	RH (%)		
-	PVA	MMT Na^+	DB[1]	SL[2]	100 µm	40	85	2.8	[189]
PET (36 µm)	PVA	Hec	DB	SL	3.7 µm	23	50	0.02	[190]
PEN (125 µm)	PVA/PDAC	MMT/GO	DC[3]	ML[4]	48 nm	23	50	3.1×10^{-3}	[183]
-	PVB	Glass flake	DB	SL	78 µm	40	85	2.1	[186]
-	PVA	Glass flake	DB	SL	100 µm	25	75	1.2	[201]
-	PVA	Silica	DC	SL	60 µm	37.8	90	1.28	[184]

[1] DB: doctor blading.
[2] SL: single layer structure.
[3] DC: dip coating.
[4] ML: multilayer structure.

2.5 Water vapor transmission rate measurement methods

WVTR is a key factor for assessing the effectiveness of encapsulation in providing moisture protection. To date, various WVTR measurement methods are available [202]. This section provides a brief description of three WVTR measurement methods: the coulometric method, the calcium (Ca) test method, and the gravimetric method.

2.5.1 Coulometric method

Utilizing a coulometric device, an inert carrier gas is employed to transport the permeated water to a sensor. This sensor employs a phosphorus pentoxide (P_4O_{10}), a potent desiccant, as the electrolyte between two adjacent electrodes. The P_4O_{10} absorbs the transported water and becomes an ionic electrolyte, enabling the flow of current between the electrodes. The resulting current is measured and converted into a corresponding WVTR value. This methodology is often referred to as the "MOCON test", originating from its development and commercialization by MOCON, Inc. Their AQUATRAN Model 3 apparatus is acknowledged for its capacity to measure WVTR values as low as $5 \times 10^{-5}\,g\,m^{-2}\,d^{-1}$ [202].

2.5.2 Calcium test method

Ca is easily oxidized by oxygen as well as moisture. The oxidation is dominated by moisture [203].

$$Ca + 2H_2O \rightarrow Ca(OH)_2 + H_2 \tag{2.18}$$

The optical and electrical properties of Ca are changed along with the oxidation status [204, 205]. The optical Ca test uses the principle that opaque Ca becomes transparent with oxidation. The transmittance of light passing through a Ca film is measured based on the Lambert–Beer law, as follows:

$$I = I_0 e^{-\alpha h} \tag{2.19}$$

where I is the light intensity passing through the layer, I_0 is the light intensity reaching the layer, α is the absorption coefficient of the layer material, and h is the homogeneous height of the Ca layer [202].

An electrical Ca test, based on the principle that conductive Ca becomes non-conductive upon oxidation (as calcium oxides, CaO and CaOH, are non-conductive) is presented in **Figure 2.15**. When two electrodes are connected to the evaporated Ca film, the resistance increases over time in accordance with the progress of oxidation. The WVTR is calculated using the following formula [202]:

$$\text{WVTR} = -\frac{nM(H_2O)}{M(\text{Ca})} \frac{\delta \rho l b}{d(1/R)} \frac{dR}{dt} \tag{2.20}$$

where n is the number of water molecules per Ca atom, M is the molar mass, δ is the Ca density, ρ is the Ca resistivity, l is the length of the Ca layer, b is the width of the Ca layer, R is the resistance of the Ca layer, and t is time.

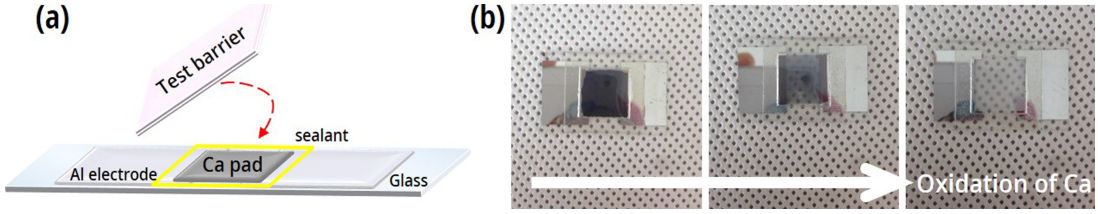

Figure 2.15: Electrical calcium test: (a) schematic diagram of the Ca pad sample; and (b) photograph of the Ca pad with increasing Ca oxidation [202]. Reproduced with permission. Copyright 2019, The Authors.

2.5.3 Gravimetric method

The gravimetric cup method, as specified by ASTM D1653 or ASTM E96/E96M [206], provides a straightforward way to measure the WVTR of a barrier film [202]. It includes two basic test methods: the wet cup method and the dry cup method (see **Figure 2.16**). In both methods, a test dish is covered with the film sample being tested and filled with either water or a desiccant. This creates a difference in partial water vapor pressure between the controlled climatic conditions within the test environment (e.g. a climate chamber) and the interior of the sample vial, leading to moisture permeating through the film sample. The amount of moisture permeation is determined by weighing the mass change of the test dish.

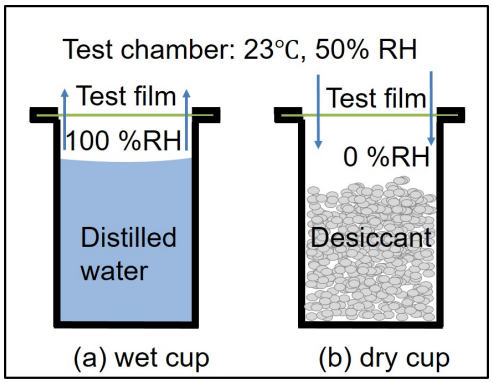

Figure 2.16: Illustration of the gravimetric method: (a) wet cup method and (b) dry cup method. The test condition refers to ASTM E96/E96M [206].

In the dry cup method, the sample is sealed to a test dish containing a desiccant, and the assembly is placed under controlled test conditions. The WVTR is assessed by periodic weighings as moisture permeates the sample into the desiccant, causing an increase in the total mass of the assembly. The wet cup method differs in that the test dish is filled with distilled water instead of a desiccant. The moisture moves from the test dish toward the outside, decreasing the mass of the assembly over time.

3 Moisture influence on the performance of printed structures using nanoparticle inks

Moisture can contribute to the degradation of printed electronic devices, resulting in a worse and unreliable performance. In this chapter, the moisture influences on the electrical performance of inkjet printed conductive tracks and capacitors using specific nanoparticle inks are investigated. The printed test structures are subjected to three environmental tests. Whether moisture brings positive or negative influence on the performance and reliability of those test structures is discussed. Potential solutions to take advantage of moisture positive and avoid negative influences are suggested. **Figure 3.1** shows the structure of this chapter. [1]

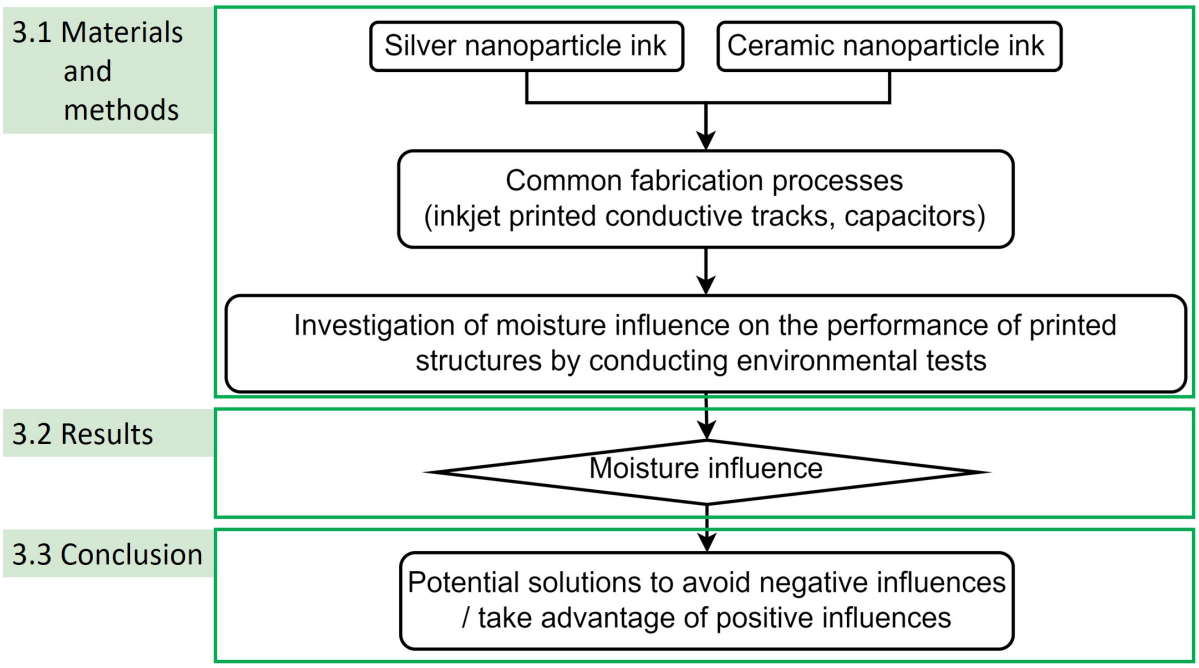

Figure 3.1: Structure of chapter 3 - investigation of moisture impact on the performance of printed structures using nanoparticle inks

[1] Parts of this chapter are published in: [207] Martin Ungerer, Zehua Chen, Tim Pang Mach, Klaus-Martin Reichert, Ulrich Gengenbach, Moritz Lindmüller, Joachim R. Binder, Markus Reischl, and Liane Koker. Automated characterisation of printed electronics under adjustable ambient conditions. In 2024 International Semiconductor Conference (CAS), pages 69–72. IEEE, oct 2024. doi: 10.1109/cas62834.2024.10736741.

3.1 Materials and methods

In this section, materials, an automated characterization setup for the test structures, as well as the environmental tests based on various standards are described.

3.1.1 Materials

Substrates

- DuPont Teijin PET films Melinex ST506 (175 µm thick);
- DuPont Kapton HN PI films (75 µm thick).

Inkjet printable inks

- Silver nanoparticle ink (Silverjet DGP 40LT-15C, Sigma Aldrich). This silver nanoparticle ink contains 30 wt% to 35 wt% silver nanoparticles (Ag NPs). The manufacturer recommends a sintering temperature between 100 °C and 150 °C.
- Ceramic nanoparticle ink (developed at KIT IAM-ESS [47]). This ceramic nanoparticle ink consists of $Ba_{0.6}Sr_{0.4}TiO_3$ (BST) nanoparticles and polyvinylidene fluoride-co-trifluoroethylene (P(VDF-TrFE)). A comprehensive description of the production process for this BST/P(VDF-TrFE) ink can be found in [47].

3.1.2 Automated characterization setup for printed electronics

To accelerate the electrical characterization of printed electronic devices, an automated measurement setup has been established (see **Figure 3.2** [207]). A test adapter is designed to contact multiple devices on a 55 mm × 55 mm substrate and combined with an in-house built multiplexer, enabling the automated readout of measurement data from the LCR meter for several test structures on one substrate. Test conditions can be provided by the Memmert CTC256 climate chamber and can be controlled by the software "Celsius" provided by the manufacturer of climate chamber.

Test adapter A test adapter is developed to contact multiple electronic devices on a substrate of 55 mm × 55 mm. As shown in **Figure 3.3**, this test adapter features an Ingun MA 350/F manual test fixture, equipped with a lever-based parallel stroke mechanism (20 mm) for closing (1), along with a customized, interchangeable test fixture kit, consisting of a pressure frame plate (2), a moving plate (3), protruded test probes (4), and a probe plate (5). The connection cable (6) of this test adapter allow its integration into an automated measurement setup for the

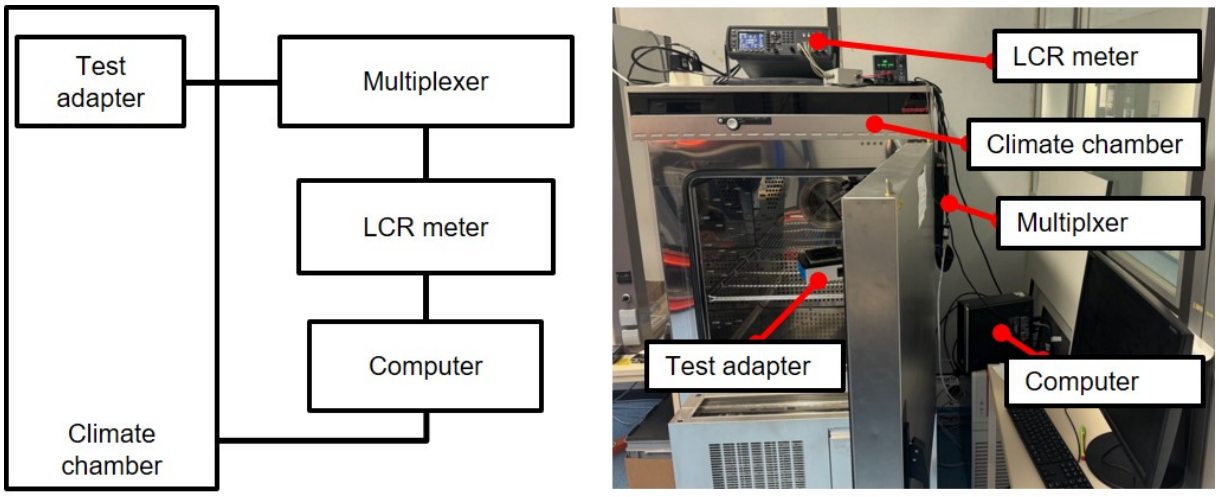

Figure 3.2: Measurement setup for the automated characterization of printed electronic devices in a climate chamber (adapted from [207], own publication).

characterization of printed electronic devices. The inlet (7) enables the exposure of test structures to preconditioned air from below. This test adapter can withstand a maximum temperature of 60 °C. The exchangeable components designed for the printing layout in this dissertation, as well as the assembly of the test adapter, are developed by Ing. Ludwig Rausch GmbH (Langenzersdorf, Austria).

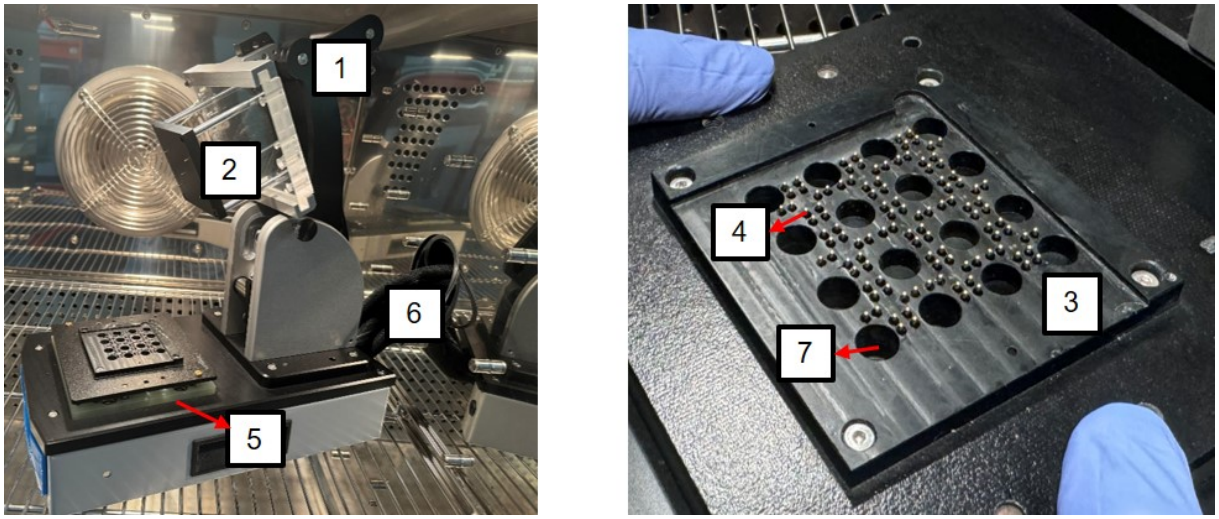

Figure 3.3: Test adapter with lever (1) , test fixture kit which consists of a pressure frame plate (2), a moving plate (3), protruding test probes (4), a probe plate (5), and a connection cable (6) to external measurement equipment. The inlet (7) is for the exposure of test structures to preconditioned air from below (adapted from [207], own publication).

This test adapter can simultaneously contact multiple test structures on a single substrate. The test probes are arranged in nine test fields, positioned in a grid with 2.54 mm spacing on the probe plate, as shown in **Figure 3.3 right**. The overall test layout is determined by the configuration of the test fields, with each test field comprising 12 contact pins.

To perform four-point measurements for characterizing passive components such as resistors, capacitors, and related sensors, the 12 contact pins within each test field are utilized to contact six pads, with each pad connected by two pins (see **Figure 3.4**). The standard pad size for four-point measurements is defined as 3.9 mm × 2.0 mm. The contact pads in each test field enclose a free area of 5 mm × 5 mm, allowing devices to be positioned either in this free area or directly above a through-hole in the moving and probe plate.

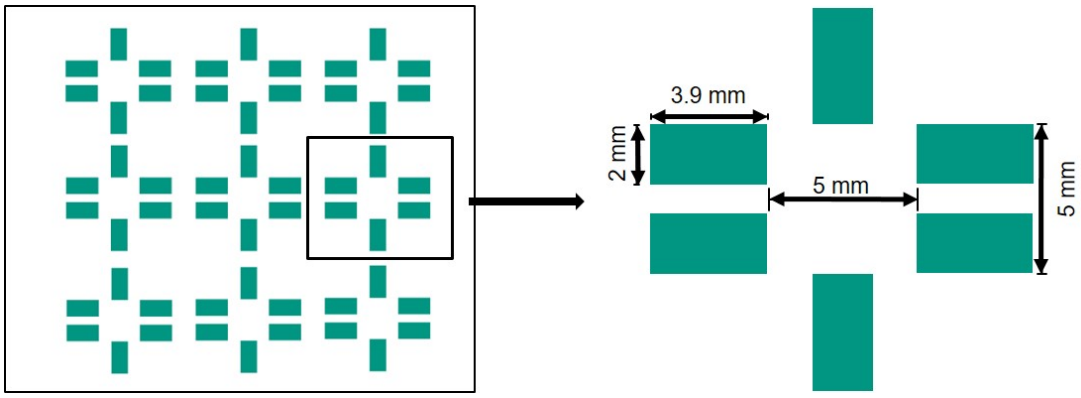

Figure 3.4: The general layout of the test structures on a single substrate is designed to fit the test adapter (adapted from [207], own publication).

Multiplexer Each probe of the test adapter is controlled by two relays (3570-1419-054, Comus International), allowing for flexible switching between high and low states. This configuration enables the setup to adapt to various measurement tasks, such as switching between devices or altering the polarity of the devices. A Raspberry Pi Pico is used to control the multiplexer, ensuring efficient management of the switching processes. The four BNC outputs of the multiplexer are connected to the respective measurement instrument, which is a LCR meter (Keysight E4980AL) in this work.

Control of the characterization process The automated setup is managed using proprietary Python and MicroPython scripts running on both the PC and the Raspberry Pi controlling the multiplexer. Each probe can be individually activated and configured with different settings, such as varying bias voltages. To facilitate automated measurements under controlled environmental conditions, the setup can be synchronized with the climate chamber via its network port using the "Celsius" software. This integration allows for precise control of ambient conditions, enabling consistent testing and data collection.

3.1.3 Environmental tests setup

Static accelerated aging test setup ASTM F1980-21 is a standard guide developed by ASTM International, specifically by the committee on Medical and Surgical Materials and Devices.

The full title is "Standard Guide for Accelerated Aging of Sterile Barrier Systems for Medical Devices." ASTM F1980-21 provides a scientific approach for accelerating the aging process of sterile barrier systems in medical devices, ensuring that these products can be reliably tested for longevity and performance in a shorter time frame [208]. This standard applies a storage of samples at an elevated temperature in order to simulate real time aging in a reduced amount of time. An accelerated aging factor (AAF) estimate is calculated by the following equation:

$$AAF = Q_{10}^{\frac{T_{AA}-T_{RT}}{10}} \tag{3.1}$$

where: T_{AA} is the accelerated aging temperature (°C), and T_{RT} is the representative ambient temperature (23 °C in this work). Using the Arrhenius equation with Q_{10} set to 2 is a common and conservative means of calculating an aging factor [208].

The accelerated aging time (AAT) needed to establish equivalence to real time aging is determined by dividing the desired (or required) shelf life by the AAF:

$$AAT = \frac{T_{desired}}{AAF} \tag{3.2}$$

In this work, static accelerated aging (SAG) test conditions are adopted by this standard. An accelerated aging temperature T_{AA} higher than 60 °C is not recommended in this standard due to the higher probability in many polymeric systems to experience nonlinear changes, such as crystallinity, formation of free radicals, and peroxide degradation [208]. However, this is not relevant for the materials in this work. For this accelerated aging test, the samples are placed in the climate chamber under the test condition of 85 °C and 50 %RH. According to the data sheet of suppliers, the utilized substrates and inks can withstand this specific test condition. With the desired life time set to one year, the calculated AAF is 73, and the calculated AAT is five days.

Static damp heat test setup The international standard IEC 60068 provides a test method for determining the suitability of electrotechnical products, components or equipment for transportation, storage and use under conditions of high humidity. The test is primarily intended to permit the observation of the effect of high humidity at constant temperature without condensation on the specimen over a prescribed period. This test provides a number of preferred test severities of high temperature, high humidity and test duration. The test severity is defined by a combination of temperature, relative humidity and total test duration. Unless otherwise specified in the relevant specification, temperature and relative humidity severities may be selected from the following **Table 3.1**. Preferred test durations are: 12 hours, 16 hours, 24 hours, 2 days, 4 days, 10 days, 21 days or 56 days [209].

Table 3.1: Recommended temperature and relative humidity severities IEC 60068 [209].

Temperature	Humidity
(30 ± 2) °C	(93 ± 3) % RH
(30 ± 2) °C	(85 ± 3) % RH
(40 ± 2) °C	(93 ± 3) % RH
(40 ± 2) °C	(85 ± 3) % RH

In this work, the combination of 40 °C and 85 %RH as test condition for the static damp heat (SDH) test is selected, the test duration is set to four days.

Cyclic humidity test setup In addition to static environmental tests, a cyclic humidity test is performed. The setup for this cyclic humidity test is illustrated in **Figure 3.5**. Test structures are placed in a climate chamber, where the temperature is maintained at 23 °C. The relative humidity is cycled between 35 %RH and 85 %RH, with measurements taken at intervals of 10 %RH. This humidity cycling process is repeated three times to ensure comprehensive evaluation of the test structure performance under varying moisture conditions.

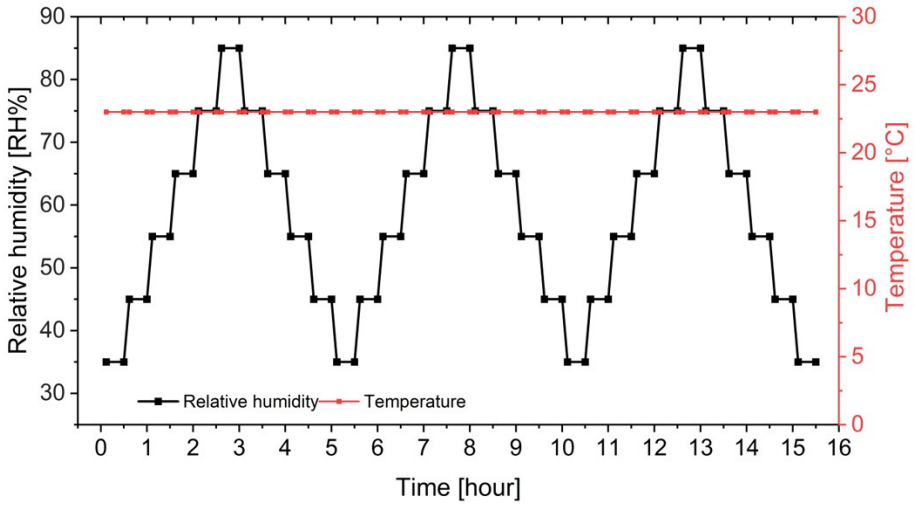

Figure 3.5: Temperature and relative humidity profile for the cyclic humidity test conducted for investigating moisture influence on the performance of printed test structures during use.

3.1.4 Test structures

Due to the thermal resistance limitation of the utilized test adapter, three test structures are designed for different environmental test conditions. Two designs of conductive tracks are applied for the static environmental tests and cyclic humidity tests.

Test structure 1 - inkjet printed conductive tracks for static environmental tests

Inkjet printed silver tracks on Melinex ST506 PET films are utilized as test structures for the static accelerated aging test and the damp heat test. The designed Ag tracks have a length of 45 mm, with pads at both ends measuring 1.5 mm × 3.5 mm (see **Figure 3.6**).

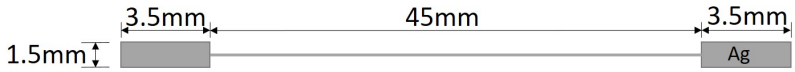

Figure 3.6: Test structure 1 - inkjet printed conductive tracks for static environmental tests

As mentioned in section 3.1.2, the developed test adapter can withstand a maximal temperature of 60 °C, however, the static accelerated aging test requires test structures subjected to a test condition of 85 °C and 50 %RH, which exceeds the maximal acceptable temperature of the test adapter. Thus, the characterization of test structures before and after those static environmental tests is conducted manually using a B&K Precision LCR-Meter 981 connected to a Formfactor EPS150 probestation, with 150 µm probe tips.

Test structure 2 - inkjet printed conductive tracks for cyclic humidity tests

For the cyclic humidity tests, the layout of inkjet printed conductive tracks is designed as shown in **Figure 3.7**, consisting of two conductive tracks (contact pad ① to contact pad ② and contact pad ① to contact pad ③), allowing the automated characterization described in section 3.1.2.

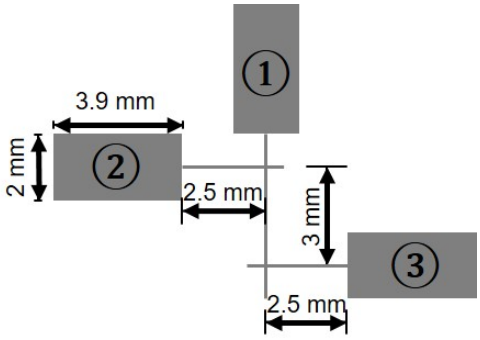

Figure 3.7: Test structure 2 - inkjet printed conductive tracks for cyclic humidity tests

Test structure 1 and 2 are printed on Melinex PET substrates. The hotplate of the printer (Autodrop Gantry inkjet printer, MD-K-140 print head) is heated to 85 °C. The printing parameters are set to a voltage of 170 V, a pulse width of 45 µs, a vacuum pressure of 7 mbar, and a drop distance of 100 µm. The Ag tracks in test structure 1 are printed in two passes, test structure 2 in one pass. After printing, the printed Ag tracks undergo a commonly applied thermal sintering process in an oven at 120 °C for one hour.

Test structure 3 - inkjet printed capacitors A capacitor setup with two printed bottom electrodes (contact pads ② and ③), one top electrode (contact pad ①) and an extended dielectric (see **Figure 3.8**) is applied as the layout of inkjet printed capacitors, allowing the automated characterization described in section 3.1.2. This layout based on a design by [47] contains two capacitors at the intersections of electrodes. Two types of substrate, Melinex ST506 PET films and Kapton HN PI films, are utilized. Ag NP ink is utilized for top and bottom electrodes. The bottom electrodes are printed on the substrate with the printer hotplate heated to 80 °C. Afterwards, the bottom electrodes are sintered in an oven at 120 °C for one hour. The BST/P(VDF-TrFE) ink is printed as dielectric on top with the printer hotplate heated to 55 °C. Finally, the top electrode is printed with the printer hotplate heated to 80 °C. The printed capacitor is dried in a vacuum drying oven at 90 °C for 20 hours [47].

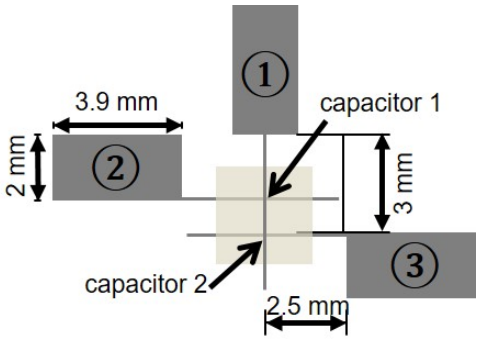

Figure 3.8: Test structure 3 - inkjet printed capacitors for both static environmental tests and cyclic humidity tests.

3.2 Results

To evaluate the performance and reliability of the inkjet printed test structures (Ag conductive tracks and capacitors), three environmental tests are conducted. Resistance and capacitance of the test structures are measured before and after static environmental test as well as during the cyclic humidity test to analyze the moisture influences on their electrical properties. The results are discussed in the following sections.

3.2.1 Environmental test results of inkjet printed silver tracks

The results of the SAG test and the SDH test for inkjet printed Ag tracks are shown in **Figure 3.9**. After the SAG test, the resistance of thermally sintered Ag tracks decreases by 13 %, suggesting that the sintering process continues under the test conditions of 85 °C and 50 %RH. Further investigation is needed to determine whether the temperature of 85 °C, the humidity of 50 %RH, or a combination of both contribute to this finding. In contrast, the resistance of Ag tracks after the SDH test shows minimal change, confirming the constant performance of these one-hour 120 °C sintered Ag tracks under SDH conditions.

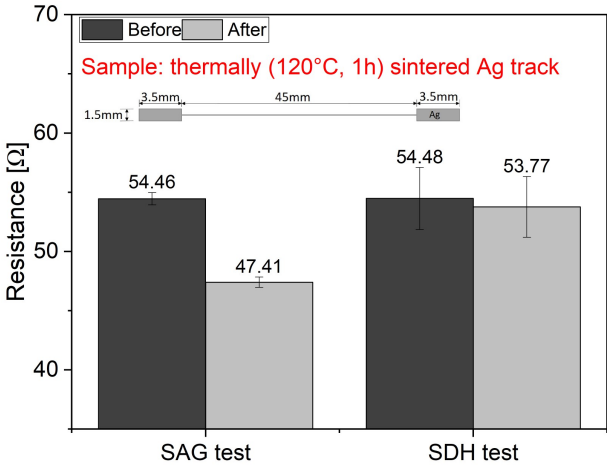

Figure 3.9: Static environmental test result of thermally sintered (120 °C, one hour) silver tracks. Six printed silver tracks are measured. Error bars represent standard deviations.

Similar to the SDH test results, as shown in **Figure 3.10**, the resistance of Ag tracks during the cyclic humidity test remains stable both during and between each humidity cycle, further confirming the reliability of these Ag tracks under cyclic humidity conditions.

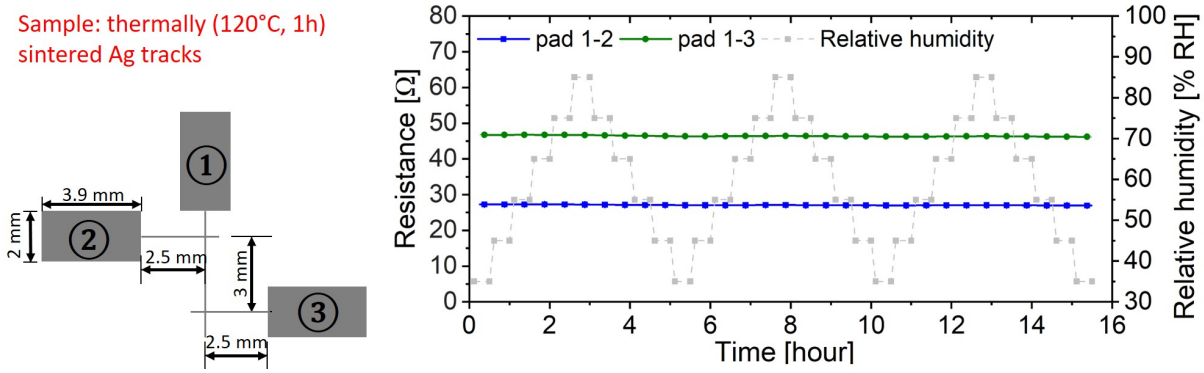

Figure 3.10: Cyclic humidity test result of thermally sintered (120 °C, one hour) silver tracks. Six printed silver tracks are analyzed. Error bars represent standard deviations.

3.2.2 Environmental test results of inkjet printed capacitors

The capacitance of the printed capacitors is depending on the thickness of BST/P(VDF-TrFE) dielectric layer and the line widths of the bottom and top silver lines. These values are highly dependent on the inkjet printing quality. Measuring the thickness of the BST/P(VDF-TrFE) dielectric layer requires cutting the samples, which would destroy the capacitors. Therefore, assuming that the thickness of the BST/P(VDF-TrFE) dielectric layer remains consistent across samples, the widths of bottom and top silver lines are measured using a Keyence VHX 7000 microscope.

Table 3.2 summarizes the measured widths of the bottom and top silver lines, the resulting calculated surface areas, and the measured capacitances of the printed capacitors on Melinex ST506 PET substrates and Kapton HN PI substrates for the SAG test, the SDH test and the cyclic humidity (CH) test. The variation in capacitor surface area contributes to the observed differences in their absolute capacitance.

Table 3.2: Measured widths of the silver lines, calculated surface areas, and measured capacitances of printed capacitors on Melinex ST506 PET films and Kapton HN PI films (five samples each for SAG and SDH tests, three samples each for CH test).

	SAG test samples		SDH test samples		CH test samples	
Substrate	Melinex ST506	Kapton HN	Melinex ST506	Kapton HN	Melinex ST506	Kapton HN
Bottom silver line [µm]	159.0 ± 4.2	180.0 ± 10.4	156.2 ± 4.4	178.8 ± 6.1	127.7 ± 4.5	184.0 ± 4.4
Top silver line [µm]	94.4 ± 3.0	100.6 ± 2.4	90.6 ± 3.8	92.6 ± 1.1	83.7 ± 2.1	95.0 ± 1.0
Surface area [mm^2]	0.015	0.018	0.014	0.017	0.011	0.017
Capacitance before test [pF]	2.64 ± 0.19	3.37 ± 0.27	2.68 ± 0.31	3.11 ± 0.10	2.19 ± 0.13	3.13 ± 0.19

Both on Melinex ST506 PET and Kapton HN PI substrates, the change in capacitance is negligible before and after these two static environmental tests (see **Figure 3.11**). This result confirms the constant performance of capacitors printed with the Ag NP ink and the BST/P(VDF-TrFE) ink under SAG and SDH test conditions.

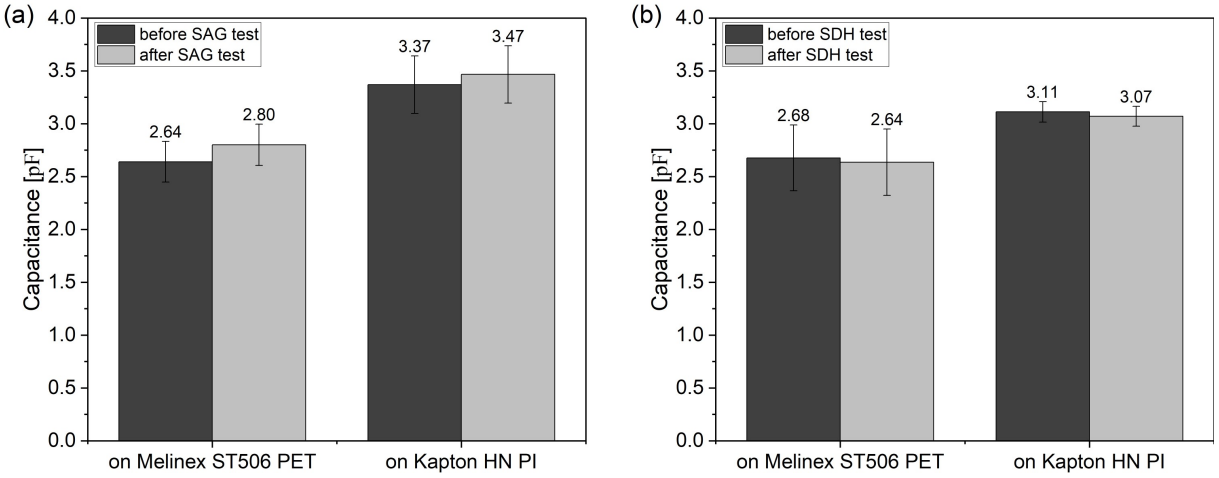

Figure 3.11: Static environmental test result of inkjet printed capacitors using an Ag NP ink and a BST/P(VDF-TrFE) ink. The measured capacitance (a) before and after the static accelerated aging (SAG) test and (b) before and after the static damp heat (SDH) test. Five samples on each type of substrates are measured. Error bars represent standard deviations.

Figure 3.12 shows the capacitance changes of printed capacitors under cyclic humidity conditions (35 %RH to 85 %RH and back to 35 %RH, three cycles, at 23 °C). The variation in capacitor surface area contributes to the observed differences in their absolute capacitance (see **Table 3.2**). Nevertheless, the trend of capacitance change in response to humidity is similar on both PET and

PI substrates. Capacitance increases with increasing humidity and decreases with decreasing humidity. A hysteresis is observed between the increase and subsequent decrease of humidity. This behavior is attributed to the differing rates of humidity absorption and desorption in the polymer components in the BST/P(VDF-TrFE) dielectric layer [207].

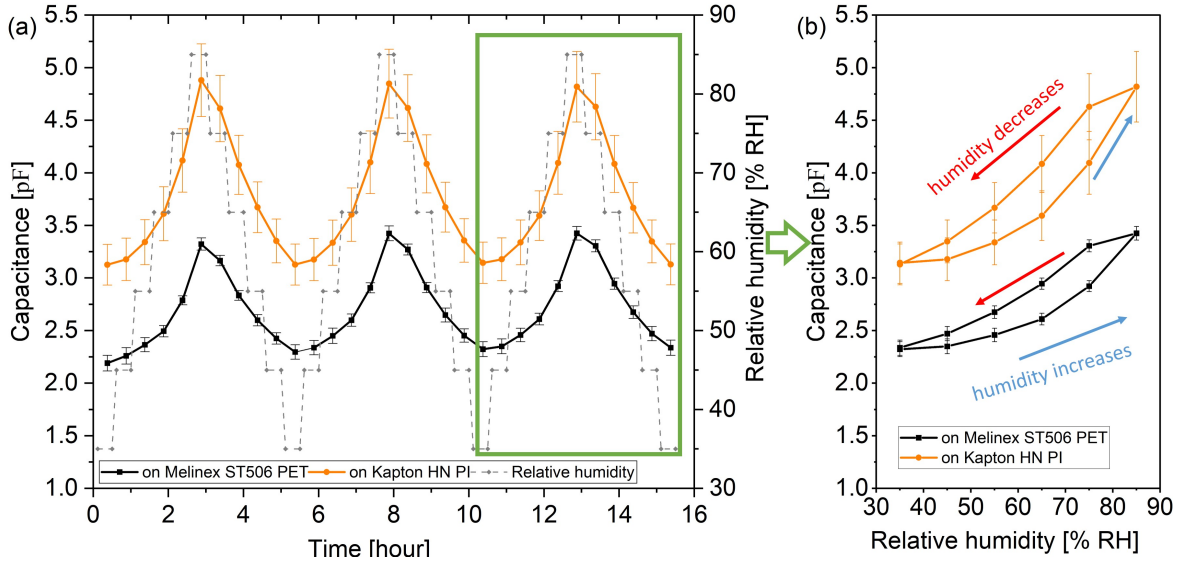

Figure 3.12: Absolute capacitance of inkjet printed capacitors on Melinex ST506 PET and Kapton HN PI substrates during cyclic humidity tests. (a) Capacitance over time at 23 °C for three measurement cycles. (b) Capacitance over relative humidity in the last measurement cycle. Three samples on each type of substrate are measured. Error bars represent standard deviations.

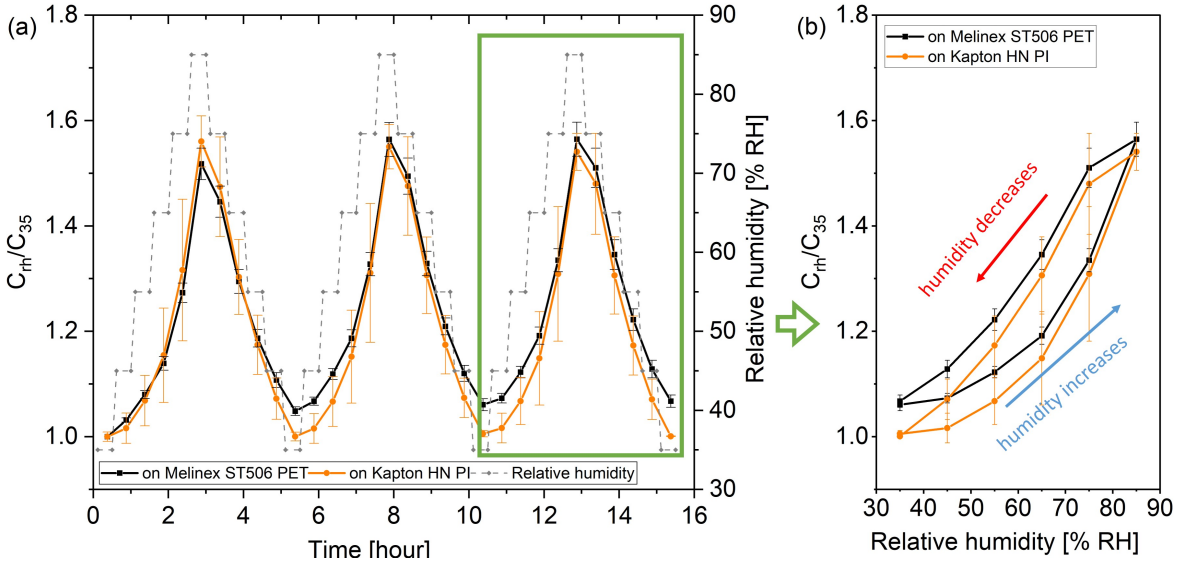

Figure 3.13: Relative capacitance of inkjet printed capacitors on Melinex ST506 PET and Kapton HN PI substrates during cyclic humidity tests. (a) Relative capacitance over time at 23 °C for three measurement cycles. (b) Relative capacitance over relative humidity in the last measurement cycle. Three samples on each type of substrates are measured. Error bars represent standard deviations.

Despite the variation in absolute capacitance between capacitors on PET and PI substrates, the relative capacitance (normalized to the capacitance at 35 %RH in the first measurement cycle) shows less difference between the two substrate types. As shown in **Figure 3.13**, capacitance increases by approximately 55 % for capacitors both on PET substrates and PI substrates as the relative humidity increases from 35 %RH to 85 %RH. These findings indicate the necessity of a proper encapsulation to mitigate the influence of moisture on the printed capacitors' performance.

3.3 Conclusion

In this chapter, inkjet printed Ag tracks (thermally sintered at 120 °C for one hour) and capacitors printed with the Ag NP ink and the BST/P(VDF-TrFE) ink are subjected to three environmental tests based on various standards. After SAG test, a decrease in resistance of printed Ag tracks is observed, which indicates that the thermally sintered Ag NPs can be additionally sintered under the condition of 85 °C and 50 %RH. As reported in previous studies [210, 211], polyvinyl pyrrolidone (PVP) is the capping agent to stabilize the Ag NPs. At the temperature of 85 °C, a thermal decomposition of the capping layer can be excluded, as the thermal decomposition of PVP starts between 250 °C and 600 °C [212]. Moreover, the melting point of Ag NP is significantly higher than 85 °C, suggesting that this additional sintering effect may be influenced by moisture. A similar observation is reported by Bourassa et al. [105]. They report an enhanced sintering effect of Ag NPs by placing a cup of water (10 g) on a bottom tray in an oven at 120 °C for one hour. They suggest that the enhanced sintering effect is influenced by the interaction of water with the capping layer and by the sintering pressure on the Ag NPs due to the surface tension of water. To explore the role of moisture in sintering of Ag NPs at a low temperature of 85 °C, a systematic investigation is necessary. If verified, this effect could enable the development of a novel low-temperature sintering process for Ag NPs, effective even at 85 °C.

The inkjet printed capacitor shows negligible changes in capacitance after the SAG and the SDH tests. However, a dynamic variation in capacitance with changes in humidity reveals the moisture sensitivity of the dielectric BST/P(VDF-TrFE) material. This characteristic shows promising potential for applications in humidity sensing. However, the moisture sensitivity raises concerns regarding the long-term stability and reliability of these capacitors in humid environments. Addressing these challenges requires further investigation to mitigate the effects of moisture. Potential solutions include encapsulation techniques to enhance both functionality and durability of these devices in practical applications.

4 Moisture influence on the sintering of a silver nanoparticle ink

The findings in chapter 3 indicate that moisture may enhance the sintering effect of PVP capped Ag NPs at a low temperature of 85 °C. In this chapter, two novel low-temperature sintering methods, controlled damp heat sintering and water sintering, are introduced. A systematic investigation is conducted to explore the role of moisture in sintering of Ag NPs in a low temperature range (23 °C to 85 °C). Additionally, the influence of two drying methods on the water sintering effect is explored. Furthermore, three environmental tests are conducted to evaluate the stability of printed silver tracks sintered using different processes. A comprehensive explanation of the sintering mechanism of PVP capped Ag NPs at low temperature ranges is provided. [1]

4.1 Materials and methods

Materials and methods utilized in this chapter are described in the following sections.

4.1.1 Materials

Substrates Three types of substrates are utilized:

- Mitsubishi NB-TP-3GU100 PET films (138 µm thick [213]). NB-TP-3GU100 PET films exhibit significant deformation at temperatures exceeding 100 °C, attributed to the nanoporous coating on one surface.
- DuPont Teijin Films Melinex ST506 PET films (175 µm thick). Melinex ST506 PET films are heat-stabilized PET substrates capable of withstanding processing temperatures up to 150 °C [214].
- DuPont Kapton HN PI films (75 µm thick). Kapton HN films are well-known for their thermal stability, withstanding temperatures as high as 400 °C.

[1] Parts of this chapter are published in: [68] Zehua Chen, Ulrich Gengenbach, Liane Koker, Liyu Huang, Tim P. Mach, Klaus-Martin Reichert, Richard Thelen, and Martin Ungerer. Systematic investigation of novel, controlled low-temperature sintering processes for inkjet printed silver nanoparticle ink. Small, December 2023. ISSN 1613-6829. doi: 10.1002/smll.202306865.

Inkjet printable conductive ink The silver nanoparticle ink, Silverjet DGP 40LT-15C (Sigma Aldrich), contains 30 wt% to 35 wt% Ag NPs dispersed in triethylene glycol monomethyl ether (TGME) as the solvent. Polyvinyl pyrrolidone (PVP) is the capping agent to stabilize the nanoparticles [210, 211]. According to the technical data sheet, this ink exhibits a specific resistivity of 11 µΩ cm after sintering at 250 °C for three hours.

Silicone oil Silicone oil for the oil bath is purchased from VWR Chemicals (VWR catalog number: 24610.363) and is utilized to study the influence of heat transfer by a liquid during the sintering process.

4.1.2 Test structure - inkjet printed silver tracks

The inkjet printed Ag tracks are utilized as test structures. These Ag tracks have a length of 45 mm, with pads at both ends measuring 1.5 mm × 3.5 mm (see **Figure 3.6**).

The Ag tracks are printed on NB-TP-3GU100 substrates at room temperature (RT) and left to dry for seven days under the same conditions. When Melinex ST506 and Kapton HN are used as substrates, the printer hotplate temperature is set to 85 °C during printing to minimize ink spreading. After printing, the samples are dried on the hotplate for an additional 45 minutes at 85 °C. The printing parameters, voltage and pulse width, are set to 170 V and 45 µs, respectively. A vacuum pressure of 7 mbar is applied to the ink vessel. The drop distance is adjusted to 50 µm for NB-TP-3GU100, and 100 µm for Melinex ST506 and Kapton HN. The Ag tracks are printed in two passes.

4.1.3 Two novel low-temperature sintering processes for inkjet printed silver tracks

Damp heat sintering Damp heat sintering processes are conducted in a climate chamber (Memmert CTC 256). The test conditions are set to 85 %RH and three different temperatures: 23 °C, 55 °C, and 85 °C. At each temperature, three to five Ag tracks are sintered. The resistance of these Ag tracks is measured before sintering and after one hour, three hours, and 24 hours of sintering.

The detailed settings for the damp heat sintering experiments are listed in **Table 4.1**. To compare the damp heat sintering results, reference printed Ag tracks are thermally sintered in a convection oven (Memmert UF30 plus). The thermal sintering temperatures are 85 °C for the printed Ag tracks on NB-TP-3GU100 and Melinex ST506 substrates, and 250 °C for the printed Ag tracks on Kapton HN substrates.

Table 4.1: Damp heat sintering process parameters (adapted from [68], own publication)

Substrate	Humidity (% RH)	Climate chamber temperatures (°C)			Durations (h)		
NB-TP-3GU100	85	23	55	85	1	3	24
Melinex ST506	85	23	55	85	1	3	24
Kapton HN	85		85		1	3	24

Water sintering To ensure optimal exposure of the printed Ag tracks to water at various temperatures, they are immersed in deionized water (DIW) at different temperatures, 23 °C, 55 °C, and 85 °C. The detailed settings for the water sintering experiments are listed in **Table 4.2**. Four-point resistance measurements are conducted before and after each immersion.

Table 4.2: Water sintering process parameters (adapted from [68], own publication)

Substrate	DIW temperatures (°C)			Durations (min)			
NB-TP-3GU100	23	55	85	1	4	16	64
Melinex ST506	23	55	85	1	4	16	64
Kapton HN		85		1	4	16	64

Water exhibits distinctive chemical properties, such as high polarity, and physical properties, including high surface energy and heat capacity. These chemical and physical influences are analyzed separately. A possible explanation for the observed sintering effect could be physical, specifically due to the enhanced heat transfer provided by a fluid with high heat capacity. To explore the impact of intensified heat transfer in a fluid with high heat capacity, reference test structures printed on NB-TP-3GU100 and Melinex ST506 PET substrates are immersed in a silicone oil bath at 85 °C for the same durations as those used in the water sintering process (see **Table 4.2**).

4.1.4 Investigation of the influence of drying processes on water sintering

Before water sintering, the printed Ag tracks must be dried to prevent damage during immersion. The following investigation evaluates the influence of two different drying processes on the final water sintering outcome. A baseline water sintering process, conducted at 85 °C in DIW for 16 minutes, is established to assess how these drying processes influence the removal of ink solvents and affect the subsequent water sintering.

Vacuum drying Test structures are printed on Melinex ST506 substrates at three different temperatures (23 °C, 55 °C, 85 °C) and left on the hot plate for a total of 15 minutes. To remove ink solvents, the test structures undergo vacuum drying for 40 minutes at a pressure of 0.3 mbar in a plasma oven chamber (Diener Atto). After drying, they are electrically characterized and then subjected to 16 minutes of water sintering (see **Figure 4.1**).

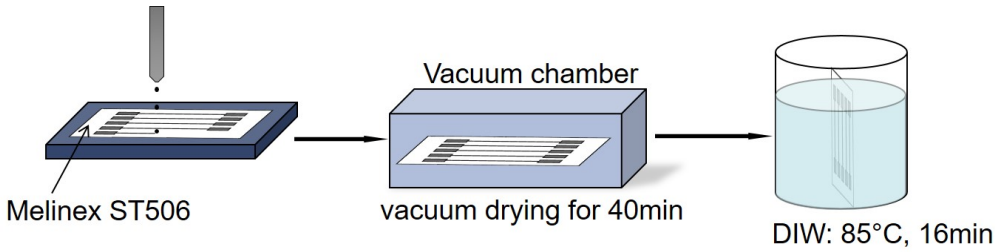

Figure 4.1: Schematic illustration of the vacuum drying process prior to the water sintering process (published in [68], own publication).

Thermal drying To examine whether a thermal drying process affects the subsequent water sintering, additional test structures are printed on Melinex ST506 substrates. During printing, the hotplate temperature is set to 85 °C, and the test structures remain on the hotplate for a total of 15 minutes. Following this, the test structures are divided into four groups for further thermal drying processes.

- Group A: test structures are directly immersed in DIW at 85 °C for 16 minutes;
- Group B: test structures stay on the printer hotplate at 85 °C for additional 75 minutes before immersion in DIW at 85 °C for 16 minutes;
- Group C: test structures are placed in the oven at 85 °C for two hours before immersion in DIW at 85 °C for 16 minutes;
- Group D: test structures are placed in the oven at 100 °C for one hour before being immersed in DIW at 85 °C for 16 minutes.

The experimental setup is illustrated in **Figure 4.2**.

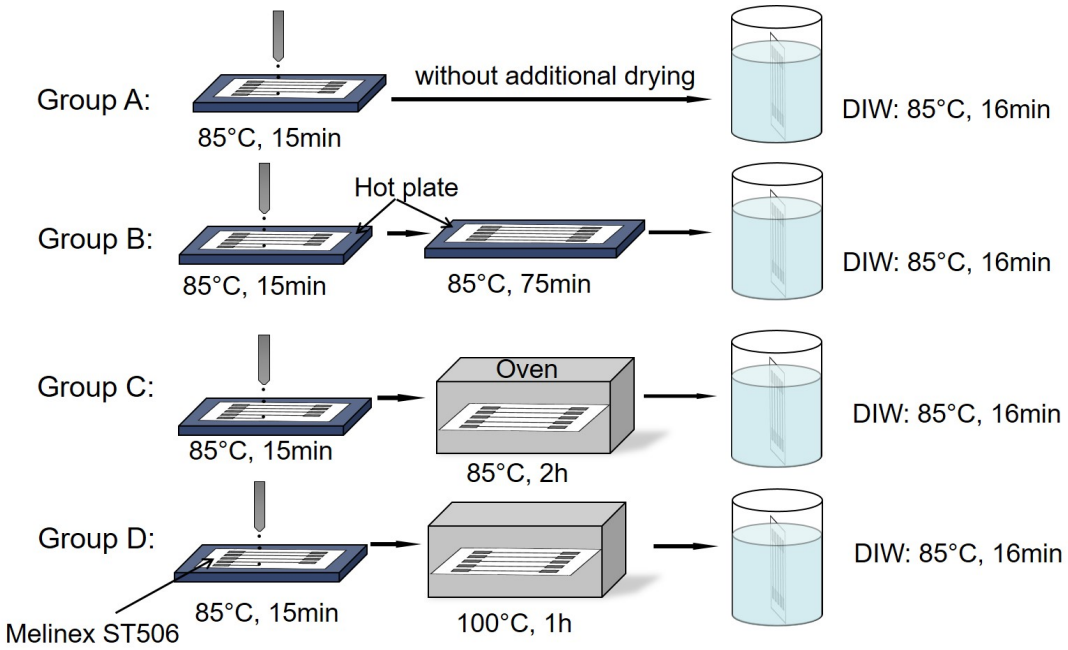

Figure 4.2: Schematic illustration of the thermal drying processes prior to the water sintering process (published in [68], own publication).

4.1.5 Characterization of inkjet printed silver tracks

The linewidth of the printed Ag tracks is firstly measured using a Keyence VHX 7000 microscope. In addition, the linewidth, cross-sectional area, and roughness of the printed Ag tracks on three different substrates are assessed with a MahrSurf CM select confocal microscope. Data obtained from these measurements are analyzed using the MountainsLab software. Scanning electron microscopy (SEM) images of the Ag tracks are captured from the top using a Zeiss SUPRA 60 VP. Energy-dispersive X-ray spectroscopy (EDX) analysis is conducted using an Ultim Extreme silicon drift detector (Oxford Instruments, AZtec software) at a Zeiss SUPRA 55, operating at an acceleration voltage of 4 kV, to determine the elemental composition. Atomic force microscopy (AFM) image of printed Ag NPs is taken using a Veeco Dimension Icon Atomic Force Microscope. Four-point resistance measurements are conducted using a B&K Precision LCR-Meter 981 connected to a Formfactor EPS150 probestation, with 150 µm probe tips. Environmental tests described in section 3.1.3 are conducted to evaluate the stability of the printed silver tracks sintered by different sintering methods.

4.2 Results

The printed Ag tracks on three different substrate types are optically characterized. They are sintered using two novel low-temperature sintering methods. Additionally, the influence of two drying processes on the water sintering is investigated. Furthermore, these novel sintering

methods are compared with the thermal sintering by evaluating the conductivity stability of the printed Ag tracks. The results are presented in the following sections.

4.2.1 Optical inspection results of the inkjet printed Ag tracks

As shown in **Figure 4.3**, the printed Ag tracks on NB-TP-3GU100 substrates exhibit significant differences compared to those on Melinex ST506 and Kapton HN substrates. The Ag tracks on NB-TP-3GU100 show significantly narrower widths than those printed on Melinex ST506 and Kapton HN.

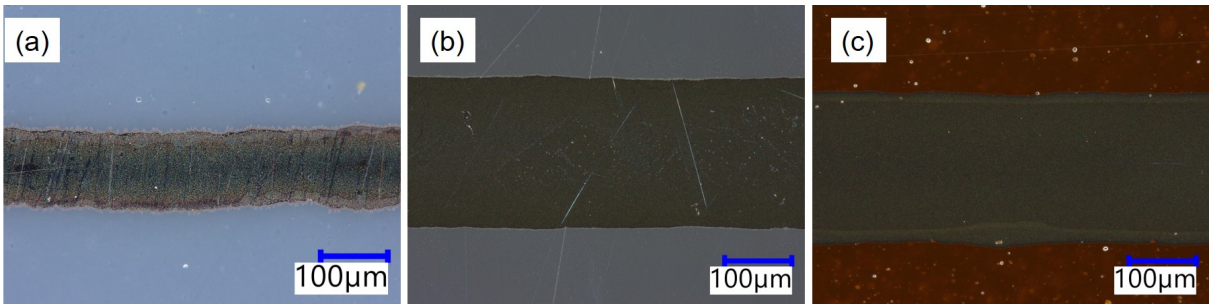

Figure 4.3: Inkjet printed Ag tracks on (a) NB-TP-3GU100, (b) Melinex ST506, and (c) Kapton HN substrates (published in [68], own publication).

In order to explain these differences, the surface roughness of the three substrates is measured using a MahrSurf CM select confocal microscope. The measured surface roughness values are presented in **Table 4.3**. Among the tested substrates, the NB-TP-3GU100 PET substrate exhibits the highest roughness, followed by the Kapton HN PI substrate, while the Melinex ST506 PET substrate has the smoothest surface.

Table 4.3: Measured roughnesses of the three substrates. For every substrate, six areas are selected for the measurement (published in [68], own publication).

Substrate	NB-TP-3GU100	Melinex ST506	Kapton HN
Roughness [nm]	152.30 ± 57.75	13.10 ± 2.79	83.47 ± 20.65

The variation of surface properties of these three substrates results in different inkjet printing outcomes of the Ag tracks. The measured mean width and cross-sectional area of the Ag tracks are 122.13 ± 6.91 µm and 149.27 ± 20.20 µm^2 on NB-TP-3GU100, 229.13 ± 9.55 µm and 127.00 ± 7.96 µm^2 on Melinex ST506, and 222.60 ± 12.82 µm and 131.60 ± 10.61 µm^2 on Kapton HN substrates, respectively (see **Figure 4.4**).

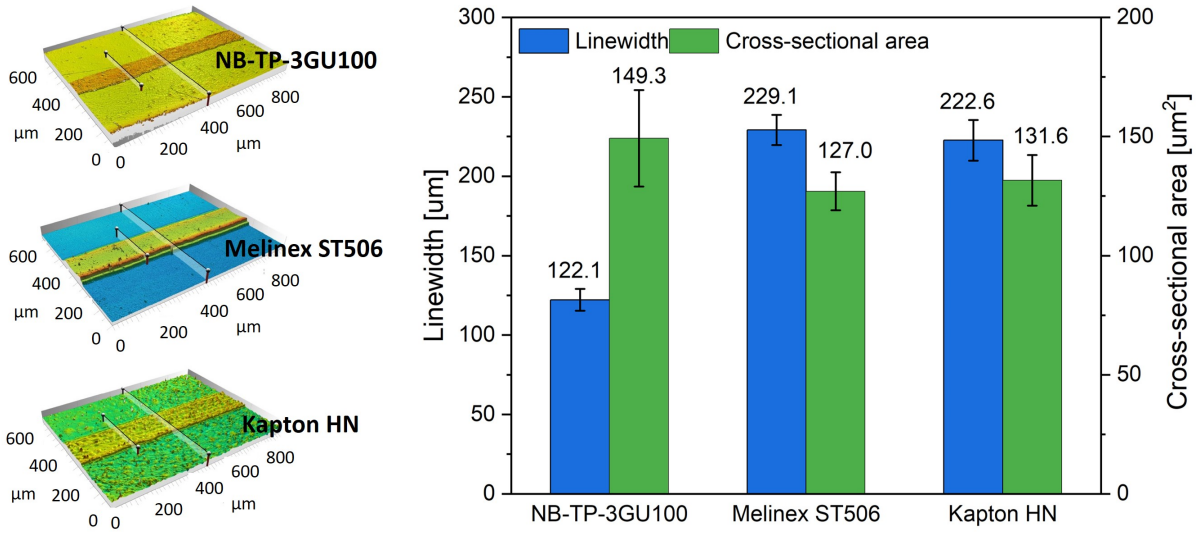

Figure 4.4: Measured linewidth and cross-sectional area of the printed Ag tracks on three different substrates. Three Ag tracks on each substrate, and five profiles (with a 10 mm spacing between each) on each Ag track are measured. Error bars represent standard deviations (adapted from [68], own publication).

4.2.2 Damp heat sintering results

A high humidity environment positively influences the sintering process. The resistances and the reduction in resistance after sintering of Ag tracks printed on three types of substrates are measured. Under constant humidity of 85 %RH, the resistance decreases further as the applied sintering temperature increases.

When NB-TP-3GU100 PET films are used as substrates, Ag tracks are printed and left to dry completely at room temperature for seven days. Reference Ag tracks on NB-TP-3GU100 substrates are thermally sintered in an oven at 85 °C.

As shown in **Figure 4.5**, even at a very low temperature of 23 °C, the resistance of printed Ag tracks decreases significantly over time, from 124.98 Ω to 99.99 Ω after one hour, then to 91.64 Ω after three hours, and finally to 77.45 Ω after 24 hours. At a higher temperature of 55 °C, the resistance drops more rapidly, decreasing by 45 % from 136.08 Ω to 75.30 Ω after one hour, and further to 57.58 Ω after 24 hours.

The most effective sintering occurs at 85 °C and 85 %RH, where the resistance sharply decreases from 134.92 Ω to 45.30 Ω after one hour, then to 41.80 Ω after three hours. However, with a prolonged sintering duration of 24 hours, the resistance slightly increases to 42.67 Ω. Without a high humidity environment, the sintering effect is significantly reduced. For reference, Ag tracks sintered in an oven at 85 °C for 24 hours show only a 12 % reduction in resistance, compared to a 69 % reduction under 85 °C and 85 %RH.

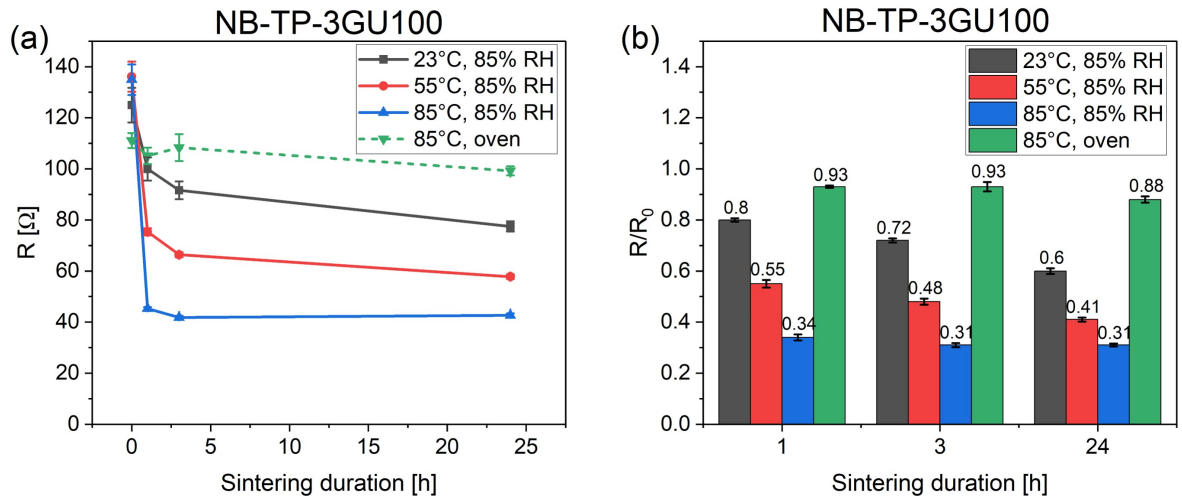

Figure 4.5: (a) The resistances R and (b) the resistance reduction R/R_0 of printed Ag tracks on NB-TP-3GU100 substrates are measured after one hour, three hours, and 24 hours of damp heat sintering. R_0 is the resistance before sintering. Three to five printed Ag tracks are characterized for each condition. Error bars represent standard deviations (adapted from [68], own publication).

Similar tendencies are observed in samples printed on Melinex ST506 substrates, as shown in **Figure 4.6**. The optimal damp heat sintering effect is achieved under conditions of 85 °C and 85 %RH, where the resistance decreases with extended sintering durations. After 24 hours, the resistance of samples decreases by 57 % on Melinex ST506 substrates.

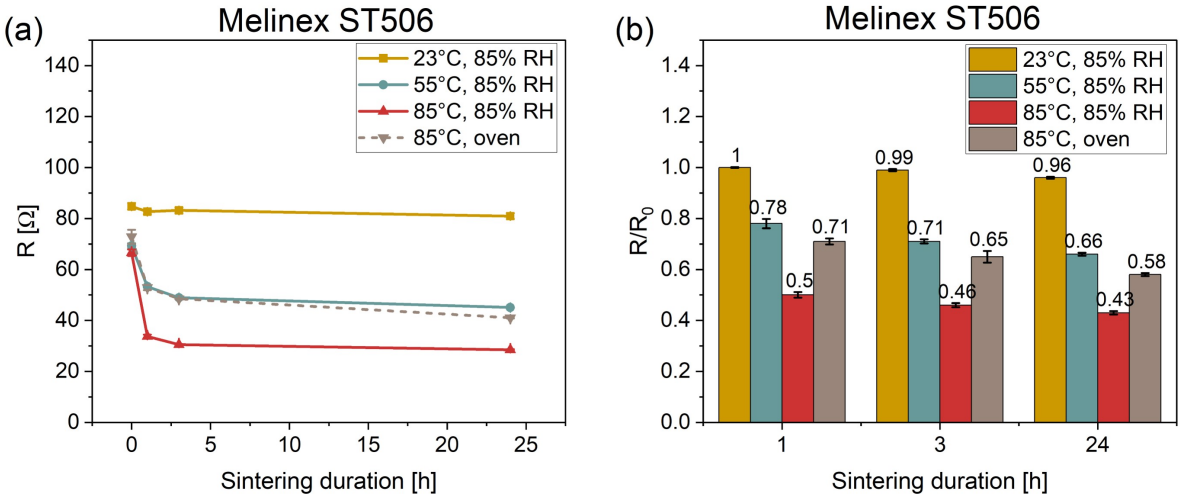

Figure 4.6: (a) The resistances R and (b) the resistance reduction R/R_0 of printed Ag tracks on Melinex ST506 substrates are measured after one hour, three hours, and 24 hours of damp heat sintering. R_0 is the resistance before sintering. Three to five printed Ag tracks are characterized for each condition. Error bars represent standard deviations (adapted from [68], own publication).

However, unlike NB-TP-3GU100 substrates, the sintering effect on Melinex ST506 substrates at 23 °C and 85 %RH is negligible. This difference can be attributed to the water adsorption properties of the substrates. NB-TP-3GU100 substrates feature a porous coating approximately 38 µm thick [213], which facilitates greater moisture adsorption. This enhanced moisture uptake

promotes neck formation between Ag NPs, leading to improved conductivity even at a low temperature of 23 °C. In contrast, the smoother surface of Melinex ST506 substrates is less prone to water adsorption, resulting in less neck formation between Ag NPs at low temperatures.

Additionally, the nanoporous coating on NB-TP-3GU100 substrates makes them thermally more sensitive in a dry state. Slight bending is observed after sintering in an oven at 85 °C, while this effect is not observed in the climate chamber with conditions set to 85 °C and 85 %RH. This small deformation may introduce mechanical stress to the printed Ag tracks and lead to poor conductivity. Melinex ST506 substrates are capable of withstanding temperatures up to 150 °C, with no deformation observed when heated in an oven at 85 °C.

The effectiveness of damp heat sintering at 85 °C and 85 %RH on printed Ag tracks on Kapton HN substrates is presented in **Figure 4.7**. Prior to sintering, the resistance of the printed Ag tracks on Kapton HN substrates is 66.00 Ω. After one hour of damp heat sintering, the resistance decreases significantly to 23.38 Ω, which is approximately twice the resistance of Ag tracks thermally sintered at 250 °C for one hour (10.65 Ω).

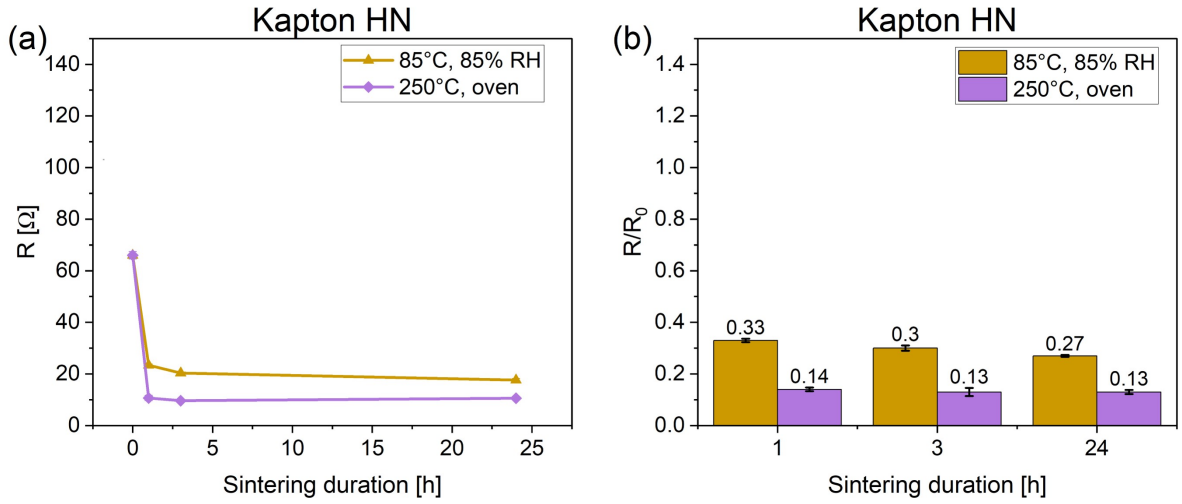

Figure 4.7: (a) The resistances R and (b) the resistance reduction R/R_0 of printed Ag tracks on Kapton HN substrates are measured after one hour, three hours, and 24 hours of damp heat sintering. R_0 is the resistance before sintering. Three to five printed Ag tracks are characterized for each condition. Error bars represent standard deviations (adapted from [68], own publication).

After 24 hours of damp heat sintering, the resistance further decreases to 17.66 Ω with a calculated resistivity of 5.16 µΩ cm, which is only 1.7 times that of the Ag tracks thermally sintered at 250 °C for 24 hours (10.58 Ω), with a calculated resistivity of 3.09 µΩ cm.

Figure 4.8 compares the damp heat sintering effect (85 °C, 85 %RH) on printed Ag tracks across three types of substrates. As shown in **Figure 4.8 (a)**, the resistance of Ag tracks on NB-TP-3GU100 substrates is higher than that of Ag tracks printed on Melinex ST506 and Kapton HN substrates. This difference arises because the NB-TP-3GU100 substrates are at room temperature during printing, while the Melinex ST506 and Kapton HN substrates are heated to

85 °C. **Figure 4.8 (b)** demonstrates that the resistance of Ag tracks decreases more significantly on NB-TP-3GU100 and Kapton HN substrates compared to Melinex ST506 substrates.

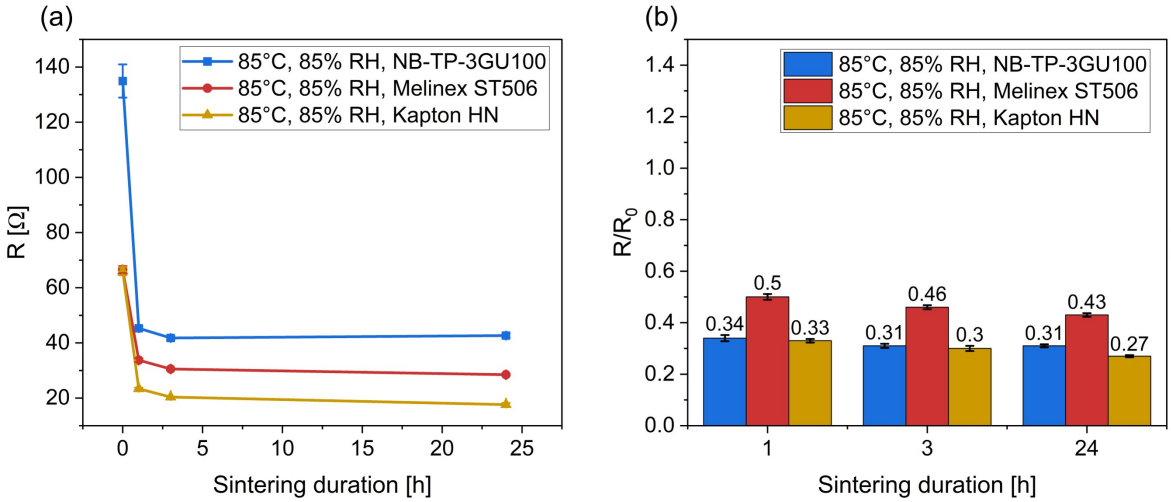

Figure 4.8: Comparison of damp heat sintering effect (85 °C, 85 %RH) among printed Ag tracks on NB-TP-3GU100, Melinex ST506, and Kapton HN substrates. The resistances R of printed Ag tracks are measured after one hour, three hours, and 24 hours of sintering. R/R_0 represents the resistance reduction after the respective sintering durations, where R_0 is the resistance before sintering. Three to five printed Ag tracks are characterized for each condition. Error bars represent standard deviations (adapted from [68], own publication).

The SEM images in **Figure 4.9** provide morphological evidence supporting the resistivity data. Sintering Ag NPs in a high humidity environment (85 %RH), even at low temperatures below 100 °C, results in noticeable particle necking and the formation of a porous, mesh-like network structure without significant growth of the Ag NPs. The SEM images show that higher temperatures promote more extensive neck formation between Ag NPs, contributing to reduced resistance.

Moreover, these images confirm that the presence of moisture is critical for neck formation between Ag NPs. **Figure 4.9 (i) and (j)** reveal distinct structural differences between Ag NPs sintered under damp heat conditions (85 °C, 85 %RH) and those sintered in an oven at 250 °C. Under damp heat conditions, more pronounced neck formation is observed, whereas thermal sintering in an oven at 250 °C leads to stronger growth and coalescence of the Ag NPs.

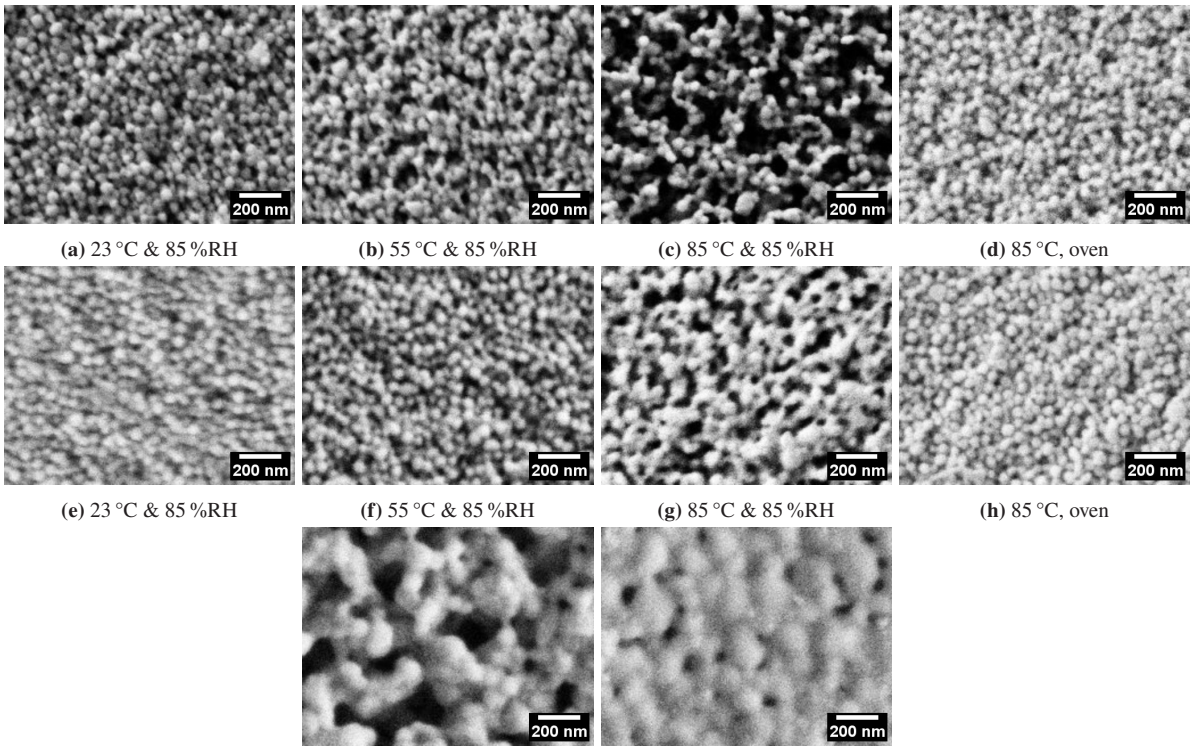

(a) 23 °C & 85 %RH **(b)** 55 °C & 85 %RH **(c)** 85 °C & 85 %RH **(d)** 85 °C, oven

(e) 23 °C & 85 %RH **(f)** 55 °C & 85 %RH **(g)** 85 °C & 85 %RH **(h)** 85 °C, oven

(i) 85 °C & 85 %RH **(j)** 250 °C, oven

Figure 4.9: SEM images of Ag NPs on different substrates after sintering under different conditions. All images have the same magnification.
(a)-(d): Ag NPs on **NB-TP-3GU100** substrates sintered in a climate chamber under damp heat conditions for 24 hours.
(e)-(h): Ag NPs on **Melinex ST506** substrates sintered in a climate chamber under damp heat conditions for 24 hours.
(i)-(j): Ag NPs on **Kapton HN** substrates sintered in a climate chamber (i) and in an oven (j) for 24 hours (published in [68], own publication).

4.2.3 Water sintering results

The resistances and the reduction in resistance before and after water sintering of Ag tracks printed on three types of substrates with various water sintering durations are measured. To isolate the influence of fluid heat transfer, reference Ag tracks are immersed in oil at 85 °C for the same durations as the water sintering processes.

When using NB-TP-3GU100 films as substrates (see **Figure 4.10**), immersing Ag tracks in 23 °C DIW for 64 min only results in a 17 % reduction in resistance. However, as the temperature of DIW increases to 55 °C, a noticeable decrease of resistance by 56 % after 64 min is observed. The best sintering effect occurs when the temperature of DIW is raised to 85 °C. Even after just one minute of immersion, the resistance drops sharply by 60 %. After 64 minutes of immersion, the resistance drops by 81 %.

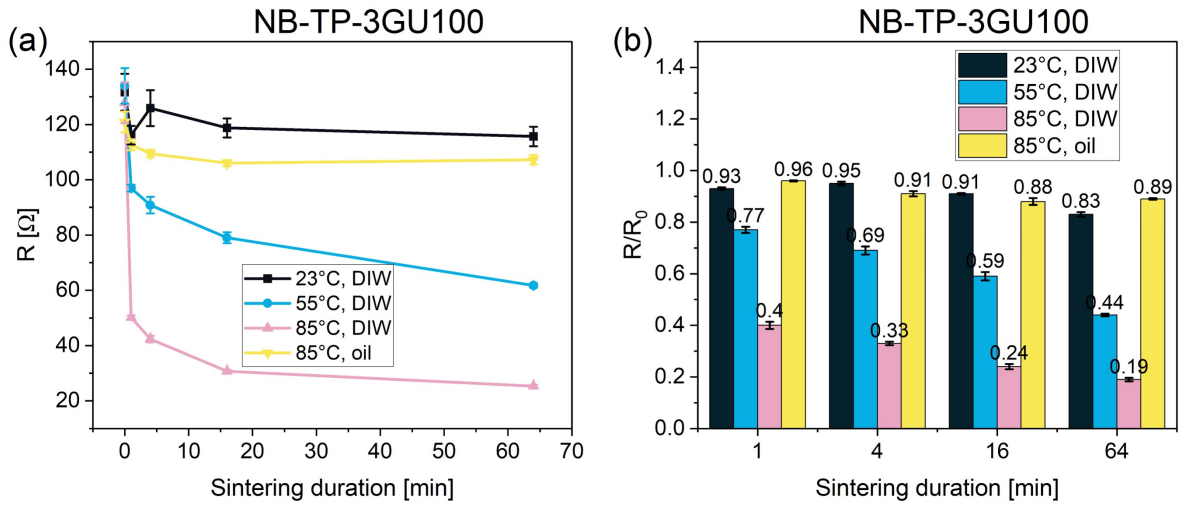

Figure 4.10: (a) The resistances R and (b) the resistance reduction R/R_0 of printed Ag tracks on NB-TP-3GU100 substrates after water sintering. R_0 is the resistance before before each immersion in DIW/oil. The sintering durations are set to 0 min (unsintered samples), 1 min, 4 min, 16 min, 64 min. Three to five printed Ag tracks are characterized for each condition. Error bars represent standard deviations (adapted from [68], own publication).

When using Melinex ST506 films as substrates (see **Figure 4.11**), no difference in resistance is observed between the non-sintered samples and those sintered in DIW at 23 °C. However, as the temperature of DIW increases to 55 °C, the effect of water sintering becomes evident, with the resistance decreasing by 31 % within the first 16 minutes. Similar to the results obtained on NB-TP-3GU100 substrates, the most effective water sintering on Melinex ST506 occurs at 85 °C, where the resistance decreases sharply, even within the first minute of immersion.

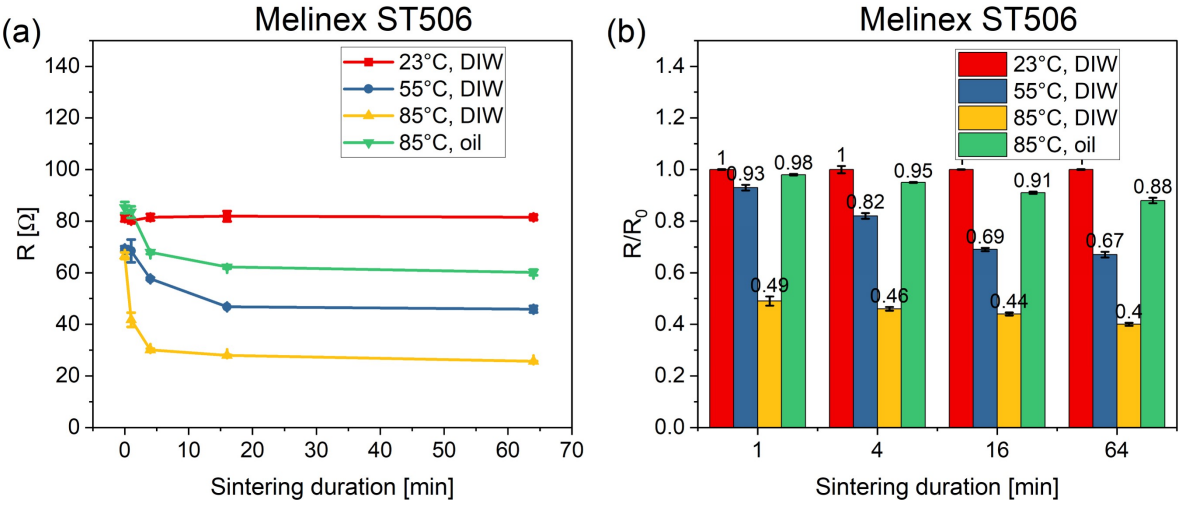

Figure 4.11: (a) The resistances R and (b) the resistance reduction R/R_0 of printed Ag tracks on Melinex ST506 substrates after water sintering. R_0 is the resistance before before each immersion in DIW/oil. The sintering durations are set to 0 min (unsintered samples), 1 min, 4 min, 16 min, 64 min. Three to five printed Ag tracks are characterized for each condition. Error bars represent standard deviations (adapted from [68], own publication).

To distinguish the influence of fluid heat transfer from the supposed influence of water on the capping agents, printed Ag tracks on both NB-TP-3GU100 and Melinex ST506 substrates are immersed in silicone oil at 85 °C. For both substrates, after 64 minutes of immersion in silicone oil, the reduction in resistance is significantly less than that observed for Ag tracks immersed in DIW at 85 °C. This provides strong evidence that, compared to heat transfer alone, the influence of water plays a dominant role in the sintering process.

When using Kapton HN films as substrates (see **Figure 4.12**), a significant reduction in resistance is also observed. Immersing Ag tracks in DIW at 85 °C results in resistance reductions of 67 % after one minute and 72 % after four minutes. However, the adhesion between the printed Ag tracks and the Kapton HN substrate is notably weak, with the tracks peeling off the substrate after just four minutes of immersion (see **Figure 4.13**).

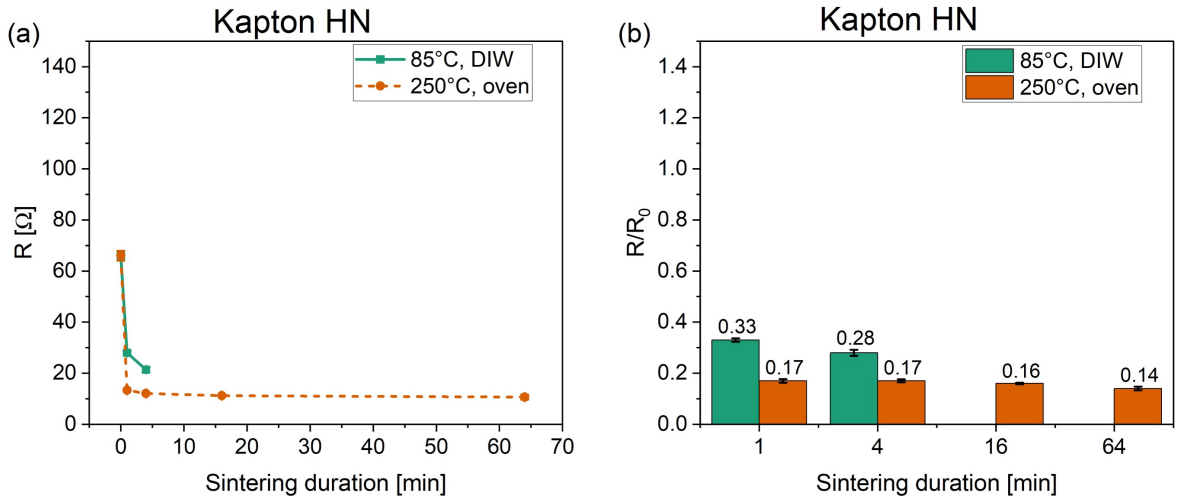

Figure 4.12: (a) The resistances R and (b) the resistance reduction R/R_0 of printed Ag tracks on Kapton HN substrates after water sintering. R_0 is the resistance before before each immersion in DIW/oil. The sintering durations are set to 0 min (unsintered samples), 1 min, 4 min, 16 min, 64 min. Three to five printed Ag tracks are characterized for each condition. Error bars represent standard deviations (adapted from [68], own publication).

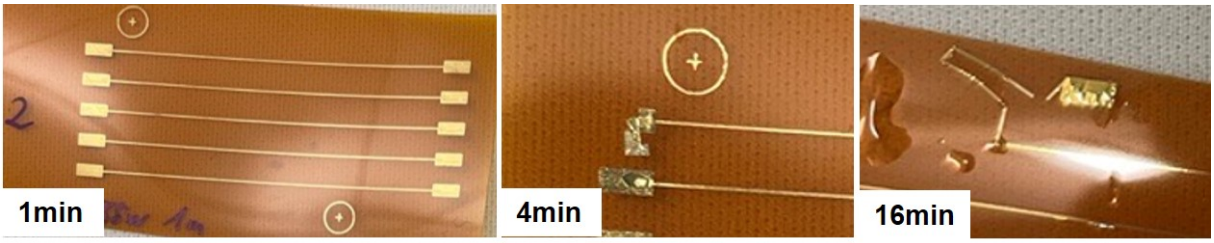

Figure 4.13: Ag tracks printed on Kapton HN substrates after immersing into DIW at 85 °C for different durations (published in [68], own publication).

Nevertheless, the Ag tracks remain intact on the Kapton HN substrate when the immersion duration is set to one minute, and the resulting resistance is only twice that of Ag tracks sintered

in an oven at 250 °C for one minute. The phenomenon of sectional detachment of the printed Ag tracks and pads while retaining their original shape suggests that the cohesion among the Ag NPs is significantly stronger than their adhesion to the Kapton HN substrate. This observation supports the assumption of a noticeable sintering level.

Figure 4.14 compares the water sintering effects on printed Ag tracks across these three types of substrates. Similar to damp heat sintering, water sintering occurs most effective for the Ag tracks on Kapton HN substrates. However, as previously mentioned, the adhesion issue between the Ag tracks and the Kapton HN substrate remains a challenge that requires a solution.

For Ag tracks on NB-TP-3GU100 substrates, the initial resistance of the non-sintered samples is higher than those printed on Melinex ST506 substrates. This is probably due to different substrate temperatures during printing. Nevertheless, after 16 min of 85 °C water sintering, the resistance difference between the two substrates becomes less, and after 64 min, it is nearly negligible.

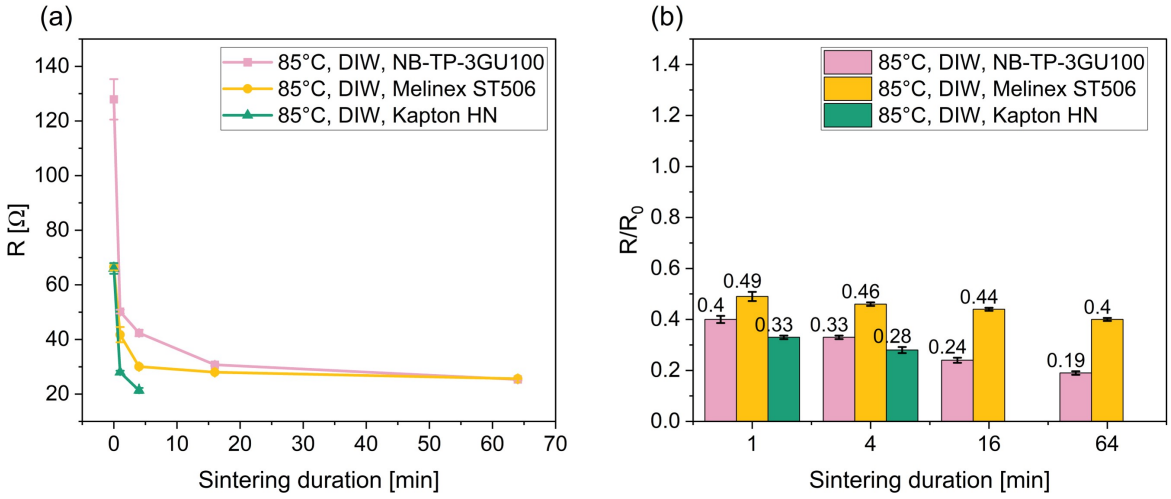

Figure 4.14: Comparison of water sintering effect (85 °C of DIW) among the printed Ag tracks on NB-TP-3GU100, Melinex ST506, and Kapton HN substrates. The resistances are measured before and after immersing the samples in DIW/oil. R_0 is the resistance before each immersion in DIW/oil. R represents the resistance of Ag tracks after each immersion in DIW, while R/R_0 represents the resistance reduction. For each sintering duration, five printed Ag tracks are measured. Error bars represent standard deviations (adapted from [68], own publication).

Figure 4.15 shows SEM images of the surface morphology of water sintered Ag NPs. Similar to the results from damp heat sintering, a porous, mesh-like network structure of Ag NPs is observed after sintering in DIW. Moreover, the formation of this network occurs faster and more pronounced with increasing DIW temperature.

Figure 4.15 (d) and (h) show SEM images of Ag NPs sintered in an oil bath at 85 °C for 64 min. No significant neck formation is observed, indicating that water plays a critical role in promoting neck formation between Ag NPs, yielding more conductive paths, thus, leading to enhanced conductivity.

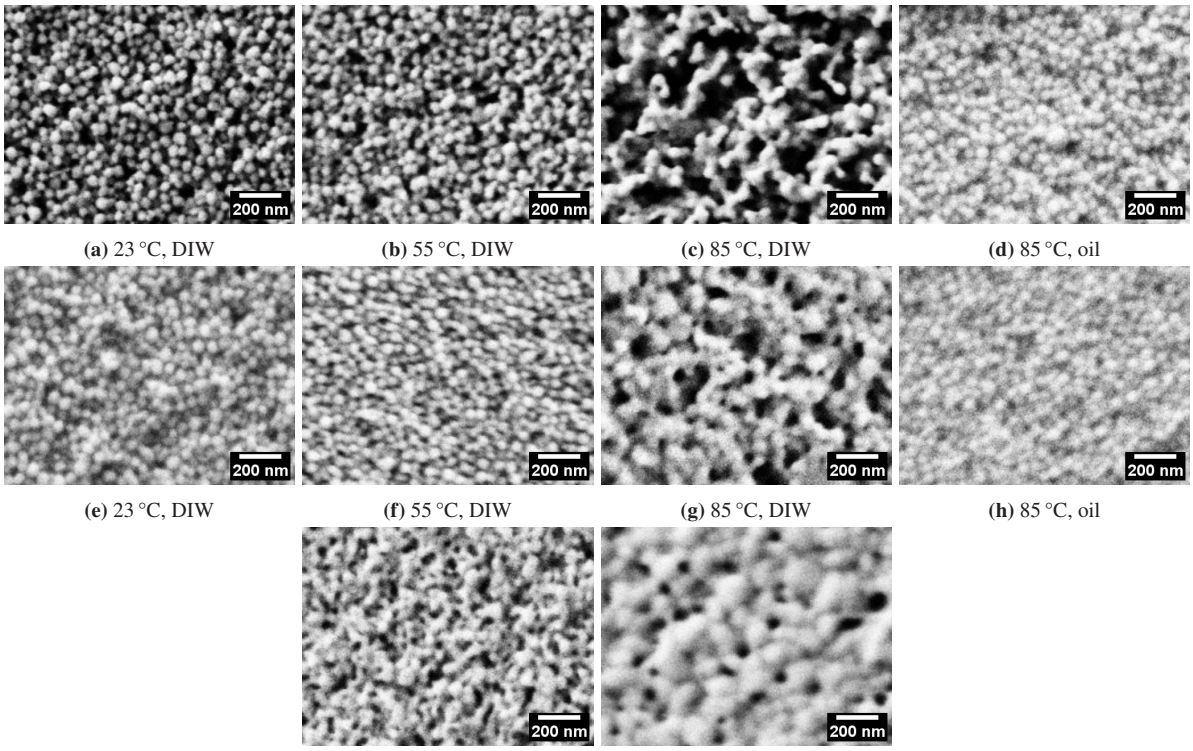

(a) 23 °C, DIW **(b)** 55 °C, DIW **(c)** 85 °C, DIW **(d)** 85 °C, oil

(e) 23 °C, DIW **(f)** 55 °C, DIW **(g)** 85 °C, DIW **(h)** 85 °C, oil

(i) 85 °C, DIW **(j)** 250 °C, oven

Figure 4.15: SEM images of Ag NPs on different substrates after sintering under different conditions. All images have the same magnification. (a)-(d): Ag NPs on **NB-TP-3GU100** substrates sintered for 64 min. (e)-(h): Ag NPs on **Melinex ST506** substrates sintered for 64 min. (i)-(j): Ag NPs on **Kapton HN** substrates sintered for 4 min in (i) DIW at 85 °C, and (j) in the oven at 250 °C (published in [68], own publication).

4.2.4 Influence of two drying processes on the water sintering effect

To prevent damage during immersion in water, the printed Ag tracks must be dried before water sintering. Section 4.2.3 reveals that a water sintering duration of 16 min is sufficient to achieve a significant reduction in resistance for Ag tracks on Melinex ST506 substrates. Therefore, this process is used as a baseline to evaluate the influence of two drying methods on the final water sintering effect.

Vacuum drying The substrate temperature during printing plays a role in the removal of ink solvents. To investigate this effect, Ag tracks are printed on Melinex ST506 substrates at three different temperatures (23 °C, 55 °C, and 85 °C) and subsequently vacuum dried for 40 min. As summarized in **Table 4.4**, the Ag tracks printed at 23 °C or 55 °C and then vacuum dried remain non-conductive even after three days of storage under room conditions, whereas the printed Ag tracks not subjected to vacuum drying become conductive (399.67 Ω and 178.60 Ω, respectively). However, when these vacuum dried Ag tracks are further treated with 16 min of water sintering at 85 °C, their resistance drops to 180.63 Ω and 49.86 Ω, respectively.

These results suggest that vacuum drying hinders neck formation among Ag NPs, which is critical for achieving high conductivity. In dry state, the ambient environment cannot facilitate neck formation. Conversely, when the substrate temperature during printing is 85 °C, there is no significant difference in resistance between printed Ag tracks with or without vacuum drying, both before and after water sintering. It is assumed that after extended periods on the printer hotplate at 85 °C, adsorbed water in the printed Ag tracks is already significantly removed. The vacuum drying process does not further reduce water content in the printed Ag tracks.

Table 4.4: Resistance of printed Ag tracks on Melinex ST506 substrate undergoing various treatments. Resistance values are measured from five samples in each group (published in [68], own publication).

T	Vacuum dried (40min), then stored under RT (3d)	Without vacuum, then stored under RT (3d)	Vacuum dried (40min), then 85 °C water sintered (16min)	Without vacuum, then 85 °C water sintered (16min)
23 °C	non-conductive	399.67 ± 33.65 Ω	180.63 ± 32.20 Ω	still wet, non-conductive
55 °C	non-conductive	178.60 ± 6.32 Ω	49.86 ± 3.89 Ω	still wet, non-conductive
85 °C	269.40 ± 12.93 Ω	289.40 ± 11.80 Ω	27.21 ± 1.83 Ω	26.19 ± 1.38 Ω

T: substrate temperature during printing.

Thermal drying To investigate the influence of thermal drying on the water sintering effect, four different conditions are compared:

- group A: test structures remain on the hotplate for a total of 15 minutes during printing, without further drying process;
- group B: test structures stay on the printer hotplate at 85 °C for additional 75 minutes;
- group C: test structures are placed in the oven at 85 °C for two hours;
- group D: test structures are placed in the oven at 100 °C for one hour.

Test structures from these four groups are then immersed in DIW at 85 °C for 16 min. The results show that thermal drying does not positively influence the water sintering process. As shown in **Figure 4.16 (a)**, printed Ag tracks in group D dried in the oven at a higher temperature (100 °C), exhibit however lower conductivity after water sintering compared to the Ag tracks in group A. These are just briefly dried on the printer hotplate (15 min in total, including printing and drying), and achieve the highest conductivity. This behavior can possibly be attributed to the thermally enhanced cross-linking rate of the capping agent, PVP. Tan et al. report that below the thermal decomposition point (250 °C) of PVP, the cross-linking rate increases with temperature [215].

An interesting observation is the change in color of printed Ag tracks subjected to these drying processes. As shown in **Figure 4.16 (b)**, groups C and D exhibit a brownish hue, whereas groups A and B appear more yellowish. To exclude a chemical influence such as the formation of silver oxide, EDX analysis is performed on the four groups. The results in **Table 4.5** indicate

no significant differences in the concentrations of Ag and oxygen (O_2), nor any stoichiometric relation indicative of silver oxide formation.

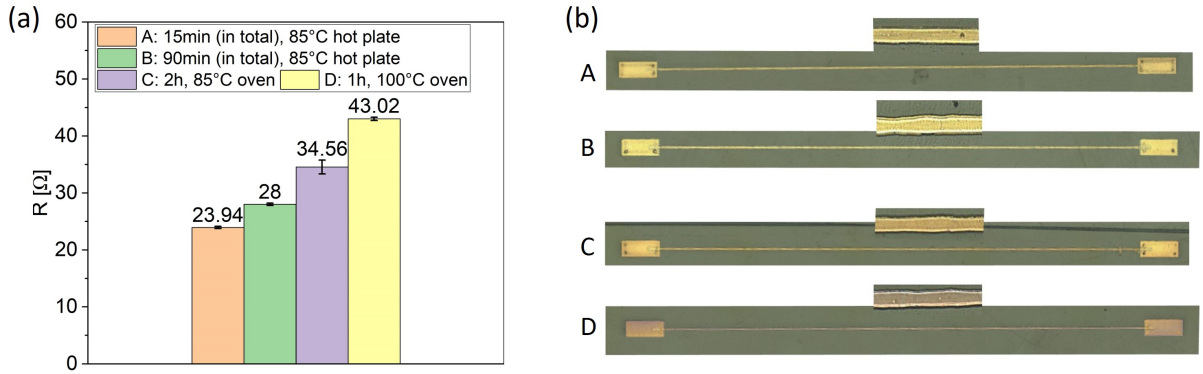

Figure 4.16: (a) Resistance and (b) color of printed Ag tracks on Melinex ST506 substrate undergoing various thermal drying processes and subsequently 16 min of water watering. For each group, five Ag tracks are printed on a substrate. Error bars represent standard deviations. Adapted from [68], own publication.

Table 4.5: Element concentration of printed Ag tracks in four groups (published in [68], own publication)

Group	Drying process	Ag [%]	O [%]	C [%]
A	15 min, 85 °C hot plate	95.87	1.16	2.97
B	90 min, 85 °C hot plate	95.02	1.18	3.79
C	2 h, 85 °C oven	94.23	1.18	4.58
D	1 h, 100 °C oven	94.81	1.43	3.76

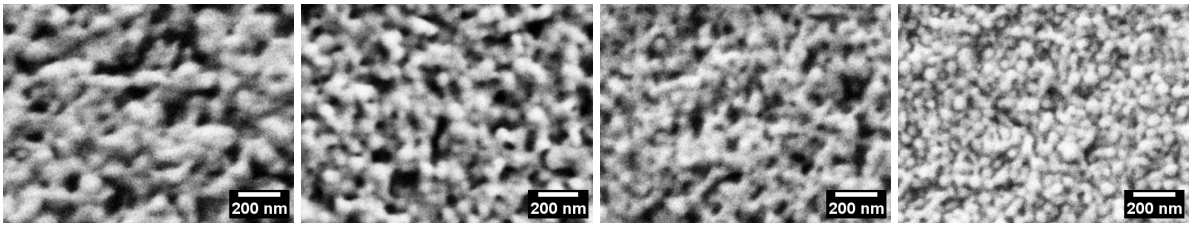

(a) 15 min 85 °C, printer hotplate **(b)** 90 min 85 °C, printer hotplate **(c)** 2 h 85 °C, oven **(d)** 1 h 100 °C, oven

Figure 4.17: SEM images of thermally dried Ag NPs after water sintering in (a) group A, (b) group B, (c) group C and (d) group D. All SEM images have the same magnification (published in [68], own publication).

Further insights are provided by SEM images in **Figure 4.17**, which reveal significant differences in neck formation between Ag NPs in the four groups. These differences result in varying porosities of the water sintered Ag films. As both the particle and pore sizes are much smaller than the wavelength of light, the observed color differences are assumed to be Rayleigh scattering caused by the nanoporous structures [216]. A similar phenomenon has been observed in a nanoporous Ag film created by oxygen plasma [217].

Overall, these findings indicate that thermal drying, whether on a hotplate or in an oven, provides no additional benefits and may even negatively affect the water sintering effect.

4.2.5 Environmental test results of inkjet printed silver tracks sintered by three sintering processes

Previous sections have demonstrated that damp heat sintering and water sintering are two promising methods for sintering PVP-capped Ag NPs to achieve high conductivity. In this section, damp heat sintering (85 °C & 85 %RH, three hours) and water sintering (85 °C, 16 min) are compared with thermal sintering (120 °C, one hour). Three environmental tests are conducted to evaluate the stability of the achieved conductivity in sintered Ag tracks.

The results of static environmental tests of inkjet printed Ag tracks (layout design see **Figure 3.6**, printed on Melinex ST506 PET substrates in two passes) sintered by different processes are as depicted in **Figure 4.18**. Both before and after the SAG test and the SDH test, the thermally (120 °C, one hour) sintered Ag tracks show the highest resistance. The damp heat and water sintered Ag tracks yield better conductivity. Besides, their resistance stays stable under the condition of a SAG test (85 °C and 50 %RH) and a SDH test (40 °C and 85 %RH). The resistance of thermally sintered Ag tracks drops by 13 % after five days of SAG test, while the resistance changes in damp heat and hot water sintered Ag tracks are negligible.

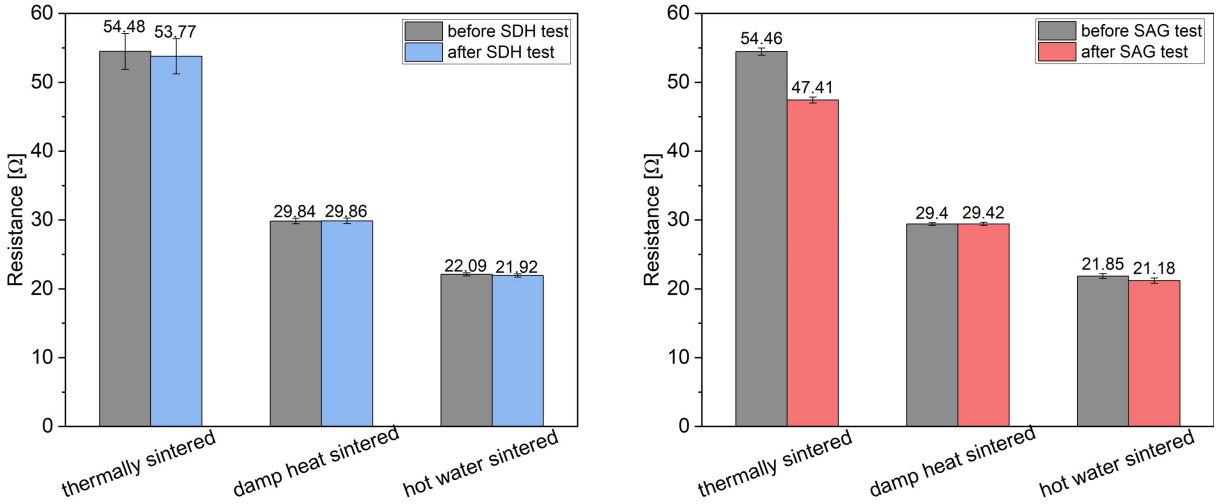

Figure 4.18: Static environmental tests result of inkjet printed silver tracks sintered by three different processes. For each sintering method, five Ag tracks are measured. Error bars represent standard deviations.

Cyclic humidity test results of inkjet printed Ag tracks (layout design see **Figure 3.7**, printed in one pass on Melinex ST506 PET substrates) subjected to three different sintering processes are shown in **Figure 4.19**. The resistance of the Ag track between contact pad ① and ② is measured. Independent of the sintering process used, the resistance of the Ag tracks remains stable both

within and between each humidity cycle. However, with the same layout, the damp heat and water sintered Ag tracks possess lower resistance than those of thermally sintered Ag tracks.

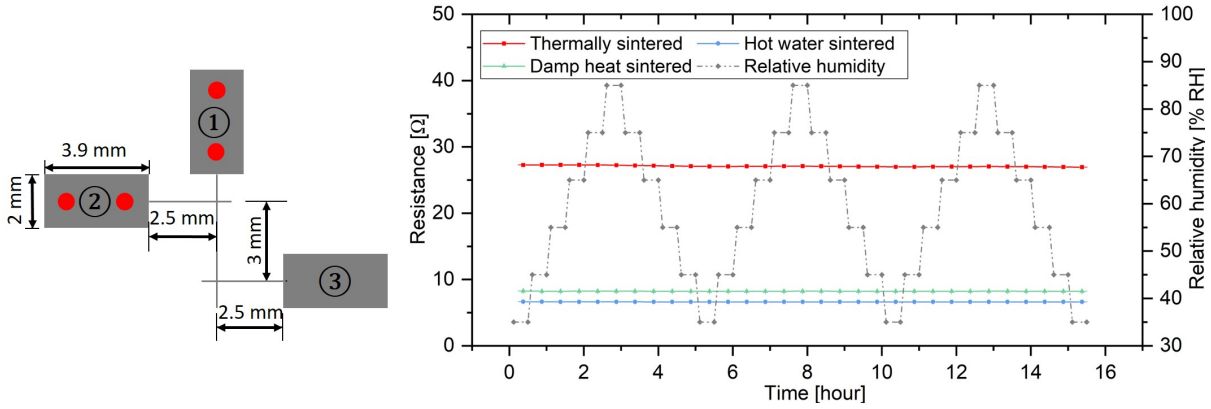

Figure 4.19: Cyclic humidity test results of inkjet printed silver tracks. The resistance of the Ag tracks between pad ① and ② is measured. For each sintering method, five Ag tracks are measured. Error bars represent standard deviations.

4.3 Discussion

The investigations of both damp heat sintering and water sintering confirm that moisture significantly enhances the sintering effect, enabling high conductivity in printed tracks using Ag NP ink (Silverjet DGP 40LT-15C) at temperatures as low as 85 °C. The calculated resistivity of Ag NPs after damp heat and water sintering is summarized in **Table 4.6**. Notably, the resistivity of Ag tracks sintered under 85 °C damp heat conditions (5.16 µΩ cm) is only about twice that of Ag NPs thermally sintered at 250 °C (3.09 µΩ cm).

Table 4.6: Calculated resistivity of Ag NPs after water/damp heat sintering (published in [68], own publication)

Substrate	85 °C, water sintering				85 °C & 85 %RH, damp heat sintering		
	1min	4min	16min	64min	1h	3h	24h
NB-TP-3GU100	16.66 µΩ cm	14.06 µΩ cm	10.20 µΩ cm	8.42 µΩ cm	15.03 µΩ cm	13.87 µΩ cm	14.16 µΩ cm
Melinex ST506	11.79 µΩ cm	8.49 µΩ cm	7.90 µΩ cm	7.24 µΩ cm	9.52 µΩ cm	8.62 µΩ cm	8.04 µΩ cm
Kapton HN	8.19 µΩ cm	6.25 µΩ cm	-	-	6.84 µΩ cm	5.96 µΩ cm	5.16 µΩ cm

Water sintering is more efficient than damp heat sintering for the three substrate types. At 85 °C, four minutes of water sintering achieves nearly the same effect as 24 hours of damp heat sintering. Experiments using silicone oil further reveal that the enhanced sintering observed at these low temperatures is not just due to fluid heat transfer. To gain a deeper understanding of the role of moisture in the sintering of PVP-capped Ag NPs, its influence on the properties of the capping layer is firstly analyzed.

4.3.1 Moisture influence on the properties of the capping layer

Low molecular weight PVP is commonly utilized in the fabrication of Ag NP ink [218]. Increasing with molecular weight, the thermal decomposition of PVP begins between 250 °C and 600 °C, with the lower decomposition threshold of 250 °C being a reasonable assumption. This is supported by measurements for PVP-capped Ru-NPs, where the decomposition of the PVP capping layer is observed at 260.98 °C [212]. Decomposition of the capping layer is a key mechanism at high temperature (above 250 °C) thermal sintering of Ag NPs on substrates that can withstand elevated temperatures, such as PI films.

States of the capping layer of an Ag NP Below the PVP decomposition point, the capping layer exhibits different states depending on environmental conditions. **Figure 4.20** depicts the PVP capping layer of an Ag NP in four different states:

(a) in a good solvent, such as TGME, the PVP capping layer is widely expanded and thus the agglomeration of NPs is inhibited [219];

(b) when the printed PVP-capped Ag NPs are dried at low temperatures or vacuum dried at RT, the PVP layer collapses and forms a dense layer around the NP;

(c) below the decomposition point but at elevated temperatures (120 °C to 150 °C) in an oven, the dry PVP layer becomes denser, brittle and starts to crack [220];

(d) the collapsing of the dried PVP layer is reversible [219], when the PVP-capped Ag NPs are subjected to water, the PVP layer can re-expand in water or in a high humidity environment.

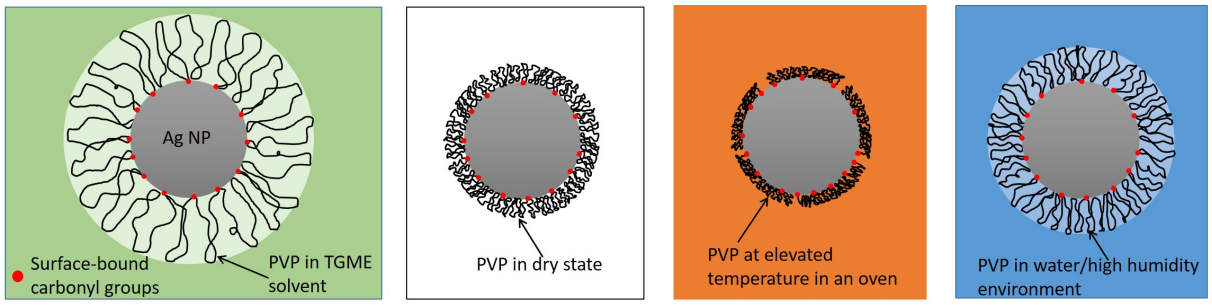

Figure 4.20: Schematic illustration of a PVP-capping layer in four different states: (a) in a good solvent such as TGME, (b) after low temperature drying or vacuum drying, (c) in an oven at an elevated temperature, and (d) in water/high humidity environment. Published in [68], own publication.

Above the PVP decomposition point, the capping layer is completely removed, allowing Ag NPs to come into direct contact and form conductive paths, resulting in enhanced conductivity. In the

lower thermal sintering range (such as 120 °C to 150 °C), cracks develop in the PVP layer (as illustrated in **Figure 4.20 (c)**), enabling metallic contact between the particles and thus lead to sintering, as shown in **Figure 4.21**.

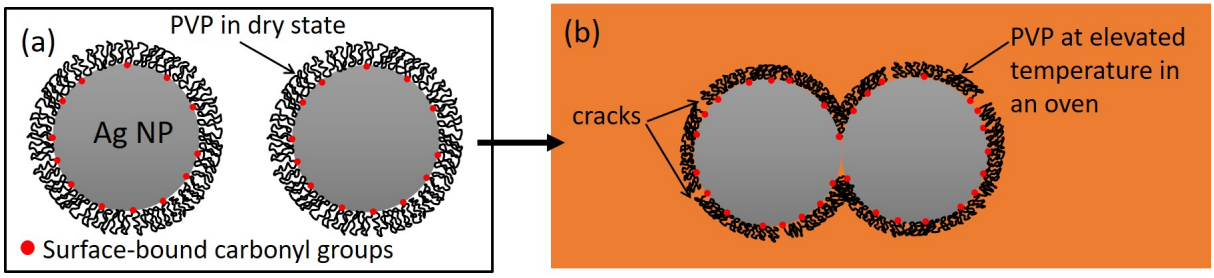

Figure 4.21: Schematic illustration of thermal sintering mechanism of PVP-capped Ag NPs at temperatures below the decomposition point (such as 120 °C–150 °C). (a) After drying, the solvent evaporates and the PVP capping layer collapses. (b) The cracks in the PVP layer allow metallic contact between the particles, leading to the sintering effect. Published in [68], own publication.

Besides the thermal effects discussed above, an aqueous environment also significantly influences the PVP capping layer, and thus the NP sintering process. As shown in **Figure 4.22**, during a chemical sintering process, the capping layer around Ag NPs can be removed in an aqueous environment using destabilizing agents such as NaCl [36]. However, since only deionized water is utilized both in the damp heat and water sintering processes, such chemical destabilization of the capping layer can be excluded. Moreover, to the best of our knowledge, no chemical coating for capping layer destabilization has been documented for Melinex ST506 and Kapton HN substrates.

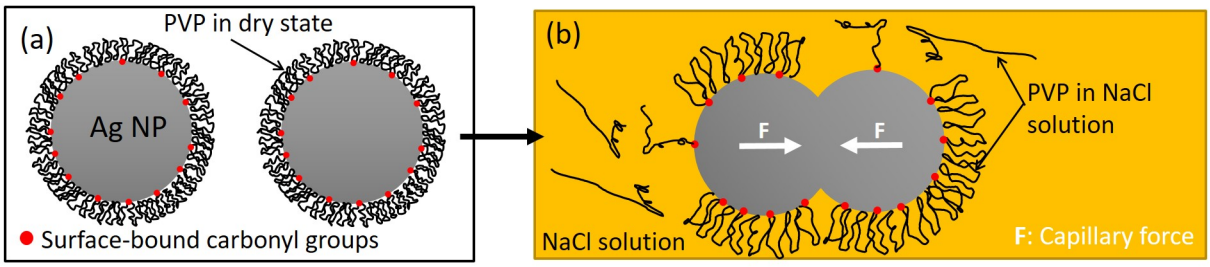

Figure 4.22: Schematic illustration of the chemical sintering of Ag NPs. (a) After drying, the solvent evaporates and the PVP capping layer collapses. (b) In an aqueous environment with destabilizing agents (NaCl solution), the PVP capping agent around the Ag NPs can be removed, leading to direct metallic contact and capillary force assisted sintering. Published in [68], own publication.

Even in the absence of destabilizing agents, moisture has a strong effect on PVP. The absorption of a solvent in the PVP capping layer is a reversible process. After the solvent TGME evaporates during the drying process, the PVP layer collapses, however, it can re-expand upon exposure to another solvent (in this case, moisture, as shown in **Figure 4.20 (d)**. Water is a relatively poor solvent for PVP compared to TGME [219], despite this, PVP exhibits a strong hygroscopic

effect, which increases exponentially with humidity [221]. The moisture influence on the stability of PVP as a capping layer has been explored in pharmaceutical applications [222]. The authors find that, even at room temperature, increasing the humidity from 0 %RH to 85 %RH lead to an increase in the polymer water content to up to 23 %. This absorbed water acts as a plasticizer, significantly lowering the polymer's glass transition temperature to below 100 °C [222]. Furthermore, Rhodamine 6G tracer experiments reveal that at a low humidity of 30 %RH, the PVP polymer swells slightly. When the humidity increases from 60 %RH to 75 %RH, the average microdiffusion coefficient for the tracer molecules increases sixfold [223].

Therefore, under the applied damp heat conditions, an increased diffusivity of Ag in the aqueous environment and a transition of the PVP capping layer from glassy to rubbery state can be assumed. As a result, contact between Ag NPs and neck formation initially due to Ostwald ripening [36] in the aqueous environment can occur. The AFM image of a damp heat sintered Ag tracks on Melinex substrate further supports this, providing visual evidence of the Ostwald ripening process (see **Figure 4.23**).

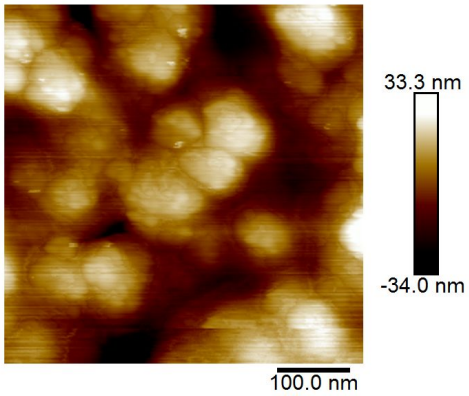

Figure 4.23: AFM image of printed Ag NPs on a Melinex ST506 substrate. This sample is damp heat sintered in a climate chamber (85 °C and 85 %RH) for 24 hours (published in [68], own publication).

4.3.2 Sintering pressure arising from capillary forces

Substantial capillary forces arise from water menisci between NPs. This phenomenon has been both observed and theoretically studied in the context of sintering processes in metallurgy by Heady et al. [224]. For closely packed spheres, they estimate an external pressure P_x equivalent to these capillary forces with the following equation 4.1:

$$P_x = 2\sqrt{2}\pi(\gamma_{LV}/R)cos\theta \tag{4.1}$$

where γ_{LV} represents the surface free energy of the liquid-vapor, R is the radius of the spheres, and θ is the contact angle of the liquid-solid-vapor system (θ is measured "in" the liquid) [224].

Given that the capping agent PVP has a hydrophilic endgroup [222], complete wetting of the Ag NPs is assumed by the water film, setting θ= 0°, R = 25 nm. Moreover, the influence of any residual TGME (a water-soluble ink solvent) on the surface energy of water is neglected. The temperature-dependent surface energy values of water are taken from the International Association for the Properties of Water and Steam (IAPWS) online calculator [225].

Under these assumptions, calculating the equivalent external pressure P_x with equation 4.1 yields 25.7 MPa at 23 °C, 23.8 MPa at 55 °C and 21.9 MPa at 85 °C. This indicates that capillary pressure decreases by approximately 15 % from 23 °C to 85 °C, due to the temperature-dependent decline of the surface energy of water. Nevertheless, the lower value still yields a substantial equivalent external pressure that will significantly contribute to nanoparticle sintering. In principle, capillary forces could also arise from other fluids such as silicone oil. However, silicone oil has a substantially lower surface energy than water and also less favorable wetting properties with the polar endgroups of the capping agent.

4.3.3 Damp heat/water sintering mechanism of PVP-capped Ag NPs

The combination of above discussed two effects explains the low temperature sintering effect observed in a damp heat environment and upon full immersion in hot water. **Figure 4.24** provides a schematic representation of the damp heat/water sintering mechanism. After drying, the solvent TGME evaporates, causing the PVP capping layer to collapse. When the dried, PVP-capped Ag NPs are exposed to a damp heat environment or immersed in hot water, the PVP capping layer re-expands and turns from a glassy state to a rubbery state. This change facilitates the Ag diffusion in the Ostwald ripening process. Meanwhile, the capillary pressure generated by water menisci adds mechanical pressure to the sintering process. As a result, neck formation between Ag NPs occurs and increases the conductive paths, leading to a substantial decrease in resistance already at temperatures significantly below the typical thermal sintering range.

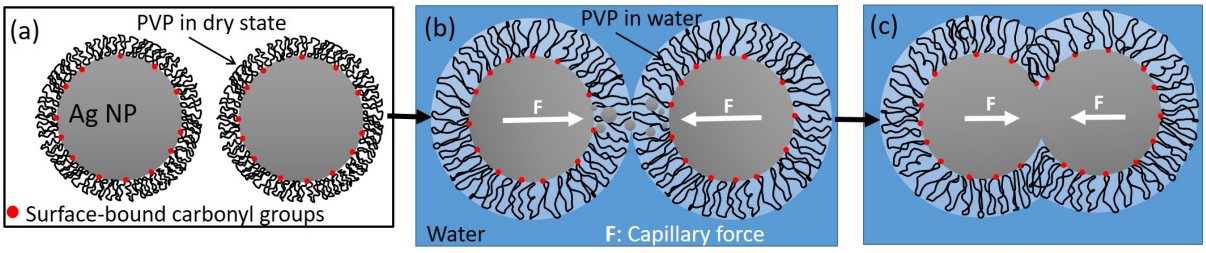

Figure 4.24: Schematic explanation of the damp heat/water sintering of Ag NPs. (a) After drying, the solvent evaporates and the PVP capping layer collapses. (b) Exposing the dried PVP-capped Ag NPs to a damp heat environment or to hot water, the PVP capping layer expands and turns from a glassy state to a rubbery state, facilitating the Ag diffusion in the Ostwald ripening process. Meanwhile, the capillary pressure generated by water menisci yields an additional force contributing to the sintering of Ag NPs. (c) Neck formation between Ag NPs occurs (published in [68], own publication).

Compared to thermal sintering, which typically requires temperatures in the range of 120 °C to 150 °C, the damp heat and water sintering processes explored in this chapter can be conducted at the significantly lower temperature of 85 °C while achieving better conductivity in the printed Ag tracks.

Chemical sintering in aqueous environments with destabilizing agents, such as Cl^- ions, can weaken the adhesion between the printed structures and the substrate. This issue occurs because destabilizing agents remove the capping layer, which has been reported as essential for maintaining adhesion [87]. This adhesion problem is not observed in the damp heat sintering process in this chapter. Instead of removing the capping layer, damp heat sintering softens it and increases its diffusivity, thereby to a certain extent preserving its role in maintaining adhesion between the printed structure and the substrate.

4.4 Conclusion

In this chapter, two novel low temperatures sintering methods, damp heat sintering and water sintering, for an Ag NP ink (Silverjet DGP 40LT-15C) are introduced. Systematic investigations are conducted to investigate moisture influence on the sintering of this Ag NP ink .

The findings reveal that both damp heat and immersion in hot water, at temperatures up to 85 °C, induce neck formation between Ag NPs, resulting in sintering effects at relatively low temperatures. It is assumed that neck formation between Ag NPs arises from two factors: (1) the humidity-dependent reduction in the glass transition temperature of the PVP capping layer, which enhances its diffusivity and promotes Ostwald ripening, and (2) the capillary pressure generated by water menisci between Ag NPs. The capillary pressure is a general influence resulting from the high surface energy of water and primarily depends on the wetting properties of the nanoparticles with their capping layer. In contrast, the reduction in glass transition temperature and the associated increase in diffusivity are specific to the PVP capping layer.

While both methods exhibit effective sintering, they each have distinct advantages and limitations. Water sintering is a simple process requiring only basic equipment, such as a hotplate and a thermal sensor to control water temperature. Immersion in hot water achieves low resistances within minutes, whereas achieving similar resistances in a damp heat atmosphere requires up to 24 hours. The sensitivity of PVP to moisture explains why water sintering is more effective than damp heat sintering. Full immersion in water further depresses the glass transition temperature of PVP, increasing the diffusivity of the PVP layer and making it more permeable. This enhances the effectiveness of capillary pressure.

However, immersion in hot water may cause delamination of the printed Ag NP structure from the PI substrate, compromising the integrity of the printed structure. This issue has to be addressed, e.g. by using an additional process step such as UV treatment reported by Olkkonen et al. [87].

The damp heat process does not exhibit delamination issues. After 24 hours of damp heat sintering, the resistivity of the printed Ag tracks reaches 5.16 µΩ cm, which is only 1.7 times that of Ag tracks thermally sintered at 250 °C.

Damp heat sintering is an efficient process, particularly suitable for low-temperature substrates such as PET films. A potential application could involve integrating a damp heat sintering chamber into a roll-to-roll production line, allowing the substrate to pass through and undergo sintering during the transfer process. In principle, this approach could also be adapted for the water sintering process, provided the delamination issue is either avoided or resolved, as outlined by Olkkonen et al. [87].

5 Solution processable encapsulation for flexible printed electronics

While moisture positively influences the sintering of the Ag NPs as outlined in the previous chapter, it may also have adverse effects on the performance of printed electronic devices during use. Moisture plays a significant role in the degradation (e.g. corrosion, swelling, and delamination of layers), making effective encapsulation critical for protecting these devices and prolonging their operational lifetime.

One promising solution processable encapsulation approach is to develop polymer barrier films to shield FPE devices from moisture. Moreover, adding fillers into a polymer matrix can create tortuous diffusion paths and improve the moisture barrier property of the resulting polymer films. Another approach is to fabricate flexible barrier films using hybrid polymers. In this chapter, both approaches are applied to develop solution processable encapsulation for the inkjet printed FPE components [1].

5.1 Solution processable polymer/filler encapsulation

In this section, a suitable polymer matrix is selected, and various inorganic fillers are investigated to fabricate effective barrier films for the encapsulation of printed test structures. An adapted WVTR measurement setup based on the ASTM-E96 standard is developed. The moisture barrier properties of the selected polymer/filler films are validated by measuring their WVTRs and by encapsulating printed Ag tracks and moisture sensitive capacitors.

[1] Parts of this chapter are published in:
[226] Zehua Chen, Ulrich Gengenbach, Shant Gananian, Daniel Moser, Klaus-Martin Reichert, and Liane Koker. Investigation of solution processable moisture barrier films based on a polymer and filler materials. In 2024 IEEE International Conference on Flexible and Printable Sensors and Systems (FLEPS). IEEE, jun 2024. doi: 10.1109/fleps61194.2024.10603898.
[227] Zehua Chen, Ulrich Gengenbach, Shant Gananian, Daniel Moser, Klaus-Martin Reichert, Liyu Huang, and Liane Koker. Solution processable barrier films using a filled polymer to encapsulate flexible printed electronics. IEEE Journal on Flexible Electronics, December 2024. doi: 10.1109/JFLEX.2024.3512473.

5.1.1 Materials and methods

This section is divided into five parts: the materials, the fabrication of various polymer/filler films, the application of selected polymer/filler films to encapsulate the printed test structures, and the characterization of the polymer/filler films.

5.1.1.1 Materials

Polymer matrix Two commonly used polymer matrices described in the literature are polyvinyl alcohol (PVA) [181, 185, 228, 201, 229, 189] and polyvinyl butyral (PVB) [147, 114]. Both are non-toxic and easy to process. Furthermore, PVA itself already yields high barrier properties against O_2. Thus, PVA (molecular weight: 146000 - 186000, Sigma-Aldrich) is appplied as polymer matrix.

Inorganic fillers Inorganic fillers utilized to fabricate polymer/filler barrier films are:

- Organically modified montmorillonite (MMT) clay (Cloisite 20A, BYK Ltd);
- Glass flakes (GF) (LUXAN F001, Eckart GmbH);
- High purity silica powder (Zandosil G220, Heraeus Quarzglas GmbH & Co);
- Graphene oxide (GO) powder (796034-1G, Sigma Aldrich).

Substrates

- DuPont Tejin Melinex ST506 PET film (175 µm thick);
- Mitsubishi NB-TP-3GU100 PET film (135 µm thick [213]).

Inkjet printable inks

- Silver nanoparticle ink (Silverjet DGP 40LT-15C, Sigma Aldrich);
- Ceramic nanoparticle ink (BST/P(VDF-TrFE) ink, developed at KIT IAM-ESS [47]).

Desiccant Calcium chloride (C1016, Sigma Aldrich) is utilized as desiccant for the WVTR measurement.

5.1.1.2 Fabrication of PVA/filler films

The fabrication process of the self-standing barrier films is illustrated in **Figure 5.1**. In step 1a, a 5 wt% PVA solution, serving as the polymer matrix, is prepared by dissolving 10 g of PVA powder in 190 g of DIW. The solution is heated on a magnetic stirrer at 80 °C for two hours to ensure complete dissolution of the PVA. In step 1b, the filler fraction is prepared by adding the required amount of the selected inorganic filler into the DIW. This mixture is stirred at an elevated temperature of 40 °C for two hours using a magnetic stirrer. Following this, the mixture undergoes ultrasonication for 30 min to break down any agglomerates. The homogeneous DIW/filler suspension is then added to the PVA solution, and the resulting PVA/filler suspension is stirred at 60 °C for an additional three hours. After this mixing step, the suspension is ultrasonicated again for 30 min and allowed to cool to room temperature (step 2). In step 3, the PVA/filler suspensions are applied onto PET carrier substrates via doctor blading using an automatic film applicator (ZAA 2300, ZUA 2000, Proceq), with the gap between the blade and the substrate set to 500 µm. After drying at RT, circular samples, with a diameter of 12 mm, are punched out using a hole punch, corresponding to the size of the screw cap utilized for subsequent WVTR measurements. Finally, the self-standing barrier films are carefully peeled off the PET carrier substrates, yielding samples ready for characterization.

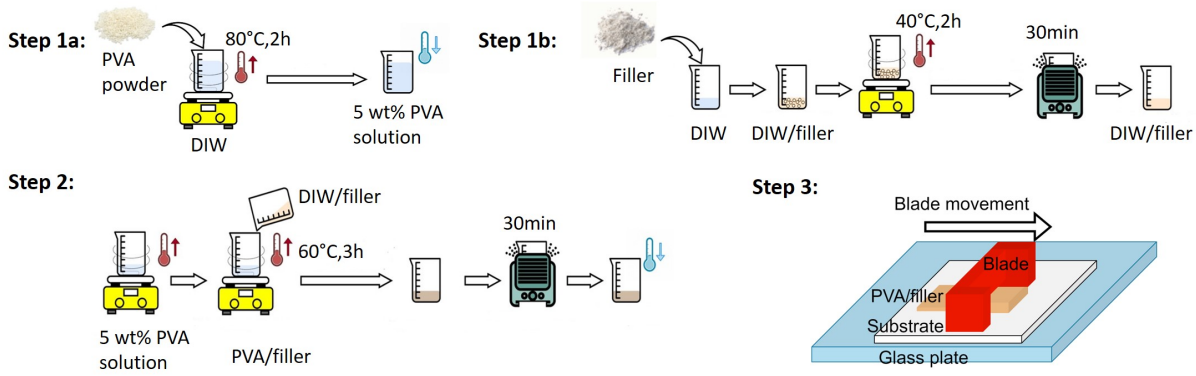

Figure 5.1: Fabrication of PVA/filler films. Step 1a: preparation of a 5 wt% PVA solution applied as polymer matrix; step 1b: preparation of a homogenized DIW/filler suspension; step 2: preparation of a homogenized PVA/filler suspension; step 3: fabrication of a PVA/filler film on a PET substrate by doctor blading. Adapted from [227], own publication.

5.1.1.3 Characterization of PVA/filler films

Development of an adapted WVTR measurement setup

The original desiccant method (see **Figure 5.2**), outlined in the ASTM-E96 standard [206], serves as the basis for evaluating the moisture barrier properties of PVA/filler films.

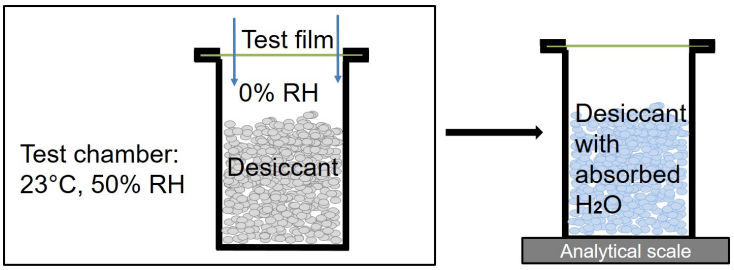

Figure 5.2: Schematic illustration of the desiccant method for measuring WVTRs of the test films. Published in [227], own publication.

In this method, metal test dishes (see **Figure 5.3 (a)**) are filled with a desiccant and sealed with a lid made from the material to be tested for water vapor permeation. Moisture that permeates through the lid is absorbed by the desiccant, and the amount of water transmitted is determined by periodically weighing the test dish. This method offers a straightforward and cost-effective testing approach, as it requires minimal specialized equipment. However, it provides limited precision, with coefficients of variation (CV) reaching two digits, as demonstrated by measurement examples provided in the standard [206].

This desiccant method is selected and adapted to suit the small diameters of the PVA/filler samples (see **Figure 5.3 (b)**). Since the standard test dishes are too large, glass vials with a diameter of 14.7 mm and screw caps featuring a central hole of 8.7 mm in diameter are utilized. These vials are partially filled with the desiccant, occupying approximately two-thirds of their volume. To accommodate the mechanical sensitivity of the thin barrier films, gaskets are chosen based on the sealing solutions recommended in the standard. The barrier film samples are placed between two gaskets and clamped onto the glass vials with the screw caps.

To evaluate moisture absorption and permeation through the gaskets and screw caps, three control vials are prepared. These vials contain 200 µm-thick stainless steel plates clamped between the gaskets and are subjected to the same test conditions as the PVA/filler samples. This approach ensures a comprehensive assessment of any potential variables that could influence the results.

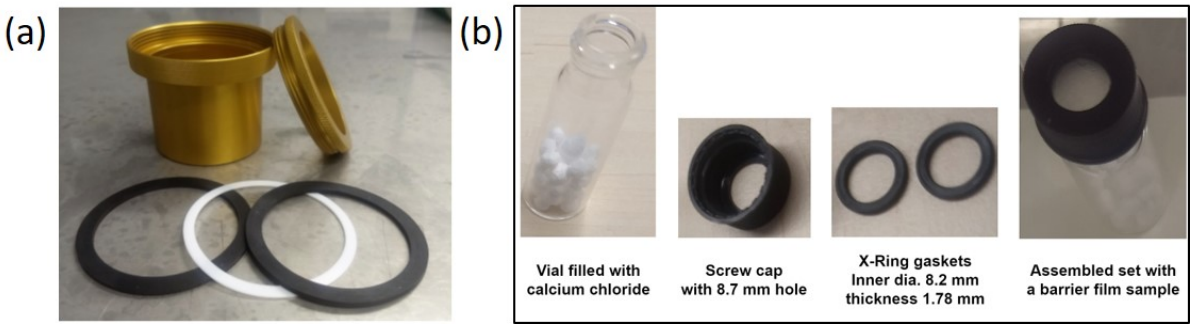

Figure 5.3: Development of the adapted desiccant method. (a) The EZ-Cup Vapometer (Thwing-Albert, USA) for measuring WVTR. (b) The adapted desiccant method using small glass vials. Published in [227], own publication.

Weight changes for all vials are measured using a Sartorius ED224s analytical scale with a resolution of 0.1 mg. The weight changes observed in the control vials are subtracted from the measurements of the film samples.

This adapted desiccant method enables the measurement of WVTR for various barrier films with small sample diameters under identical test conditions within the same test run. WVTR tests are conducted for filler selection under the test condition of 23 °C and 50 %RH. The PVA/filler film exhibiting the lowest WVTR value is then selected for further testing. These subsequent tests are conducted under the following three test conditions to determine the optimal filler ratio in the suspension:

- 23 °C, 50 %RH;
- 38 °C, 50 %RH;
- 38 °C, 65 %RH.

Preparation of cross-sections of a selected PVA/filler film

To gain further insight into the internal structure of the barrier films, cross-sections are prepared using ultramicrotome (UM) trimming and inspected under a microscope. The ultramicrotome is a precision instrument capable of producing thin sections of embedded samples or precisely cutting block faces using glass or diamond knives (cf. [230]). Initially, the membrane sample is manually cut into a smaller rectangular section using a razor blade, in preparation for embedding. The trimmed sample is then placed into a mold and embedded in epoxy resin (Spurr, Sigma-Aldrich, USA), following an optimized protocol to achieve the desired hardness.

To ensure accurate positioning of the sample within the mold and in the resulting resin block after polymerization, a custom in-house designed holding structure is employed. This structure is 3D printed from PLA, as described in [231]. The membrane sample is placed into the opening of this structure, ensuring its stability during the embedding process. Subsequently, the mold is filled with the embedding epoxy resin and then cured in an oven at 70 °C for approximately 16 hours to complete the polymerization of the epoxy resin (see **Figure 5.4 (a)**).

After cooling to room temperature, the solidified sample block is clamped into the ultramicrotome sample holder and manually pre-trimmed with a razor blade to expose the region of the embedded membrane on the block's surface. For finer trimming, an ultramicrotome (Leica EM UC7, Leica Microsystems, Germany) equipped with a diamond trimming knife (Trim 90, Diatome, Switzerland) is utilized. The sectioning speed is set to $6\,\mathrm{mm\,s^{-1}}$, with a sectioning feed of 500 nm.

The resulting block face, measuring $899.8\,\mu\mathrm{m} \times 353.4\,\mu\mathrm{m}$, is precisely trimmed, exposing the embedded membrane structure at the center of block face (see **Figure 5.4 (b)**). This prepared

sample is then imaged using a digital optical microscope (Keyence VHX 7000) to analyze the internal microstructure of the barrier film.

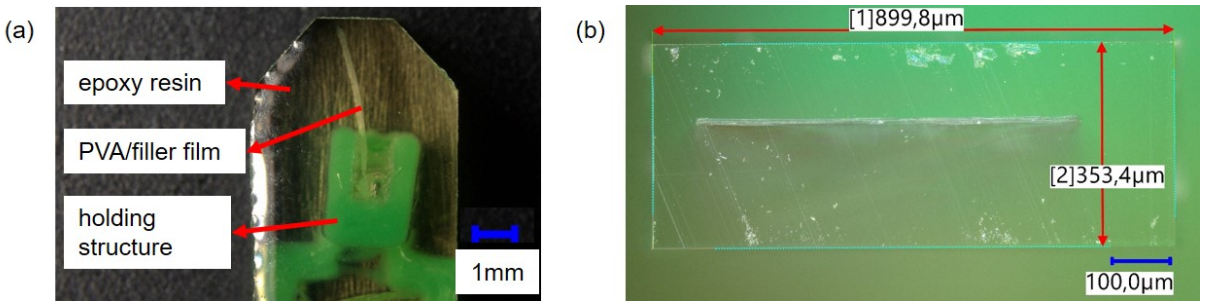

Figure 5.4: Preparation of cross-sections of a selected PVA/filler film. (a) The embedded membrane sample in a epoxy resin. (b) Precisely trimmed block face, exposing the cross-section of the embedded membrane sample at the center of block face [227].

5.1.1.4 PVA/filler encapsulation for inkjet printed silver tracks

Figure 5.5 shows the conductor structure utilized as test structure encapsulated by the PVA/filler film. This test structure with the same layout as shown in **Figure 3.6**, is printed using an Ag NP ink on an Autodrop Gantry inkjet printer (MD-K-140 print head). The printing parameters are set to a voltage of 170 V, a pulse width of 45 µs, a vacuum pressure of 7 mbar, and a drop distance of 50 µm. This test structure is printed in two passes onto NB-TP-3GU100 PET substrates under ambient conditions and then left to dry at room temperature for seven days.

As discussed in chapter 4, exposing unencapsulated Ag tracks to humid environments leads to significant sintering effects at low temperatures, resulting in a reduction in resistance [68]. Applying a protective encapsulation layer to the central conductor can mitigate this moisture-induced sintering effect, thereby preventing the associated decrease in resistance. Consequently, resistance measurements of test structures with the selected PVA/filler encapsulation can serve as an effective method for evaluating the encapsulation's performance.

The selected PVA/filler mixtures are applied to the central conductor region of the test structures by doctor blading, with a gap of 500 µm between the blade and the substrate. The encapsulated structures are left to dry at room temperature.

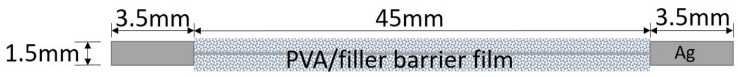

Figure 5.5: Schematic illustration of a test structure (conductor structure - inkjet printed Ag track) coated with a PVA/filler film by doctor blading. Published in [227], own publication.

Both printed Ag tracks with and without the PVA/filler encapsulation are subjected to a damp heat test in a climate chamber for four days (40 °C, 85 %RH) and then characterized by a four-point resistance measurements using a B&K Precision LCR-Meter 981, with a Formfactor EPS150

probestation equipped with 150 µm probe tips. The encapsulated Ag tracks are imaged using a digital optical microscope (Keyence VHX 7000) equipped with objective VHX-E100 (DIC OP-88324, polarizer OP-88323 installed). The acquired images of encapsulated Ag tracks are then processed and analyzed in ImageJ (Version 1.54g).

5.1.1.5 PVA/filler encapsulation for inkjet printed capacitors

Another test structure is the inkjet printed capacitor encapsulated by the selected PVA/filler film. The layout of this capacitor is the same as depicted in **Figure 3.8**. The Ag NP ink is utilized for top and bottom electrodes on a Melinex ST506 PET substrate. The bottom electrodes are printed on the substrate with the printer hotplate heated to 85 °C. Afterwards, the damp heat sintering process developed in chapter 4 is applied to sinter the bottom electrodes in a climate chamber at 85 °C and 85 %RH for three hours. The dielectric ink, BST/P(VDF-TrFE) ink [47], is printed on top and dried with the printer hotplate heated to 55 °C. Finally, the top electrode is printed with the printer hotplate heated to 85 °C. The printed capacitor is placed in a climate chamber under the condition of 85 °C and 85 %RH for three hours to sinter the top electrodes again with the damp heat sintering process.

These capacitors printed with BST/P(VDF-TrFE) ink as dielectric material are proved to be moisture-sensitive in chapter 3. The selected PVA/filler mixtures are applied as the encapsulation material over the dielectric region to evaluate the moisture barrier property of the resulting PVA/filler films.

Theoretically, the selected PVA/filler mixtures can be applied directly onto the dielectric region by doctor blading with a mask adapted to the layout. However, this approach fails due to the small size of the dielectric region to be encapsulated. During the mask separation process, parts of the dried PVA/filler film adhere to the metal mask, preventing successful encapsulation and damaging both the film and the printed capacitor. Furthermore, due to the different wetting properties of the BST/P(VDF-TrFE) dielectric area and the substrate, it is difficult to form a uniform barrier film directly on the printed capacitors by dispensing the selected PVA/filler suspension.

However, the selected PVA/filler films can be easily peeled off the carrier substrate. The self-standing PVA/filler film can be attached to the capacitors using an UV curable adhesive (Photobond AD474, DELO). The encapsulation workflow is shown in **Figure 5.6**. The UV curable adhesive is dispensed at the edge of the dielectric area using a dispensing platform MIMOSE [232] and immediately cured with UV light (wavelength λ: 365 nm, Panasonic UJ35) to form a dam to prevent uncured adhesive in the next step from flowing into the capacitor area (step 1). Afterwards, this adhesive is dispensed around the cured adhesive (step 2). The selected PVA/filler films, with a diameter of 5 mm, are punched out and removed from the carrier substrate using a hole punch and placed on top of the UV curable adhesive. The adhesive is then UV cured to firmly fix the selected PVA/filler film on the capacitors (step 3).

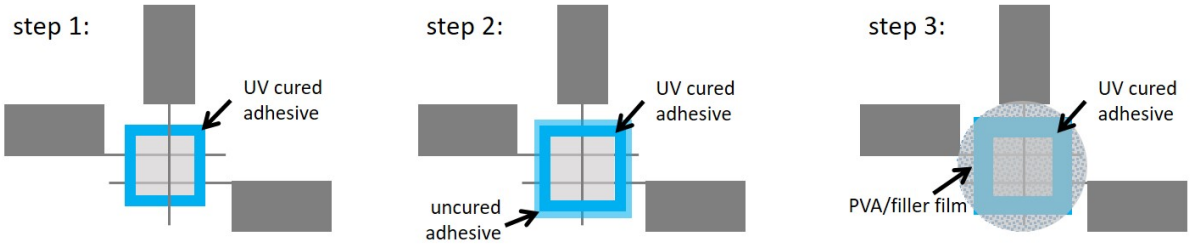

Figure 5.6: Schematic illustration of the PVA/filler encapsulation workflow for inkjet printed capacitors.
Step 1: the UV curable adhesive is dispensed around the dielectric area (in the middle) and cured by UV exposure immediately as dam to prevent the uncured adhesive from flowing into the capacitor area.
Step 2: the UV adhesive is dispensed around the cured adhesive.
Step 3: the self-standing PVA/filler film is placed on top and the adhesive is UV cured to complete the encapsulation.

The dispensing parameters for the UV curable adhesive are listed in **Table 5.1**.

Table 5.1: Dispensing parameters for the UV curable adhesive

Needle inner diameter	Dispensing time (single point)	Dispensing height[1]	Pressure
200 µm	300 ms	100 µm	0.4 bar

[1] Dispensing height: distance between the dispensing needle tip and the substrate.

Before encapsulation, a cyclic humidity test is conducted in a climate chamber, during which the capacitance of the printed capacitors is recorded under each humidity condition. To exclude any potential influence of the adhesive used in the encapsulation process, reference samples are prepared with cured adhesive dispensed around the dielectric area. Both these reference samples and the printed capacitors with the selected PVA/filler encapsulation are subjected to the cyclic humidity test in the climate chamber. The capacitance measurements are recorded to evaluate the effectiveness of the selected PVA/filler encapsulation. A 90 nm-thick layer of chromium (Cr) is sputtered onto the cured adhesive dam of a reference sample using a Quorum Q300T ES Plus sputter coater. The profile of this adhesive dam is scanned using a Sensofar S Neox confocal microscope.

5.1.2 Results

The WVTRs of the fabricated barrier films are characterized with the adapted cup method both for selecting the filler material and evaluating the barrier properties of the selected materials. CV levels of the measurements (up to 40 %) are in the same range as the examples provided in the standard, indicating the validity of the adapted cup method. In the following sections, the results of the filler comparison and selection, the optical characterization a selected PVA/filler film, and the encapsulation effectiveness of the selected PVA/filler films are presented.

5.1.2.1 Filler comparison and selection

Four fillers are added to a 5 wt% PVA solution at different ratios to prepare barrier films. The WVTR of each film is measured using the adapted desiccant method. Kapila et al. report a significant increase in elongation at break (EAB) of PVA/GO films as the concentration of GO rises from 0.1 % to 0.3 %, followed by a notable decrease with further addition of GO from 0.3 % to 0.7 % [229]. Based on these findings, PVA/GO films are prepared by adding 0.2 wt% and 0.5 wt% GO to the PVA solution, respectively.

The PVA/GO films yield lower barrier performance compared to the PVA/GF 5 wt% films. Moreover, the incorporation of GO causes the PVA films to turn black, limiting their applicability in applications that require light transmission.

Adding 20 wt% silica to the PVA solution results in the best moisture barrier property. However, the PVA/silica films produced with 10 wt% and 20 wt% silica are relatively brittle compared to the other three types of films, making them unsuitable for applications on flexible substrates.

PVA/MMT films show improved moisture barrier performance with increasing MMT content. However, the moisture barrier property of the films prepared with 10 wt% MMT are not as effective as those of the films with 5 wt% GF. This is because MMT tends to agglomerate more than GF during the film fabrication process, due to the hydrophilicity of the MMT type utilized. As a result, the filler aspect ratio achieved with MMT is less favorable compared to GF [228]. Therefore, GFs are selected as the filler material for further tests.

As shown in **Figure 5.7**, PVA with 5 wt% GF yields better moisture barrier properties compared to PVA with 20 wt% GF.

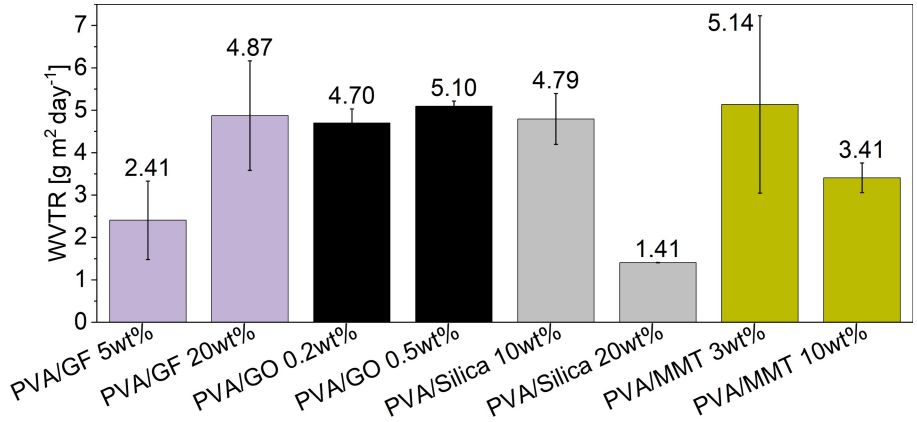

Figure 5.7: WVTR values of various PVA/filler films in the preliminary test. For each type of PVA/filler film, three samples are measured. Error bars represent standard deviations. Adapted from [227], own publication.

5.1.2.2 WVTR test results of PVA/GF films

GFs at concentrations of 3 wt%, 5 wt%, and 10 wt% are added to the PVA solution to fabricate barrier films via doctor blading. The WVTRs of five films of each concentration are measured using the adapted desiccant method under three test conditions: 23 °C, 50 %RH; 38 °C, 50 %RH; and 38 °C, 65 %RH.

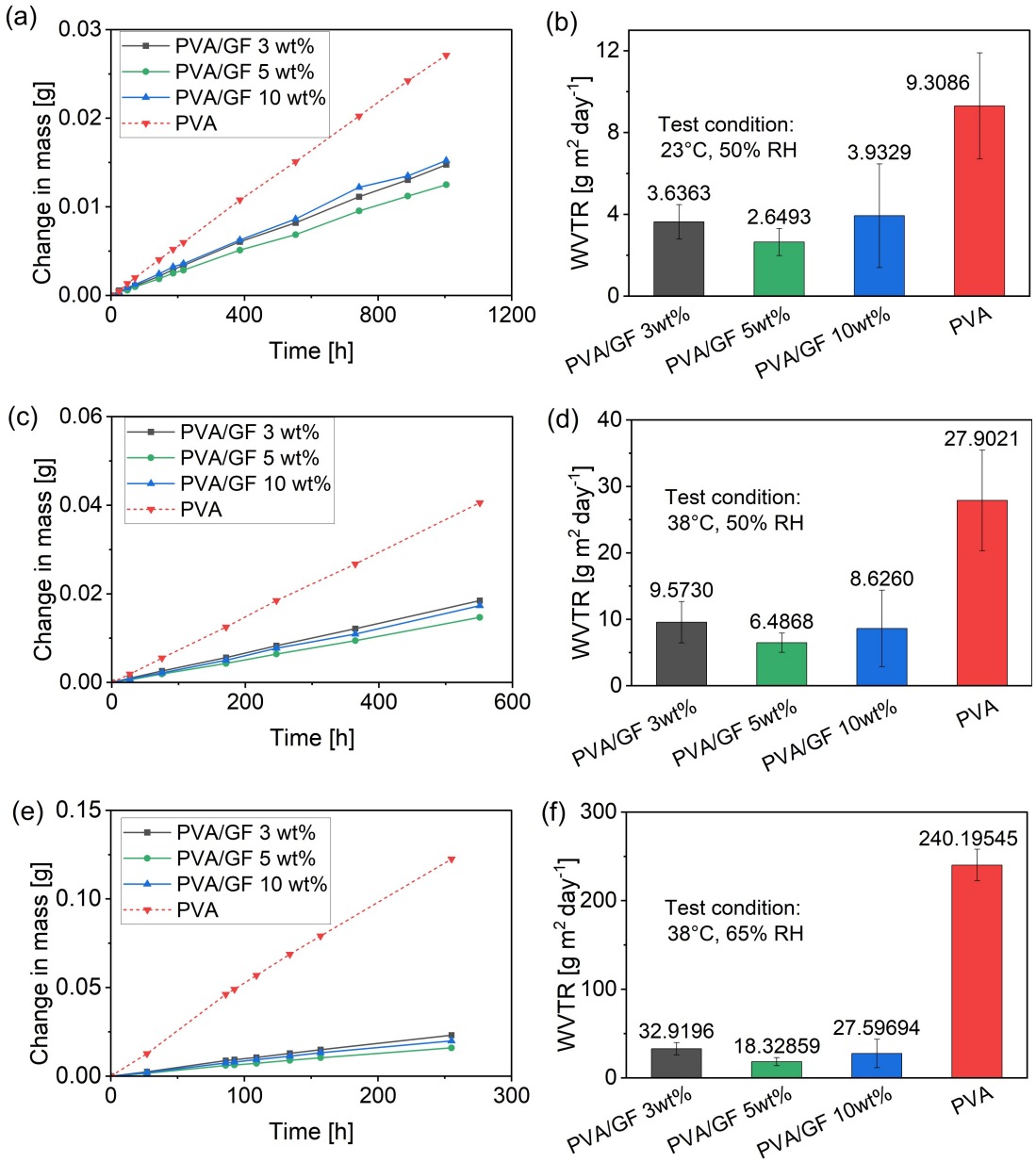

Figure 5.8: Recorded mass changes over time for the dry cups covered with PVA/GF films with different GF concentrations and their calculated WVTRs. (a), (c), (e): the weight change of the dry cup with PVA/GF films under three test conditions. (b), (d), (f): the calculated WVTRs of PVA/GF films under three test conditions. For each GF concentration, five samples are measured. Error bars represent standard deviations. Published in [227], own publication.

The changes in weight (see **Figure 5.8 (a), (c), and (e)**) are recorded to calculate the WVTR values. The calculated WVTRs are shown in **Figure 5.8 (b), (d) and (f)**. The linear increase in the mass of the test dishes further confirms the validity of the adapted desiccant method. Adding GFs into PVA solutions significantly reduces the WVTR of the resulting PVA/GF films, improving the moisture barrier properties by more than an order of magnitude compared to pure PVA films. Under all test conditions, PVA/GF films with 5 wt% GFs yield the lowest WVTR. Therefore, PVA solutions containing 5 wt% GFs are utilized to encapsulate the test structures.

5.1.2.3 Microstructure of a PVA/GF film

To gain insights into the GF arrangement within the film cross-section, a block face is prepared using UM trimming and imaged. Microscope images of the PVA/GF film block face reveal a lamellar arrangement of the glass flakes, with only few agglomerations observed (see **Figure 5.9**). The measured glass flake thicknesses range from approximately 0.9 µm to 2.3 µm. The observed longitudinal dimensions match the supplier specifications (180 µm to 200 µm, representing the D_{50} percentile of the particle size distribution) [233]. These images confirm the favorable aspect ratio of the glass flakes and a significantly increased tortuosity of the permeation path.

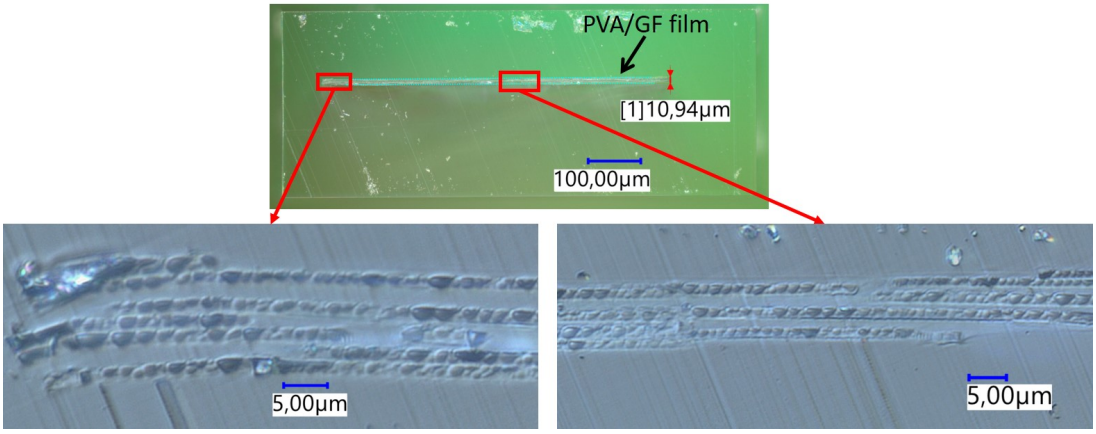

Figure 5.9: Microscope image of the PVA/GF film block face, exhibiting a lamellar arrangement of the glass flakes with only few agglomerations and a resulting tortuous path in the PVA matrix. Adapted from [227], own publication.

5.1.2.4 PVA/GF encapsulation results on inkjet printed silver tracks

Chapter 4 reveals that humid environments have positive impacts on the sintering effect of unencapsulated Ag tracks [68]. Applying a protective encapsulation layer to them can mitigate this moisture-induced sintering effect. Consequently, resistance measurements of printed Ag tracks with the PVA/GF encapsulation can serve as an effective method for evaluating the encapsulation's performance.

A group of inkjet printed Ag tracks without PVA/GF encapsulation serves as reference, yielding the resistance of 66.01 ± 0.26 Ω. For another group, PVA solutions containing 5 wt% GFs are utilized to encapsulate the Ag tracks via doctor blading under ambient conditions. Before encapsulation, the samples yield the resistance of 71.02 ± 0.34 Ω, after encapsulation, the resistance drops to 45.27 ± 1.74 Ω.

The PVA/GF encapsulation results are shown in **Figure 5.10**. Both the reference and encapsulated samples are subjected to damp heat conditions (40 °C & 85 %RH) for four days. After the damp heat test, the resistance of reference samples drops sharply by 34.7 % to 43.11 ± 0.12 Ω, attributed to the damp heat sintering effect [105, 68] described in chapter 4. In contrast, the encapsulated samples yield a more moderate resistance reduction of only 11.5 %, showing the moisture barrier effect of the PVA/GF encapsulation layer. After 27 days of ambient storage, the resistance of the reference samples increases by 17.2 % to 50.54 ± 0.97 Ω, while the encapsulated samples show a negligible resistance change of just 0.58 %. This further indicates the effective moisture barrier properties of the PVA/GF encapsulation.

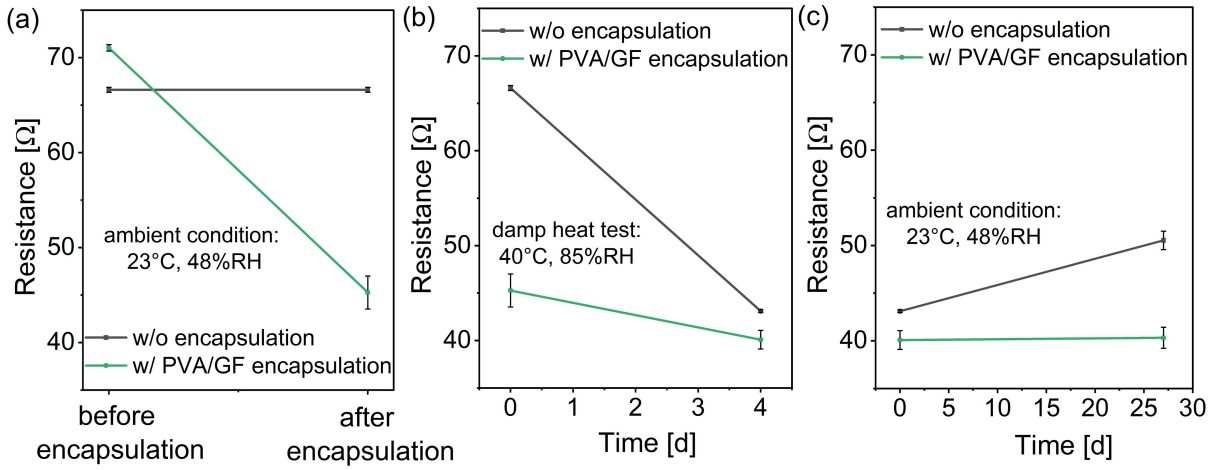

Figure 5.10: Resistance of test structures with (w/) and without (w/o) PVA/GF encapsulation. Before and after (a) encapsulation; (b) four days of damp heat test; and (c) 27 days of room storage. Three Ag tracks each are measured. Error bars represent standard deviations. Adapted from [227], own publication.

For the optical inspection, nine top view microscope images, each measuring 2 mm × 3 mm, are taken from a single Ag track with PVA/GF encapsulation. These images are taken from three locations along the printed Ag track (left edge, center, and right edge) and three additional locations above and below this track, respectively (see **Figure 5.11 (a)**).

Figure 5.11 (b), (d) and (g) presents three representative examples. The microscope images reveal that the distribution of GFs within the film varies from multiple GFs stacked on top of each other, to regions with a layer of disconnected GFs or no GFs at all and thus pure PVA only. To quantify the GF coverage rate, the images are analyzed using the ImageJ software.

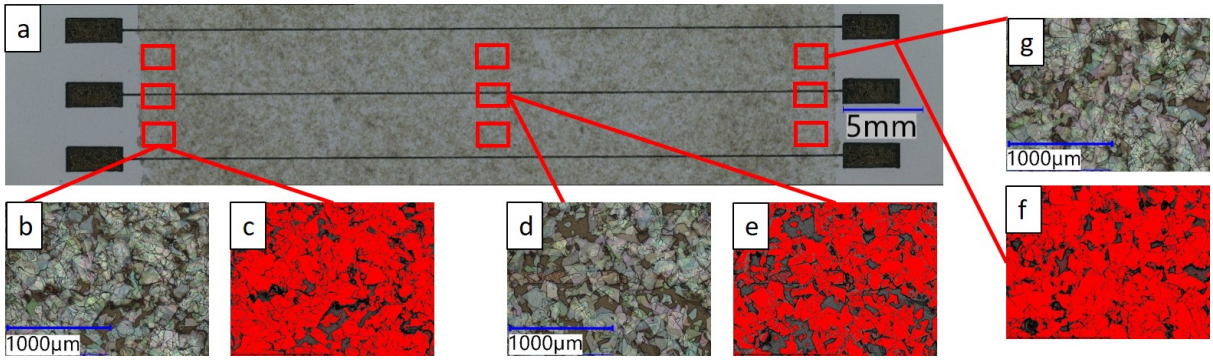

Figure 5.11: Microscope images of printed Ag tracks with PVA/GF encapsulation on a NB-TP-3GU100 PET substrate. (a) Top-view image showing red-framed areas where the nine microscope images are taken from. Examples include regions (b) below, (d) in the center, and (g) above the printed Ag track, along with their respective processed images (c), (e), and (f), analyzed using ImageJ to quantify GF coverage rates. Adapted from [227], own publication.

The microscope images are imported into ImageJ, and their contrast is enhanced using the "Enhance Contrast" function with the "histogram equalization" option selected.

The enhanced image is then split into three separate images, one for each color channel, using the "Color-Split Channels" function. Given that the original image has a greenish hue, the green channel typically shows the highest contrast, making it ideal for further analysis. The green image is processed using the "Adjust Threshold" function to isolate the GFs from the background. In most cases, a threshold value of approximately 70 % effectively separates the GFs from the background.

The thresholded image is used to calculate the surface area covered by GFs through the "Analyze Particles" function. The particle size parameter is set to "500 µm^2 - Infinity" to exclude background noise and small artifacts, while the "include holes" option ensures that hole artifacts within the GFs, caused by thresholding, are included in the surface area calculation. A visual comparison confirms that these parameter settings accurately distinguish GF-covered regions from non-covered PVA-only background areas.

This analysis yields a coverage rate between 60 % (**Figure 5.11 (e)**) and 80 % (**Figure 5.11 (f)**), with an average coverage rate of 72 % and a variance of 5.9 % across all images. **Figure 5.11 (c)** illustrates an example with a coverage rate of 73 %. Notably, no significant variance is observed in either the lateral (doctor blade width) or longitudinal directions.

However, it is important to note that some single GFs aligned parallel to the substrate plane may not be properly detected by the ImageJ image processing due to low contrast. As a result, the absolute GF coverage rates may be underestimated by a few percent.

5.1.2.5 PVA/GF encapsulation results on inkjet printed capacitors

The inkjet printed capacitors using BST/P(VDF-TrFE) ink as dielectric material are moisture-sensitive as descried in chapter 3. PVA solution containing 5 wt% GFs is applied as the encapsulation material over the dielectric region to evaluate its moisture barrier property. This PVA/GF encapsulation on the printed capacitor is completed using an UV curable adhesive. Firstly, the adhesive is cured and applied as dam around the dielectric area. The measured height of an adhesive dam is 133.17 ± 4.72 µm (see **Figure 5.12**).

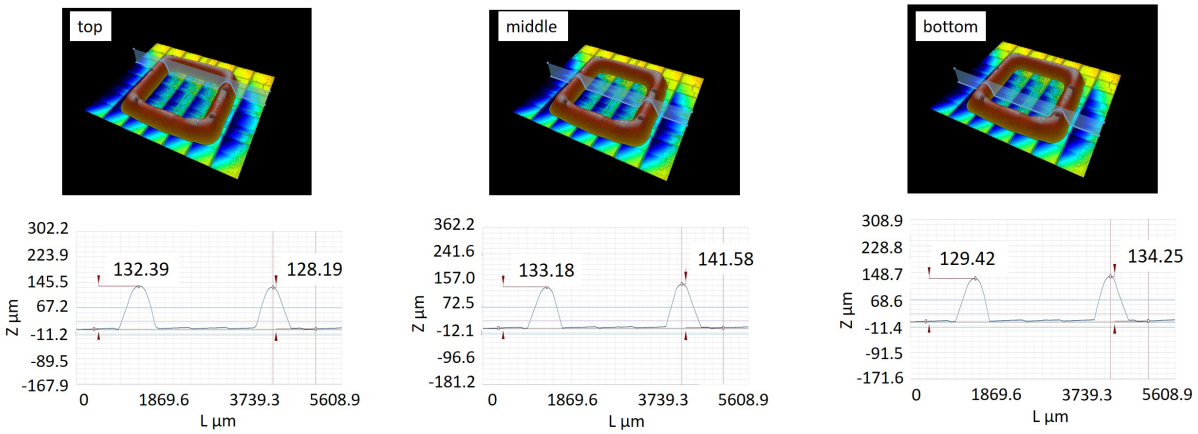

Figure 5.12: Profile along length (L) and measured height (z) of a dispensed UV curable adhesive dam.

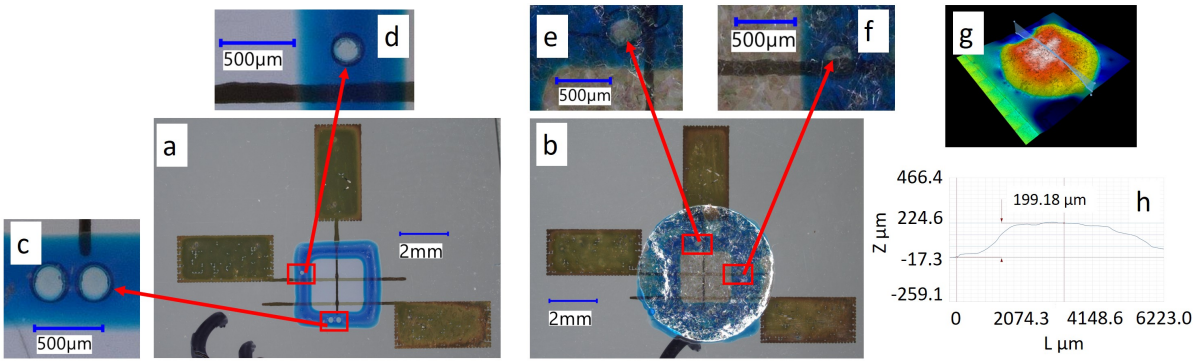

Figure 5.13: Microscope images of printed capacitors (a) with cured adhesive dam around the dielectric area and (b) with PVA/GF encapsulation. Air bubbles arising during the dispensing can be observed (c - f) in the cured dam, which can lead to leakage of the PVA/GF encapsulation. (g) Profile and (h) measured distance between the top of the PVA/GF encapsulation layer and the printed capacitor.

Figure 5.13 (a) shows a printed capacitor set with cured adhesive dam, serving as a reference sample to exclude a potential influence of the adhesive on the capacitance of the printed capacitors. **Figure 5.13 (b)** is a printed capacitor set with completed PVA/GF encapsulation. Air bubbles are observed within the cured adhesive dam (see **Figure 5.13 (c - f)**), which can contribute to leakage of the encapsulation. However, the presence of air bubbles is challenging to completely

eliminate during the dispensing process. Additional adhesive is dispensed around the cured adhesive dam, and the self-standing PVA/GF film is manually placed on top. After curing the adhesive, the PVA/GF film is securely fixed, completing the encapsulation process. The profile of the encapsulated capacitor is shown in **Figure 5.13 (g)**, the measured distance between the top of the encapsulation layer (PVA/GF film) and the printed capacitor is 199.18 µm (see **Figure 5.13 (h)**).

A potential interaction between printed capacitor and UV curable adhesive is investigated by measuring the capacitance of samples during a cyclic humidity test, both before dispensing the adhesive and after curing it. As discussed in chapter 3, variations in the printing quality of the silver lines and the BST/P(VDF-TrFE) dielectric contribute to differences in the resulting absolute capacitance. Hence, relative capacitances with the capacitance at 35 %RH in the first measurement cycle are calculated as reference (C_{rh}/C_{35}) for further evaluation.

Two groups of printed capacitors are utilized. Printed capacitors in group A are later with the adhesive dam, while printed capacitors in group B are further PVA/GF encapsulated. The measured silver line width of the utilized samples in these two groups are listed in **Table 5.2**.

Table 5.2: Measured widths of the silver lines, calculated surface areas, and measured capacitance of printed capacitors in two groups on Melinex ST506 PET substrates (three samples each).

	Group A	Group B
Substrate	Melinex ST506 PET	Melinex ST506 PET
Bottom silver line [µm]	128.33 ± 0.58	126.67 ± 11.02
Top silver line [µm]	109.00 ± 18.03	107.33 ± 22.28
Surface area [mm^2]	0.014	0.014
Capacitance (23 °C, 35 %RH) [pF]	2.34 ± 0.16	2.30 ± 0.12

The relative capacitance over time of the printed capacitors in group A during three measurement cycles is shown in **Figure 5.14**, indicating that the interaction between the printed capacitor and the utilized UV curable adhesive is negligible. Both before dispensing and after curing the adhesive dam, the dielectric area is fully exposed to the controlled conditions in the climate chamber. The capacitance increases with the rising humidity, by 35.50 ± 0.71 % before dam application and 33.40 ± 0.31 % after curing the adhesive dam (35 %RH to 85 %RH and back to 35 %RH, three cycles at 23 °C). Moreover, the hysteresis between the increase and subsequent decrease in humidity, owing to the differing rates of moisture absorption and desorption of the polymer components in the dielectric layer [207], remains basically unchanged (before: 8.45 ± 1.20 % and after: 8.67 ± 0.41 %, see **Table 5.3**). This further indicates that the adhesive dam surrounding the dielectric layer has a negligible influence on the printed capacitors' sensitivity against moisture.

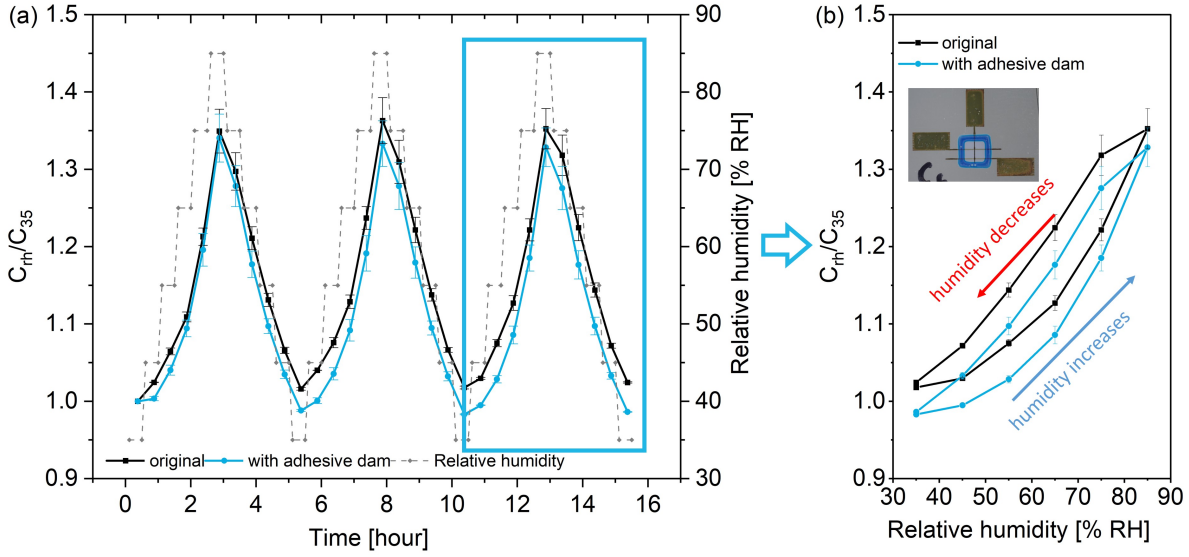

Figure 5.14: Relative capacitance of inkjet printed capacitors (group A) before/with cured adhesive around the dielectric area on Melinex ST506 substrates. (a) Relative capacitance over time at 23 °C for three measurement cycles. (b) Relative capacitance over relative humidity in the last measurement cycle. Three samples are measured. Error bars represent standard deviations.

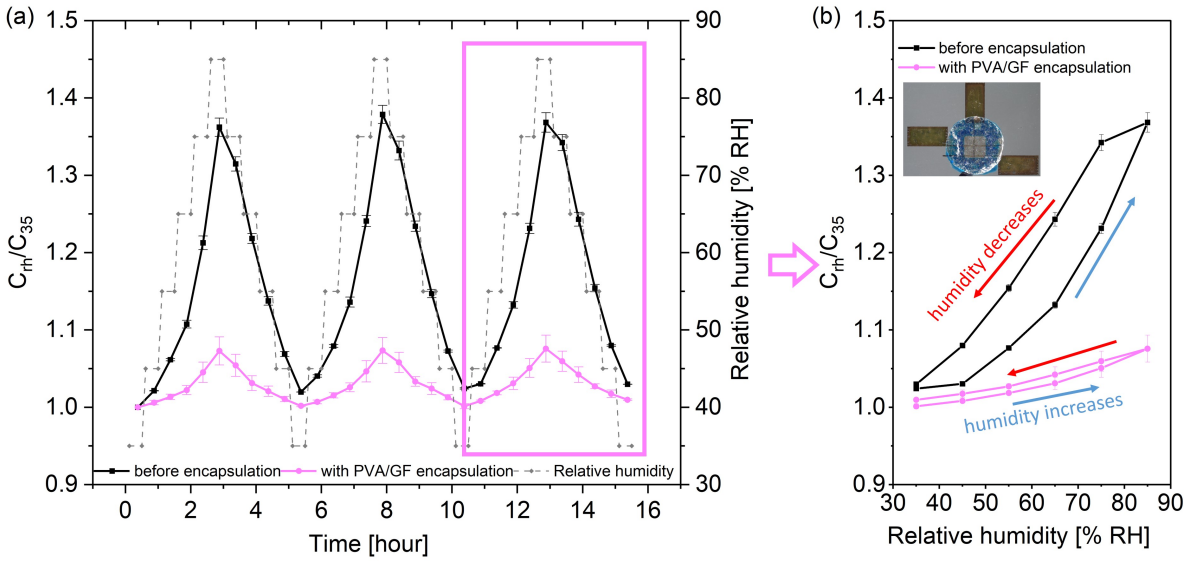

Figure 5.15: Relative capacitance of inkjet printed capacitors (group B) before/with PVA/GF encapsulation on Melinex ST506 substrates. (a) Relative capacitance over time at 23 °C for three measurement cycles. (b) Relative capacitance over relative humidity in the last measurement cycle. Three samples are measured. Error bars represent standard deviations.

The data in **Figure 5.15** and **Table 5.3** confirm the effectiveness of the PVA/GF encapsulation. Samples with PVA/GF encapsulation yield a 7.41 ± 0.07 % increase in capacitance, while before encapsulation, an increase of 36.98 ± 0.05 % is observed. Moreover, with PVA/GF encapsulation,

no significant hysteresis is observed (0.97 ± 0.16 %). These results verify the effectiveness of the PVA/GF encapsulation in mitigating moisture-induced capacitance changes. Moreover, the performance of the PVA/GF encapsulation can be further optimized if the aforementioned issue of air bubbles is solved.

Table 5.3: Increase in capacitance of the printed capacitors before and with the adhesive dam or the PVA/GF encapsulation over rising humidity (23 °C, 35 %RH to 85 %RH) and hysteresis between the increase and subsequent decrease in humidity (75 %RH to 85 %RH and then back to 75 %RH).

	Group A		Group B	
	before adhesive dam	with adhesive dam	before PVA/GF encapsulation	after PVA/GF encapsulation
increase in capacitance	35.50 ± 0.71 %	33.40 ± 0.31 %	36.98 ± 0.05 %	7.41 ± 0.07 %
hysteresis	8.45 ± 1.20 %	8.67 ± 0.41 %	10.13 ± 0.99 %	0.97 ± 0.16 %

5.1.3 Conclusion

In this section, GF, GO, MMT, and silica are compared as filler materials in a PVA matrix. An adapted desiccant method for WVTR measurement, based on the ASTM E96/E96M-22 standard, is developed to assess the WVTR of the fabricated PVA/filler films. Among the four fillers, GF proves to be the most suitable filler. Furthermore, a microscope image of a block face of a PVA/GF film confirms a lamellar arrangement of the glass flakes, with only few agglomerations and a resulting tortuous path in the PVA matrix. PVA/GF films containing 5 wt% GFs exhibit the lowest WVTR and are subsequently applied as encapsulation material.

A PVA/GF suspension is directly deposited on the printed Ag tracks by doctor blading, providing global encapsulation. The moisture barrier effectiveness of this PVA/GF encapsulation is validated by measuring changes in resistance of Ag tracks after damp heat test and room storage conditions. Optical inspection of one sample of the printed Ag tracks with PVA/GF encapsulation reveals an average GF coverage rate of 72 % with a variance of 5.9 %, as quantified from nine top view microscope images processed by ImageJ.

A local PVA/GF encapsulation for a moisture sensitive capacitor is realized using an UV curable adhesive. It is confirmed that this adhesive has a negligible influence on the performance of the printed capacitors. The barrier effectiveness of this local PVA/GF encapsulation is validated by measuring moisture-induced changes in capacitance during the cyclic humidity test.

5.2 Solution processable hybrid polymer encapsulation

Besides using solution processable PVA/GF films as encapsulation material for the test structures, this section utilizes a commercially available ORMOCER material as encapsulation material. A dispensing process for this ORMOCER material is developed, and its moisture barrier property is validated by encapsulating the printed moisture sensitive capacitors.

5.2.1 Materials and methods

The materials and processes, the test structures and the characterization methods utilized in this section are described.

5.2.1.1 Materials

Organic/inorganic hybrid polymers ORMOCER, an abbreviation for organically modified ceramics, refers to a group of hybrid polymer materials. During the sol–gel processing of ORMOCERs, an inorganic network is formed through the controlled hydrolysis and condensation of organically modified silicon alkoxides. The final curing step involves organic cross-linking [162, 164]. After curing, it can form a glass-like film. In this section, the hybrid polymer utilized is OrmoClear30 purchased from Micro Resist. The viscosity of OrmoClear30 is 30 cp, which is suitable for a dispensing process.

Substrates

- DuPont Teijin Melinex ST506 PET film (175 µm thick);
- DuPont Kapton HN PI film (75 µm thick).

Inkjet printable inks

- Silver nanoparticle ink (Silverjet DGP 40LT-15C, Sigma Aldrich);
- Ceramic nanoparticle ink (BST/P(VDF-TrFE) ink, developed at KIT IAM-ESS [47]).

5.2.1.2 Development of two dispensing strategies for a hybrid polymer

The recommended standard processing workflow of OrmoClear30 from the manufacturer Micro Resist is designed for a spin coating process, as shown in the **Table 5.4**. After substrate preparation, OrmoClear30 is spin coated onto the substrate, followed by a prebake process on a hotplate at 80 °C for two minutes. Afterwards, OrmoClear30 is cured by UV exposure. A post exposure

bake and a hardbake process are recommended. The viscosity of OrmoClear30 is 30 cp, which is also suitable for a dispensing process. Furthermore, in contrast to spin coating, dispensing is a digital process, which enables a local encapsulation. Therefore, in this section, OrmoClear30 is intended to be dispensed on substrates using the dispensing platform MIMOSE [232] to enable a local encapsulation of a moisture sensitive test structure.

Processing Details

Solvent-free types			**OrmoClear®**	**OrmoClear®30**
Substrate preparation			Spin clean with 2-propanol and dehydrate on a hotplate at 200 °C/ 392 °F for 5 min or apply O_2 plasma treatment	
Spin coating	spin speed	[rpm]	3000	
	time	[s]	30	
	acceleration	[rpm/s]	1000	
Prebake (hotplate)		[°C/ °F]	80/ 176	
		[min]	2	
Exposure dose[1]		[mJ/cm²]	1000 – 3000	
Post exposure bake		[°C/ °F]	130/ 266	
		[min]	10	
Development with OrmoDev[2]		[s]	30 – 180	
Hardbake		[°C/ °F]	150/ 302	
		[h]	3	

[1] UV broadband exposure, intensity measured at λ = 365 nm
[2] Optional step, immersion development, duration may vary depending on feature size, necessary only when UV lithography is applied or exposure is performed without inert gas

Table 5.4: Recommended processing of OrmoClear30 by the supplier Micro resist [234].

The standard processing workflow is adjusted according to the given laboratory conditions and limitations arising from the materials utilized. Since all the process steps are not conducted under inert gas, an uncured layer can form on the surface of the material after UV exposing. Experiments show that a hard bake process in an oven (120 °C, 15 h) helps to remove this layer.

Influence of the prebake step on the final shape of the resulting OrmoClear30 films

The viscosity of uncured OrmoClear30 varies with the processing temperature. This characteristic can cause the shape of the dispensed material to deform before curing, potentially causing the intended local encapsulation to fail due to deformation. A prebake process prior to UV exposure can influence the viscosity of the uncured OrmoClear30 and the final shape of the resulting films. Therefore, the potential influence of a prebake step is firstly investigated.

Two points and three groups of point matrices (4×4) are dispensed on Melinex ST506 PET substrates with identical dispensing parameters (see **Table 5.5**). One point is UV-cured (wavelength λ: 365 nm, Panasonic UJ35) without prebaking, while another point undergoes a 30-minute prebake process at 80 °C before UV exposure. The distance between the points in a matrix ranges from 750 µm to 1250 µm. One group of point matrices is UV-cured without

prebaking, while another two groups of point matrices undergo a five-minute and a 30-minute prebake process at 80 °C before UV exposure, respectively.

Table 5.5: Dispensing parameters for OrmoClear30.

Needle inner diameter	Dispensing time (per point)	Dispensing height[1]	Pressure	Vacuum
330 µm	300 ms	100 µm	3 bar	1.5 kPa

[1] Dispensing height: distance between the dispensing needle tip and the substrate.

During and after dispensing, OrmoClear30 remains in a liquid state and spreads slowly. The prebake process accelerates this spreading, which facilitates the formation of a thinner OrmoClear30 layer but makes it more challenging to control the final shape of the resulting film. As shown in **Figure 5.16 (a) and (b)**. Point (a) is UV-cured without prebaking, while point (b) undergoes a 30-minute prebake process at 80 °C before UV exposure. The diameter of the prebaked point is nearly twice that of the non-prebaked point. This effect is consistently observed across the matrices with varying dispensing distances, ranging from 750 µm to 1250 µm (**Figure 5.16 (c)**).

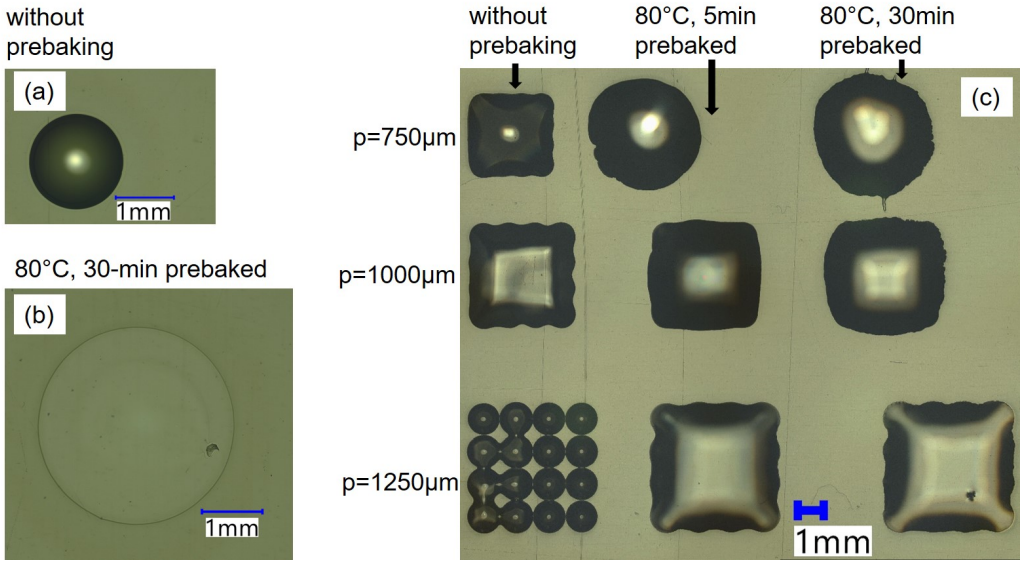

Figure 5.16: Top view images of dispensed OrmoClear30 after curing. Point (a) is UV cured without a prebake process. Point (b) undergoes a 30-minute prebake process in the oven at 80 °C before UV curing. (c) Point matrices with and without prebake, point distance p varies from 750 µm to 1250 µm.

In order to measure the thickness of the prebaked and the non-prebaked OrmoClear30 films, points matrices (6×4) with point distance of 1000 µm are dispensed on Melinex ST506 PET substrates. Dispensing parameters are summarized in **Table 5.5**. The comparison of thickness measurements between prebaked and non-prebaked OrmoClear30 films is shown in **Figure 5.17**. With a dispensing distance of 1000 µm, the amount of dispensed material is more than

sufficient to fill the area. Consequently, during the prebaking step, the viscosity of OrmoClear30 reduces, the OrmoClear30 flows outward, causing the shape to deviate from a rectangle into an irregular form. This flow reduces the film thickness to a more uniform height of 98.71 µm compared to a non-uniform thickness varying from 142.71 µm to 194.73 µm in the central region of a non-prebaked film. Therefore, a prebake is an optional step depending on requirements and dispensing strategies.

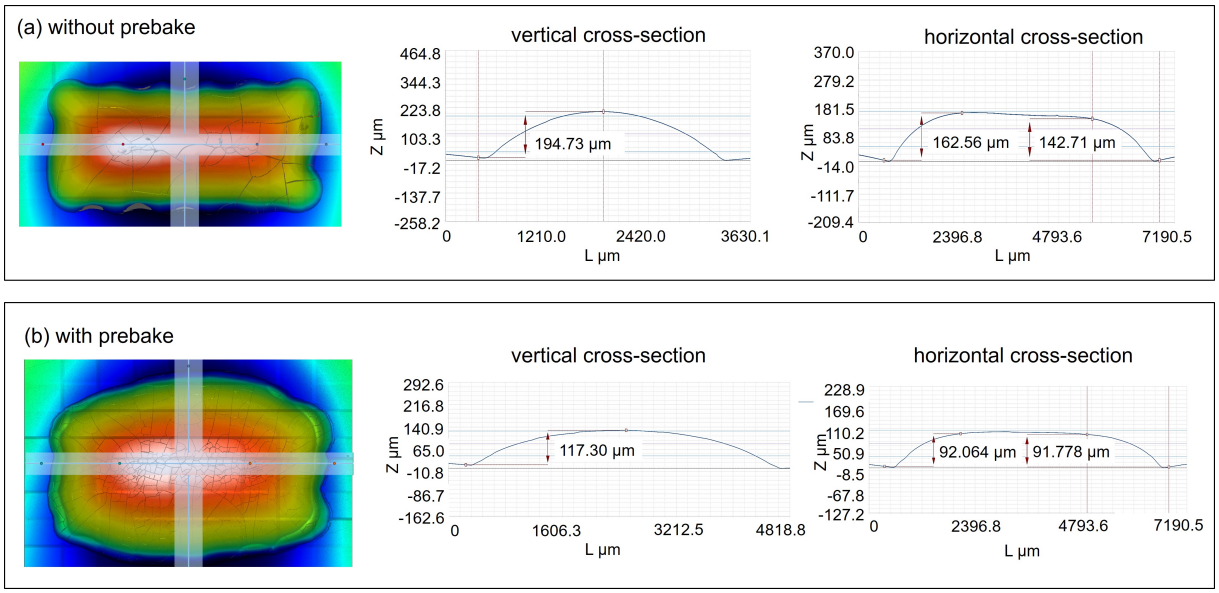

Figure 5.17: Profiles of (a) a non-prebaked and (b) a 80 °C 5 min prebaked OrmoClear30 film. Both films are dispensed using the point dispensing strategy. The point distance is set to 1000 µm.

Before dispensing OrmoClear30 directly on the test structures, two dispensing strategies are investigated to obtain a homogeneous surface of the resulting films on Melinex ST506 PET films, namely point dispensing and "dam and fill" dispensing. The PET films are cleaned by a ten-minute O_2 plasma treatment. Dispensing needles (inner diameter of 330 µm) are chosen for OrmoClear30. Before dispensing, OrmoClear30 is filled into the needle and degassed for 20 min in an in-house built degas-desiccator which is described in [64].

Point dispensing strategy The first strategy is point dispensing, namely the surface is formed by adjacent, coalescing points. For the comparison of two dispensing strategies, points matrices (6×9) with a point distance of 1000 µm are dispensed. The dispensing parameters are shown in **Table 5.5**. The modified processing of OrmoClear30 using point dispensing is summarized in **Figure 5.18**.

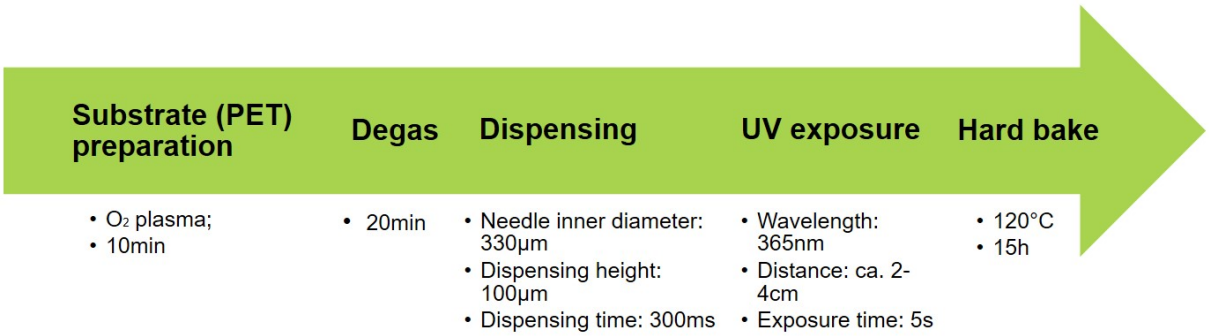

Figure 5.18: The modified processing workflow of OrmoClear30 (point dispensing).

"Dam and fill" dispensing strategy Another strategy is a "dam and fill" process (see **Figure 5.19**), which refers to a technique commonly used in microelectronics packaging, particularly for protecting delicate components such as semiconductors or integrated circuits (ICs) from environmental influences [235, 236]. Usually, two different materials are applied as "dam" and "fill" material.

- The "dam" is typically made from a viscous, non-flowing epoxy resin or silicone that is applied around the area to be encapsulated. The "dam" material is designed to create a boundary or barrier that prevents the "fill" material from flowing beyond a designated area.
- The "fill" is a lower viscosity material, such as low-viscosity epoxy, silicone gel, or polyurethane, that is poured or dispensed within the boundaries of the "dam". This material is designed to flow and fill the space, encapsulating the components inside.

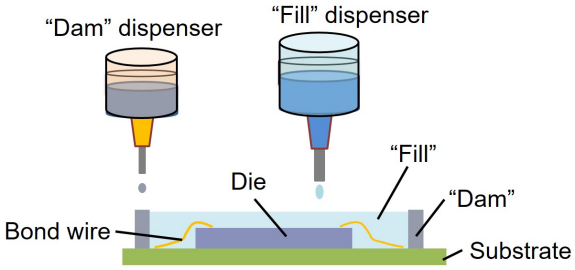

Figure 5.19: Schematic illustration of a "dam and fill" process for encapsulation of a bare semiconductor die.

A novel "dam and fill" process with a single material is developed, benefiting from the fact that OrmoClear30 can be cured by UV-exposure within seconds and a prebake process can reduce its viscosity and fill the region within the "dam". Thus, OrmoClear30 is applied both as the "dam" and the "fill" material in this section. The modified "dam and fill" process involves first applying OrmoClear30 around the perimeter of an area to create a "dam". The dispensing parameters for this "dam" are summarized in **Table 5.5**. This "dam" is then cured immediately after dispensing. Afterwards, OrmoClear30 is dispensed within this "dam" area. The dispensing

height and dispensing time for the "fill" are adjustable and depend on the size and the shape of the "fill" region. Finally, the "fill" OrmoClear30 is subjected to a prebake process in the oven under 80 °C for 30 min. This step reduces its viscosity and thus leads to spreading and to filling of the "dam" area. Afterwards, the "fill" OrmoClear30 is UV cured. The workflow of this "dam and fill" dispensing strategy is summarized in **Figure 5.20**.

For comparison of these two dispensing strategies, a dispensing pattern is designed. The horizontal side of the "dam" consists of six points, and the vertical side consists of nine points. The distance between points is set to 750 µm, the dispensing height is set to 100 µm, and the dispensing time per point is set to 300 ms. The "fill" area consists of four points with a dispensing time of 3500 ms per point and the dispensing needle height of 800 µm to accommodate the higher dispensing volume.

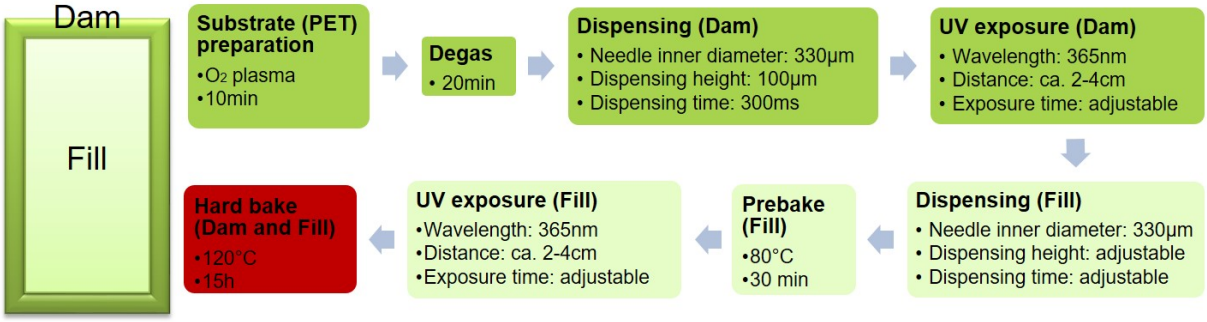

Figure 5.20: The modified processing workflow for the OrmoClear30 "dam and fill" dispensing process. UV exposure time, dispensing height and dispensing time are adjustable according to the volume of dispensed OrmoClear30.

5.2.1.3 Investigation of the influence of encapsulation process steps on the capacitance of inkjet printed capacitors

To evaluate the moisture barrier property of the dispensed OrmoClear30 films, inkjet printed capacitors are utilized as test structures. These capacitors exhibit moisture sensitivity (see chapter 3). Since OrmoClear30 is finally cured by UV exposure and undergoes a hard bake process in an oven up to 120 °C, prior to investigating the moisture barrier effectiveness of this OrmoClear30 encapsulation, the adverse influences of these UV and thermal treatments on the capacitance of these printed capacitors should be excluded. Hence, the thermal treatment in an oven at 120 °C and the UV treatment for 20 s are applied to those capacitors on Melinex ST506 PET substrates (group C and D, respectively). Both before and after those treatments, cyclic humidity tests are conducted. The capacitance is measured using the automated characterization setup described in chapter 3.

5.2.1.4 Hybrid polymer encapsulation for inkjet printed capacitors

OrmoClear30 is applied as the encapsulation material over the dielectric region using the two dispensing strategies outlined above. It is to notice that the O_2 plasma treatment is not applied for the substrate preparation to avoid its potential influence on the printed capacitors.

When the point dispensing method is applied, a point matrix (5×5) is dispensed, with a point distance of 1000 µm. When the "dam and fill" dispensing method is applied, the encapsulation workflow is schematically illustrated in **Figure 5.21**. Both the horizontal and vertical sides of the "dam" consists of six points. The distance between points is set to 750 µm, the dispensing height is set to 100 µm, and the dispensing time per point is set to 300 ms.

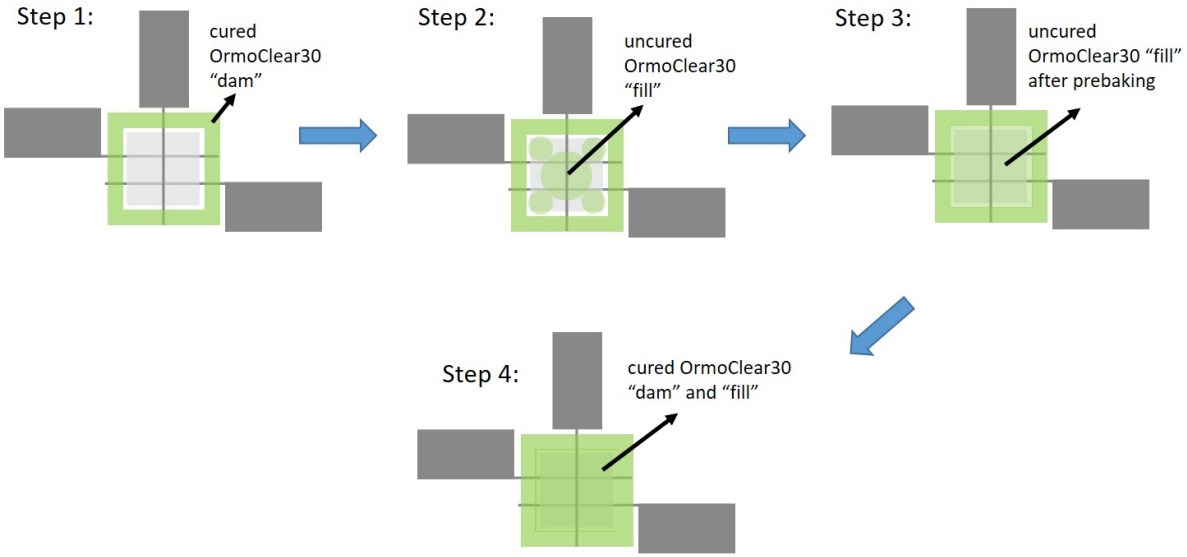

Figure 5.21: OrmoClear30 encapsulation workflow. Step 1: the OrmoClear30 is dispensed around the dielectric region and UV cured immediately after dispensing. Step 2: four small points are dispensed at the corners of the cured "dam" and a big point is dispensed in the center. Step 3: The test structure with filled "dam" is placed in an oven at 80 °C for 30 min. After this prebaking process, the uncured OrmoClear30 spreads and fills the "dam". Step 4: the "fill" OrmoClear30 is cured by UV and then placed in an oven at 120 °C for 15 h for final polymerization.

It is observed that the spreading of the uncured OrmoClear30 on the BST/P(VDF-TrFE) layer is significantly slower compared to on the PET substrate. To address this, a dispensing pattern is designed, consisting of four small points at the corners of the "dam" (dispensing time: 300 ms per point, dispensing height: 100 µm) and a larger point in the center (dispensing time: 8000 ms, dispensing height: 800 µm). This pattern facilitates the spreading flow of uncured OrmoClear30 to fill the "fill" area more effectively during the prebaking step.

The encapsulation process is completed by curing and hard baking of the OrmoClear30. For both dispensing strategies, the general dispensing parameters, including dispensing needle type, pressure, and vacuum, are taken from **Table 5.5**.

5.2.1.5 Characterization of hybrid polymer films

To characterize the moisture barrier property of the OrmoClear30 films, capacitance changes during the cyclic humidity test are calculated both before and after encapsulating the printed capacitors. Top view images are taken using a Keyence VHX 7000 digital optical microscope. To improve contrast for optical profile measurements, a 90 nm-thick layer of Cr is sputtered onto the resulting OrmoClear30 films using a Quorum Q300T ES Plus sputter coater. The OrmoClear30 films are then scanned with a Sensofar S Neox confocal microscope, and their profiles are analyzed.

5.2.2 Results

In the following sections, two dispensing strategies for OrmoClear30 — applied on PET substrates and directly on the dielectric region of printed capacitors - are compared. The hybrid polymer OrmoClear30 is applied as the encapsulation material and dispensed on the printed capacitors to achieve local encapsulation, where only the dielectric region, sensitive to moisture, requires protection. The outcomes of OrmoClear30 encapsulation are presented.

5.2.2.1 Comparison of two dispensing strategies for OrmoClear30

A cured OrmoClear30 "dam" on a PET substrate is shown in **Figure 5.22**. This "dam" consists of points with a distance of 750 µm. The measured height of the OrmoClear30 "dam" is 267.31 ± 25.99 µm (see **Figure 5.23**).

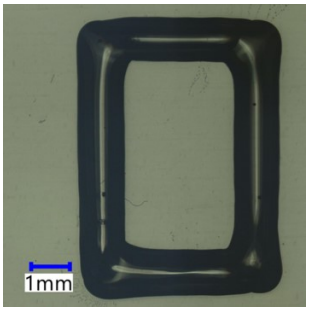

Figure 5.22: Top view image of a OrmoClear30 "dam".

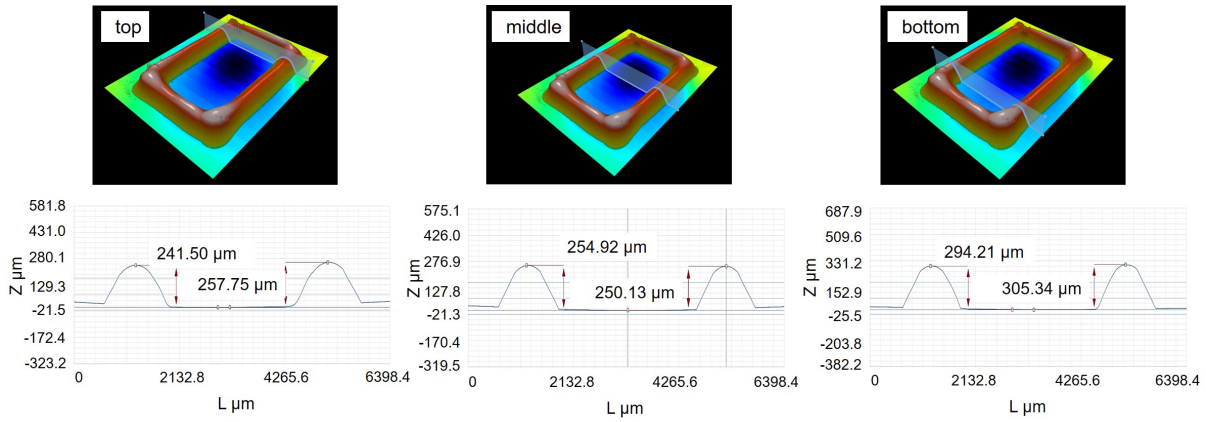

Figure 5.23: Profile of a cured OrmoClear30 dam on a PET carrier substrate manufactured by the point dispensing method. The dispensing distance is set to 750 µm. Three positions (top, middle and bottom) of the profile are taken to measure its thickness.

Figure 5.24 (a) illustrates a cured OrmoClear30 film on a PET substrate dispensed using the "dam and fill" method, while **Figure 5.24 (b)** depicts a cured OrmoClear30 film using the point dispensing method, which is cured without undergoing a prebake process. The profiles of the OrmoClear30 films obtained using these two dispensing methods are shown in **Figure 5.25**.

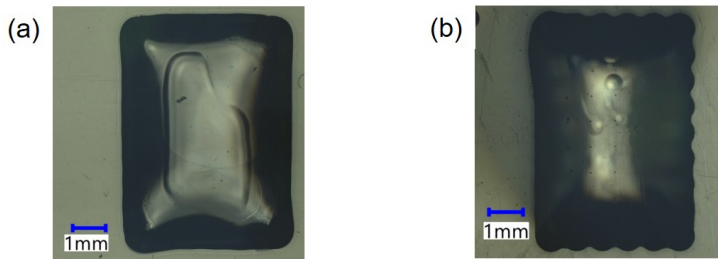

Figure 5.24: Top view image of (a) an OrmoClear30 film dispensed using the "dam and fill" method; and (b) an OrmoClear30 film dispensed using the point dispensing method.

The film produced via the point dispensing method exhibits an uneven surface with a noticeable curvature (measured thickness: top 92.681 µm, middle 290.53 µm, bottom 97.314 µm). In contrast, the "dam and fill" method allows the uncured OrmoClear30 to fill the area within the "dam" during the 30-minute prebake process, resulting in a more even surface with a measured thickness of 312.02 ± 33.79 µm (measured thickness: top 276.23 µm, middle 315.48 µm, bottom 343.94 µm). Furthermore, with the previously dispensed and cured "dam", the contour of the final Ormoclear30 films can be precisely controlled.

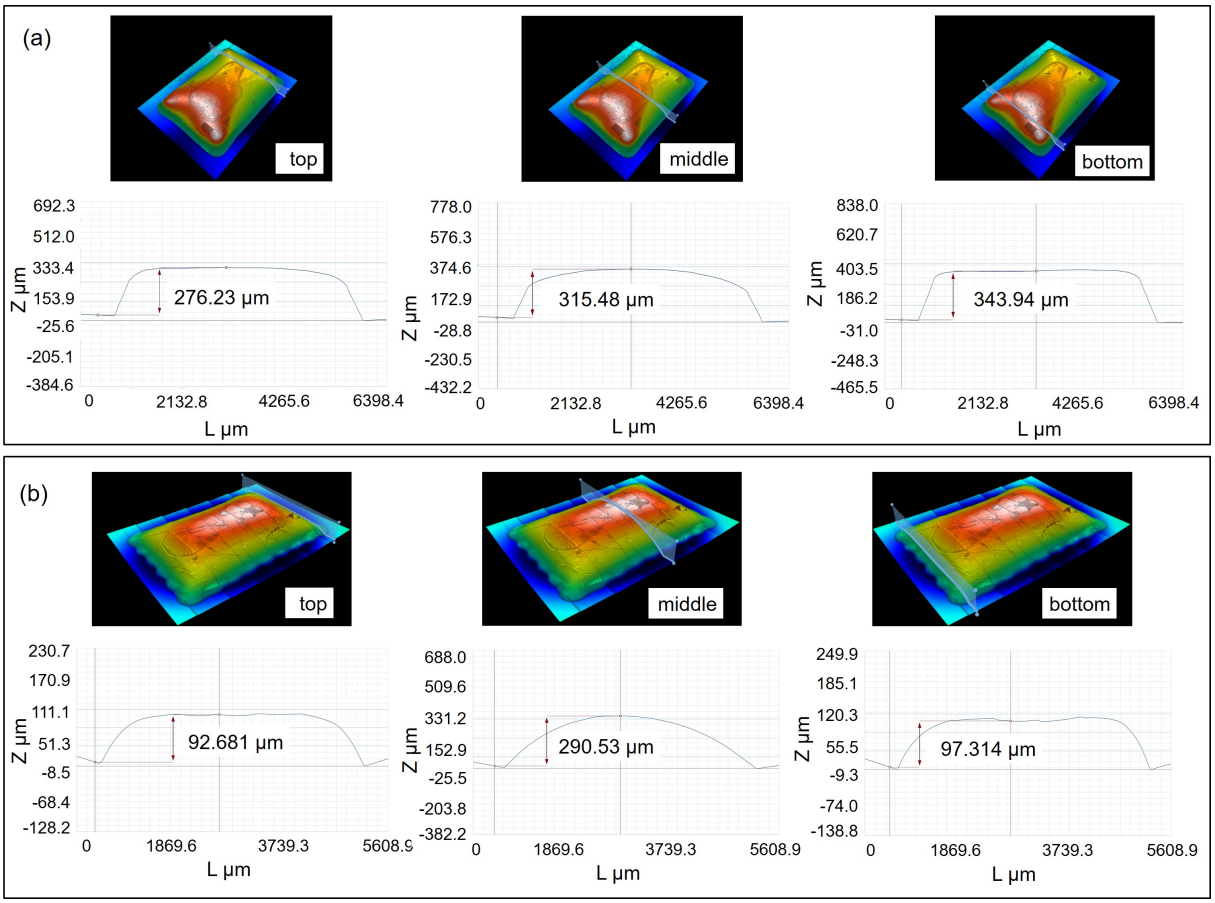

Figure 5.25: Profile of (a) a cured OrmoClear30 film using the "dam and fill" dispensing method and (b) a cured OrmoClear30 film on a PET substrate using the point dispensing method. The point distance is set to 750 µm for the "dam" area (dispensing time per point 300 ms). Four points with distances of 2500 µm and 1500 µm in x and y direction are dispensed within the "dam" (dispensing time per point 3500 ms). Three positions (top, middle and bottom) of the profiles are taken to measure their thickness.

5.2.2.2 Influence of encapsulation process steps on the moisture sensitivity of inkjet printed capacitors

To exclude the influence of the encapsulation process steps on the moisture sensitivity of printed capacitors, thermal treatment at 120 °C in an oven and UV treatment for 20 s are applied to those capacitors on PET Melinex ST506 substrates in two groups respectively. Capacitances are recorded both before and after these treatments during cyclic humidity tests.

Table 5.6: Measured widths of the silver lines, calculated surface areas, and measured capacitance of printed capacitors on Melinex ST506 PET substrates subjected to the thermal and the UV treatment (three samples each).

	Group C (thermal treatment)	Group D (UV treatment)
Substrate	Melinex ST506 PET	Melinex ST506 PET
Bottom silver line [µm]	128.33 ± 8.14	124.33 ± 3.21
Top silver line [µm]	95.00 ± 1.73	103.00 ± 20.66
Surface area [mm^2]	0.012	0.013
Capacitance (23 °C, 35 %RH) [pF]	2.32 ± 0.06	2.95 ± 0.55

As discussed in chapter 3, variations in the printing quality of the silver lines and the BST/P(VDF-TrFE) dielectric contribute to differences in absolute capacitance. The measured silver line widths of the samples are provided in **Table 5.6**. The observed capacitance variations suggest potential inhomogeneity in the printed BST/P(VDF-TrFE) dielectric layer. Therefore, the capacitance relative to a reference capacitance at 35 %RH in the first measurement cycle (C_{rh}/C_{35}) is calculated.

The results, shown in **Figure 5.26**, indicate that both thermal and UV treatments have a negligible effect on the performance of the printed capacitors during cyclic humidity tests. The BST/P(VDF-TrFE) dielectric shows no significant change in moisture sensitivity after these treatments.

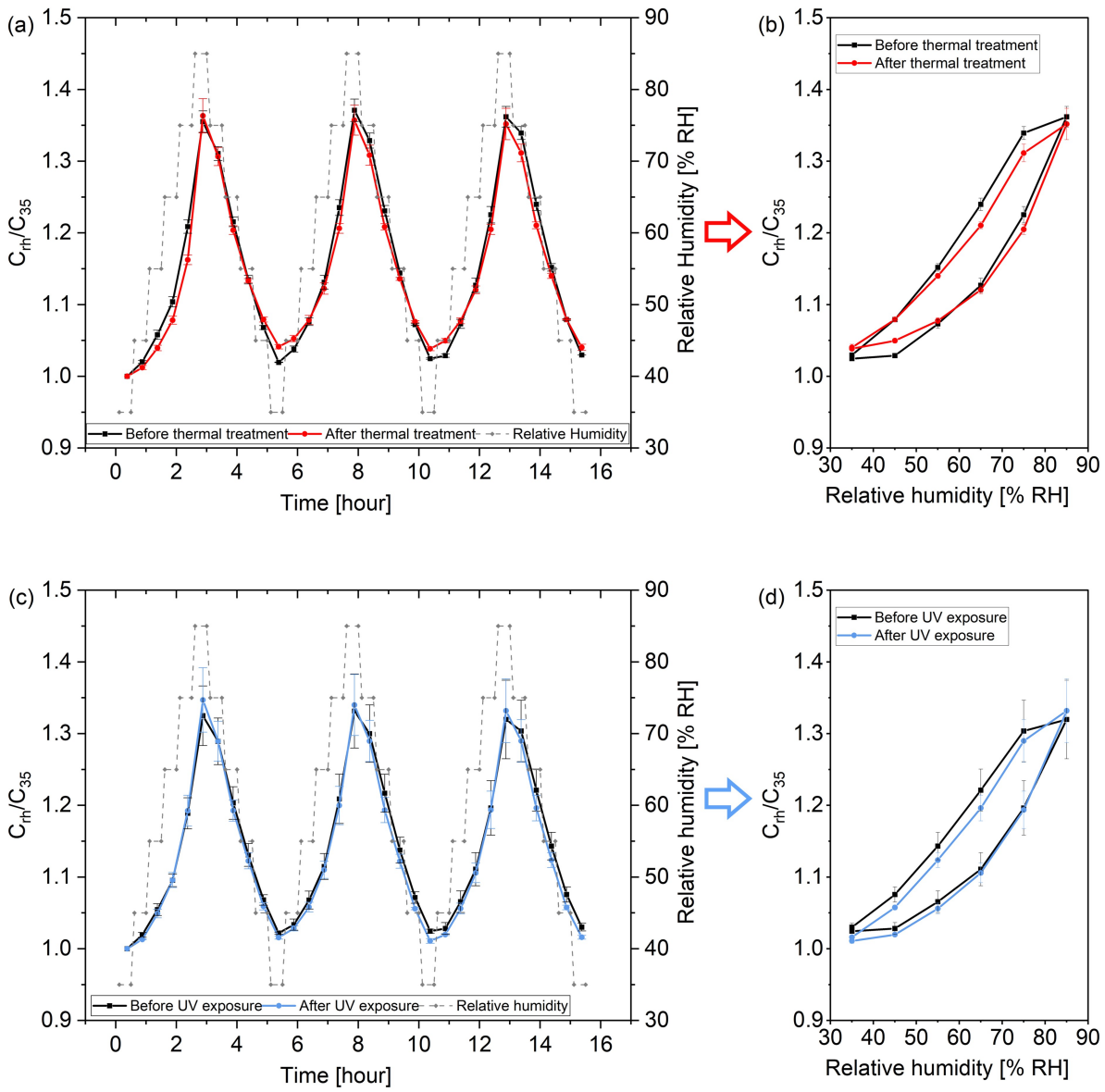

Figure 5.26: Relative capacitance of inkjet printed capacitors on Melinex ST506 PET substrates at 23 °C for three measurement cycles. (a - b): before and after the thermal treatment; (c - d): before and after the UV treatment. Three samples are measured. Error bars represent standard deviations.

5.2.2.3 Dispensing results of OrmoClear30 on inkjet printed capacitors

Two dispensing strategies are utilized to encapsulate the printed capacitors. A point matrix of OrmoClear30 (5×5) is dispensed with a point distance of 1000 µm. Due to the differing surface wetting properties of the BST/P(VDF-TrFE) dielectric area and the PET substrate, the OrmoClear30 dispensed on the BST/P(VDF-TrFE) dielectric does not connect to neighboring points, whereas it connects on the PET substrate (see **Figure 5.27**). To address this issue, the point distance needs to be adjusted. By reducing the point distance, the OrmoClear30 could be connected on the BST/P(VDF-TrFE) dielectric area. However, this adjustment may lead

to the OrmoClear30 on the PET substrate to spread into the silver pad area, causing the local encapsulation to fail. Therefore, the point dispensing method is not applied for the encapsulation of the printed capacitors.

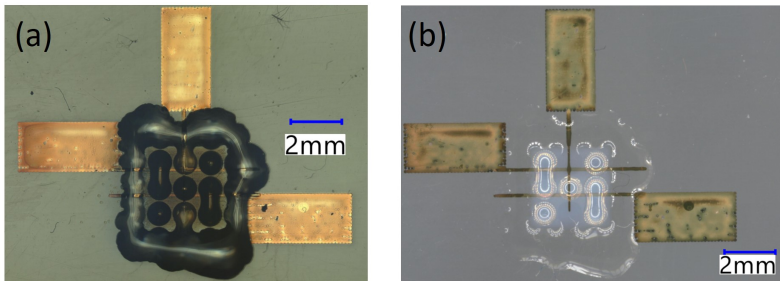

Figure 5.27: Top view images of a point matrix of OrmoClear30 (5×5) is dispensed on a printed capacitor with a dispensing distance of 1000 µm. These images are taken using (a) the transmitted illumination and (b) the epi-illumination.

Applying the "dam and fill" dispensing method, local encapsulation is successfully achieved both for the capacitors printed on the PET and the PI substrate (see **Figure 5.28**). The profile of the OrmoClear30 encapsulation layer for the printed capacitors on a PET substrate is shown in **Figure 5.29**. Its mean thickness is 190.80 ± 19.09 µm.

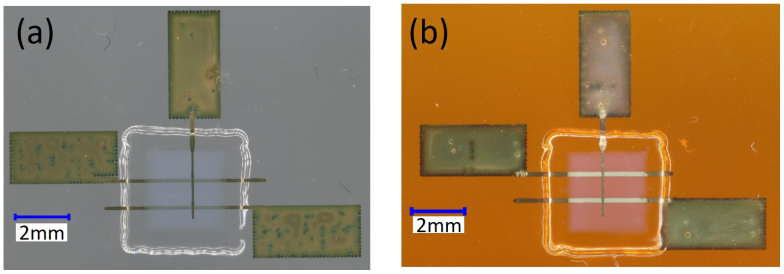

Figure 5.28: Top view images of printed capacitors on (a) a Melinex ST506 PET substrate and (b) a Kapton HN PI substrate with the OrmoClear30 encapsulation. OrmoClear30 is dispensed using the "dam and fill" method.

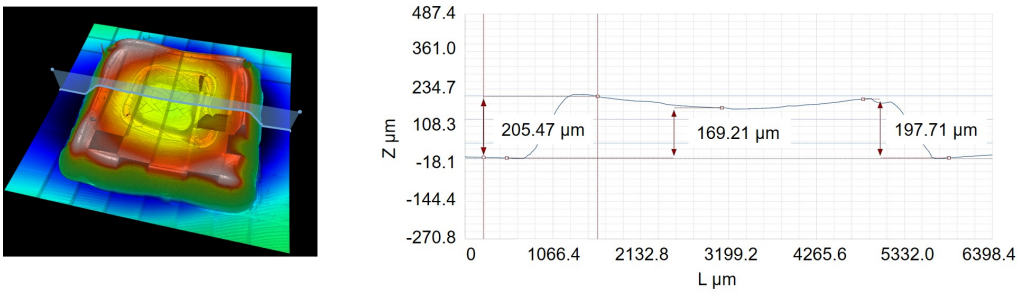

Figure 5.29: Profile and measured thickness of an OrmoClear30 encapsulation layer for the printed capacitors on a PET substrate.

5.2.2.4 OrmoClear30 encapsulation results on inkjet printed capacitors

The investigations above validate that the thermal and the UV treatment, which are necessary for the curing of OrmoClear30, have negligible effects on the moisture sensitivity of the BST/P(VDF-TrFE). Hence, these moisture-sensitive capacitors are encapsulated to evaluate the moisture barrier property of the resulting OrmoClear30 films. Due to different wetting of the ink on two substrate types, variations in the width of the printed silver lines are observed. Moreover, the variations in the printing quality of the BST/P(VDF-TrFE) dielectric also contribute to differences in the resulting absolute capacitance (see **Table 5.7**).

Table 5.7: Measured widths of the silver lines, calculated surface areas, and measured capacitance of printed capacitors with OrmoClear30 encapsulation (three samples in each group).

	Group E	Group F
Substrate	Melinex ST506 PET	Kapton HN PI
Bottom silver line [µm]	119.67 ± 2.89	180.67 ± 0.58
Top silver line [µm]	77.67 ± 2.08	88.67 ± 3.51
Surface area [mm^2]	0.009	0.016
Capacitance (23 °C, 35 %RH) [pF]	1.59 ± 0.03	2.59 ± 0.02

The capacitance relative to a reference capacitance at 35 %RH in the first measurement cycle (C_{rh}/C_{35}) is recorded during cyclic humidity tests, both before and after encapsulation. **Figure 5.30** and **Figure 5.31** present the recorded relative capacitance of the printed capacitors with OrmoClear30 encapsulation on Melinex ST506 PET and Kapton HN PI substrates, respectively.

The diagrams confirm the effectiveness of OrmoClear30 encapsulation in mitigating humidity-induced capacitance changes on both substrates. Before encapsulation, the BST/P(VDF-TrFE) dielectric dominates the moisture absorption and desorption process, the capacitance increases with the rising humidity and decreases as the humidity drops. While after encapsulation, the OrmoClear30 film effectively prevents moisture from penetrating or escaping as the ambient humidity increases or drops, thereby mitigating the moisture-induced change in capacitance.

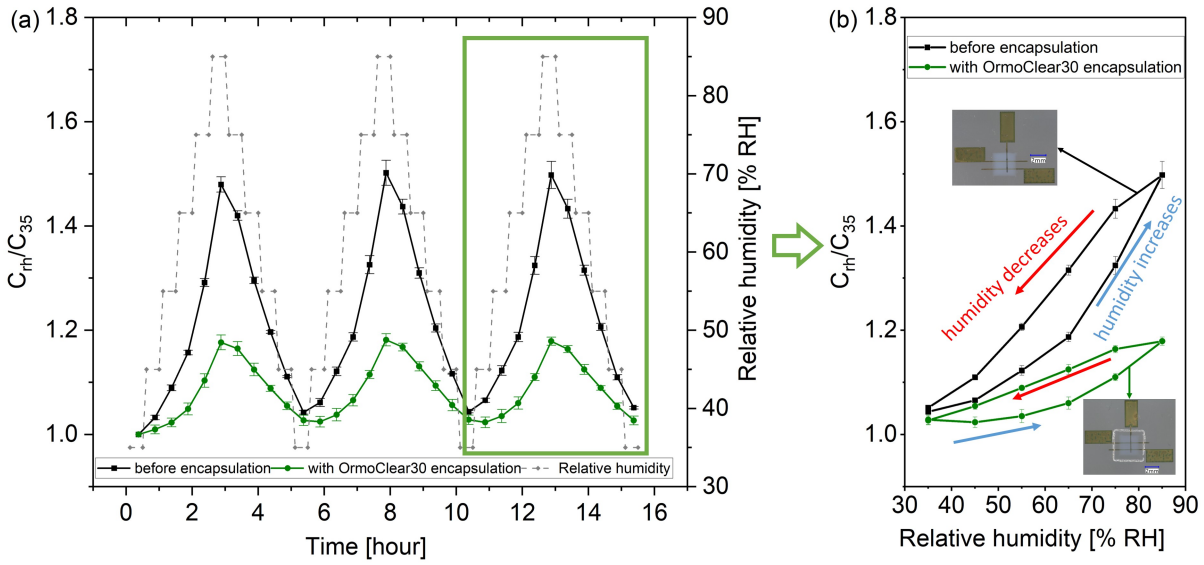

Figure 5.30: Relative capacitance of inkjet printed capacitors before/with the OrmoClear30 encapsulation on Melinex ST506 PET substrates. (a) Relative capacitance over time at 23 °C for three measurement cycles. (b) Relative capacitance over relative humidity in the last measurement cycle. Three samples are measured. Error bars represent standard deviations.

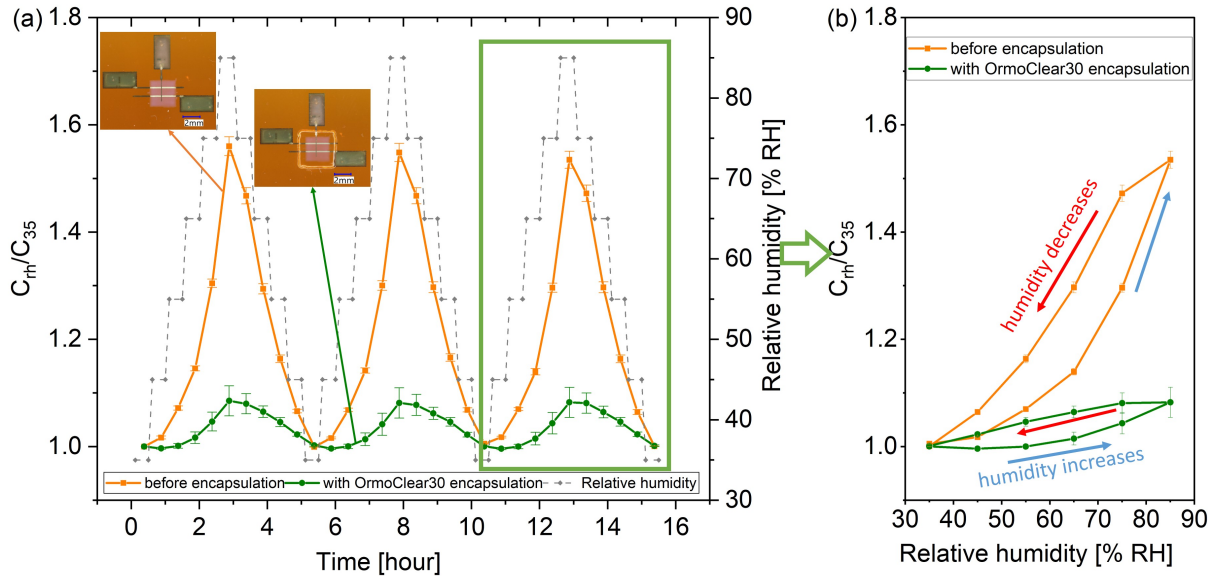

Figure 5.31: Relative capacitance of inkjet printed capacitors before/with the OrmoClear30 encapsulation on Kapton HN PI substrates. (a) Relative capacitance over time at 23 °C for three measurement cycles. (b) Relative capacitance over relative humidity in the last measurement cycle. Three samples are measured. Error bars represent standard deviations.

As summarized in **Table 5.8**, for PET substrates, the capacitance increases by 49.32 ± 0.61 % before encapsulation, whereas the increase is reduced to 17.91 ± 0.27 % with OrmoClear30

encapsulation. An expected reduced hysteresis due to the presence of the encapsulation layer is observed as well (after encapsulation 5.59 ± 0.47 % compared to 11.62 ± 1.07 % before encapsulation).

For PI substrates, a more pronounced barrier effect is observed. The capacitance increases by 54.79 ± 1.27 % before encapsulation, whereas the increase is sharply reduced to 8.31 ± 0.20 % with OrmoClear30 encapsulation. Moreover, a reduced hysteresis is observed as well (after encapsulation 3.56 ± 0.22 % compared to 16.88 ± 0.65 % before encapsulation), which is more significant compared to the encapsulated capacitors on PET substrates.

Table 5.8: Increase in capacitance over rising humidity (23 °C, 35 %RH to 85 %RH) and hysteresis between the increase and subsequent decrease in humidity (75 %RH to 85 %RH and then back to 75 %RH).

	Group E (substrate: PET)		Group F (substrate: PI)	
	before OrmoClear30 encapsulation	after OrmoClear30 encapsulation	before OrmoClear30 encapsulation	after OrmoClear30 encapsulation
increase in capacitance	49.32 ± 0.61 %	17.91 ± 0.27 %	54.79 ± 1.27 %	8.31 ± 0.20 %
hysteresis	11.62 ± 1.07 %	5.59 ± 0.47 %	16.88 ± 0.65 %	3.56 ± 0.22 %

5.2.3 Conclusion

In this section, a commercially available hybrid polymer, OrmoClear30, is applied as an encapsulation material to protect printed capacitors from moisture. Its processing workflow is adapted to the given laboratory conditions and encapsulation requirements. A prebake step, performed before curing the OrmoClear30, influences the final shape of the resulting films which is critical for achieving local encapsulation. Furthermore, two dispensing methods, the point dispensing method and the novel "dam and fill" dispensing method, are investigated. In comparison to the point dispensing method, by applying the novel "dam and fill" dispensing method, a more homogeneous OrmoClear30 film and a local encapsulation can be realized for the printed capacitors on both PET and PI substrates. The barrier effectiveness of this OrmoClear30 encapsulation is validated by measuring moisture-induced changes in capacitance during the cyclic humidity test.

5.3 Comparison between PVA/GF and OrmoClear30 encapsulation

The previous sections have described two solution processable encapsulation methods for the moisture-sensitive capacitors, the PVA/GF encapsulation and the OrmoClear30 encapsulation. Both encapsulation methods effectively protect the printed capacitors from moisture. In this section, a comparison of these two encapsulation methods is provided.

As shown in **Table 5.9**, for the printed capacitors on PET substrates, the moisture-induced capacitance change reduces from 36.98 ± 0.05 % to 7.41 ± 0.07 % after PVA/GF encapsulation (group B), and from 49.32 ± 0.61 % to 17.91 ± 0.27 % after OrmoClear30 encapsulation (group E). For the printed capacitor on PI substrates, after OrmoClear30 encapsulation, the moisture-induced capacitance change decreases from 54.79 ± 1.27 % to 8.31 ± 0.20 % (group F). In addition, less hysteresis is observed for the printed capacitors encapsulated with the PVA/GF films.

Table 5.9: Increase in capacitance over rising humidity (23 °C, 35 %RH to 85 %RH) and hysteresis between the increase and subsequent decrease in humidity (75 %RH to 85 %RH and then back to 75 %RH).

	PVA/GF encapsulation (group B, substrate: PET)		OrmoClear30 encapsulation (group E, substrate: PET)		OrmoClear30 encapsulation (group F, substrate: PI)	
	before	after	before	after	before	after
increase in capacitance	36.98 ± 0.05 %	7.41 ± 0.07 %	49.32 ± 0.61 %	17.91 ± 0.27 %	54.79 ± 1.27 %	8.31 ± 0.20 %
hysteresis	10.13 ± 0.99 %	0.97 ± 0.16 %	11.62 ± 1.07 %	5.59 ± 0.47 %	16.88 ± 0.65 %	3.56 ± 0.22 %

To better express the effectiveness of these encapsulations under these test conditions, a "Barrier effectiveness" is defined for the encapsulation of the printed moisture-sensitive capacitors utilized in this dissertation. It is expressed as follows:

$$\text{Barrier effectiveness}(\Delta RH) = 1 - \left| \frac{\text{Capacitance change after encapsulation}(\Delta RH)}{\text{Capacitance change before encapsulation}(\Delta RH)} \right| \quad (5.1)$$

Where RH is the relative humidity in the climate chamber during the cyclic humidity test, and $\Delta RH = RH - 35$ %RH, as the cyclic humidity test in this dissertation starts with 35 %RH.

With this expression, barrier effectiveness of an encapsulation layer yields a value between zero and one. Without encapsulation, the barrier effectiveness is defined as zero. For a perfect encapsulation, it equals one, meaning that after encapsulation, there is no change in capacitance with varying ambient humidity. **Figure 5.32** compares the barrier effectiveness of these two encapsulation methods for the printed moisture-sensitive capacitors on PET and PI substrates.

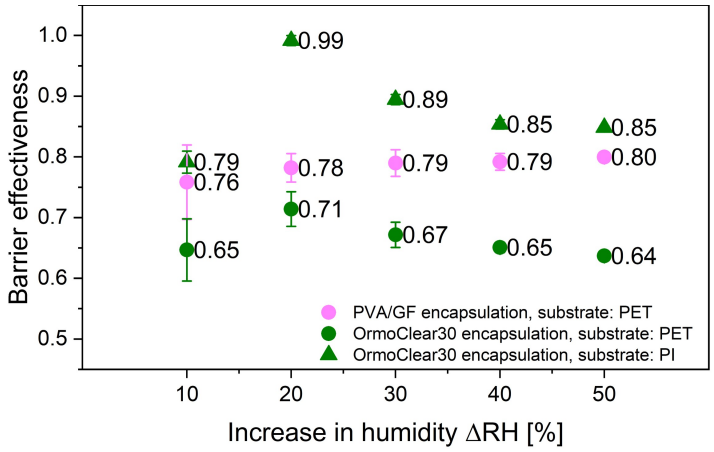

Figure 5.32: Barrier effectiveness of the PVA/GF and the OrmoClear30 encapsulation for the printed capacitors utilized in this dissertation.

Figure 5.33 schematically illustrates the structure of these two encapsulation methods. There is a space between the PVA/GF film and the dielectric layer, whereas the OrmoClear30 films are directly coated onto the dielectric layer. Furthermore, the OrmoClear30 film is larger than the dielectric region, resulting in an area where the OrmoClear30 film directly attaches to the substrate.

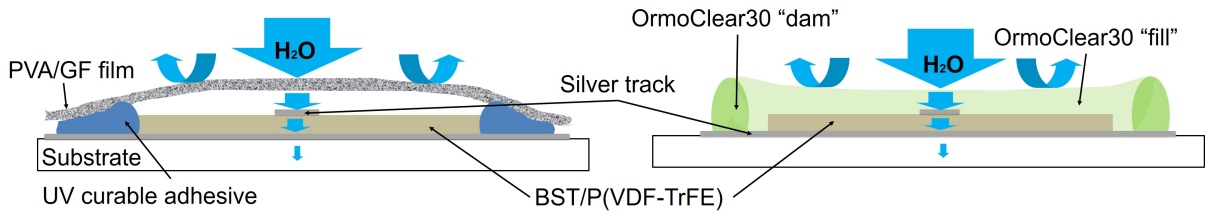

Figure 5.33: Schematic illustration for a PVA/GF and an OrmoClear30 encapsulation for printed capacitors.

The structure illustration helps to discuss the data presented in **Table 5.9** and **Figure 5.32**. Due to the existence of the space between the PVA/GF film and the dielectric layer, as humidity decreases, water molecules encounter less resistance to leave the dielectric layer compared to the OrmoClear30 encapsulation, resulting in less hysteresis as observed.

According to these data, the PVA/GF encapsulation appears to exhibit a better barrier effectiveness for these printed capacitors than the OrmoClear30 encapsulation. However, it should be noted that a direct comparison between the two encapsulation methods is not entirely straightforward, as the structure of the encapsulation is different and some influence of the substrate type can also be assumed from the data in **Table 5.9** and **Figure 5.32**.

Both encapsulation methods provide effective protection against moisture for the printed capacitors using BST/P(VDF-TrFE) dielectric ink. However, they each have distinct advantages and limitations.

- Moisture barrier property: A ca. 11 µm thick PVA/GF film provides better moisture barrier effectiveness as a ca. 200 µm thick OrmoClear30 layer. Furthermore, it exhibits less pronounced hysteresis.
- Encapsulation type: The OrmoClear30 material is suitable for dispensing. This enables a local encapsulation where the components need to be locally protected from moisture. In contrast, a PVA solution containing 5 wt% GFs is not suitable for dispensing. PVA/GF suspension can be directly coated on the printed components via doctor blading to achieve a global encapsulation for the printed components. Otherwise, an additional mask needs to be correspondingly designed to enable a local encapsulation only for the components to be protected from moisture. Another approach is to utilize adhesive to fix the self-standing PVA/GF film on the corresponding area. However, in this way, the self-standing PVA/GF film should be cut into suitable shape, and the film preparation and application process are more complex.
- Flexibility: The resulting PVA/GF films are thinner as the OrmoClear30 films. As a result, they provide better flexibility.
- Transparency: The OrmoClear30 films are transparent thus they are suitable as encapsulation material for applications which require transparency. In contrast, due to the presence of GFs, the transparency of PVA/GF films is reduced which limits its application range.

6 Conclusion and outlook

Flexible printed electronics (FPE) is a rapidly growing technology with promising applications, including wearables, sensors, and flexible displays. However, moisture-induced degradation remains one of the key challenges for the longevity and reliability of FPE devices.

In this dissertation, a polyvinyl pyrrolidone (PVP) capped silver nanoparticle (Ag NP) ink and a ceramic nanoparticle (BST/P(VDF-TrFE)) ink are utilized to print conductive tracks and capacitors on polymer films. These conductive tracks and capacitors are utilized as test structures. The moisture influence on their electrical properties is systematically investigated by subjecting them to environmental tests. Based on the environmental tests results, an identified positive moisture influence is analyzed and two solution processable encapsulation methods are developed to minimize negative moisture influences. Firstly, theoretical foundations and related work are outlined, including:

1. Materials and techniques applied in the fabrication of FPE devices;
2. Reported moisture influences on FPE devices during their fabrication and usage;
3. Fundamental principles of permeation, factors affecting the moisture permeability of polymers and current methods to improve polymer moisture barrier properties;
4. Materials and methods to develop solution processable moisture barrier films;
5. Water vapor transmission rate (WVTR) measurement methods for the assessment of moisture barrier effectiveness.

Moisture is found to play both a positive role in improving the conductivity of printed Ag tracks and a negative role in altering the capacitance of capacitors printed with BST/P(VDF-TrFE) dielectric ink. Based on these findings, methods to take advantage of the positive effects of moisture as well as to mitigate its negative effects are developed.

The **key results** of this dissertation are:

I) Two novel low-temperature sintering methods for a PVP capped Ag NP ink are developed: damp heat sintering and water sintering.

a) Both sintering methods induce neck formation between Ag NPs at temperatures up to 85 °C, resulting in the sintering of Ag NPs.

b) The role of moisture in the sintering of a PVP capped Ag NP ink is explained. The moisture induced neck formation between the Ag NPs is assumed to arise from two factors: (1) the humidity-dependent reduction of the glass transition temperature of the PVP capping layer, which enhances its diffusivity and promotes Ostwald ripening, and (2) the capillary pressure generated by water menisci between the Ag NPs.

II) Solution processable barrier films for printed electronics are developed.

a) A solution processable polymer/filler moisture barrier film is developed. PVA is chosen as polymer matrix due to its non-toxic and straightforward processing properties. Glass flakes (GFs) turn out to be the most effective filler material in a PVA matrix among four investigated filler types. PVA/GF films containing 5 wt% GFs exhibit the lowest WVTR.

b) A global (i.e. large surface) PVA/GF encapsulation is realized by directly depositing the PVA/GF suspension on the printed Ag tracks by doctor blading. The moisture barrier effectiveness of this PVA/GF encapsulation is validated by measuring changes in resistance of silver tracks after damp heat test and room storage conditions.

c) A local (i.e. restricted to the individual device) PVA/GF encapsulation for a moisture-sensitive capacitor based on BST/P(VDF-TrFE) dielectric ink is realized with assistance of an UV curable adhesive. The barrier effectiveness of this local PVA/GF encapsulation is validated by the significant reduction of the moisture-induced changes in capacitance.

d) Another solution processable moisture barrier film is fabricated using a commercially available dispensable hybrid polymer, OrmoClear30. Two dispensing methods for OrmoClear30 are developed, the point dispensing and the "dam and fill" dispensing. In comparison to the point dispensing method, by applying the "dam and fill" dispensing method, a more homogeneous OrmoClear30 film is realized.

e) A local OrmoClear30 encapsulation for the moisture-sensitive capacitor is realized. With this encapsulation layer, the moisture-induced capacitance change is significantly reduced for the printed capacitors both on PET and PI substrates.

f) A comparison between the PVA/GF encapsulation and the OrmoClear30 encapsulation for the printed capacitors is provided. Their pros and cons are discussed.

In summary, this dissertation explores the moisture impact on specific printed components. Solutions to take advantage of positive influences and minimizing the negative ones are provided. These solutions can improve the functionality and reliability of printed components and can expand the application of FPE devices.

From the findings of this dissertation, **future work** can be focused on the following fields:

1. Further experiments with damp heat and hot water sintering should be conducted with other metallic NP inks using PVP as the capping agent, to assess whether these sintering processes are generally applicable to this class of inks. Furthermore, metallic NP inks with other polymer capping agents (e.g. PVA) should be studied to evaluate whether similar moisture-induced effects on these capping agents can be observed, leading to neck formation at low temperatures. If these effects are confirmed across a broad range of metallic NP inks, damp heat and hot water processing at low temperatures can emerge as alternative, effective, low-cost, and scalable sintering methods.
2. Other hybrid polymers, such as polysilazanes (PSZ), are promising solution processable encapsulation materials. The permeability of PSZ coatings against moisture depends on the curing methods and the curing environment [177]. Optimal curing processes should be further investigated to accelerate and precisely control the conversion of PSZ into silica.
3. The encapsulation should have minimal impact on the original flexibility of the FPE devices. A bending test setup to evaluate the flexibility and reliability of encapsulated FPE devices should be established.

List of Figures

List of Tables

List of Publications

Journal articles

[28] Alexander Scholz, Lukas Zimmermann, Ulrich Gengenbach, Liane Koker, Zehua Chen, Horst Hahn, Axel Sikora, Mehdi B. Tahoori, and Jasmin Aghassi-Hagmann. Hybrid low-voltage physical unclonable function based on inkjet-printed metal-oxide transistors. *Nature Communications*, 11(1), nov 2020. doi: 10.1038/s41467-020-19324-5.

[64] Zehua Chen, Ulrich Gengenbach, Xinnan Liu, Alexander Scholz, Lukas Zimmermann, Jasmin Aghassi-Hagmann, and Liane Koker. An automated room temperature flip-chip mounting process for hybrid printed electronics. *Micromachines*, 13(4):583, apr 2022. doi: 10.3390/mi13040583.

[68] Zehua Chen, Ulrich Gengenbach, Liane Koker, Liyu Huang, Tim P. Mach, Klaus-Martin Reichert, Richard Thelen, and Martin Ungerer. Systematic investigation of novel, controlled low-temperature sintering processes for inkjet printed silver nanoparticle ink. *Small*, December 2023. ISSN 1613-6829. doi: 10.1002/smll.202306865.

[227] Zehua Chen, Ulrich Gengenbach, Shant Gananian, Daniel Moser, Klaus-Martin Reichert, Liyu Huang, and Liane Koker. Solution processable barrier films using a filled polymer to encapsulate flexible printed electronics. *IEEE Journal on Flexible Electronics*, December 2024. doi: 10.1109/JFLEX.2024.3512473.

Conference contributions

[14] Zehua Chen, Ulrich Gengenbach, Maher Mansour, and Liane Koker. Approaches for solution-processed encapsulation of printed medical wearable devices. *Current Directions in Biomedical Engineering*, 6(3):131–134, sep 2020. doi: 10.1515/cdbme-2020-3034.

[226] Zehua Chen, Ulrich Gengenbach, Shant Gananian, Daniel Moser, Klaus-Martin Reichert, and Liane Koker. Investigation of solution processable moisture barrier films based on a polymer and filler materials. In *2024 IEEE International Conference on Flexible and Printable Sensors and Systems (FLEPS)*. IEEE, jun 2024. doi: 10.1109/fleps61194.2024.10603898.

[207] Martin Ungerer, Zehua Chen, Tim Pang Mach, Klaus-Martin Reichert, Ulrich Gengenbach, Moritz Lindmüller, Joachim R. Binder, Markus Reischl, and Liane Koker. Automated characterisation of printed electronics under adjustable ambient conditions. In *2024 International Semiconductor Conference (CAS)*, pages 69–72. IEEE, oct 2024. doi: 10.1109/cas62834.2024.10736741.

Bibliography

[1] Zheng Cui. *Printed Electronics: Materials, Technologies and Applications*. Wiley, April 2016. ISBN 9781118920954. doi: 10.1002/9781118920954.

[2] Andreas Albrecht. *Printed Sensors for the internet of things*. PhD thesis, Technische Universität München, 2018.

[3] Yue Dong, Chao Bao, and Woo Soo Kim. Sustainable additive manufacturing of printed circuit boards. *Joule*, 2(4):579–582, April 2018. ISSN 2542-4351. doi: 10.1016/j.joule.2018.03.015.

[4] Wei Wu. *Printed Electronics Technologies*. The Royal Society of Chemistry, July 2022. ISBN 9781788019699. doi: 10.1039/9781788019699.

[5] Xuepei Wang, Mengjie Zhang, Luwei Zhang, Jinchao Xu, Xinqing Xiao, and Xiaoshuan Zhang. Inkjet-printed flexible sensors: From function materials, manufacture process, and applications perspective. *Materials Today Communications*, 31:103263, June 2022. ISSN 2352-4928. doi: 10.1016/j.mtcomm.2022.103263.

[6] Yasser Khan, Arno Thielens, Sifat Muin, Jonathan Ting, Carol Baumbauer, and Ana C. Arias. A new frontier of printed electronics: Flexible hybrid electronics. *Advanced Materials*, 32 (15):1905279, nov 2019. doi: 10.1002/adma.201905279.

[7] John A. Rogers, Xiaodong Chen, and Xue Feng. Flexible hybrid electronics. *Advanced Materials*, 32(15):1905590, apr 2020. doi: 10.1002/adma.201905590.

[8] Simon Züfle. *Degradation Analysis and Parameter Extraction of Organic Semiconductor Devices : Investigation by means of Complementary Measurement Techniques combined with Numerical Simulation*. PhD thesis, 2017.

[9] Vera Steinmann and Lorenza Moro. Encapsulation requirements to enable stable organic ultra-thin and stretchable devices. *Journal of Materials Research*, 33(13):1925–1936, jul 2018. doi: 10.1557/jmr.2018.194.

[10] Haibo Li, Yinji Ma, and Yonggang Huang. Material innovation and mechanics design for substrates and encapsulation of flexible electronics: a review. *Materials Horizons*, 8(2): 383–400, 2021. doi: 10.1039/d0mh00483a.

[11] Hatice Ceylan Koydemir and Aydogan Ozcan. Wearable and implantable sensors for biomedical applications. *Annual Review of Analytical Chemistry*, 11(1):127–146, jun 2018. doi: 10.1146/annurev-anchem-061417-125956.

[12] Minjeong Ha, Seongdong Lim, and Hyunhyub Ko. Wearable and flexible sensors for user-interactive health-monitoring devices. *Journal of Materials Chemistry B*, 6(24):4043–4064, 2018. doi: 10.1039/c8tb01063c.

[13] K. D. Harris, A. L. Elias, and H.-J. Chung. Flexible electronics under strain: a review of mechanical characterization and durability enhancement strategies. *Journal of Materials Science*, 51(6):2771–2805, dec 2015. doi: 10.1007/s10853-015-9643-3.

[14] Zehua Chen, Ulrich Gengenbach, Liane Koker, and Maher Mansour. Approaches for solution-processed encapsulation of printed medical wearable devices. *Current Directions in Biomedical Engineering*, 6(3):131–134, sep 2020. doi: 10.1515/cdbme-2020-3034.

[15] Jessica Ortigoza-Diaz, Kee Scholten, Christopher Larson, Angelica Cobo, Trevor Hudson, James Yoo, Alex Baldwin, Ahuva Weltman Hirschberg, and Ellis Meng. Techniques and considerations in the microfabrication of parylene c microelectromechanical systems. *Micromachines*, 9(9):422, aug 2018. doi: 10.3390/mi9090422.

[16] P. F. Carcia, R. S. McLean, M. H. Reilly, M. D. Groner, and S. M. George. Ca test of al2o3 gas diffusion barriers grown by atomic layer deposition on polymers. *Applied Physics Letters*, 89(3), jul 2006. doi: 10.1063/1.2221912.

[17] Woong-Sun Kim, Myoung-Gyun Ko, Tae-Sub Kim, Sang-Kyun Park, Yeon-Keon Moon, Su-Hwan Lee, Jae-Gun Park, and Jong-Wan Park. Titanium dioxide thin films deposited by plasma enhanced atomic layer deposition for OLED passivation. *Journal of Nanoscience and Nanotechnology*, 8(9):4726–4729, sep 2008. doi: 10.1166/jnn.2008.ic48.

[18] Peter Antony Premkumar, Sergey A. Starostin, Mariadriana Creatore, Hindrik de Vries, Roger M. J. Paffen, Paul M. Koenraad, and Mauritius C. M. van de Sanden. Smooth and self-similar SiO2-like films on polymers synthesized in roll-to-roll atmospheric pressure-PECVD for gas diffusion barrier applications. *Plasma Processes and Polymers*, 7(8):635–639, jul 2010. doi: 10.1002/ppap.200900179.

[19] Shiyu Zhang, Wei Xue, and Zhinong Yu. Moisture barrier evaluation of SiO /SiN stacks on polyimide substrates using electrical calcium test. *Thin Solid Films*, 580:101–105, apr 2015. doi: 10.1016/j.tsf.2015.02.023.

[20] Yun Li, Yingfei Xiong, Huizhi Yang, Kun Cao, and Rong Chen. Thin film encapsulation for the organic light-emitting diodes display via atomic layer deposition. *Journal of Materials Research*, 35(7):681–700, nov 2019. doi: 10.1557/jmr.2019.331.

[21] Massimo Mariello, Kyungjin Kim, Kangling Wu, Stephanie P. Lacour, and Yves Leterrier. Recent advances in encapsulation of flexible bioelectronic implants: Materials, technologies, and characterization methods. *Advanced Materials*, 34(34):2201129, jul 2022. doi: 10.1002/adma.202201129.

[22] Yifei Luo, Mohammad Reza Abidian, Jong-Hyun Ahn, et al. Technology roadmap for flexible sensors. *ACS Nano*, 17(6):5211–5295, mar 2023. doi: 10.1021/acsnano.2c12606.

[23] Dongdong Li, Wen-Yong Lai, Yi-Zhou Zhang, and Wei Huang. Printable transparent conductive films for flexible electronics. *Advanced Materials*, 30(10):1704738, jan 2018. doi: 10.1002/adma.201704738.

[24] Hamed Abdolmaleki, Preben Kidmose, and Shweta Agarwala. Droplet-based techniques for printing of functional inks for flexible physical sensors. *Advanced Materials*, 33(20): 2006792, mar 2021. doi: 10.1002/adma.202006792.

[25] P. Martins, N. Pereira, A. C. Lima, A. Garcia, C. Mendes-Filipe, R. Policia, V. Correia, and S. Lanceros-Mendez. Advances in printing and electronics: From engagement to commitment. *Advanced Functional Materials*, 33(16), feb 2023. doi: 10.1002/adfm.202213744.

[26] Kang-Jun Baeg and Jiyoul Lee. Flexible electronic systems on plastic substrates and textiles for smart wearable technologies. *Advanced Materials Technologies*, 5(7):2000071, jun 2020. doi: 10.1002/admt.202000071.

[27] Katsuaki Suganuma. *Introduction to Printed Electronics*. Springer New York, 2014. doi: 10.1007/978-1-4614-9625-0.

[28] Alexander Scholz, Lukas Zimmermann, Ulrich Gengenbach, Liane Koker, Zehua Chen, Horst Hahn, Axel Sikora, Mehdi B. Tahoori, and Jasmin Aghassi-Hagmann. Hybrid low-voltage physical unclonable function based on inkjet-printed metal-oxide transistors. *Nature Communications*, 11(1), nov 2020. doi: 10.1038/s41467-020-19324-5.

[29] Sung-Jei Hong, Yong-Hoon Kim, and Jeong-In Han. Development of ultrafine indium tin oxide (ITO) nanoparticle for ink-jet printing by low-temperature synthetic method. *IEEE Transactions on Nanotechnology*, 7(2):172–176, mar 2008. doi: 10.1109/tnano.2008.917846.

[30] Saeideh Kholghi Eshkalak, Amutha Chinnappan, W.A.D.M. Jayathilaka, Marziyeh Khatibzadeh, Elaheh Kowsari, and Seeram Ramakrishna. A review on inkjet printing of CNT composites for smart applications. *Applied Materials Today*, 9:372–386, dec 2017. doi: 10.1016/j.apmt.2017.09.003.

[31] Felice Torrisi, Tawfique Hasan, Weiping Wu, Zhipei Sun, Antonio Lombardo, Tero S. Kulmala, Gen-Wen Hsieh, Sungjune Jung, Francesco Bonaccorso, Philip J. Paul, Daping Chu, and Andrea C. Ferrari. Inkjet-printed graphene electronics. *ACS Nano*, 6(4):2992–3006, mar 2012. doi: 10.1021/nn2044609.

[32] Pei He, Jianyun Cao, Hui Ding, Chongguang Liu, Joseph Neilson, Zheling Li, Ian A. Kinloch, and Brian Derby. Screen-printing of a highly conductive graphene ink for flexible printed electronics. *ACS Applied Materials & Interfaces*, 11(35):32225–32234, aug 2019. doi: 10.1021/acsami.9b04589.

[33] Livio Gamba, Zachary T. Johnson, Jackie Atterberg, Santiago Diaz-Arauzo, Julia R. Downing, Jonathan C. Claussen, Mark C. Hersam, and Ethan B. Secor. Systematic design of a graphene ink formulation for aerosol jet printing. *ACS Applied Materials & Interfaces*, 15 (2):3325–3335, jan 2023. doi: 10.1021/acsami.2c18838.

[34] Iara J. Fernandes, Angelica F. Aroche, Ariadna Schuck, Paola Lamberty, Celso R. Peter, Willyan Hasenkamp, and Tatiana L. A. C. Rocha. Silver nanoparticle conductive inks: synthesis, characterization, and fabrication of inkjet-printed flexible electrodes. *Scientific Reports*, 10(1), jun 2020. doi: 10.1038/s41598-020-65698-3.

[35] Venkata Krishna Rao R., Venkata Abhinav K., Karthik P. S., and Surya Prakash Singh. Conductive silver inks and their applications in printed and flexible electronics. *RSC Advances*, 5(95):77760–77790, 2015. doi: 10.1039/c5ra12013f.

[36] Lixin Mo, Zhenxin Guo, Li Yang, Qingqing Zhang, Yi Fang, Zhiqing Xin, Zheng Chen, Kun Hu, Lu Han, and Luhai Li. Silver nanoparticles based ink with moderate sintering in flexible and printed electronics. *International Journal of Molecular Sciences*, 20(9):2124, apr 2019. doi: 10.3390/ijms20092124.

[37] Xianghui Zeng, Pei He, Minglu Hu, Weikai Zhao, Huitong Chen, Longhui Liu, Jia Sun, and Junliang Yang. Copper inks for printed electronics: a review. *Nanoscale*, 14(43): 16003–16032, 2022. doi: 10.1039/d2nr03990g.

[38] Jiuhong Yi and Yunlei Xianyu. Gold nanomaterials-implemented wearable sensors for healthcare applications. *Advanced Functional Materials*, 32(19):2113012, feb 2022. doi: 10.1002/adfm.202113012.

[39] Giuseppe Arrabito, Yana Aleeva, Riccardo Pezzilli, Vittorio Ferrara, Pier Gianni Medaglia, Bruno Pignataro, and Giuseppe Prestopino. Printing ZnO inks: From principles to devices. *Crystals*, 10(6):449, may 2020. doi: 10.3390/cryst10060449.

[40] Sunho Jeong, Hae Chon Song, Won Woo Lee, Hye Jung Suk, Sun Sook Lee, Taek Ahn, Jae-Won Ka, Youngmin Choi, Mi Hye Yi, and Beyong-Hwan Ryu. Printed cu source/drain electrode capped by CuO hole injection layer for organic thin film transistors. *Journal of Materials Chemistry*, 21(29):10619, 2011. doi: 10.1039/c1jm11273b.

[41] Yeonjun Oh, Ho Gyu Yoon, Sung-Nam Lee, Han-Ki Kim, and Jihoon Kim. Inkjet-printing of TiO2 co-solvent ink: From uniform ink-droplet to TiO2 photoelectrode for

dye-sensitized solar cells. *Journal of The Electrochemical Society*, 159(1):B34–B38, 2011. doi: 10.1149/2.024201jes.

[42] Nehru Devabharathi, Arun M. Umarji, and Subho Dasgupta. Fully inkjet-printed mesoporous SnO2-based ultrasensitive gas sensors for trace amount NO2 detection. *ACS Applied Materials & Interfaces*, 12(51):57207–57217, dec 2020. doi: 10.1021/acsami.0c14704.

[43] Daniel Corzo, Khulud Almasabi, Eloise Bihar, Sky Macphee, Diego Rosas-Villalva, Nicola Gasparini, Sahika Inal, and Derya Baran. Digital inkjet printing of high-efficiency large-area nonfullerene organic solar cells. *Advanced Materials Technologies*, 4(7):1900040, apr 2019. doi: 10.1002/admt.201900040.

[44] Giulio Pipan, Marco Bogar, Andrea Ciavatti, Laura Basirico, Tobias Cramer, Beatrice Fraboni, and Alessandro Fraleoni-Morgera. Direct inkjet printing of TIPS-pentacene single crystals onto interdigitated electrodes by chemical confinement. *Advanced Materials Interfaces*, 5(3):1700925, nov 2017. doi: 10.1002/admi.201700925.

[45] Ulrich Gengenbach, Martin Ungerer, Liane Koker, Klaus-Martin Reichert, Peter Stiller, Stephan Allgeier, Bernd Köhler, Xiaoqi Zhu, Chengyuan Huang, and Veit Hagenmeyer. Automated fabrication of hybrid printed electronic circuits. *Mechatronics*, 70:102403, oct 2020. doi: 10.1016/j.mechatronics.2020.102403.

[46] Timo Reinheimer, Raheleh Azmi, and Joachim R. Binder. Polymerizable ceramic ink system for thin inkjet-printed dielectric layers. *ACS Applied Materials & Interfaces*, 12(2): 2974–2982, dec 2019. doi: 10.1021/acsami.9b18610.

[47] Tim P. Mach, Yingfang Ding, and Joachim R. Binder. Impact of particle and crystallite size of ba0.6sr0.4tio3 on the dielectric properties of BST/p(VDF-TrFE) composites in fully printed varactors. *Polymers*, 14(22):5027, nov 2022. doi: 10.3390/polym14225027.

[48] Xiang Ding, Yongxiang Li, Dong Wang, and Qingrui Yin. Fabrication of BaTiO3 dielectric films by direct ink-jet printing. *Ceramics International*, 30(7):1885–1887, jan 2004. doi: 10.1016/j.ceramint.2003.12.050.

[49] Jaehoon Jeong, Gabriel Cadilha Marques, Xiaowei Feng, Dominic Boll, Surya Abhishek Singaraju, Jasmin Aghassi-Hagmann, Horst Hahn, and Ben Breitung. Ink-jet printable, self-assembled, and chemically crosslinked ion-gel as electrolyte for thin film, printable transistors. *Advanced Materials Interfaces*, 6(21):1901074, sep 2019. doi: 10.1002/admi.201901074.

[50] Lu Zhou and Yifeng Jiang. Recent progress in dielectric nanocomposites. *Materials Science and Technology*, 36(1):1–16, January 2020. ISSN 1743-2847. doi: 10.1080/02670836.2019.1675335.

[51] Min Wang, Wenfang Li, Xi Zuo, Wen Zhu, and Guoge Zhang. Structure and dielectric properties of barium strontium titanate ferroelectric thin film prepared by dc micro-arc oxidation. *Applied Physics A*, 126(9), September 2020. ISSN 1432-0630. doi: 10.1007/s00339-020-03937-0.

[52] R.K. Goyal, S.S. Katkade, and D.M. Mule. Dielectric, mechanical and thermal properties of polymer/BaTiO3 composites for embedded capacitor. *Composites Part B: Engineering*, 44(1):128–132, jan 2013. doi: 10.1016/j.compositesb.2012.06.019.

[53] Bhagyashree Mishra and Yihong Maggie Chen. All-aerosol-jet-printed carbon nanotube transistor with cross-linked polymer dielectrics. *Nanomaterials*, 12(24):4487, dec 2022. doi: 10.3390/nano12244487.

[54] Moriom R. Momota, Tamanna Ferdous, Tomoko Fujiwara, and Bashir I. Morshed. Fabrication and characterization of flexible solid-state MIM supercapacitor with inkjet-printing of stacked ag NP and polymer dielectric layers. In *2023 IEEE 16th Dallas Circuits and Systems Conference (DCAS)*. IEEE, apr 2023. doi: 10.1109/dcas57389.2023.10130228.

[55] Weimin Xia and Zhicheng Zhang. PVDF-based dielectric polymers and their applications in electronic materials. *IET Nanodielectrics*, 1(1):17–31, apr 2018. doi: 10.1049/iet-nde.2018.0001.

[56] Arjun Singh, Monica Katiyar, and Ashish Garg. Understanding the formation of PEDOT:PSS films by ink-jet printing for organic solar cell applications. *RSC Advances*, 5(96):78677–78685, 2015. doi: 10.1039/c5ra11032g.

[57] Simone Neermann, Matthias Scheetz, Joerg Franke, Jewgeni Roudenko, Julian Schirmer, and Marcus Reichenberger. Substrate pretreatments: An investigation of the effects on aerosol jet printed structures. In *Advances in Production Research*, pages 352–360. Springer International Publishing, nov 2018. doi: 10.1007/978-3-030-03451-1_35.

[58] Giovanni Nisato, Donald Lupo, and Simone Ganz. *Organic and printed electronics*, volume 2. CRC Press, Taylor & Francis Group, 2016.

[59] Helmut Kipphan. *Handbook of Print Media*. Springer Berlin Heidelberg, 2001. ISBN 9783540299004. doi: 10.1007/978-3-540-29900-4.

[60] Giorgio Mattana, Alberto Loi, Marion Woytasik, Massimo Barbaro, Vincent Noeel, and Benoit Piro. Inkjet-printing: A new fabrication technology for organic transistors. *Advanced Materials Technologies*, 2(10):1700063, sep 2017. doi: 10.1002/admt.201700063.

[61] Kye-Si Kwon, Md. Khalilur Rahman, Thanh Huy Phung, Steve Hoath, SunHo Jeong, and Jang Sub Kim. Review of digital printing technologies for electronic materials. *Flexible and Printed Electronics*, November 2020. ISSN 2058-8585. doi: 10.1088/2058-8585/abc8ca.

[62] Oke Oktavianty, Yoshie Ishii, Shigeyuki Haruyama, Tadayuki Kyoutani, Zefry Darmawan, and Suluh Elman Swara. Controlling droplet behaviour and quality of dod inkjet printer by designing actuation waveform for multi-drop method. *IOP Conference Series: Materials Science and Engineering*, 1034(1):012091, February 2021. ISSN 1757-899X. doi: 10.1088/1757-899x/1034/1/012091.

[63] A. Berni, M. Mennig, and H. Schmidt. *Doctor Blade*, pages 89–92. Springer US, 2004. ISBN 9780387889535. doi: 10.1007/978-0-387-88953-5_10.

[64] Zehua Chen, Ulrich Gengenbach, Xinnan Liu, Alexander Scholz, Lukas Zimmermann, Jasmin Aghassi-Hagmann, and Liane Koker. An automated room temperature flip-chip mounting process for hybrid printed electronics. *Micromachines*, 13(4):583, apr 2022. doi: 10.3390/mi13040583.

[65] Nabih Othman. *Entwicklung eines Verfahrens zum präzisen Punkt- und Linienauftrag von hochviskosem Leitkleber mit einem geregelten Mikrodosiersystem.* PhD thesis, 2005.

[66] Li Jianping and Deng Guiling. Technology development and basic theory study of fluid dispensing - a review. In *Proceedings of the Sixth IEEE CPMT Conference on High Density Microsystem Design and Packaging and Component Failure Analysis (HDP '04)*, pages 198–205, 2004. doi: 10.1109/HPD.2004.1346698.

[67] Qijin Huang and Yong Zhu. Printing conductive nanomaterials for flexible and stretchable electronics: A review of materials, processes, and applications. *Advanced Materials Technologies*, 4(5):1800546, jan 2019. doi: 10.1002/admt.201800546.

[68] Zehua Chen, Ulrich Gengenbach, Liane Koker, Liyu Huang, Tim P. Mach, Klaus-Martin Reichert, Richard Thelen, and Martin Ungerer. Systematic investigation of novel, controlled low-temperature sintering processes for inkjet printed silver nanoparticle ink. *Small*, December 2023. ISSN 1613-6829. doi: 10.1002/smll.202306865.

[69] Fan Gao and Zhiyong Gu. Melting temperature of metallic nanoparticles. In *Handbook of Nanoparticles*, pages 661–690. Springer International Publishing, 2016. doi: 10.1007/978-3-319-15338-4_6.

[70] Ph. Buffat and J-P. Borel. Size effect on the melting temperature of gold particles. *Physical Review A*, 13(6):2287–2298, jun 1976. doi: 10.1103/physreva.13.2287.

[71] I. Shyjumon, M. Gopinadhan, O. Ivanova, M. Quaas, H. Wulff, C. A. Helm, and R. Hippler. Structural deformation, melting point and lattice parameter studies of size selected silver clusters. *The European Physical Journal D*, 37(3):409–415, nov 2005. doi: 10.1140/epjd/e2005-00319-x.

[72] Wenhua Luo, Wangyu Hu, and Shifang Xiao. Size effect on the thermodynamic properties of silver nanoparticles. *The Journal of Physical Chemistry C*, 112(7):2359–2369, jan 2008. doi: 10.1021/jp0770155.

[73] Kan-Sen Chou, Kuo-Cheng Huang, and Hsien-Hsuen Lee. Fabrication and sintering effect on the morphologies and conductivity of nano-ag particle films by the spin coating method. *Nanotechnology*, 16(6):779–784, apr 2005. doi: 10.1088/0957-4484/16/6/027.

[74] Julia R. Greer and Robert A. Street. Thermal cure effects on electrical performance of nanoparticle silver inks. *Acta Materialia*, 55(18):6345–6349, oct 2007. doi: 10.1016/j.actamat.2007.07.040.

[75] Clara Cano-Raya, Zlatan Z. Denchev, Sílvia F. Cruz, and Júlio C. Viana. Chemistry of solid metal-based inks and pastes for printed electronics - a review. *Applied Materials Today*, 15:416–430, jun 2019. doi: 10.1016/j.apmt.2019.02.012.

[76] Jolke Perelaer, Robert Abbel, Sebastian Wünscher, Robin Jani, Tim van Lammeren, and Ulrich S. Schubert. Roll-to-roll compatible sintering of inkjet printed features by photonic and microwave exposure: From non-conductive ink to 40% bulk silver conductivity in less than 15 seconds. *Advanced Materials*, 24(19):2620–2625, apr 2012. doi: 10.1002/adma.201104417.

[77] Mark L Allen, Mikko Aronniemi, Tomi Mattila, Ari Alastalo, Kimmo Ojanperä, Mika Suhonen, and Heikki Seppä. Electrical sintering of nanoparticle structures. *Nanotechnology*, 19(17):175201, mar 2008. doi: 10.1088/0957-4484/19/17/175201.

[78] Mark Allen, Ari Alastalo, Mika Suhonen, Tomi Mattila, Jaakko Leppaniemi, and Heikki Seppa. Contactless electrical sintering of silver nanoparticles on flexible substrates. *IEEE Transactions on Microwave Theory and Techniques*, 59(5):1419–1429, may 2011. doi: 10.1109/tmtt.2011.2123910.

[79] Shin Jang, Dong Jun Lee, Dohyung Lee, and Je Hoon Oh. Electrical sintering characteristics of inkjet-printed conductive ag lines on a paper substrate. *Thin Solid Films*, 546:157–161, nov 2013. doi: 10.1016/j.tsf.2013.05.015.

[80] Juha Niittynen, Robert Abbel, Matti Mäntysalo, Jolke Perelaer, Ulrich S. Schubert, and Donald Lupo. Alternative sintering methods compared to conventional thermal sintering for inkjet printed silver nanoparticle ink. *Thin Solid Films*, 556:452–459, apr 2014. doi: 10.1016/j.tsf.2014.02.001.

[81] Yong-Rae Jang, Sung-Jun Joo, Ji-Hyeon Chu, Hui-Jin Uhm, Jong-Whi Park, Chung-Hyeon Ryu, Myeong-Hyeon Yu, and Hak-Sung Kim. A review on intense pulsed light sintering technologies for conductive electrodes in printed electronics. *International Journal of Precision Engineering and Manufacturing-Green Technology*, 8(1):327–363, feb 2020. doi: 10.1007/s40684-020-00193-8.

[82] Michael J. Renn, Matthew Schrandt, Jaxon Renn, and James Q. Feng. Localized laser sintering of metal nanoparticle inks printed with aerosol jet® technology for flexible electronics. *Journal of Microelectronics and Electronic Packaging*, 14(4):132–139, oct 2017. doi: 10.4071/imaps.521797.

[83] Aurore Denneulin, Anne Blayo, Charles Neuman, and Julien Bras. Infra-red assisted sintering of inkjet printed silver tracks on paper substrates. *Journal of Nanoparticle Research*, 13(9):3815–3823, mar 2011. doi: 10.1007/s11051-011-0306-2.

[84] Ho Sun Lim, Soo Jin Kim, Ho Won Jang, and Jung Ah Lim. Intense pulsed light for split-second structural development of nanomaterials. *Journal of Materials Chemistry C*, 5 (29):7142–7160, 2017. doi: 10.1039/c7tc01848g.

[85] Franziska M. Wolf, Jolke Perelaer, Steffi Stumpf, Dirk Bollen, Frank Kriebel, and Ulrich S. Schubert. Rapid low-pressure plasma sintering of inkjet-printed silver nanoparticles for RFID antennas. *Journal of Materials Research*, 28(9):1254–1261, may 2013. doi: 10.1557/jmr. 2013.73.

[86] Shlomo Magdassi, Michael Grouchko, Oleg Berezin, and Alexander Kamyshny. Triggering the sintering of silver nanoparticles at room temperature. *ACS Nano*, 4(4):1943–1948, apr 2010. doi: 10.1021/nn901868t.

[87] Juuso Olkkonen, Jaakko Leppäniemi, Tomi Mattila, and Kim Eiroma. Sintering of inkjet printed silver tracks with boiling salt water. *Journal of Materials Chemistry C*, 2(18):3577, 2014. doi: 10.1039/c3tc32565b.

[88] Peng Peng, Lihang Li, Wei Guo, Zhuang Hui, Jian Fu, Chao Jin, Yangai Liu, and Ying Zhu. Room-temperature joining of silver nanoparticles using potassium chloride solution for flexible electrode application. *The Journal of Physical Chemistry C*, 122(5):2704–2711, jan 2018. doi: 10.1021/acs.jpcc.7b10601.

[89] Y. Xiao, Z.H. Zhang, M. Yang, H.F. Yang, M.Y. Li, and Y. Cao. The effect of NaOH on room-temperature sintering of ag nanoparticles for high-performance flexible electronic application. *Materials Letters*, 222:16–20, jul 2018. doi: 10.1016/j.matlet.2018.03.164.

[90] Yao Tang, Wei He, Guoyun Zhou, Shouxu Wang, Xiaojian Yang, Zhihua Tao, and Juncheng Zhou. A new approach causing the patterns fabricated by silver nanoparticles to be conductive without sintering. *Nanotechnology*, 23(35):355304, aug 2012. doi: 10.1088/0957-4484/23/35/355304.

[91] Pei-Chun Chiang, Wha-Tzong Whang, Sheng-Chang Wu, and Kuen-Ru Chuang. Effects of titania content and plasma treatment on the interfacial adhesion mechanism of nano titania-hybridized polyimide and copper system. *Polymer*, 45(13):4465–4472, jun 2004. doi: 10.1016/j.polymer.2004.04.024.

[92] Zhaoyang Zhong, Kyoohee Woo, Inhyuk Kim, Hyewon Hwang, Sin Kwon, Young-Man Choi, Youngu Lee, Taik-Min Lee, Kwangyoung Kim, and Jooho Moon. Roll-to-roll-compatible, flexible, transparent electrodes based on self-nanoembedded cu nanowires using intense pulsed light irradiation. *Nanoscale*, 8(16):8995–9003, 2016. doi: 10.1039/c6nr00444j.

[93] Yi Li, Russel Torah, Steve Beeby, and John Tudor. An all-inkjet printed flexible capacitor on a textile using a new poly(4-vinylphenol) dielectric ink for wearable applications. In *2012 IEEE Sensors*. IEEE, oct 2012. doi: 10.1109/icsens.2012.6411117.

[94] Cristian Mendes-Felipe, Juliana Oliveira, Ikerne Etxebarria, José Luis Vilas-Vilela, and Senentxu Lanceros-Mendez. State-of-the-art and future challenges of UV curable polymer-based smart materials for printing technologies. *Advanced Materials Technologies*, 4(3): 1800618, jan 2019. doi: 10.1002/admt.201800618.

[95] Oshadha K. Ranasingha, Mahdi Haghzadeh, Margaret J. Sobkowicz, Edward Kingsley, Craig Armiento, and Alkim Akyurtlu. Formulation and characterization of sinterless barium strontium titanate (BST) dielectric nanoparticle ink for printed RF and microwave applications. *Journal of Electronic Materials*, 50(6):3241–3248, apr 2021. doi: 10.1007/s11664-021-08915-7.

[96] Mahmuda Akter Monne, Chandan Qumar Howlader, Bhagyashree Mishra, and Maggie Yihong Chen. Synthesis of printable polyvinyl alcohol for aerosol jet and inkjet printing technology. *Micromachines*, 12(2):220, feb 2021. doi: 10.3390/mi12020220.

[97] Neil Graddage, Ta-Ya Chu, Heping Ding, Christophe Py, Afshin Dadvand, and Ye Tao. Inkjet printed thin and uniform dielectrics for capacitors and organic thin film transistors enabled by the coffee ring effect. *Organic Electronics*, 29:114–119, feb 2016. doi: 10.1016/j.orgel.2015.11.039.

[98] Y NOH and H SIRRINGHAUS. Ultra-thin polymer gate dielectrics for top-gate polymer field-effect transistors. *Organic Electronics*, 10(1):174–180, feb 2009. doi: 10.1016/j.orgel.2008.10.021.

[99] Rubaiyet Iftekharul Haque, Rémy Vié, Michel Germainy, Laurie Valbin, Patrick Benaben, and Xavier Boddaert. Inkjet printing of high molecular weight PVDF-TrFE for flexible electronics. *Flexible and Printed Electronics*, 1(1):015001, oct 2015. doi: 10.1088/2058-8585/1/1/015001.

[100] Benjamin S. Cook, James R. Cooper, and Manos M. Tentzeris. Multi-layer RF capacitors on flexible substrates utilizing inkjet printed dielectric polymers. *IEEE Microwave and Wireless Components Letters*, 23(7):353–355, jul 2013. doi: 10.1109/lmwc.2013.2264658.

[101] Lisa Petani, Anja Schweizer, Christian Pylatiuk, Peter Stiller, Klaus-Martin Reichert, Ulrich Gengenbach, and Martin Ungerer. Optimised inkjet-printing parameters and processing

techniques for an exemplary structure of an oxygen sensor on a polyimide substrate. In *2023 IEEE International Conference on Flexible and Printable Sensors and Systems (FLEPS)*, pages 1–4. IEEE, July 2023. doi: 10.1109/fleps57599.2023.10220420.

[102] Colin Tong. *Substrate and Encapsulation Materials for Printed Flexible Electronics*, pages 221–255. Springer International Publishing, October 2021. ISBN 9783030798048. doi: 10.1007/978-3-030-79804-8_5.

[103] Jenny Wiklund, Alp Karakoç, Toni Palko, Hüseyin Yiğitler, Kalle Ruttik, Riku Jäntti, and Jouni Paltakari. A review on printed electronics: Fabrication methods, inks, substrates, applications and environmental impacts. *Journal of Manufacturing and Materials Processing*, 5(3):89, aug 2021. doi: 10.3390/jmmp5030089.

[104] Mark Allen, Jaakko Leppäniemi, Marja Vilkman, Ari Alastalo, and Tomi Mattila. Substrate-facilitated nanoparticle sintering and component interconnection procedure. *Nanotechnology*, 21(47):475204, oct 2010. doi: 10.1088/0957-4484/21/47/475204.

[105] Justin Bourassa, Alex Ramm, James Q. Feng, and Michael J. Renn. Water vapor-assisted sintering of silver nanoparticle inks for printed electronics. *SN Applied Sciences*, 1(6), may 2019. doi: 10.1007/s42452-019-0542-0.

[106] Zuofeng Chen, Shengrong Ye, Ian E. Stewart, and Benjamin J. Wiley. Copper nanowire networks with transparent oxide shells that prevent oxidation without reducing transmittance. *ACS Nano*, 8(9):9673–9679, sep 2014. doi: 10.1021/nn504308n.

[107] Yan Li, Tianke Qi, Miao Chen, and Fei Xiao. Mixed ink of copper nanoparticles and copper formate complex with low sintering temperatures. *Journal of Materials Science: Materials in Electronics*, 27(11):11432–11438, jul 2016. doi: 10.1007/s10854-016-5269-8.

[108] S. Gardonio, L. Gregoratti, P. Melpignano, L. Aballe, V. Biondo, R. Zamboni, M. Murgia, S. Caria, and M. Kiskinova. Degradation of organic light-emitting diodes under different environment at high drive conditions. *Organic Electronics*, 8(1):37–43, feb 2007. doi: 10.1016/j.orgel.2006.10.005.

[109] Qian Lu, Zhichun Yang, Xin Meng, Youfeng Yue, Muhammad Ashfaq Ahmad, Wenjun Zhang, Shasha Zhang, Yiqiang Zhang, Zonghao Liu, and Wei Chen. A review on encapsulation technology from organic light emitting diodes to organic and perovskite solar cells. *Advanced Functional Materials*, 31(23):2100151, mar 2021. doi: 10.1002/adfm.202100151.

[110] Se Hyun Kim, Kihyon Hong, Wei Xie, Keun Hyung Lee, Sipei Zhang, Timothy P. Lodge, and C. Daniel Frisbie. Electrolyte-gated transistors for organic and printed electronics. *Advanced Materials*, 25(13):1822–1846, December 2012. ISSN 1521-4095. doi: 10.1002/adma.201202790.

[111] Gabriel Cadilha Marques, Falk von Seggern, Simone Dehm, Ben Breitung, Horst Hahn, Subho Dasgupta, Mehdi B. Tahoori, and Jasmin Aghassi-Hagmann. Influence of humidity on the performance of composite polymer electrolyte-gated field-effect transistors and circuits. *IEEE Transactions on Electron Devices*, 66(5):2202–2207, may 2019. doi: 10.1109/ted.2019.2903456.

[112] S. Logothetidis, A. Laskarakis, D. Georgiou, S. Amberg-Schwab, U. Weber, K. Noller, M. Schmidt, E. Küçükpinar-Niarchos, and W. Lohwasser. Ultra high barrier materials for encapsulation of flexible organic electronics. *The European Physical Journal Applied Physics*, 51(3):33203, sep 2010. doi: 10.1051/epjap/2010102.

[113] K. Prasad, M. Nikzad, and I. Sbarski. Permeability control in polymeric systems: a review. *Journal of Polymer Research*, 25(11), oct 2018. doi: 10.1007/s10965-018-1636-x.

[114] Iftikhar Ahmed Channa, Andreas Distler, Christoph J. Brabec, and Hans-Joachim Egelhaaf. Solution-coated barriers for organic electronics. In *Organic Flexible Electronics*, pages 249–303. Elsevier, 2021. doi: 10.1016/b978-0-12-818890-3.00009-6.

[115] Valentina Siracusa. Food packaging permeability behaviour: A report. *International Journal of Polymer Science*, 2012:1–11, 2012. doi: 10.1155/2012/302029.

[116] Esra Kucukpinar and Pemra Doruker. Molecular simulations of small gas diffusion and solubility in copolymers of styrene. *Polymer*, 44(12):3607–3620, jun 2003. doi: 10.1016/s0032-3861(03)00166-6.

[117] G. Choudalakis and A.D. Gotsis. Permeability of polymer/clay nanocomposites: A review. *European Polymer Journal*, 45(4):967–984, apr 2009. doi: 10.1016/j.eurpolymj.2009.01.027.

[118] B. Tan and N.L. Thomas. A review of the water barrier properties of polymer/clay and polymer/graphene nanocomposites. *Journal of Membrane Science*, 514:595–612, sep 2016. doi: 10.1016/j.memsci.2016.05.026.

[119] Philip Hülsmann, Daniel Philipp, and Michael Köhl. Measuring temperature-dependent water vapor and gas permeation through high barrier films. *Review of Scientific Instruments*, 80(11), nov 2009. doi: 10.1063/1.3250866.

[120] Soney C George and Sabu Thomas. Transport phenomena through polymeric systems. *Progress in Polymer Science*, 26(6):985–1017, aug 2001. doi: 10.1016/s0079-6700(00)00036-8.

[121] Sina Ebnesajjad. Chemical properties of fluoropolymers. In *Fluoroplastics*, pages 432–474. Elsevier, 2015. doi: 10.1016/b978-1-4557-3197-8.00015-8.

[122] Maryam Fereydoon and Sina Ebnesajjad. Development of high-barrier film for food packaging. In *Plastic Films in Food Packaging*, pages 71–92. Elsevier, 2013. doi: 10.1016/b978-1-4557-3112-1.00005-3.

[123] Charles M. Hansen. *Hansen Solubility Parameters: A User's Handbook, Second Edition*. CRC Press, June 2007. ISBN 9780429127526. doi: 10.1201/9781420006834.

[124] R. Gref, Q. T. Nguyen, P. Schaetzel, and J. Néel. Transport properties of poly(vinyl alcohol) membranes of different degrees of crystallinity. i. pervaporation results. *Journal of Applied Polymer Science*, 49(2):209–218, jul 1993. doi: 10.1002/app.1993.070490203.

[125] Tarek M Madkour, Sahar K Mohamed, and Abdalla M Barakat. Interplay of the polymer stiffness and the permeability behavior of silane and siloxane polymers. *Polymer*, 43(2): 533–539, January 2002. ISSN 0032-3861. doi: 10.1016/s0032-3861(01)00415-3.

[126] Sina Ebnesajjad and Pradip R. Khaladkar. 4 - selecting fluoropolymers for corrosion control. In Sina Ebnesajjad and Pradip R. Khaladkar, editors, *Fluoropolymer Applications in the Chemical Processing Industries (Second Edition)*, Plastics Design Library, pages 129–184. William Andrew Publishing, second edition edition, 2018. ISBN 978-0-323-44716-4. doi: https://doi.org/10.1016/B978-0-323-44716-4.00004-X. URL `https://www.sciencedirect.com/science/article/pii/B978032344716400004X`.

[127] Sanjeevamuthu Suganthi, Subramanian Mohanapriya, Vairamuthu Raj, Selvaraj Kanaga, Ramamurthy Dhandapani, Shanmugam Vignesh, and Jeyaperumal Kalyana Sundar. Tunable physicochemical and bactericidal activity of multicarboxylic-acids-crosslinked polyvinyl alcohol membrane for food packaging applications. *ChemistrySelect*, 3(40):11167–11176, oct 2018. doi: 10.1002/slct.201801851.

[128] Mijin Lim, Hyok Kwon, Dowan Kim, Jongchul Seo, Haksoo Han, and Sher Bahadar Khan. Highly-enhanced water resistant and oxygen barrier properties of cross-linked poly(vinyl alcohol) hybrid films for packaging applications. *Progress in Organic Coatings*, 85:68–75, aug 2015. doi: 10.1016/j.porgcoat.2015.03.005.

[129] Brian Bolto, Thuy Tran, Manh Hoang, and Zongli Xie. Crosslinked poly(vinyl alcohol) membranes. *Progress in Polymer Science*, 34(9):969–981, sep 2009. doi: 10.1016/j.progpolymsci.2009.05.003.

[130] Kaiyan Qiu and Anil N. Netravali. Halloysite nanotube reinforced biodegradable nanocomposites using noncrosslinked and malonic acid crosslinked polyvinyl alcohol. *Polymer Composites*, 34(5):799–809, apr 2013. doi: 10.1002/pc.22482.

[131] Katia C. S. Figueiredo, Tito L. M. Alves, and Cristiano P. Borges. Poly(vinyl alcohol) films crosslinked by glutaraldehyde under mild conditions. *Journal of Applied Polymer Science*, 111(6):3074–3080, jan 2009. doi: 10.1002/app.29263.

[132] Jie Chen, Yadong Li, Yin Zhang, and Yangguang Zhu. Preparation and characterization of graphene oxide reinforced PVA film with boric acid as crosslinker. *Journal of Applied Polymer Science*, 132(22):n/a–n/a, feb 2015. doi: 10.1002/app.42000.

[133] Divya Nataraj, Roopa Reddy, and Narendra Reddy. Crosslinking electrospun poly (vinyl) alcohol fibers with citric acid to impart aqueous stability for medical applications. *European Polymer Journal*, 124:109484, feb 2020. doi: 10.1016/j.eurpolymj.2020.109484.

[134] Fabio Roberto Passador, Adhemar Collà Ruvolo-Filho, and Luiz Antonio Pessan. Structural, thermal, and gas transport properties of HDPE/LLDPE blend-based nanocomposites using a mixture of HDPE-g-MA and LLDPE-g-MA as compatibilizer. *Polymer Engineering & Science*, 56(7):765–775, mar 2016. doi: 10.1002/pen.24305.

[135] Yaowen Liu, Shuyao Wang, and Wenting Lan. Fabrication of antibacterial chitosan-PVA blended film using electrospray technique for food packaging applications. *International Journal of Biological Macromolecules*, 107:848–854, feb 2018. doi: 10.1016/j.ijbiomac .2017.09.044.

[136] Zhaogang Liu, Hongchao Lu, Huili Zhang, and Li Li. Poly (vinyl alcohol)/polylactic acid blend film with enhanced processability, compatibility, and mechanical property fabricated via melt processing. *Journal of Applied Polymer Science*, 138(41), may 2021. doi: 10.1002/app.51204.

[137] Jinho Hah, Michael Sulkis, Chao Ren, Minsoo Kang, Kyoung sik Moon, Samuel Graham, and C. P. Wong. Moisture barrier, mechanical, and thermal properties of PDMS-PIB blends for solar photovoltaic (PV) module encapsulant. In *2019 IEEE 69th Electronic Components and Technology Conference (ECTC)*. IEEE, may 2019. doi: 10.1109/ectc.2019.00303.

[138] A. Sorrentino, M. Tortora, and V. Vittoria. Diffusion behavior in polymer-clay nanocomposites. *Journal of Polymer Science Part B: Polymer Physics*, 44(2):265–274, 2005. doi: 10.1002/polb.20684.

[139] Ankush A. Gokhale and Ilsoon Lee. Recent advances in the fabrication of nanostructured barrier films. *Journal of Nanoscience and Nanotechnology*, 14(3):2157–2177, mar 2014. doi: 10.1166/jnn.2014.8517.

[140] Lawrence E. Nielsen. Models for the permeability of filled polymer systems. *Journal of Macromolecular Science: Part A - Chemistry*, 1(5):929–942, aug 1967. doi: 10.1080/ 10601326708053745.

[141] R. K. Bharadwaj. Modeling the barrier properties of polymer-layered silicate nanocomposites. *Macromolecules*, 34(26):9189–9192, nov 2001. doi: 10.1021/ma010780b.

[142] Yanbin Cui, S. Kumar, Balakantha Rao Kona, and Daniel van Houcke. Gas barrier properties of polymer/clay nanocomposites. *RSC Advances*, 5(78):63669–63690, 2015. doi: 10.1039/c5ra10333a.

[143] Jaime C. Grunlan, Ani Grigorian, Charles B. Hamilton, and Ali R. Mehrabi. Effect of clay concentration on the oxygen permeability and optical properties of a modified poly(vinyl alcohol). *Journal of Applied Polymer Science*, 93(3):1102–1109, 2004. doi: 10.1002/app.20564.

[144] Julien Gaume, Christine Taviot-Gueho, Stéphane Cros, Agnès Rivaton, Sandrine Thérias, and Jean-Luc Gardette. Optimization of PVA clay nanocomposite for ultra-barrier multilayer encapsulation of organic solar cells. *Solar Energy Materials and Solar Cells*, 99:240–249, apr 2012. doi: 10.1016/j.solmat.2011.12.005.

[145] Xiang-Yun Du, Zheng-Bai Zhao, Rui Cheng, and Ji-Dong Liu. Study the factors affecting water vapor barrier properties of organic-inorganic hybrid coatings. *Ceramics International*, 49(1):1521–1528, jan 2023. doi: 10.1016/j.ceramint.2022.10.255.

[146] Lina Sun, Kaho Uemura, Tatsuhiro Takahashi, Tsukasa Yoshida, and Yoshiyuki Suzuri. Interfacial engineering in solution processing of silicon-based hybrid multilayer for high performance thin film encapsulation. *ACS Applied Materials & Interfaces*, 11(46):43425–43432, oct 2019. doi: 10.1021/acsami.9b14994.

[147] Iftikhar Ahmed Channa, Andreas Distler, Michael Zaiser, Christoph J. Brabec, and Hans-Joachim Egelhaaf. Thin film encapsulation of organic solar cells by direct deposition of polysilazanes from solution. *Advanced Energy Materials*, page 1900598, may 2019. doi: 10.1002/aenm.201900598.

[148] Won Jae Lee, Jin Yeong Park, Hyun Jin Nam, and Sung-Hoon Choa. The development of a highly stretchable, durable, and printable textile electrode. *Textile Research Journal*, 89 (19-20):4104–4113, feb 2019. doi: 10.1177/0040517519828992.

[149] A. Abellán-Llobregat, Itthipon Jeerapan, A. Bandodkar, L. Vidal, A. Canals, J. Wang, and E. Morallón. A stretchable and screen-printed electrochemical sensor for glucose determination in human perspiration. *Biosensors and Bioelectronics*, 91:885–891, may 2017. doi: 10.1016/j.bios.2017.01.058.

[150] Ana Moya, Enrico Sowade, Francisco J. del Campo, Kalyan Y. Mitra, Eloi Ramon, Rosa Villa, Reinhard R. Baumann, and Gemma Gabriel. All-inkjet-printed dissolved oxygen sensors on flexible plastic substrates. *Organic Electronics*, 39:168–176, dec 2016. doi: 10.1016/j.orgel.2016.10.002.

[151] Yen-Cheng Kung, Nahid Hosseini, Dumitru Dumcenco, Georg E. Fantner, and Andras Kis. Air and water-stable n-type doping and encapsulation of flexible MoS2 devices with SU8. *Advanced Electronic Materials*, 5(1):1800492, jan 2019. doi: 10.1002/aelm.201800492.

[152] Wei Yuan, Xinzhou Wu, Weibing Gu, Jian Lin, and Zheng Cui. Printed stretchable circuit on soft elastic substrate for wearable application. *Journal of Semiconductors*, 39(1):015002, jan 2018. doi: 10.1088/1674-4926/39/1/015002.

[153] Jongsu Oh, Jin-Ho Kim, So Young Lee, Min Su Kim, Jae Moon Kim, Keechan Park, and Yong-Sang Kim. Bending performance of flexible organic thin-film transistors with/without encapsulation layer. *IEEE Transactions on Device and Materials Reliability*, 18(1):1–4, mar 2018. doi: 10.1109/tdmr.2017.2780267.

[154] A. Cazalé, W. Sant, F. Ginot, J.-C. Launay, G. Savourey, F. Revol-Cavalier, J.M. Lagarde, D. Heinry, J. Launay, and P. Temple-Boyer. Physiological stress monitoring using sodium ion potentiometric microsensors for sweat analysis. *Sensors and Actuators B: Chemical*, 225: 1–9, mar 2016. doi: 10.1016/j.snb.2015.10.114.

[155] Yoon Kyeung Lee, Jeonghyun Kim, Yerim Kim, Jean Won Kwak, Younghee Yoon, and John A. Rogers. Room temperature electrochemical sintering of zn microparticles and its use in printable conducting inks for bioresorbable electronics. *Advanced Materials*, 29(38): 1702665, aug 2017. doi: 10.1002/adma.201702665.

[156] Yasser Khan, Felippe J. Pavinatto, Monica C. Lin, Amy Liao, Sarah L. Swisher, Kaylee Mann, Vivek Subramanian, Michel M. Maharbiz, and Ana C. Arias. Inkjet-printed flexible gold electrode arrays for bioelectronic interfaces. *Advanced Functional Materials*, 26(7): 1004–1013, dec 2015. doi: 10.1002/adfm.201503316.

[157] D. Yang, Y. q. Yang, Y. Duan, P. Chen, C. L. Zang, Y. Xie, D. M. Liu, X. Wang, Y. H. Duan, F. B. Sun, Q. Gao, and K. W. Xue. Passivation properties of UV-curable polymer for organic light emitting diodes. *ECS Solid State Letters*, 2(9):R31–R33, jun 2013. doi: 10.1149/2.007309ssl.

[158] Bolin Chen, Yizhou Jiang, Xiaohui Tang, Yayue Pan, and Shan Hu. Fully packaged carbon nanotube supercapacitors by direct ink writing on flexible substrates. *ACS Applied Materials & Interfaces*, 9(34):28433–28440, aug 2017. doi: 10.1021/acsami.7b06804.

[159] BASF. Ecoflex: Das Original seit 1998 – zertifiziert kompostierbarer Kunststoff. `https://plastics-rubber.basf.com/global/de/performance_polymers/products/ecoflex.html`. accessed 2020-04-02.

[160] Malo Robin, Wenlin Kuai, Maria Amela-Cortes, Stéphane Cordier, Yann Molard, Tayeb Mohammed-Brahim, Emmanuel Jacques, and Maxime Harnois. Epoxy based ink as versatile

material for inkjet-printed devices. *ACS Applied Materials & Interfaces*, 7(39):21975–21984, sep 2015. doi: 10.1021/acsami.5b06678.

[161] Sjeung Jae Moon, Malo Robin, Kuai Wenlin, Molard Yann, Byung Seong Bae, Tayeb Mohammed-Brahim, Emmanuel Jacques, and Maxime Harnois. Morphological impact of insulator on inkjet-printed transistor. *Flexible and Printed Electronics*, 2(3):035008, sep 2017. doi: 10.1088/2058-8585/aa8760.

[162] S. Amberg-Schwab, M. Hoffmann, H. Bader, and M. Gessler. Inorganic-organic polymers with barrier properties for water vapor, oxygen and flavors. *Journal of Sol-Gel Science and Technology*, 13(1/3):141–146, 1998. doi: 10.1023/a:1008628029870.

[163] K.-H. Haas, S. Amberg-Schwab, K. Rose, and G. Schottner. Functionalized coatings based on inorganic-organic polymers (ORMOCERs) and their combination with vapor deposited inorganic thin films. *Surface and Coatings Technology*, 111(1):72–79, jan 1999. doi: 10.1016/s0257-8972(98)00711-7.

[164] Karl-Heinz Haas and Herbert Wolter. Synthesis, properties and applications of inorganic–organic copolymers (ORMOCERs). *Current Opinion in Solid State and Materials Science*, 4(6):571–580, dec 1999. doi: 10.1016/s1359-0286(00)00009-7.

[165] Clément Sanchez, Philippe Belleville, Michael Popall, and Lionel Nicole. Applications of advanced hybrid organic-inorganic nanomaterials: from laboratory to market. *Chemical Society Reviews*, 40(2):696, 2011. doi: 10.1039/c0cs00136h.

[166] John Fahlteich, Sabine Amberg-Schwab, Ulrike Weber, Klaus Noller, Oliver Miesbauer, Christine Boeffel, and Nicolas Schiller. 29.1: Ultra-high barriers for encapsulation of flexible displays and lighting devices. *SID Symposium Digest of Technical Papers*, 44(1):354–357, jun 2013. doi: 10.1002/j.2168-0159.2013.tb06219.x.

[167] Giovanni Nisato, Hannes Klumbies, John Fahlteich, Lars Müller-Meskamp, Peter van de Weijer, Piet Bouten, Christine Boeffel, David Leunberger, Wülf Graehlert, Steven Edge, Stéphane Cros, Paul Brewer, Esra Kucukpinar, Julia de Girolamo, and Padmanabhan Srinivasan. Experimental comparison of high-performance water vapor permeation measurement methods. *Organic Electronics*, 15(12):3746–3755, dec 2014. doi: 10.1016/j.orgel.2014.10.014.

[168] Sergio Castro-Hermosa, Michiel Top, Janardan Dagar, John Fahlteich, and Thomas M. Brown. Quantifying performance of permeation barrier-encapsulation systems for flexible and glass-based electronics and their application to perovskite solar cells. *Advanced Electronic Materials*, 5(10):1800978, aug 2019. doi: 10.1002/aelm.201800978.

[169] Sabine Amberg-Schwab, Kajetan Müller, Ferdinand Somorowsky, and Sven Sängerlaub. UV-activated, transparent oxygen scavenger coating based on inorganic-organic hybrid

polymer (ORMOCER) with high oxygen absorption capacity. *Coatings*, 13(2):473, feb 2023. doi: 10.3390/coatings13020473.

[170] R. Houbertz, J. Schulz, L. Fröhlich, G. Domann, and M. Popall. Inorganic-organic hybrid materials for polymer electronic applications. *MRS Proceedings*, 769, 2003. doi: 10.1557/proc-769-h7.4.

[171] Huaijun Zhu, Zilin Dai, and Weiping Tu. Study on the preparation and performance of low gas permeability trifluoropropyl phenyl silicone rubber. *RSC Advances*, 7(63):39739–39747, 2017. doi: 10.1039/c7ra07195g.

[172] Arnaud Morlier, Stéphane Cros, Jean-Paul Garandet, and Nicole Alberola. Gas barrier properties of solution processed composite multilayer structures for organic solar cells encapsulation. *Solar Energy Materials and Solar Cells*, 115:93–99, aug 2013. doi: 10.1016/j.solmat.2013.03.033.

[173] Ying Zhan. *Rapid Curing and Boron Modification of Polysilazane-Derived Functional Coatings*. PhD thesis, 2022.

[174] Yuta KOBAYASHI, Hirotaka YOKOTA, Yasushi FUCHITA, Atsushi TAKAHASHI, and Yoshiyuki SUGAHARA. Characterization of gas barrier silica coatings prepared from perhydropolysilazane films by vacuum ultraviolet irradiation. *Journal of the Ceramic Society of Japan*, 121(1410):215–218, 2013. doi: 10.2109/jcersj2.121.215.

[175] Ying Zhan, Ralf Grottenmüller, Wei Li, Farhan Javaid, and Ralf Riedel. Evaluation of mechanical properties and hydrophobicity of room-temperature, moisture-curable polysilazane coatings. *Journal of Applied Polymer Science*, 138(21), jan 2021. doi: 10.1002/app.50469.

[176] Rene Sønderbæk-Jørgensen. *Polysilazanes for Coating Applications*. PhD thesis, 2022.

[177] Iftikhar Ahmed Channa, Aqeel Ahmed Shah, Muhammad Rizwan, Muhammad Atif Makhdoom, Ali Dad Chandio, Muhammad Ali Shar, and Asif Mahmood. Process parameter optimization of a polymer derived ceramic coatings for producing ultra-high gas barrier. *Materials*, 14(22):7000, November 2021. ISSN 1996-1944. doi: 10.3390/ma14227000.

[178] Luke J. Sutherland, Hasitha C. Weerasinghe, and George P. Simon. A review on emerging barrier materials and encapsulation strategies for flexible perovskite and organic photovoltaics. *Advanced Energy Materials*, 11(34), jul 2021. doi: 10.1002/aenm.202101383.

[179] D.R. Paul and L.M. Robeson. Polymer nanotechnology: Nanocomposites. *Polymer*, 49 (15):3187–3204, jul 2008. doi: 10.1016/j.polymer.2008.04.017.

[180] Daniel A. Kunz, Jasmin Schmid, Patrick Feicht, Johann Erath, Andreas Fery, and Josef Breu. Clay-based nanocomposite coating for flexible optoelectronics applying commercial polymers. *ACS Nano*, 7(5):4275–4280, apr 2013. doi: 10.1021/nn400713e.

[181] Evgeny S. Tsurko, Patrick Feicht, Christoph Habel, Theresa Schilling, Matthias Daab, Sabine Rosenfeldt, and Josef Breu. Can high oxygen and water vapor barrier nanocomposite coatings be obtained with a waterborne formulation. *Journal of Membrane Science*, 540: 212–218, oct 2017. doi: 10.1016/j.memsci.2017.06.051.

[182] Chenwei Chen, Youji Chen, Jing Xie, Zhewei Xu, Zhipeng Tang, Fuxin Yang, and Kaijia Fu. Effects of montmorillonite on the properties of cross-linked poly(vinyl alcohol)/boric acid films. *Progress in Organic Coatings*, 112:66–74, nov 2017. doi: 10.1016/j.porgcoat .2017.06.003.

[183] Se Jung Kim, Tan young Kim, Byung Hyun Kang, Gun-Hwan Lee, and Byeong-Kwon Ju. Fabrication of graphene oxide/montmorillonite nanocomposite flexible thin films with improved gas-barrier properties. *RSC Advances*, 8(68):39083–39089, 2018. doi: 10.1039/c8ra08232d.

[184] Chenwei Chen, Rong Ding, Shaohua Yang, Jiaxi Wang, Wenjun Chen, Lin Zong, and Jing Xie. Development of thermal insulation packaging film based on poly(vinyl alcohol) incorporated with silica aerogel for food packaging application. *LWT*, 129:109568, July 2020. ISSN 0023-6438. doi: 10.1016/j.lwt.2020.109568.

[185] Xiao Zhang, Weifeng Liu, Wenqiang Liu, and Xueqing Qiu. High performance PVA/lignin nanocomposite films with excellent water vapor barrier and UV-shielding properties. *International Journal of Biological Macromolecules*, 142:551–558, jan 2020. doi: 10.1016/j.ijbiomac.2019.09.129.

[186] Iftikhar Ahmed Channa, Andreas Distler, Benedikt Scharfe, Sarmad Feroze, Karen Forberich, Benjamin Lipovšek, Christoph J Brabec, and Hans-Joachim Egelhaaf. Solution processed oxygen and moisture barrier based on glass flakes for encapsulation of organic (opto-) electronic devices. *Flexible and Printed Electronics*, 6(2):025006, jun 2021. doi: 10.1088/2058-8585/ac0716.

[187] Zainab Waheed Abdullah, Yu Dong, Ian Jeffery Davies, and Salim Barbhuiya. PVA, PVA blends, and their nanocomposites for biodegradable packaging application. *Polymer-Plastics Technology and Engineering*, 56(12):1307–1344, jan 2017. doi: 10.1080/03602559.2016. 1275684.

[188] Mohammad Karimi. Diffusion in polymer solids and solutions. *Mass transfer in chemical engineering processes*, 25:17, 2011.

[189] Ali Chandio, Iftikhar Channa, Muhammad Rizwan, Shakeel Akram, Muhammad Javed, Sajid Siyal, Muhammad Saleem, Muhammad Makhdoom, Tayyaba Ashfaq, Safia Khan, Shahid Hussain, Munirah Albaqami, and Reham Alotabi. Polyvinyl alcohol and nano-clay based solution processed packaging coatings. *Coatings*, 11(8):942, aug 2021. doi: 10.3390/coatings11080942.

[190] Maximilian Röhrl, Lukas K. S. Federer, Renee L. Timmins, Sabine Rosenfeldt, Theresa Dörres, Christoph Habel, and Josef Breu. Disorder-order transition-improving the moisture sensitivity of waterborne nanocomposite barriers. *ACS Applied Materials & Interfaces*, 13 (40):48101–48109, sep 2021. doi: 10.1021/acsami.1c14246.

[191] Suprakas Sinha Ray and Masami Okamoto. Polymer/layered silicate nanocomposites: a review from preparation to processing. *Progress in Polymer Science*, 28(11):1539–1641, nov 2003. doi: 10.1016/j.progpolymsci.2003.08.002.

[192] Hyunwoo Kim, Ahmed A. Abdala, and Christopher W. Macosko. Graphene/polymer nanocomposites. *Macromolecules*, 43(16):6515–6530, jul 2010. doi: 10.1021/ma100572e.

[193] Haesung Yun, Moo Kon Kim, Hyo Won Kwak, Jeong Yun Lee, Min Hwa Kim, Eui Hwa Kim, and Ki Hoon Lee. Preparation and characterization of silk sericin/glycerol/graphene oxide nanocomposite film. *Fibers and Polymers*, 14(12):2111–2116, dec 2013. doi: 10.1007/s12221-013-2111-2.

[194] Kazuhisa Yano, Arimitsu Usuki, Akane Okada, Toshio Kurauchi, and Osami Kamigaito. Synthesis and properties of polyimide–clay hybrid. *Journal of Polymer Science Part A: Polymer Chemistry*, 31(10):2493–2498, sep 1993. doi: 10.1002/pola.1993.080311009.

[195] Hua-Dong Huang, Peng-Gang Ren, Jun Chen, Wei-Qin Zhang, Xu Ji, and Zhong-Ming Li. High barrier graphene oxide nanosheet/poly(vinyl alcohol) nanocomposite films. *Journal of Membrane Science*, 409-410:156–163, aug 2012. doi: 10.1016/j.memsci.2012.03.051.

[196] Mei-Hui Tsai, Chi-Jung Chang, Horng-Hwa Lu, Yu-Fu Liao, and I-Hsiang Tseng. Properties of magnetron-sputtered moisture barrier layer on transparent polyimide/graphene nanocomposite film. *Thin Solid Films*, 544:324–330, oct 2013. doi: 10.1016/j.tsf.2013.02.105.

[197] I-Hsiang Tseng, Mei-Hui Tsai, and Chi-Wei Chung. Flexible and transparent polyimide films containing two-dimensional alumina nanosheets templated by graphene oxide for improved barrier property. *ACS Applied Materials & Interfaces*, 6(15):13098–13105, jul 2014. doi: 10.1021/am502962b.

[198] Chi-Hao Chang, Tsao-Cheng Huang, Chih-Wei Peng, Tzu-Chun Yeh, Hsin-I Lu, Wei-I Hung, Chang-Jian Weng, Ta-I Yang, and Jui-Ming Yeh. Novel anticorrosion coatings prepared from polyaniline/graphene composites. *Carbon*, 50(14):5044–5051, nov 2012. doi: 10.1016/j.carbon.2012.06.043.

[199] Bryan Pajarito and Masatoshi Kubouchi. Flake-filled polymers for corrosion protection. *JOURNAL OF CHEMICAL ENGINEERING OF JAPAN*, 46(1):18–26, 2013. doi: 10.1252/jcej.12we133.

[200] Iftikhar Ahmed Channa. *Development of Solution Processed Thin Film Barriers for Encapsulating Thin Film Electronics*. PhD thesis, Friedrich-Alexander-Universität Erlangen-Nürnberg (FAU), 2019.

[201] Iftikhar Ahmed Channa, Jaweria Ashfaq, Sadaf Jamal Gilani, Ali Dad Chandio, Sumra Yousuf, Muhammad Atif Makhdoom, and May Nasser bin Jumah. Sustainable and eco-friendly packaging films based on poly (vinyl alcohol) and glass flakes. *Membranes*, 12(7): 701, jul 2022. doi: 10.3390/membranes12070701.

[202] Eun Gyo Jeong, Jeong Hyun Kwon, Ki Suk Kang, So Yeong Jeong, and Kyung Cheol Choi. A review of highly reliable flexible encapsulation technologies towards rollable and foldable OLEDs. *Journal of Information Display*, 21(1):19–32, nov 2019. doi: 10.1080/15980316.2019.1688694.

[203] S. Cros, M. Firon, S. Lenfant, P. Trouslard, and L. Beck. Study of thin calcium electrode degradation by ion beam analysis. *Nuclear Instruments and Methods in Physics Research Section B: Beam Interactions with Materials and Atoms*, 251(1):257–260, sep 2006. doi: 10.1016/j.nimb.2006.06.014.

[204] Patrick Boldrighini, Aurélie Fauveau, Sandrine Thérias, Jean Luc Gardette, Manuel Hidalgo, and Stéphane Cros. Optical calcium test for measurement of multiple permeation pathways in flexible organic optoelectronic encapsulation. *Review of Scientific Instruments*, 90(1), jan 2019. doi: 10.1063/1.5021182.

[205] R.S Kumar, Mark Auch, Eric Ou, Guenther Ewald, and Chua Soo Jin. Low moisture permeation measurement through polymer substrates for organic light emitting devices. *Thin Solid Films*, 417(1-2):120–126, sep 2002. doi: 10.1016/s0040-6090(02)00584-9.

[206] Atsm e96 standard test methods for water vapor transmission of materials. `http://compass.astm.org/` accessed 3.4.2024, 2024.

[207] Martin Ungerer, Zehua Chen, Tim Pang Mach, Klaus-Martin Reichert, Ulrich Gengenbach, Moritz Lindmüller, Joachim R. Binder, Markus Reischl, and Liane Koker. Automated characterisation of printed electronics under adjustable ambient conditions. In *2024 International Semiconductor Conference (CAS)*, pages 69–72. IEEE, October 2024. doi: 10.1109/cas62834.2024.10736741.

[208] American Society for Testing and Materials (ASTM). Astm f1980-21 standard guide for accelerated aging of sterile barrier systems and medical devices1.

[209] INTERNATIONAL ELECTROTECHNICAL COMMISSION (IEC). Iec 60068 environmental testing – part 2-78: Tests – test cab: Damp heat, steady state.

[210] Henrik Andersson, Anatoliy Manuilskiy, Tomas Unander, Cecilia Lidenmark, Sven Forsberg, and Hans-Erik Nilsson. Inkjet printed silver nanoparticle humidity sensor with memory effect on paper. *IEEE Sensors Journal*, 12(6):1901–1905, jun 2012. doi: 10.1109/jsen.2011.2182044.

[211] Sanghyeok Kim, Sejeong Won, Gi-Dong Sim, Inkyu Park, and Soon-Bok Lee. Tensile characteristics of metal nanoparticle films on flexible polymer substrates for printed electronics applications. *Nanotechnology*, 24(8):085701, feb 2013. doi: 10.1088/0957-4484/24/8/085701.

[212] Manish Kumar, Pooja Devi, and V D Shivling. Thermal stability and electrochemical properties of pvp-protected ru nanoparticles synthesized at room temperature. *Materials Research Express*, 4(8):085006, August 2017. ISSN 2053-1591. doi: 10.1088/2053-1591/aa7b42.

[213] Martin Ungerer, Waldemar Spomer, Irene Wacker, Rasmus Schröder, and Ulrich Gengenbach. A method for the analysis of the nano- and micromorphology of printed structures on flexible polymer films: Analysis of the cross section of inkjet-printed conductive traces on pet film substrates based on ultramicrotome sectioning and sem imaging. *International Journal on Advances in Intelligent Systems*, 10(3-4):383–392, 2017. URL `http://www.iariajournals.org/intelligent_systems/intsys_v10_n34_2017_paged.pdf`.

[214] William A. MacDonald, Robert Eveson, Duncan MacKerron, Raymond Adam, Keith Rollins, Robert Rustin, M. Kieran Looney, John Stewart, and Katsuyuki Hashimoto. P-50: The impact of thermal stress, mechanical stress and environment on dimensional reproducibility of polyester film during flexible electronics processing. *SID Symposium Digest of Technical Papers*, 38(1):373–376, may 2007. doi: 10.1889/1.2785310.

[215] Lin Tan, Xiajun Zheng, Lijuan Chen, and Yanmei Wang. Quality testing of human albumin by capillary electrophoresis using thermally cross-linked poly(vinyl pyrrolidone)-coated fused-silica capillary. *Journal of Separation Science*, 37(20):2974–2982, September 2014. ISSN 1615-9314. doi: 10.1002/jssc.201400463.

[216] Kaixuan Li, Chang Li, Huizeng Li, Mingzhu Li, and Yanlin Song. Designable structural coloration by colloidal particle assembly: from nature to artificial manufacturing. *iScience*, 24(2):102121, February 2021. ISSN 2589-0042. doi: 10.1016/j.isci.2021.102121.

[217] Chaoxiong Ma, Michael J. Trujillo, and Jon P. Camden. Nanoporous silver film fabricated by oxygen plasma: A facile approach for sers substrates. *ACS Applied Materials Interfaces*, 8(36):23978–23984, August 2016. ISSN 1944-8252. doi: 10.1021/acsami.6b08191.

[218] Andrea Rónavári, Péter Bélteky, Eszter Boka, Dalma Zakupszky, Nóra Igaz, Bettina Szerencsés, Ilona Pfeiffer, Zoltán Kónya, and Mónika Kiricsi. Polyvinyl-pyrrolidone-coated silver nanoparticles—the colloidal, chemical, and biological consequences of steric

stabilization under biorelevant conditions. *International Journal of Molecular Sciences*, 22 (16):8673, August 2021. ISSN 1422-0067. doi: 10.3390/ijms22168673.

[219] Tung-Han Yang, Jaewan Ahn, Shi Shi, and Dong Qin. Understanding the role of poly(vinylpyrrolidone) in stabilizing and capping colloidal silver nanocrystals. *ACS Nano*, 15(9):14242–14252, August 2021. ISSN 1936-086X. doi: 10.1021/acsnano.1c01668.

[220] A. Jarray, V. Gerbaud, and M. Hemati. Polymer-plasticizer compatibility during coating formulation: A multi-scale investigation. *Progress in Organic Coatings*, 101:195–206, December 2016. ISSN 0300-9440. doi: 10.1016/j.porgcoat.2016.08.008.

[221] F Haaf, A Sanner, and F Straub. Polymers of n-vinylpyrrolidone: Synthesis, characterization and uses. *Polymer Journal*, 17(1):143–152, January 1985. ISSN 1349-0540. doi: 10.1295/polymj.17.143.

[222] Shaun Fitzpatrick, James F McCabe, Catherine R Petts, and Steven W Booth. Effect of moisture on polyvinylpyrrolidone in accelerated stability testing. *International Journal of Pharmaceutics*, 246(1–2):143–151, October 2002. ISSN 0378-5173. doi: 10.1016/s0378-5173(02)00375-7.

[223] Sukanya Bhattacharya, Dharmendar Kumar Sharma, Saumya Saurabh, Suman De, Anirban Sain, Amitabha Nandi, and Arindam Chowdhury. Plasticization of poly(vinylpyrrolidone) thin films under ambient humidity: Insight from single-molecule tracer diffusion dynamics. *The Journal of Physical Chemistry B*, 117(25):7771–7782, June 2013. ISSN 1520-5207. doi: 10.1021/jp401704e.

[224] Ronald B. Heady and John W. Cahn. An analysis of the capillary forces in liquid-phase sintering of spherical particles. *Metallurgical Transactions*, 1(1):185–189, January 1970. ISSN 2379-0083. doi: 10.1007/bf02819260.

[225] The international association for the properties of water and steam (iapws). `http://www.iapws.org/` accessed 15.4.2023, 2023.

[226] Zehua Chen, Ulrich Gengenbach, Shant Gananian, Daniel Moser, Klaus-Martin Reichert, and Liane Koker. Investigation of solution processable moisture barrier films based on a polymer and filler materials. In *2024 IEEE International Conference on Flexible and Printable Sensors and Systems (FLEPS)*. IEEE, June 2024. doi: 10.1109/fleps61194.2024.10603898.

[227] Zehua Chen, Ulrich Gengenbach, Shant Gananian, Daniel Moser, Klaus-Martin Reichert, Liyu Huang, and Liane Koker. Solution processable barrier films using a filled polymer to encapsulate flexible printed electronics. *IEEE Journal on Flexible Electronics*, December 2024. doi: 10.1109/JFLEX.2024.3512473.

[228] Iftikhar Ahmed Channa, Jaweria Ashfaq, Sadaf Jamal Gilani, Aqeel Ahmed Shah, Ali Dad Chandio, and May Nasser bin Jumah. UV blocking and oxygen barrier coatings based on polyvinyl alcohol and zinc oxide nanoparticles for packaging applications. *Coatings*, 12(7): 897, jun 2022. doi: 10.3390/coatings12070897.

[229] Karanjit Kapila, Sushen Kirtania, Lourembam Monika Devi, Akuleti Saikumar, Laxmikant S Badwaik, and Muzamil A Rather. Potential perspectives on the use of poly (vinyl alcohol)/graphene oxide nanocomposite films and its characterization. *Journal of Food Measurement and Characterization*, 18(2):1012–1025, November 2023. ISSN 2193-4134. doi: 10.1007/s11694-023-02264-1.

[230] M. A. Hayat. *Principles and Techniques of Electron Microscopy: Biological Applications*. Cambridge University Press, Cambridge, UK, 4. edition edition, April 2000. ISBN 978-0-521-63287-4.

[231] Irene Wacker, Ronald Curticean, Daniel Ryklin, Britta Weidinger, Frederik Mayer, Li-Yu Huang, Julian Hoffmann, Monsur Islam, Nadine von Coelln, Tanja Schmitt, Christian Huck, Petra Tegeder, Florian Feist, Jochen A. Kammerer, Christopher Barner-Kowollik, Martin Wegener, Eva Blasco, Ulrich Gengenbach, and Rasmus R. Schröder. Deconstructing 3d structured materials by modern ultramicrotomy for multimodal imaging and volume analysis across length scales. *Advanced Functional Materials*, 34(20), July 2023. ISSN 1616-3028. doi: 10.1002/adfm.202302025.

[232] U. Gengenbach, M. Ungerer, E. Aytac, L. Koker, K.-M. Reichert, P. Stiller, and V. Hagenmeyer. An integrated workflow to automatically fabricate flexible electronics by functional printing and SMT component mounting. In *2018 IEEE 14th International Conference on Automation Science and Engineering (CASE)*. IEEE, aug 2018. doi: 10.1109/coase.2018.8560456.

[233] Eckart GmbH. Data sheet of luxan f001. `https://www.eckart.net/en/luxan-f001-038013l90`, accessed 22.8.2024, 2024.

[234] G. Gruetzner, J. Klein, M. Vogler, and A. Schleunitz. Uv-curable hybrid polymers for optical applications: technical challenges, industrial solutions, and future developments. In Georg von Freymann, Winston V. Schoenfeld, and Raymond C. Rumpf, editors, *Advanced Fabrication Technologies for Micro/Nano Optics and Photonics VII*, volume 8974, page 897406. SPIE, March 2014. doi: 10.1117/12.2043038.

[235] Alexandr Otáhal, Imrich Gablech, Josef Skácel, and Ivan Szendiuch. Investigation of the influence of dam and fill encapsulating material shrinkage on a semiconductor substrate warpage. In *2023 46th International Spring Seminar on Electronics Technology (ISSE)*, pages 1–5. IEEE, May 2023. doi: 10.1109/isse57496.2023.10168456.

[236] Mitsuhiro Koden. *Encapsulating Technologies*, pages 71–79. Springer Nature Singapore, 2022. ISBN 9789811935442. doi: 10.1007/978-981-19-3544-2_6.